



HAL
open science

Electronic transport on monolayer MoS₂

Ivanovitch Castillo Arvelo

► **To cite this version:**

Ivanovitch Castillo Arvelo. Electronic transport on monolayer MoS₂. Cristallography. Université de Montpellier, 2022. English. NNT : 2022UMONS046 . tel-04257335

HAL Id: tel-04257335

<https://theses.hal.science/tel-04257335>

Submitted on 25 Oct 2023

HAL is a multi-disciplinary open access archive for the deposit and dissemination of scientific research documents, whether they are published or not. The documents may come from teaching and research institutions in France or abroad, or from public or private research centers.

L'archive ouverte pluridisciplinaire **HAL**, est destinée au dépôt et à la diffusion de documents scientifiques de niveau recherche, publiés ou non, émanant des établissements d'enseignement et de recherche français ou étrangers, des laboratoires publics ou privés.

THÈSE POUR OBTENIR LE GRADE DE DOCTEUR DE L'UNIVERSITÉ DE MONTPELLIER

En Physique

École doctorale Information, Structures et Systèmes (I2S)

Unité de recherche Laboratoire Charles Coulomb

Electronic transport on monolayer MoS₂

Présentée par Ivanovitch CASTILLO ARVELO

le 8 novembre 2022

Sous la direction de Benoit JOUAULT
et Sébastien NANOT

Devant le jury composé de

Benoit JOUAULT, Directeur de Recherche (CNRS), L2C

Sébastien NANOT, Maître de Conférence (Université de Montpellier), L2C

Frédéric TEPPE, L2C, Directeur de Recherche (CNRS)

Emmanuel BAUDIN, Maître de Conférence, LPENS, HDR (ENS Paris)

Yahya MOUBARAK MEZIANI, Associate Professor, Salamanca University (Spain)

Olivier GAUTHIER-LAFAYE, Directeur de Recherche (CNRS), LAAS

Directeur de thèse

Co-encadrant

Président du Jury

Rapporteur

Rapporteur

Examineur



UNIVERSITÉ
DE MONTPELLIER

A mi madre y abuela...

Contents

| | |
|--|-------------|
| Acknowledgements | V |
| Abstract | VII |
| Résumé en Français | IX |
| Introduction | XVII |
| 1 Theory | 1 |
| 1.1 Transition Metal Dichalcogenides | 1 |
| 1.1.1 Crystal structure | 2 |
| 1.1.2 Monolayer MoS ₂ | 2 |
| 1.1.3 Original thesis objective: gate tunable Josephson junction | 8 |
| 1.1.4 State of the art: MoS ₂ FET transistors | 11 |
| 1.2 Classical electronic transport | 12 |
| 1.2.1 Drude model of conduction | 13 |
| 1.2.2 Hall effect | 14 |
| 1.3 Mesoscopic transport: the metal–insulator transition | 15 |
| 1.3.1 Mott transition | 16 |
| 1.3.2 Anderson transition | 17 |
| 1.3.3 Mobility edge | 17 |
| 1.3.4 Ioffe-Regel criteria | 18 |
| 1.3.5 Scaling theory of localization | 19 |
| 1.3.6 Hopping transport | 21 |
| 1.3.7 Percolation method | 25 |
| 1.4 Metal-semiconductor interface: the Schottky barrier | 27 |

| | | |
|----------|--|-----------|
| 1.4.1 | Thermionic emission | 28 |
| 1.4.2 | Tunneling | 29 |
| 1.5 | Conclusion | 30 |
| 2 | Experimental techniques | 31 |
| 2.1 | Device working principle | 31 |
| 2.1.1 | Field effect transistor | 31 |
| 2.1.2 | Devices geometries | 33 |
| 2.1.3 | DC measurements | 35 |
| 2.2 | Fabrication | 37 |
| 2.2.1 | MoS ₂ grown by CVD | 37 |
| 2.2.2 | Design of the devices | 38 |
| 2.2.3 | Electron beam lithography (EBL) | 40 |
| 2.2.4 | Plasma etching | 41 |
| 2.2.5 | Description of the lithography process | 41 |
| 2.2.6 | Fabricated devices | 45 |
| 2.3 | Experimental setups | 53 |
| 2.3.1 | Raman spectroscopy | 53 |
| 2.3.2 | Reflectometry | 54 |
| 2.3.3 | Ball bonding | 54 |
| 2.3.4 | Probe Station | 57 |
| 2.3.5 | Doping control | 57 |
| 2.3.6 | He free cryostat | 58 |
| 2.3.7 | Low Temperature & High Magnetic Field | 59 |
| 2.4 | Device Performance | 60 |
| 2.4.1 | Reflectometry and Raman spectra | 61 |
| 2.4.2 | Probe Station | 63 |
| 2.4.3 | Current annealing | 63 |
| 2.4.4 | Ionic liquid gating | 66 |
| 2.4.5 | Photogating | 73 |
| 2.4.6 | Thermal annealing | 75 |
| 2.4.7 | Hysteresis | 78 |
| 2.5 | Conclusion | 81 |

| | |
|---|------------|
| <i>CONTENTS</i> | III |
| 3 Electronic transport through the MoS₂ | 83 |
| 3.1 2- and 4-probe I-V | 84 |
| 3.2 Conductivity: Metallic and insulating behavior | 86 |
| 3.3 Transport mechanisms in the insulating regime | 90 |
| 3.3.1 Thermally activated transport | 91 |
| 3.3.2 Variable Range Hopping | 92 |
| 3.4 Effective mobility, effective doping and metallic regime | 100 |
| 3.4.1 FET & effective mobilities | 100 |
| 3.4.2 Capacitive & effective doping | 103 |
| 3.4.3 Metallic conduction | 104 |
| 3.5 A genuine MIT? | 105 |
| 3.6 Conclusion | 110 |
| 4 Transport at the MoS₂-contact interface | 113 |
| 4.1 Contact inhomogeneity | 113 |
| 4.1.1 Transmission line measurement | 113 |
| 4.1.2 Non linear IVs | 116 |
| 4.1.3 Contact resistance | 117 |
| 4.2 Electronic transport and Schottky barrier | 119 |
| 4.2.1 Schottky barrier | 121 |
| 4.2.2 Thermionic emission | 121 |
| 4.2.3 Tunneling | 125 |
| 4.3 Conclusion | 126 |
| Conclusion & Outlook | 131 |
| Appendix A Variable range hopping | 133 |
| Appendix B On the presence of Helium gas at atmospheric pressure | 137 |
| Bibliography | 149 |

Acknowledgements

I want to express to my supervisors Benoit Joault and Sébastien Nanot all my gratitude for welcoming me to the laboratoire Charles Coulomb, introducing me to this field of research, and supporting me during this three short years. Thank you for all the unconditional support.

I warmly thank Christophe Coillot for kindly showing me around the lab when I first arrived, and for his support and example in being a sporty and green person.

Special thanks to Dilek Cakiroglu for teaching how to use all the instruments at the clean room, and for organizing all the hiking activities.

My warm thanks go to Sylvie Contreras for her support, availability and valuable advices.

Sandrine, Périne, I express to you my deep gratitude for your support and for your good spirits.

A big thank you to Christophe Consejo for his help and support in all the manipulations.

I express my gratitude to Walter Escoffier and Mathieu Pierre, with whom I had the chance to be part of a wonderful and friendly team.

Thanks to all the members of the laboratory who in one way or another contributed to the completion of this work.

Abstract

This thesis presents an investigation of electronic transport on monolayer MoS₂ devices. The samples have been fabricated from monolayer MoS₂ flakes grown by CVD, using standard electron beam lithography. The electrical measurements have been performed after *in-situ* annealing at $T = 600$ K. The thermal annealing moved the Fermi level close to the conduction band edge, and made the contacts more ohmic even at low temperatures. Conductivity and mobility have been measured *via* four-probe measurements, and an effective mobility of $\sim 200 \text{ cm}^2\text{V}^{-1}\text{s}^{-1}$, among the largest obtained in CVD-grown MoS₂ monolayer devices, has been observed.

Tuning the electron density leads to an apparent metal-insulator transition. If the Fermi energy lies in the tail of the conduction band, the conductivity is then driven by variable range hopping, with a universal and constant hopping prefactor, indicating that hopping is not phonon-mediated. Moreover, if the Fermi energy lies deep in the conduction band and the temperature is above 100 K, the conductivity is well modeled by the Boltzmann equation for a non-interacting Fermi gas, taking into account both, phonon and impurity scattering. The possibility of a genuine 2D metal-insulator transition cannot be ruled out, as one-parameter scaling on conductivity can be realized, and a clear power-law diverging localization length close to the transition is observed.

Finally, the 2-probe resistance is also analysed. I show that the transmission through the metal-semiconductor interface is governed by Schottky barriers, with thermionic emission and Direct tunneling of electrons occurring at high and low temperatures respectively.

Résumé en Français

La découverte du graphène par Andre Geim et Novoselov a suscité un intérêt croissant pour les systèmes bidimensionnels (2D), aussi bien pour des applications telles que l'électronique de nouvelle génération qu'en recherche en physique fondamentale. Parmi ceux-ci, les dichalcogénures de métaux de transition (TMD) forment une famille de matériaux 2D avec des propriétés uniques. Les TMD sont des matériaux cristallins de la forme MX_2 où M est un métal de transition et X_2 sont deux atomes de la famille des chalcogènes, la plupart formant des structures en couches. Ils peuvent exister sous forme de monocouches avec une structure en nid d'abeille comparable au graphène. Ils présentent une large gamme de bandes interdites (de 0 à ~ 2 eV), combinés à de forts couplages spin-orbite. De tous les TMD, MoS_2 reste le plus étudié à ce jour. Les monocouches de MoS_2 ont une large bande interdite (~ 1.9 eV) directe située aux points K du réseau réciproque. Ce 'gap' les qualifie pour de nombreuses applications photoniques, et leur excellente flexibilité mécanique en fait un matériau semiconducteur prometteur pour l'électronique flexible.

En 2012, il a été observé pour la première fois qu'un contrôle électrostatique du dopage de quelques couches de MoS_2 induisait une transition de la phase isolante vers une phase métallique, jusqu'à atteindre une phase supraconductrice à haute densité électronique, avec une température critique pouvant atteindre 10.8 K. Sur la Fig. 1 sont reproduits les résultats de la première observation de cette transition dans MoS_2 , où la résistance est tracée en fonction de la température et de la densité électronique.

Suite à cette découverte, deux groupes expérimentaux ont indépendamment mis en évidence que les champs critiques dans le plan du matériau monocouche étaient plusieurs fois supérieurs à ceux de plusieurs couches, et six fois supérieurs aux limites de Pauli. En raison du couplage spin-orbite (SOC) et de l'absence de centre d'inversion, les spins des électrons sont orientés dans la direction perpendiculaire au plan 2D. Ce type de couplage est généralement appelé "Ising SOC" pour le distinguer du Rashba SOC, qui maintient les spins

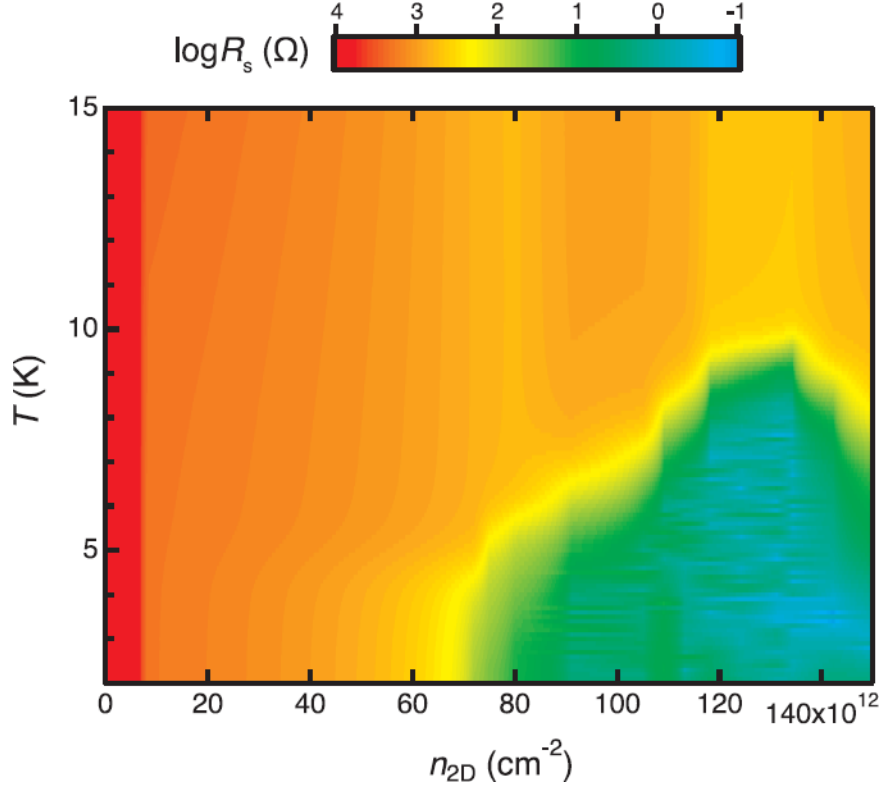


Figure 1: Dôme supraconducteur en fonction de la densité électronique observée dans MoS₂. Les états de l'isolant et du métal sont également observés. De [1].

électroniques dans des directions dans le plan. En raison du fort ancrage hors-plan des spins électroniques des électrons formant les paires de Cooper, les champs magnétiques externes dans le plan sont beaucoup moins efficaces pour séparer celles-ci et supprimer la supraconductivité. En conséquence, les champs magnétiques critiques dans le plan dans du MoS₂ peuvent atteindre plusieurs dizaines de Teslas. Ce type de supraconducteurs non conventionnels est appelé supraconducteurs d'Ising, et se révèle être un candidat pour la formation d'états topologiques tels que les fermions de Majorana. Plus généralement, ce couplage rend les composants à base de MoS₂ prometteurs pour la spintronique, et la vallétronique.

L'objectif original de ce projet, bien qu'encore loin d'être atteint, est de développer une jonction Josephson contrôlable par des grilles électrostatiques. Celles-ci permettraient la formation de jonctions S-I-S à S-M-S et même S-S'-S, à base de monocristaux de TMD. S, M et I représentent respectivement les régions supraconductrices, métalliques et isolantes, S' étant un état supraconducteur légèrement différent. Des monocristaux (multicouches ou monocouches) peuvent être utilisées comme matériau unique formant la jonction, où la phase électronique sera accordée par des grilles locales constituées de nanotubes de carbone (NTC), comme le montre le schéma simplifié de la Fig. 2. En conséquence, la jonction proposée sera

constituée d'un seul matériau et sera entièrement contrôlée *in situ*. L'état supraconducteur du MoS₂ sera atteint avec l'utilisation de grilles à base de liquide ionique. Le liquide ionique permet d'atteindre dans les TMD une densité de porteurs d'environ $1 \times 10^{14} \text{ cm}^{-2}$, nécessaire à l'obtention de l'état supraconducteur.

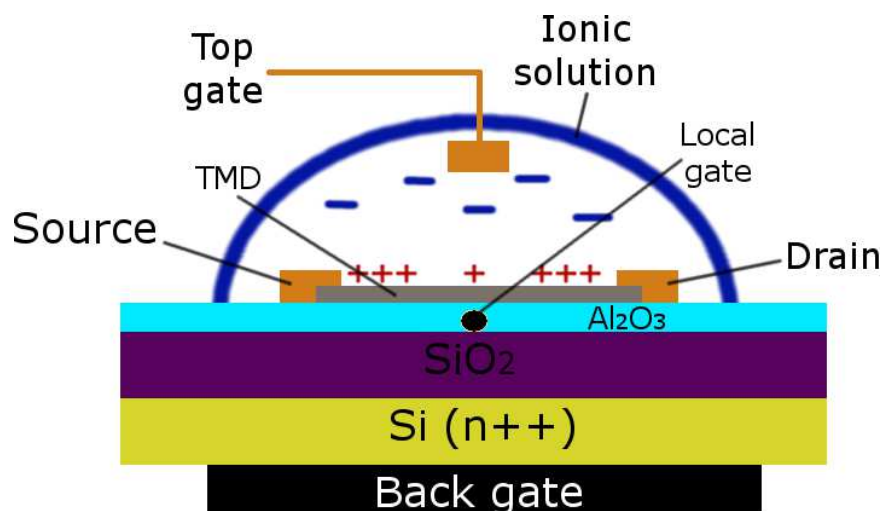


Figure 2: Schéma simplifié du dispositif d'une jonction Josephson. Le liquide ionique, le CNT et le Si hautement dopé sont, respectivement, les grilles supérieure, locale et arrière.

Afin d'atteindre cet objectif, ou plus généralement, de pouvoir développer des applications (opto-)électroniques réalistes à base de MoS₂, une compréhension plus fine de ses propriétés électroniques est nécessaire. A ce jour, différents régimes de transport ont été reportés dans le régime isolant dans la littérature [2–6]. De même, une description précise de la transition vers un régime métallique [5, 7, 8] et des mécanismes de diffusion dans ce régime [9–12] sont encore nécessaires. De plus, même pour des problèmes en apparence plus basiques, tels qu'à l'interface de contact avec un métal, il n'y a pas d'étude complète des mécanismes en jeu selon le dopage et la température [13–15]. Cette thèse présente nos efforts dans le développement d'un procédé de fabrication contrôlé de composants à base de MoS₂ CVD. De nombreuses approches tentant de rendre les contacts plus ohmiques, et de les doper le plus efficacement possible ont été étudiés. Après avoir observé que le recuit *in-situ* était le plus efficace, nous avons étudié en détail le transport dans les régimes isolants et métalliques et la transition entre ces deux régimes, ainsi que le transport à l'interface or/MoS₂.

Ce manuscrit est divisé en 4 chapitres principaux:

Dans le chapitre 1, Théorie, nous décrivons les bases théoriques et d'état de l'art nécessaires à la compréhension des chapitres suivants. Dans sa première partie, les TMD

sont présentés en nous concentrant sur MoS₂ et ses structures de bandes cristallographiques et électroniques. Nous présentons ensuite la motivation derrière le projet: les jonctions Josephson accordables par grille, et quelques-unes de ses utilités possibles. Dans une seconde partie, le modèle classique de Drude de la conduction électrique dans les métaux est présenté. Le débat de longue date sur la transition métal-isolant est présenté dans une troisième partie, ainsi que les modèles de transport électronique les plus ‘populaires’ dans le régime isolant. La dernière partie est consacrée aux modèles de transport électronique à l’interface métal-MoS₂.

Dans le chapitre 2, Techniques Expérimentales, le processus de croissance de MoS₂ et les méthodes de fabrication des différents dispositifs sont présentés. Le MoS₂ est cru par CVD, et de grandes surfaces avec des feuillets monocouches, comme le montre la Fig. 3a, ont été obtenues. La majorité des composants fabriqués sont des barres de Hall, sans pouvoir construire la jonction Josephson souhaitée. Certains autres dispositifs ont également été fabriqués pour extraire des informations sur le MoS₂, comme la méthode de van der Pauw et la méthode “transfer length” (TLM). Les montages expérimentaux utilisés pour caractériser ces dispositifs sont également présentés. Les monocouches de MoS₂ sont identifiées grâce à des mesures de spectroscopie Raman et de réflectométrie. Les couches sélectionnées sont ensuite gravées selon la forme désirée et connectées via des couches de Ti/Au à l’aide d’un système de lithographie électronique, comme le montre la Fig 3b. Quelques résultats préliminaires typiques sont présentés, ceux-ci illustrent les difficultés techniques rencontrées. En particulier, lors des premières mesures, différentes techniques ont été utilisées pour contrôler la densité électronique des transistors MoS₂ (photodopage avec des LED et grille ionique en particulier), avec plus ou moins de succès. Le recuit thermique des échantillons (sous vide à $T = 600$ K) s’est avéré être l’une des meilleures façons d’augmenter la qualité des échantillons. L’ensemble complet des données présentées dans les deux chapitres suivants a été obtenu juste après ce type de recuit (sans exposition intermédiaire à l’air).

Ainsi, de manière générale, la densité électronique s’est avérée être une variable difficile à contrôler en raison des impuretés sur les échantillons, de la faible densité électronique intrinsèque, et de la grande bande interdite de la monocouche MoS₂. La présence d’une grande densité d’états (DoS) dans la bande interdite liée aux impuretés implique qu’une grande tension de grille est nécessaire pour remplir ces états et déplacer le niveau de Fermi vers la bande de conduction. La densité électronique n’a pas pu être augmentée suffisamment pour observer la supraconductivité, mais a permis l’observation de la transition métal-isolant.

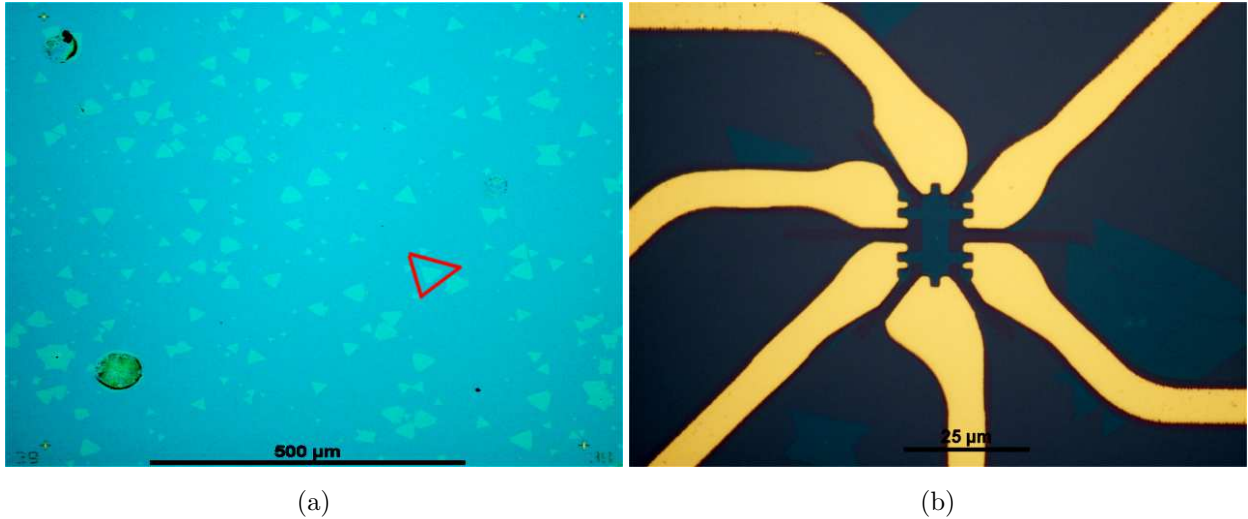


Figure 3: Mise en forme d'un monocouche MoS_2 en une barre Hall par lithographie électronique. (a) Vue d'ensemble de feuillets de MoS_2 monocouches. Le triangle rouge indique la monocouche utilisée pour la fabrication. (b) Barre de Hall fabriquée avec des contacts Ti/Au.

Le chapitre 3, Transport électronique intrinsèque du MoS_2 , se concentre sur l'étude du mécanisme de transport électronique dans les régimes isolant et métallique, et adresse le débat (de longue date) sur la nature de la transition métal-isolant dans les systèmes bi-dimensionnels. Les mesures approfondies de 3 barres de Hall différentes sont analysées. Le recuit thermique préliminaire, à $T = 600$ K, a déplacé le niveau de Fermi près de la bande de conduction, et la transition métal-isolant a pu être observée. Dans le régime isolant, le transport électronique suit le modèle VRH (Variable Range Hopping), mais avec des différences entre les dispositifs. Le VRH d'Efros-Shklovskii (ES) est observé pour l'un des composants, comme le montre la Fig. 4a, mais un VRH intermédiaire (entre ES et Mott) semble se produire sur un échantillon. Il est également montré que le VRH n'est pas assisté par des phonons, comme on le pense généralement. Ceci peut se constater grâce à la présence d'un préfacteur indépendant de la température et égal à e^2/h dans le modèle de conductivité VRH, comme le montre la Fig. 4b.

La possibilité d'une véritable transition de phase "Metal-insulator transition" (MIT) est discutée. Une mise à l'échelle de la conductivité est effectuée à l'aide de l'expression $\sigma = \sigma_c(T)f(|x - x_c(T)|t(T))$, et également sur la longueur de localisation avec l'expression $\xi \sim |n_{2D} - n_c|^{-\nu}$. L'ensemble des points mis à l'échelle coïncident sur deux branches (une pour chaque régime) comme le montre la Fig. 5, suggérant une véritable transition de phase. Cependant, ce n'est pas une condition suffisante, et une étude des différentes

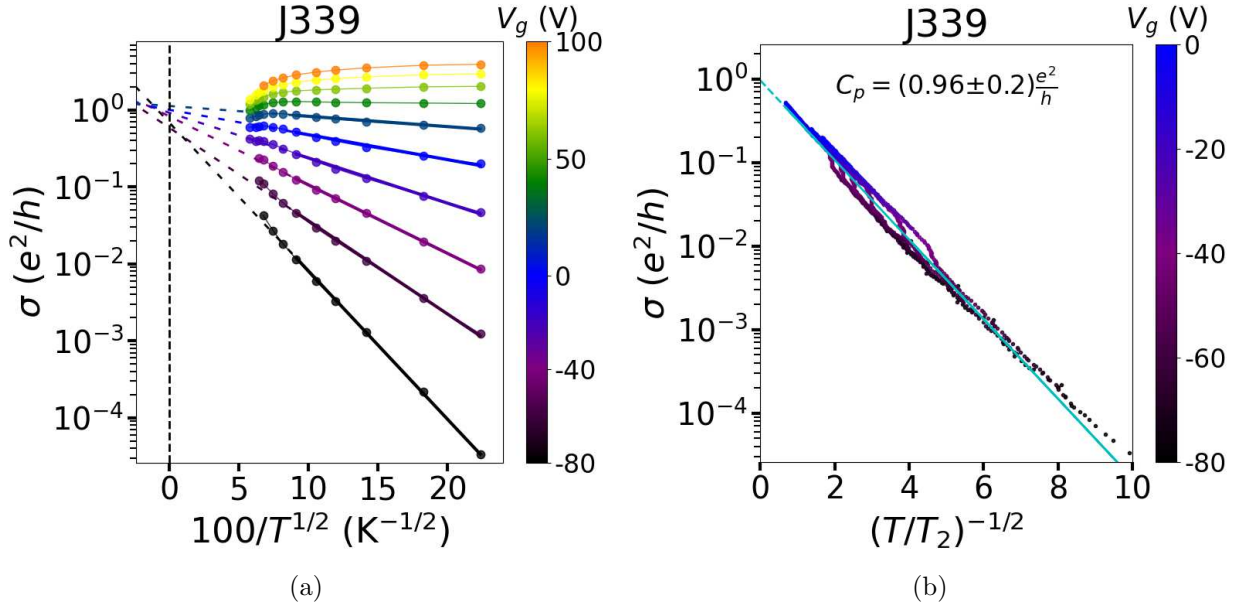


Figure 4: (a) Dépendance à la température de la conductivité par rapport à $T^{-1/2}$ (courbe ES). Seul un jeu de données réduit est indiqué pour plus de clarté, représenté par des points reliés par de fines lignes pleines. Les lignes épaisses sont les résultats d'ajustement avec le modèle ES, d'où T_2 (la température caractéristique de modèle ES) est extraite. Les données ci-dessous $T = 120$ K et $V_g = 20$ V ont été ajustées. (b) Conductivité sans dimension σ en fonction de $(T/T_2)^{-1/2}$. L'ajustement linéaire est indiqué par une ligne cyan, qui est extrapolée à $T^{-1} = 0$, et interceptée avec l'axe y . Cette intersection donne une valeur pour le préfacteur C_p proche de la conductance quantique e^2/h .

échelles d'énergie en jeu suggère qu'une transition liée à la diffusion *via* les phonons ne peut pas être définitivement exclue à ce stade.

Le dernier chapitre, Transport à l'interface métal-MoS₂, est consacré à l'analyse des données de mesure 2 pointes du transport électronique des mêmes échantillons que précédemment, en se concentrant sur le transport électronique métal-MoS₂. La résistance de contact est extraite et étudiée en fonction de la tension de grille et de la température, avec la valeur la plus faible atteint de ~ 90 k $\Omega \cdot \mu\text{m}$ comparable à l'état de l'art. Les deux modèles standard de transport à ce type d'interface sont comparés aux mesures: l'émission thermionique d'électrons au-dessus de la barrière Schottky (SB) et l'effet tunnel à travers celle-ci. La hauteur de barrière extraite grâce aux mesures à faible dopage dominées par l'émission thermionique est d'environ 100 meV, comme le montre la Fig. 6a. A suffisamment fort dopage, compte tenu de la faible résistance de contact et de la réduction de la hauteur de barrière effective, le transport au niveau du métal-MoS₂ se fait principalement par effet tunnel, comme le montre la Fig. 6b.

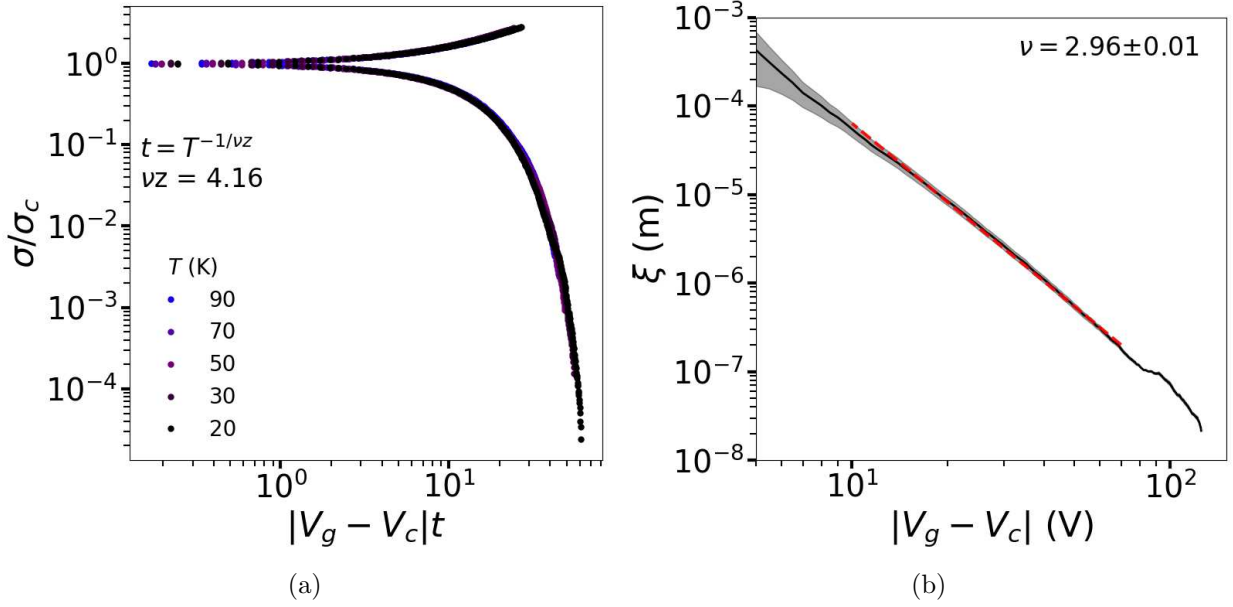


Figure 5: Mise à l'échelle MIT. (a) Mise à l'échelle sur la conductivité. (b) Mise à l'échelle sur la longueur de localisation.

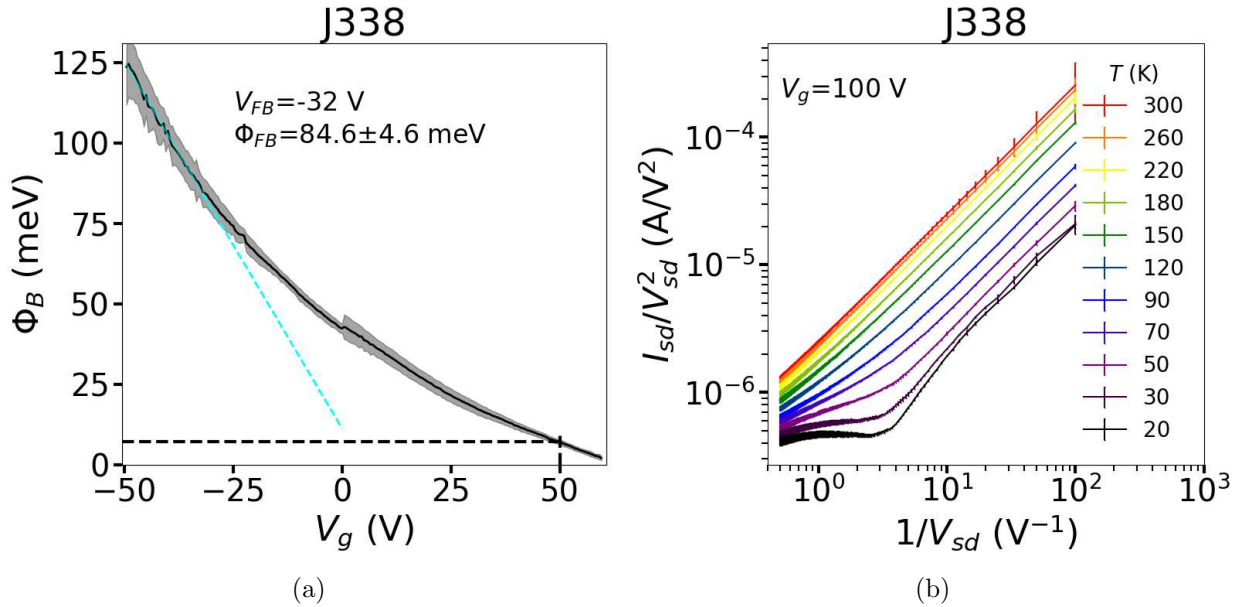


Figure 6: (a) Barrière Schottky extraite Φ_B pour le dispositif J338 en fonction de la tension de grille V_g . (b) Graphe de l'effet tunnel direct pour le même dispositif: la linéarité indique que les contacts sont ohmiques, ou qu'un effet tunnel direct se produit.

Enfin, une annexe est ajoutée où un mécanisme de transport VRH intermédiaire est dérivé. Ce modèle est dérivé en prenant ensemble l'espacement énergétique moyen entre les impuretés utilisé par Mott, et l'interaction de Coulomb entre les états utilisés par ES. Le modèle dérivé est ensuite appliqué avec succès à la conductivité d'un composant. Il convient de mentionner que les superviseurs ne supportent pas cette dérivation.

Introduction

The discovery of graphene by Andre Geim et Novoselov in 2004 awoke a huge interest by the scientific community. Graphene is a bi-dimensional material composed only by carbon atoms arranged in a hexagonal way like a honeycomb. It is considered as one of the most promising materials due to its unique properties: stronger than steel, lighter than aluminium, better conductor than copper, flexible and almost transparent. Since this discovery that led to a Nobel Prize, there has been a growing interest in two dimensional (2D) systems for applied and fundamental physics research.

Among them, Transition Metal Dichalcogenides (TMDs) represent a family of 2D materials with unique properties. The TMDs have the form MX_2 where M is the transition metal and X_2 are two chalcogen atoms. They can also exist in monolayer form and have a honeycomb structure like graphene. They can exhibit a wide range of band gaps (0–2 eV), and strong spin orbit coupling strengths (150–460 meV), making them suitable for spintronics and valleytronics. Bulk (or 3D) TMDs have been known and used for a very long time, but most of the older applications (*i.e.* as solid lubricants) were related to their mechanical properties determined by the presence of van der Waals bonding between the layers. It is only recently, following the success of graphene, that TMDs moved to the forefront of solid state research, with most of the research realized on mono and few-layer structures. Of all TMDs, MoS_2 has been so far the most studied one. Monolayer MoS_2 has a large direct band gap at the K-points of 1.8–1.9 eV, which qualifies it for numerous photonic applications, and it has excellent mechanical flexibility, which makes it a compelling semiconducting material for flexible electronics.

One of the most interesting features of this material is that it can behave as an insulator, a metal, or even a superconductor, depending on its carrier density. Given those characteristics, the project “Josephson Junctions by Electrostatic tuning of Dichalcogenides” (JJEDi) was born. This project aims to make a Josephson junction with the use of TMDs, by con-

trolling the electron density with three different electrostatic gates. To reach this goal, or to develop MoS₂ potential for realistic (opto)-electronic applications, a better understanding of its electronics properties is still needed. To this day, many different transport regimes in the insulating phase have been reported. Similarly, a precise description of the transition to a metallic state regime and of scattering in this last one are still needed. Moreover, even problems which could appear as basic, such as the contact interface with the metal, still lacks of a comprehensive study of the mechanisms involved as a function of doping and temperature.

This thesis work aimed at developing a controlled fabrication of CVD MoS₂-based transistors, with the most ohmic contacts possible, at studying the most efficient gating techniques. We then studied the transport in the insulating & metallic regime, as well as at the MoS₂-metal interface. The thesis is outlined as follow. In Chapter 1 are described some of the features of monolayer MoS₂, and the classical and quantum electronic transport mechanism that take place within the material. The transport mechanisms at the metal-MoS₂ interface is also briefly discussed. In Chapter 2 is introduced the growth process of MoS₂ and the fabrication method for the different devices. It is also shown how to extract intrinsic quantities of the MoS₂, together with the experimental setup used to characterize these devices. Finally, some typical preliminary results are presented, which illustrate the technical difficulties encountered. In Chapter 3, a detailed electronic transport of 3 different Hall bars is presented, focusing on the 4-probe conductivity data extracted after thermally annealing the samples. Different transport mechanism are observed depending on the temperature and electron density, and a discussion on the metal-insulator transition is presented. Finally, Chapter 4 is devoted to the analysis of the 2-probe data, focusing at the metal-MoS₂ electronic transport. The models of thermionic emission of electrons over the Schottky barrier and the tunneling across it are presented.

Chapter 1

Theory

We will describe in the first part of this Chapter what are TMDs, focusing on MoS₂ and its crystallographic and electronic band structures. We will then present the motivation behind the project: gate tunable Josephson junctions, and some of its possible utilities. On the second part is presented the classical Drude model of electric conduction in metals. The long-standing debate of the metal-insulator transition is presented in the third part of the Chapter, together with the most ‘popular’ electronic transport models in the insulator regime. The last part is devoted to the electronic transport models at the metal-MoS₂ interface.

1.1 Transition Metal Dichalcogenides

Transition metal dichalcogenides (TMDs) are a class of materials of type MX₂ in which M is a transition metal of groups 4–10 and X is a chalcogen atom. There are about sixty in number, with two-thirds forming layered structures [16]. In Fig. 1.1a the periodic table of elements is shown with the chalcogen atoms highlighted in orange, the transition metals that form layered structures highlighted in different colours, and those metals that form layered structures with some chalcogens but not with others are colour-framed, e.g. while NiTe₂ has a layered structure NiS₂ possesses a three-dimensional structure. For those that form layered materials the stability of the crystal is ensured by weak van der Waals (vdW) interactions between layers, as schematically shown in Fig. 1.1b.

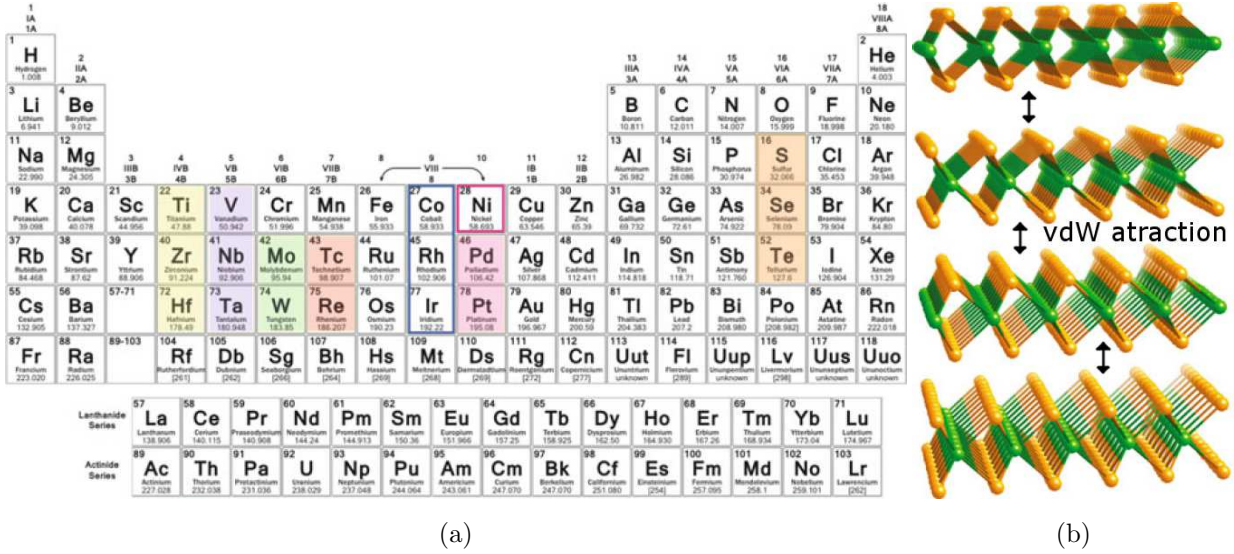


Figure 1.1: (a) The transition metals and the three chalcogen elements that crystallise into layered structures are highlighted in the Periodic Table. The transition metals that crystallise into layered structures with some chalcogens but not with others are color-framed. (b) Three-dimensional representation of a typical layered MX₂ structure, with the metal atoms shown in green and the chalcogen atoms shown in orange. Adapted from [16].

1.1.1 Crystal structure

Layered TMDs are usually found in three polymorphs called 1T, 2H and 3R. Here the numbers stand for the number of layers in the unit cell and the letters indicate symmetry (T-trigonal, H-hexagonal, and R-rhombohedral). These polymorphs are schematically shown in Fig. 1.2 [16]. Each layer is formed of transition metal atoms sandwiched between two layers of chalcogen atoms, to which they are covalently bonded. The unit cell is defined with the *c*-axis perpendicular to the layers while the parameter *a* represents the minimal in-plane distance between two chalcogen atoms.

1.1.2 Monolayer MoS₂

Molybdenum disulfide (MoS₂) is certainly the most known and the most studied of all TMDs. The most remarkable properties of MoS₂ monolayers are their large direct band gap (1.8–1.9 eV [4, 17–19]), which qualify them for numerous photonic applications, and their excellent mechanical flexibility which makes them a compelling semiconducting material for flexible electronics [20, 21].

The most stable structure of MoS₂ is the 2H. When viewed from the top, a monolayer

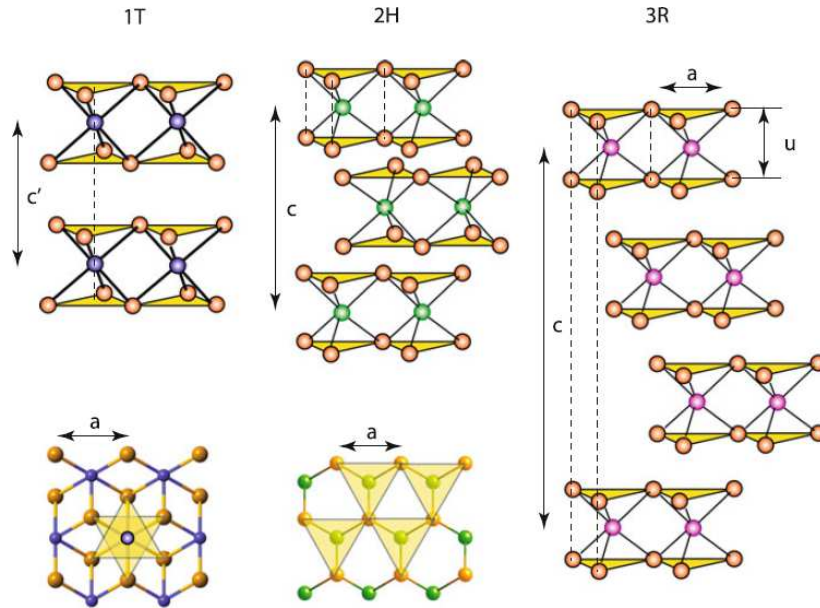


Figure 1.2: Schematics of the structural polytypes of TMDs. From left to right: 1T (tetragonal symmetry, one layer per unit cell, octahedral coordination of the metal), 2H (hexagonal symmetry, two layers per unit cell, trigonal prismatic coordination) and 3R (rhombohedral symmetry, three layers per unit cell, trigonal prismatic coordination). The yellow-filled triangles highlight the spatial position of the chalcogen atoms within one layer. For the 1T and 2H polytypes, top views are additionally shown. From [16].

MoS₂ has a honeycomb lattice structure like graphene, as shown in Fig. 1.3. It also exhibits a strong spin-orbit coupling (SOC) and lack of inversion symmetry, both of which open the doors to new fundamental physics. We will briefly described them in more details in this Section.

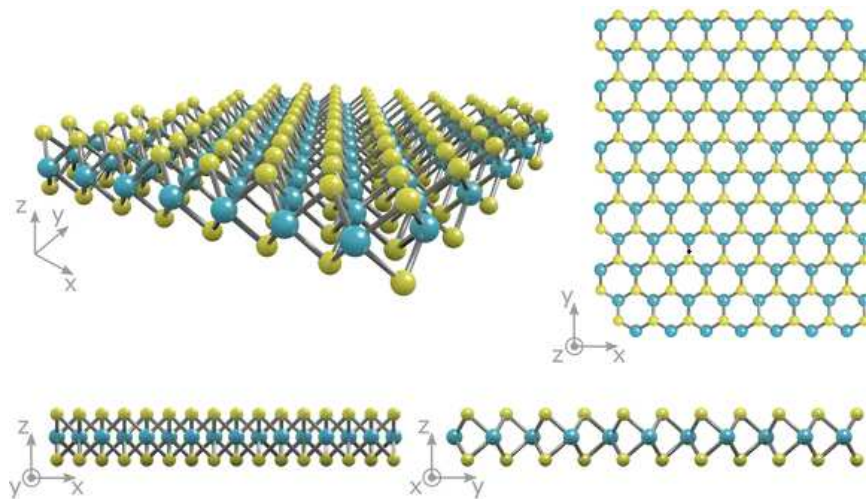


Figure 1.3: The crystal structure of monolayer MoS₂ showing a layer of molybdenum atoms (blue) sandwiched between two layers of sulfur atoms (yellow). From [22].

Brillouin zone

The two Bravais primitive lattice vectors are (Fig. 1.4a):

$$\vec{R}_1 = (a, 0, 0) \quad (1.1)$$

$$\vec{R}_2 = \left(\frac{a}{2}, \frac{\sqrt{3}a}{2}, 0 \right), \quad (1.2)$$

where $a = 3.16 \text{ \AA}$ is the lattice constant. The S atoms are located in planes 1.56 \AA above and below the Mo plane. This yields a distance between neighboring Mo and S atoms of $d = 2.40 \text{ \AA}$. The angle between the Mo-S bond and the Mo plane is $\theta = 40.6^\circ$ [23]. The MoS₂ Brillouin zone is hexagonal, the most important symmetry points and symmetry lines are indicated in Fig. 1.4b, namely, $\Gamma = (0,0)$, $\mathbf{K} = (\frac{2\pi}{3a}, \frac{-2\pi}{\sqrt{3}a})$, $\mathbf{M} = (\frac{\pi}{a}, \frac{-\pi}{\sqrt{3}a})$ and the \mathbf{Q} point, which is located half way between the Γ and \mathbf{K} points [23, 24]. The reciprocal lattice basis vectors are:

$$\vec{K}_1 = \frac{4\pi}{\sqrt{3}} \left(\frac{\sqrt{3}a}{2}, \frac{-1}{2}, 0 \right) \quad (1.3)$$

$$\vec{K}_2 = \frac{4\pi}{\sqrt{3}a} (0, 1, 0) \quad (1.4)$$

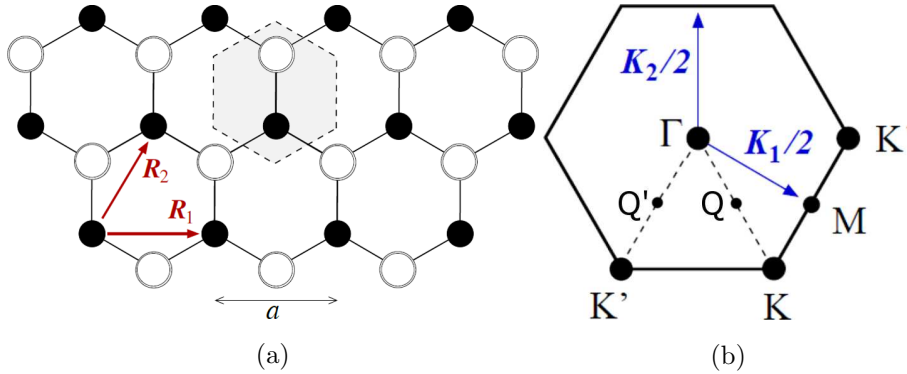


Figure 1.4: (a) Top view of the MoS₂ lattice structure. Dark (light) circles represent Mo (S) atoms. Notice that in this view two S atoms sit on top of each other. The unit cell is shown in the highlighted hexagon. The lattice constant in the Mo plane is a . The two Bravais lattice vectors (\vec{R}_1 and \vec{R}_2) are indicated. Brillouin zone for the MoS₂ lattice. \vec{K}_1 and \vec{K}_2 are the reciprocal lattice basis vectors, and Γ , \mathbf{K} , \mathbf{K}' , \mathbf{M} , \mathbf{Q} and \mathbf{Q}' are the symmetry high points. Adapted from [23].

Band structure

First-principles band structure calculations for bulk and a few layer MoS₂ show that the minimum of the conduction band (CBM) is located at the \mathbf{Q} point, between the \mathbf{K} and

Γ points in the Brillouin zone, and the maximum of the valence band (VBM) is located at the Γ point [25]. In more recent studies [26], using density functional theory (DFT) calculations, it has been shown that the direct band gap at the \mathbf{K} point of the Brillouin zone barely changes as a function of the number of layers, while the indirect band gap increases monotonically as the number of layers decreases. In the case of a monolayer, the band gap becomes direct and located at the \mathbf{K} points corresponding to the corners of the hexagonal Brillouin zone, as shown in Fig. 1.5. The energy gap between the CBM and VBM for bulk MoS₂ is 1.2 eV while it is 1.9 eV for monolayer [27]. The \mathbf{Q} point is important in electronic transport even for monolayer MoS₂, since its energy is close to the CBM, with an energy difference of 0.1–0.3 eV depending on the position of the Fermi energy [23, 24].

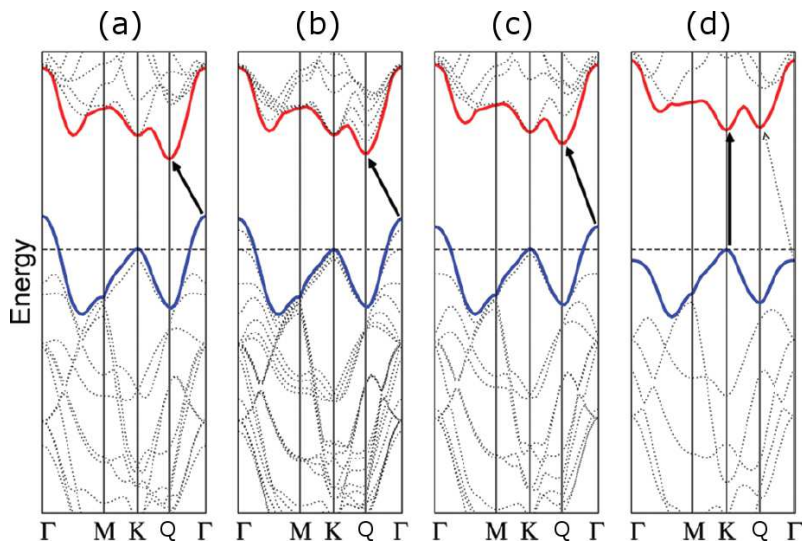


Figure 1.5: Density functional theory results of band structures of (a) bulk MoS₂, (b) quadrilayer MoS₂, (c) bilayer MoS₂, and (d) monolayer MoS₂. The solid arrows indicate the lowest energy transitions. Bulk and few layers MoS₂ are characterized by an indirect bandgap while monolayer is direct occurring at the \mathbf{K} point. Adapted from [26].

Spin orbit coupling

A tight binding model [28] reveals that the Bloch states near the band edge for the valence and conduction bands mainly originate from the metal d orbitals (the contribution of the s and p orbitals is negligible), especially the d_{z^2} , d_{xy} and $d_{x^2-y^2}$, as shown in Fig. 1.6a. The conduction band, which in a first approximation is composed mainly from d_{z^2} orbitals, remains almost spin degenerate at the \mathbf{K} points, whereas the VBM splits, as schematically shown in Fig. 1.6b. Furthermore, d orbitals are a source of strong spin-orbit coupling (SOC).

The valence-band spin splitting at the \mathbf{K} points is the consequence of SOC and inversion symmetry breaking in monolayer. The maximal spin splitting of the VBM at the \mathbf{K} point amounts to 148, 183, 426, and 456 meV for the MoS₂, MoSe₂, WS₂, and WSe₂ monolayer, respectively [29].

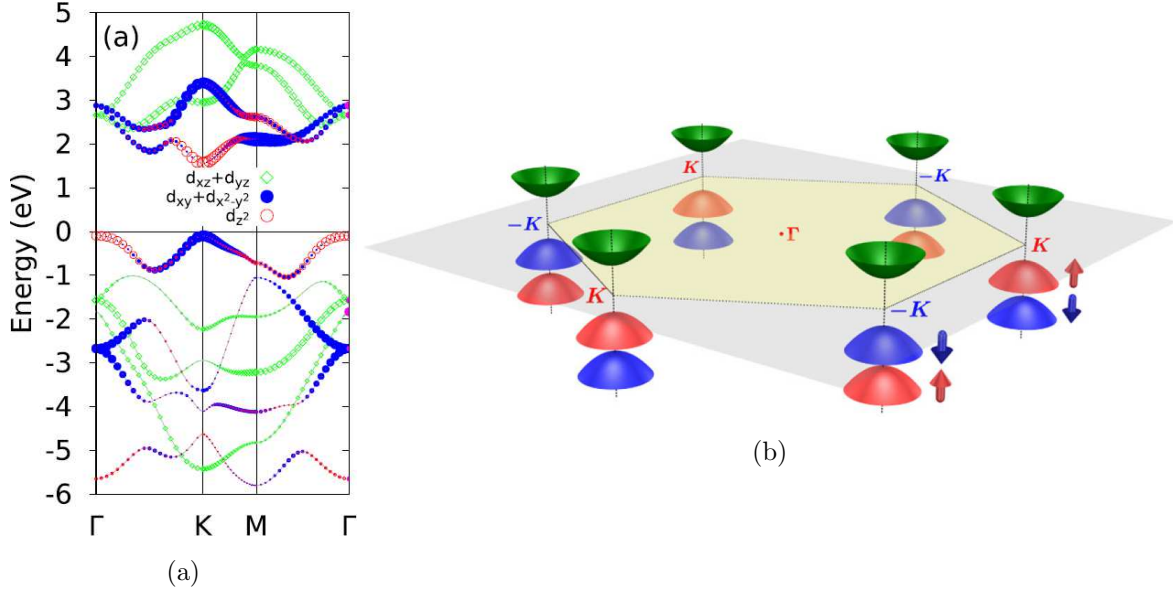


Figure 1.6: (a) Orbital projected band structures for monolayer MoS₂. Contributions from Mo d -orbitals: blue dots for d_{xy} and $d_{x^2-y^2}$, red open circles for d_{z^2} , and green open diamonds for d_{xz} and d_{yz} . The size of the symbols is proportional to the population in the corresponding state. From [28]. (b) Schematic drawing of the band structure at the band edges located at the \mathbf{K} points. From [30].

Ising superconductivity

Superconductivity is the ability of certain materials to conduct electric current without energy losses and expel magnetic fields. It was first observed in 1911 by H. K. Onnes, a Dutch physicist [31], conducting experiments with mercury at liquid helium temperature. He observed an abrupt drop on the resistance of mercury when cooling it down. It wasn't until 1957 when John Bardeen, Leon Cooper, and John Robert Schrieffer developed a model explaining this phenomena, describing superconductivity as a microscopic effect caused by a condensation of Cooper pairs [32]. The Nobel Prize in Physics 1972 was awarded jointly to John Bardeen, Leon Neil Cooper and John Robert Schrieffer “for their jointly developed theory of superconductivity, usually called the BCS-theory” [33].

Nowadays exist a group of superconductors called “unconventional superconductors”, which do not follow the BCS theory. In several unconventional superconductors the transition

temperature (the temperature at which the abrupt drop on resistivity occurs) has a maximum as a function of external parameters such as chemical doping or pressure. In 2012 [1] it was observed for the first time that few layers of MoS₂ undergo a superconducting transition at high electron density, with a critical temperature as high as 10.8 K. In Fig. 1.7 is reproduced the results of the first observed superconductivity transition in MoS₂ [1], as a function of temperature and electron density.

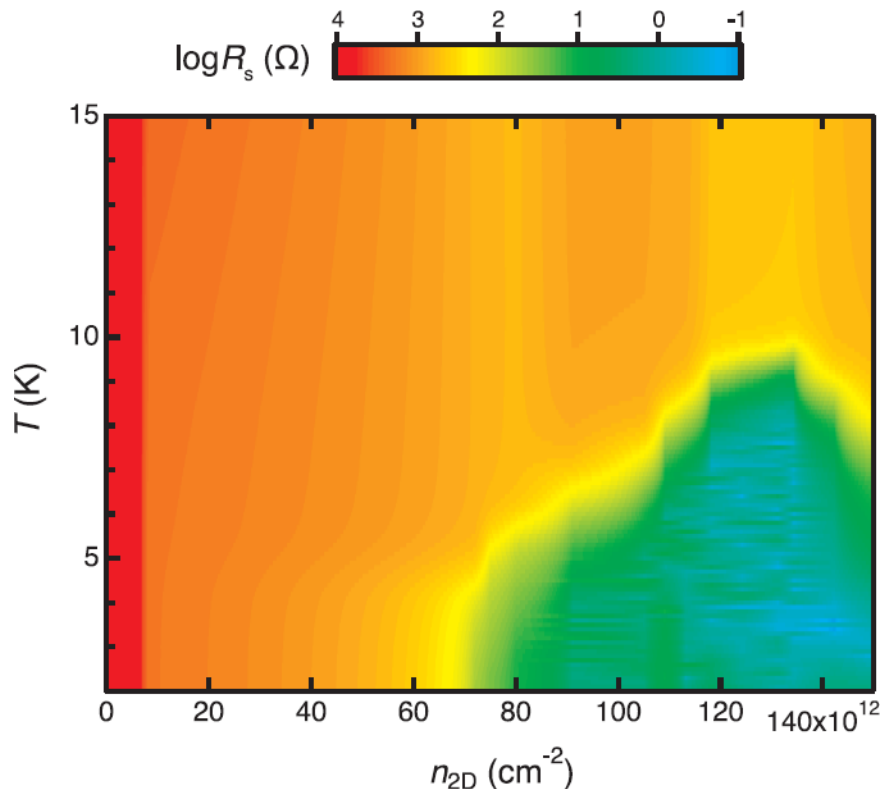


Figure 1.7: Superconducting dome as a function of electron density observed in MoS₂. The insulator and metal states are also observed. From [1].

After gated MoS₂ was found to be superconducting, two experimental groups independently discovered that the in-plane upper critical fields of the material were several times higher than the bulk material and six times higher than the Pauli limits [34, 35]. Due to the SOC and broken in-plane mirror symmetry, the electron spin is pinned in the out-of-plane directions and is generally called “Ising SOC” to distinguish it from the Rashba SOC, which pins electron spins in the in-plane directions [36]. Owing to the strong pinning of electron spins in the out-of-plane directions by Ising SOC, external in-plane magnetic fields are much less effective in aligning electron spins. As a result, the resistance to in-plane magnetic fields in MoS₂ superconductors is enhanced. In Fig. 1.8 are reproduced the results of applying a perpendicular and parallel magnetic field to a few layers MoS₂ transistor [35]. This special

type of superconductors are referred to as Ising superconductors, and has been studied in the formation of Majorana states [36], spintronic and valleytronic physics [30].

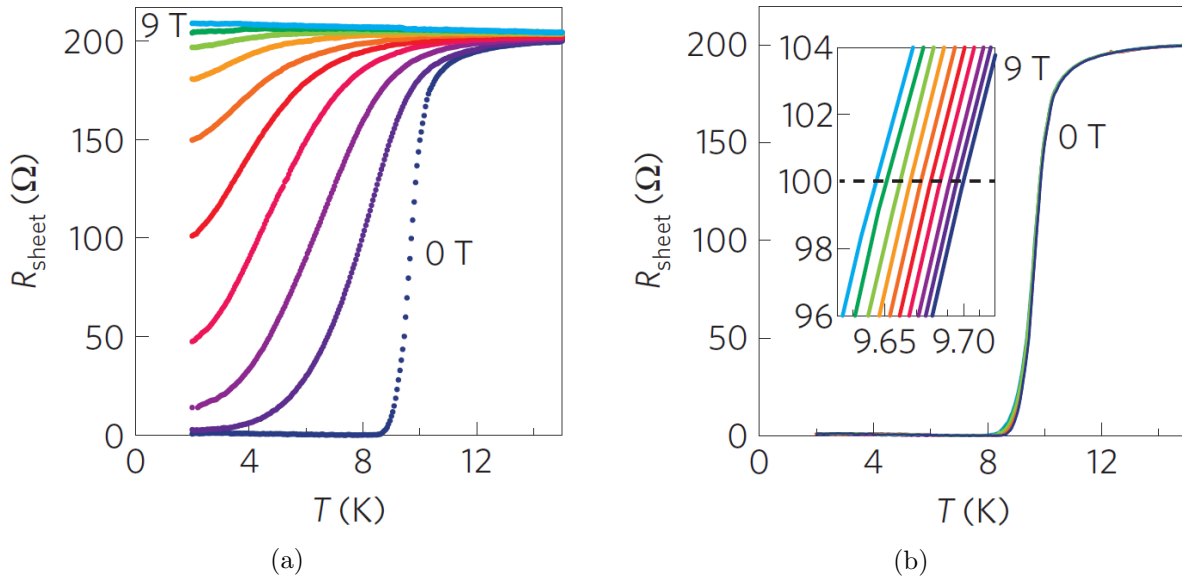


Figure 1.8: Sheet resistance of few layers MoS₂ as a function of temperature under the application of perpendicular magnetic fields (a), and parallel magnetic fields (b). The magnetic field varies in 1 T step. From [35].

1.1.3 Original thesis objective: gate tunable Josephson junction

A Josephson Junction (JJ) is a device that consists of two or more superconductors coupled by a weak link, as shown in the simplified sketch in Fig 1.9a. The weak link can be a thin insulating barrier, a short section of non-superconducting metal, or a physical constriction that weakens the superconductivity at the region of contact. The device is named after Brian Josephson, who predicted in 1962 that pairs of superconducting electrons (Cooper pairs) could tunnel through the barrier from one superconductor to another, predicting also the form of the current and voltage relations for the junction [37]. A supercurrent will exist until a critical current is reached, after which the JJ behaves as a resistor, as shown in the I-V diagram in Fig. 1.9b. The Nobel Prize in Physics 1973 was given to Leo Esaki and Ivar Giaever “for their experimental discoveries regarding tunneling phenomena in semiconductors and superconductors”, and to Brian David Josephson “for his theoretical predictions of the properties of a supercurrent through a tunnel barrier” [38]. Josephson junctions have important applications in quantum-mechanical circuits, such as superconducting quantum interference device (SQUID) for low magnetic field measurements [39], long lifetime

superconducting qubits [40, 41], and rapid single flux quantum for high-performance digital electronics [42].

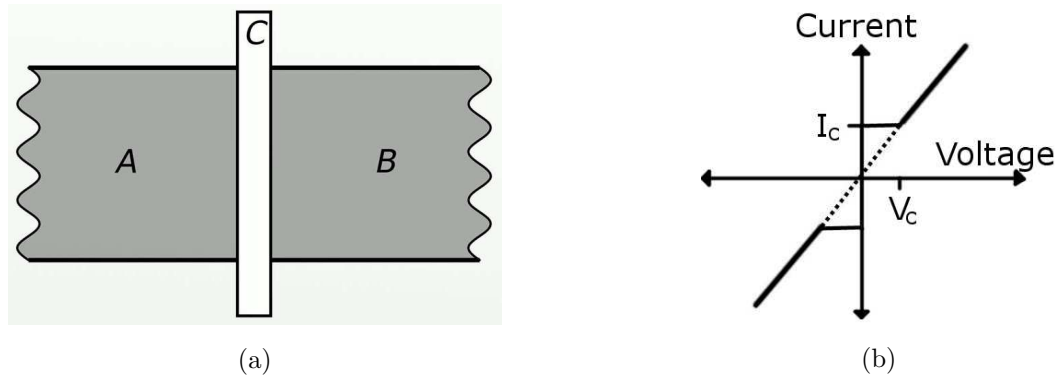


Figure 1.9: (a) Simplified sketch of a JJ. (b) I-V diagram of a JJ. After reaching a critical current, a voltage appears and the JJ behaves as a resistor.

The objective of this project is to develop gate tunable JJ forming S-I-S to S-M-S and even S-S'-S, based on transition metal dichalcogenides (TMDs). S, M and I stand for superconductor, metal and insulator respectively, with S' being a slightly different superconducting quantum state. Single crystals of multilayer and monolayers will be used as the unique material forming the junction, where the electronic phase will be tuned by local gates made of carbon nanotubes (CNTs), as schematically shown in Fig. 1.10. As a consequence, the proposed junction will be made of a single material and be fully controlled *in-situ*.

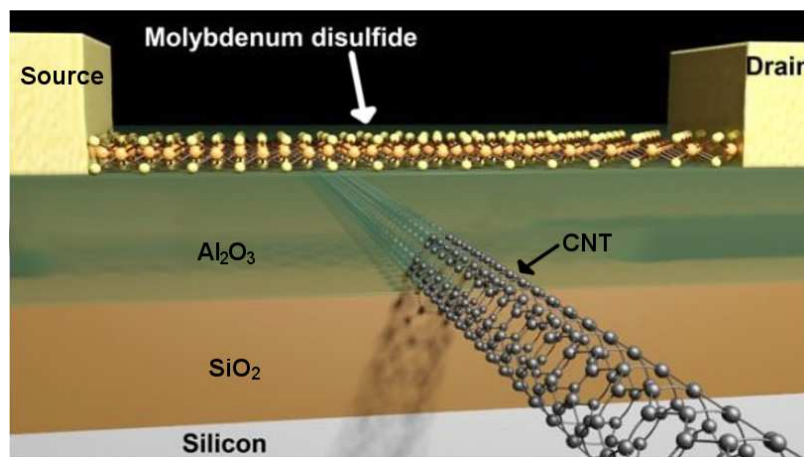


Figure 1.10: Goal device: tunable JJ. Adapted from [43].

The superconducting state of the MoS₂ will be reached with the use of the ionic liquid gating technique. Ionic liquid can push the carrier density on TMDs as high as $\sim 1 \times 10^{14} \text{ cm}^{-2}$ [1, 19, 34, 35, 44–47], which allows the superconducting state to manifest. Therefore, the

whole MoS₂ sample will be in a superconducting state except in the region surrounding the local gate. This local gate will tune the carrier density in a small region around it, and is expected to modify and even destroy the superconducting state, making the weak link in the JJ. A back gate, made of highly doped Si, will act as a fine control on the electron density. In Fig. 1.11 is shown a simplified sketch of the goal device.

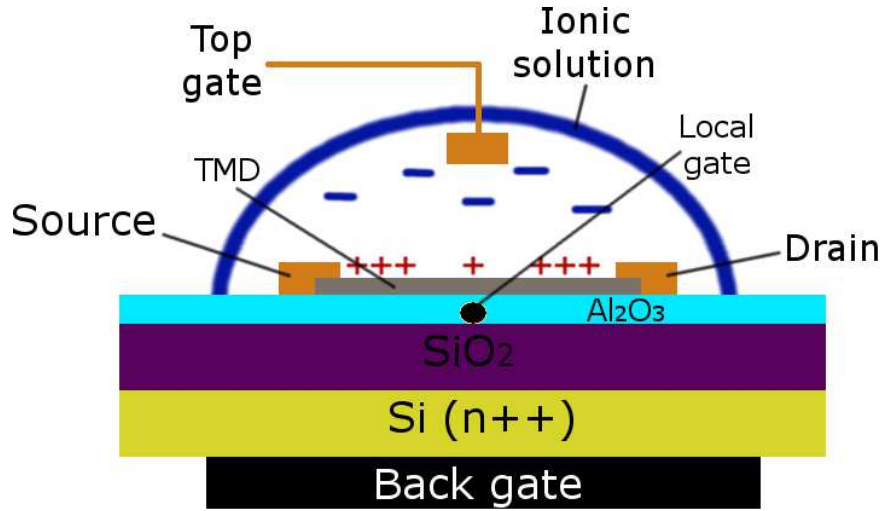


Figure 1.11: Simplified sketch of the goal device. The ionic liquid, the CNT and the highly doped Si will act as the top, local and back gates respectively.

JJ made with superconductors exhibiting strong spin-orbit coupling are of prime interest since they could host topological states called Majorana fermions [36, 48–51]. These states and their manipulation are expected to lead to applications in quantum computing and other condensed matter areas of physics. First hints in one-dimensional and bidimensional materials have been already reported [48, 51], but they require hybrid materials where superconductivity is induced by proximity into conductors with strong spin-orbit coupling, or by placing magnetic materials in proximity with normal superconductors. In Fig. 1.12a, one can see an example of such state unveiled by electrical measurements: what are thought to be Majorana states, in green oval, lead to non-zero resistance in the middle of the superconducting gap without field dependence of their energy.

A tunable JJ could also find uses in the area of metrology. In 1963, Shapiro [52] showed that when a JJ is under microwave excitation the critical current is reduced and voltage steps appears. Those steps, now called Shapiro steps, are directly proportional to the excitation frequency, and are of particular interest for the volt standard [53], since these voltage steps are linked to frequency only through fundamental constants as $V_{DC} = nhf/2e$, where n is

an integer.

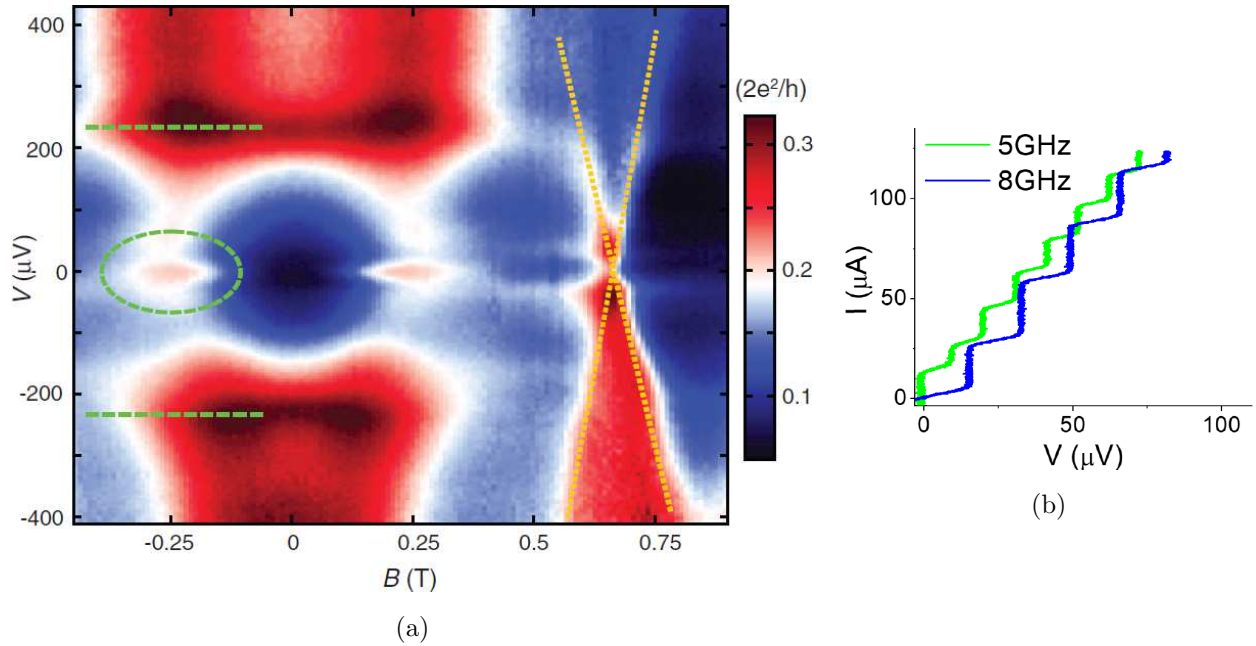


Figure 1.12: (a) Conductance dI/dV versus magnetic field and bias voltage of a topological JJ (InSb nanowires partially contacted by superconductors and non-superconductors). The green dashed oval corresponds to the onset of a Majorana fermion, the superconducting gap is given by the green dashed lines, and yellow lines underlines other types of sub-bandgap states, called bound Andreev states. From [48]. (b) Characteristic current versus bias voltage of a Josephson junction with microwave excitation. The steps formed are called Shapiro steps. Adapted from [54].

1.1.4 State of the art: MoS₂ FET transistors

A description of a Field Effect Transistor (FET) will be given in the next Chapter, here is presented a small overview of transistor devices usually found in the literature. One of the first FET 2D MoS₂ transistors was made by Novoselov *et al.* [55]. They measured mobilities at room temperature between 0.5 and 3 cm²/Vs for different samples. In Fig. 1.13a is shown some of their field effect results for different materials.

The mobility at room temperature was found to improve upon the deposition of a high- κ dielectric on top of the transistor. Radisavljevic *et al.* [56] measured mobilities above 200 cm²/Vs on monolayer MoS₂ by depositing a 30 nm of HfO₂ on top of it. Their results, together with an sketch of the device, are shown in Fig. 1.13c.

In a more recent study performed by Moon *et al.* [5] on multilayer MoS₂, is revealed a complex temperature and doping dependence of the conductivity, as shown in Fig. 1.13b.

It is shown that monolayer MoS₂ transistor devices are commonly found in the literature, having different shapes depending on the utility. A more complete review can be found in [57].

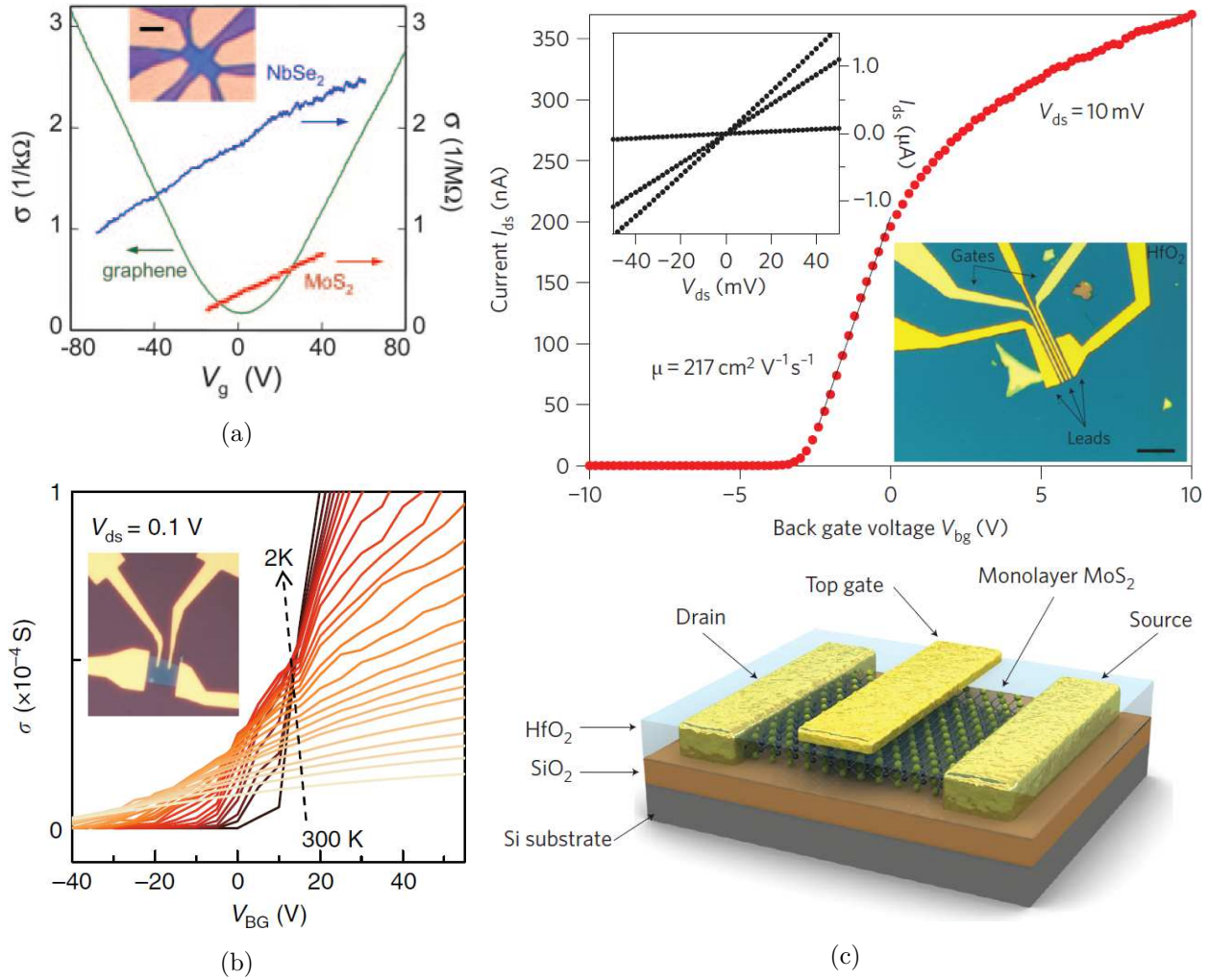


Figure 1.13: (a) Electric field effect in single-atomic-sheet crystals at $T = 300$ K. The inset shows a typical devices used for such measurements. Scale bar: $5 \mu\text{m}$. From [55]. (b) Room-temperature electric field effect of monolayer MoS₂. Backgate voltage is applied to the substrate and the top gate is disconnected. The top left inset shows the current-voltage curves at different backgate voltages, whereas the lower right inset shows a optical image of the device used. Scale bar: $10 \mu\text{m}$. Adapted from [56]. (c) Conductivity σ vs. backgate bias V_{BG} for various temperatures. The inset shows a optical image of the device. From [5].

1.2 Classical electronic transport

Electrical transport involves the motion of charges under the influence of electric and/or magnetic fields. In non-ballistic systems, the charge carriers are, on one hand, accelerated

by the driving fields and, on the other hand, scattered when colliding onto the medium's defects, phonons or between themselves. These opposite interactions lead to a constant mean velocity of the charge carriers. The classical treatment of conduction relies on the Drude model, which introduces a mean scattering time to take into account the diffusion processes. This model will be presented with and without magnetic field in the following Sections.

1.2.1 Drude model of conduction

The Drude model was proposed in 1900 by Paul Drude to explain the transport of electrons in metals [58]. The model treats electrons as classical balls, free and independents. The electron-electron interactions are neglected and the interactions with the ions and with the impurities are described by a drag force which is proportional to the electron's velocity.

Effect of electric field

The displacement of an electron of charge $-e$ and of mass m under an electric field \vec{E} is described by the following equation (from Newton's second law):

$$\frac{\partial \vec{P}}{\partial t} = \frac{\partial \vec{P}_e}{\partial t} + \frac{\partial \vec{P}_d}{\partial t} = -e\vec{E} - \frac{m\vec{v}}{\tau}, \quad (1.5)$$

where \vec{P} is the total momentum, $\frac{\partial \vec{P}_e}{\partial t}$ is the force due to the electric field and $\frac{\partial \vec{P}_d}{\partial t}$ is the "drag force" due to collisions, and τ is the average collision time.

In steady state, the velocity has the following expression:

$$\vec{v} = -\frac{e\tau}{m}\vec{E} \quad (1.6)$$

The current density in the material is given by:

$$\vec{j} = -ne\vec{v} = \frac{ne^2\tau}{m}\vec{E} \equiv \sigma_0\vec{E}, \quad (1.7)$$

where σ_0 is the conductivity of the material.

The mobility is defined as $\vec{v} = \mu\vec{E}$:

$$\mu = q\frac{\tau}{m} \quad (1.8)$$

Effect of electric and magnetic field

The force \vec{F} acting on a particle of electric charge q with velocity \vec{v} , due to an external electric field \vec{E} and magnetic field \vec{B} , is given by the commonly known Lorentz force [59]:

$$\vec{F} = q(\vec{E} + \vec{v} \times \vec{B}) \quad (1.9)$$

The electron's velocity in the material is then given by:

$$\vec{v} = -\frac{e\tau}{m}(\vec{E} + \vec{v} \times \vec{B}), \quad (1.10)$$

then, the current density is given by the following expression:

$$\vec{j} = -ne\vec{v} = \frac{ne^2\tau}{m} \left(\vec{E} - \frac{1}{ne} \vec{j} \times \vec{B} \right) \quad (1.11)$$

This expression can be expressed in terms of the electric field in a matrix form, in 2D ones get:

$$\begin{pmatrix} E_x \\ E_y \end{pmatrix} = \begin{pmatrix} \frac{1}{\sigma_0} & \frac{\omega_c\tau}{\sigma_0} \\ -\frac{\omega_c\tau}{\sigma_0} & \frac{1}{\sigma_0} \end{pmatrix} \begin{pmatrix} j_x \\ j_y \end{pmatrix}, \quad (1.12)$$

where $\omega_c = eB/m$ is the cyclotron frequency of the electron.

Since $\vec{E} = \rho\vec{j}$, and using the expression 1.8 for the mobility, we obtain the elements of the resistivity tensor ρ :

$$\rho_{xx} = \rho_{yy} = \frac{1}{\sigma_0} \Rightarrow \rho_{xx} = \rho_{yy} = \frac{1}{ne\mu} \quad (1.13)$$

$$\rho_{xy} = -\rho_{yx} = \frac{\omega_c\tau}{\sigma_0} \Rightarrow \rho_{xy} = -\rho_{yx} = \frac{B}{ne} \quad (1.14)$$

According to the previous equations, the longitudinal resistivity is independent of magnetic field, but the transverse resistivity (often called Hall resistivity) varies linearly with magnetic field.

1.2.2 Hall effect

If a conductor in which a current is flowing is placed in a region with a magnetic field, the carriers (electrons or holes) will experience the Lorentz force and will deviate from their main trajectory. If the conductor has a finite width, the carriers will start to accumulate at the edges and, eventually, generate an electric field as shown in Figure 1.14. The steady state is reached when the electric force cancels the magnetic force, and the electrons then travel without any deviation. This induced electric field is responsible for the Hall voltage V_H , and was discovered by Edwin Hall in 1879 [60].

For 2D materials, resistances are related to resistivities by the following equations:

$$R_{xx} = \frac{V_x}{I_x} = \frac{L}{W} \frac{E_x}{j_x} = \frac{L}{W} \rho_{xx} \quad (1.15)$$

$$R_{xy} = \frac{V_y}{I_x} = \frac{W}{L} \frac{E_y}{j_x} = \rho_{xy} \quad (1.16)$$

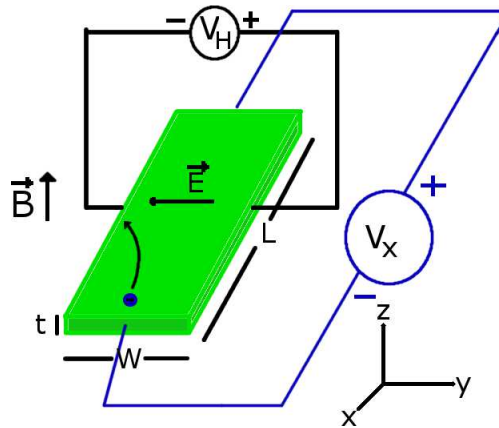


Figure 1.14: Hall effect measurement setup for electrons.

and the resistivities are related to the conductivities by the following equations:

$$\rho_{xx} = \frac{\sigma_{xx}}{\sigma_{xx}^2 + \sigma_{xy}^2} \iff \sigma_{xx} = \frac{\rho_{xx}}{\rho_{xx}^2 + \rho_{xy}^2} \quad (1.17)$$

$$\rho_{xy} = -\frac{\sigma_{xy}}{\sigma_{xx}^2 + \sigma_{xy}^2} \iff \sigma_{xy} = -\frac{\rho_{xy}}{\rho_{xx}^2 + \rho_{xy}^2} \quad (1.18)$$

The Hall resistivity, with the help of expression 1.14, is often written in the following form:

$$R_H = R_{xy} = \frac{B}{ne} = K_H B, \quad (1.19)$$

where $K_H = 1/ne$ is the Hall coefficient. By measuring the Hall resistivity, the charge density can be determined with the use of Eq. 1.14, and by measuring the longitudinal resistivity, the mobility of the material can be calculated with the use of Eq. 1.13.

1.3 Mesoscopic transport: the metal–insulator transition

The metallic and insulating state of a material are defined by the temperature dependence of its conductivity at low temperatures: if the conductivity decreases as temperature tends to zero the material then falls into the insulator category, but if the opposite occurs it is then considered a metal. A variety of materials can show both states, transitioning from one to another (metal–insulator transition) depending on external parameters others than temperature. The study of the metal–insulator transition (MIT) has been an important field of research in solid state physics for more than half a century, the reason being that the MIT raised unsolved fundamental question. One of the first explanation for the MIT phenomena was given by Anderson in the late 50's [61] and Mott in the early 60's [62].

In the Mott model the transition occurs because of electron screening of their host atom's potential at high enough electron density, while in the Anderson model electron localization occurs if the disorder in the lattice is sufficiently large. The Nobel Prize in Physics 1977 was awarded jointly to Philip Warren Anderson, Sir Nevill Francis Mott and John Hasbrouck Van Vleck “for their fundamental theoretical investigations of the electronic structure of magnetic and disordered systems” [63]. Those models are referred today as “Mott transition” and “Anderson transition” and will be presented in the following Sections. Good reviews can be found in [64–66].

1.3.1 Mott transition

The model developed by Mott starts from a cubic crystalline array of hydrogen-like (one-electron) atoms with a lattice parameter d [67], as shown in Fig. 1.15 . The system can be a metal or an insulator depending on d : for large values of d the array is an insulator, but for small values of d the array will be a metal. When decreasing d , the electron density increases and starts to screen the potential they feel from the nucleus of the atom. This potential can be expressed by the Yukawa potential $V(r) = (e/r)\exp(-r/\lambda_{TF})$, where $\lambda_{TF}^{-2} = 4m^*e^2(3n/\pi)^{1/3}/\hbar^2$ is the Thomas-Fermi length. At some critical d or, equivalently, a critical value for the density n_c , the MIT occurs. Mott estimated this critical value by comparing the Thomas-Fermi length to the effective Bohr radius: $\lambda_{TF} \sim a_B^*$, where $a_B^* = 4\pi\epsilon_0\epsilon_r\hbar^2/m^*e^2$, finding $n_c^{1/3}a_B^* \simeq 0.25$. Besides its simplicity, this criteria is obeyed by a large number of semiconducting materials, as shown in Fig. 1.16.

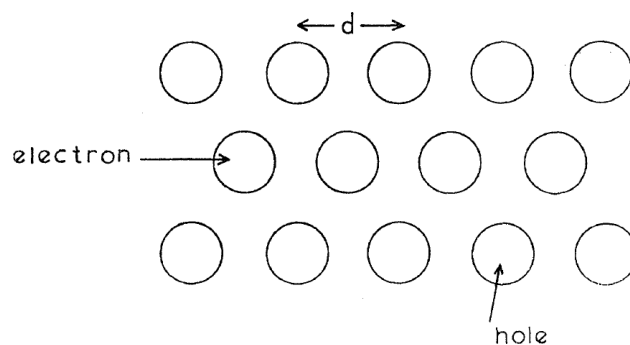


Figure 1.15: A crystalline array of hydrogen-like atoms. From [67].

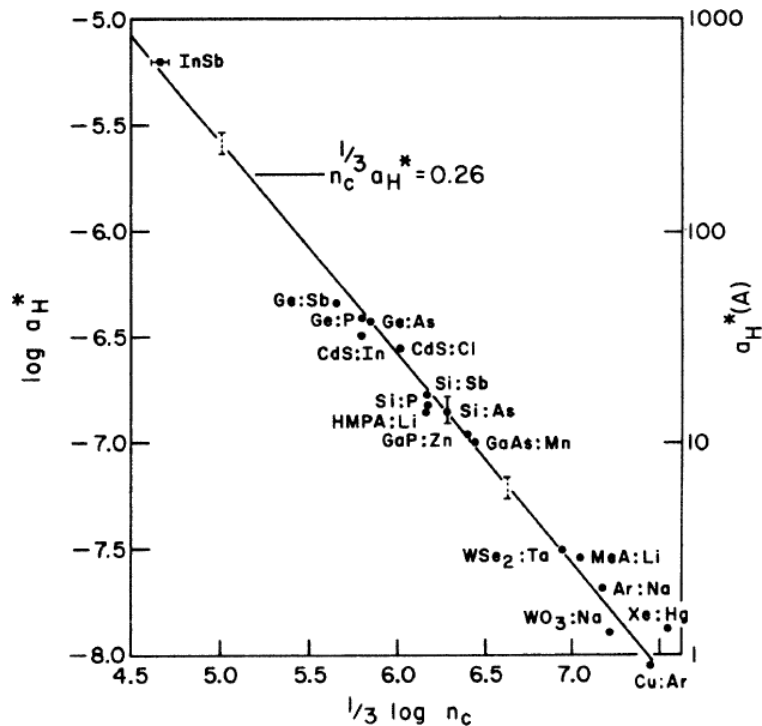


Figure 1.16: Critical density n_c at the MIT, and atomic Bohr radius a_B^* , in a variety of semiconducting materials. The straight line follows the criteria developed by Mott. From [68].

1.3.2 Anderson transition

In 1958 Anderson published his paper on “the absence of diffusion in certain random lattices” [61], in which Anderson assumed distributed sites in three-dimensional space that can be occupied by any particle. If the site j is occupied, it will have an energy E_j , which is a stochastic variable distributed over a band of energies completely random, with a probability distribution $P(E)dE$. This band of energy can be characterized by a width W , called impurity band, and schematically shown in Fig. 1.17. This model also assumes that between two sites, j and k , there is an interaction matrix element $V_{jk}(r_{jk})$, which transfers the particle from one site to the next. Anderson showed that if V_0/W (V_0 being the average value of the interactions) is lower than a certain critical value, the solutions of the Schrodinger equation for any energy in the band are no longer extended Bloch states, but are localized in space.

1.3.3 Mobility edge

Mott [69] first pointed out that, if V_0/W lies above the critical value, localized states will nonetheless exist for energies near the extremities of a band, and that an energy E_c must separate energies where states are localized from energies where they are extended (see Fig.

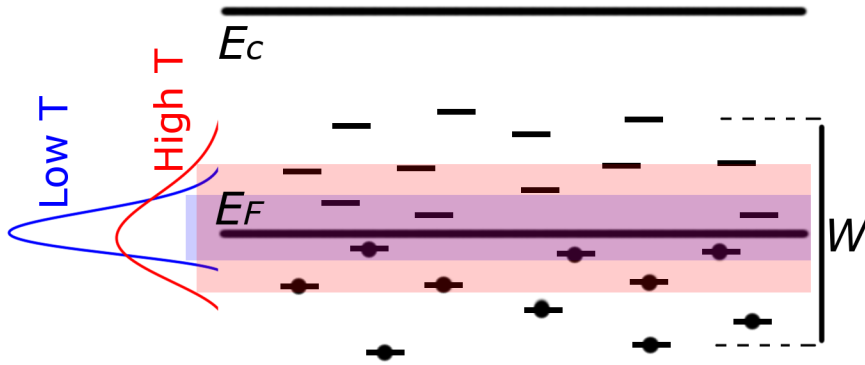


Figure 1.17: Random impurities states below the conduction band E_c used by Anderson. The impurity band have a width W . States below the Fermi energy E_F are all occupied at $T = 0$ K, while at finite T they can hop between states that fall in the thermal energy band.

1.18); E_c was later called the “mobility edge” [70]. If $E_F > E_c$, where E_F is the Fermi energy, then the system is “metallic”, and the conductivity σ tends to a finite value as $T \rightarrow 0$. If on the other hand $E_F < E_c$, then electrons can only move by thermally activated hopping and σ goes to zero as $T \rightarrow 0$.

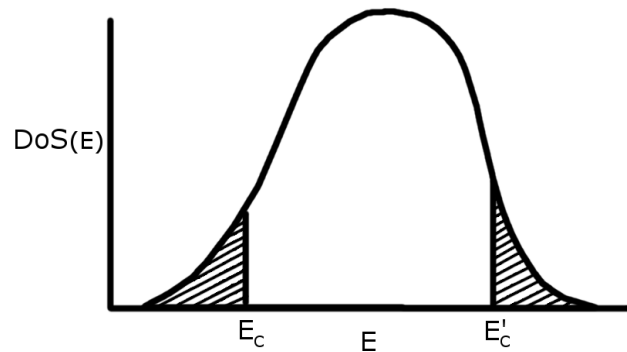


Figure 1.18: Density of states (DoS) in an Anderson band with the two mobility edges E_C and E'_C separating localized (shaded regions) and delocalized states.

For E_F near the mobility edge on the metallic side, Mott found a minimum metallic conductivity value of $\sigma_{min} = 0.03e^2/\hbar a$ [71], where a is the mean distance between defects at E_F .

1.3.4 Ioffe-Regel criteria

Ioffe and Regel [72] were the first to point out that values of the mean free path l such that $k_F l < 1/2\pi$ are impossible because, in metals, this mean $l \sim d$ where d is the distance between atoms, thus, setting a minimum value for the mean free path. Using the distance

between impurities instead of the distance between atoms, Ioffe and Regel found a minimum for the conductivity:

$$\sigma_{IR} \sim e^2/3\hbar d, \quad (1.20)$$

being one order of magnitude higher than σ_{\min} found by Mott. This idea of minimum conductivity was later abandoned when came out Abrahams work on scaling theory of localization.

The Ioffe-Regel criterion can be used in two-dimensional systems, even if the localization theory demonstrates that all these systems are insulators at zero temperature. The Ioffe-Regel criteria can still be used because it separates the strongly localized regime from the weakly localized one. This idea has been largely developed by Das Sarma and Hwang [73]. Some materials undergo a MIT as a function of external parameters such as doping, where decreasing 2D carrier density drives the system from being a 2D metal at high density to being a 2D insulator at lower density, as the Fermi level moves through the mobility edge. Das Sarma treats the metallic state as a weakly localized high-density state, and the insulating state as a low-density strongly localized state, viewing the MIT as a transition from weak to strong localization. This transition is then expected to happen around $k_F l = 1$, where k_F is the wavevector at E_F , and l is the mean free path of the carriers. Since both k_F and l are doping dependent, the transition then occurs at a critical electron density n_c , with $n > n_c$ being a metal and $n < n_c$ being an insulator.

One can obtain the conductivity at the transition using the Ioffe-Regel criteria $k_F l = 1$, where $l = v_F \tau$; $v_F = p_F/m = \hbar k_F/m$ is the Fermi velocity; τ is the transport relaxation time; $k_F = (4\pi n/g_s g_v)^{1/2}$ for a 2D electron gas, with g_s and g_v being, respectively, the spin and valley degeneracy factor. Substituting all this on the Drude formula for the electrical conductivity presented in Eq. 1.7, Das Sarma got the following condition for the critical conductivity $\sigma_c = \sigma(n_c)$ at the transition [73]:

$$\sigma_c = \frac{g_s g_v}{2} \frac{e^2}{h} \quad (1.21)$$

Values close to this critical conductivity at the transition have been observed numerous times on MoS₂ as well as other TMDs [5, 8, 10, 12, 74–76].

1.3.5 Scaling theory of localization

In order to account more generally for the dimensionality of the system, a scaling theory of localization was introduced by Abrahams *et al.* in 1979 [77], based on concepts of Thouless.

Thouless [78] imagined a system where the electrons move in a wire of length L which have a uniform potential but with enough irregularities to give the conductivity of the bulk metal a finite value at zero temperature. The time that takes an electron to travel from end to end is $\tau = L^2/D$, where D is the diffusion constant for an electron. This can be related to the conductivity by the Einstein relation for a degenerate electron gas $\sigma = (1/2)e^2 D dn/dE$, where dn/dE is the density of electron states per unit volume per unit energy. Combining those terms Thouless got:

$$\frac{\hbar}{\tau} = \frac{2\hbar\sigma dE}{e^2 L^2 dn} = \frac{2\hbar\sigma}{e^2} \frac{dE}{dN}, \quad (1.22)$$

where dE/dN is the average spacing between energy levels, with N being the number of energy levels available. According to Thouless, the individual energy levels are sensitive to the boundary conditions applied at the ends of the wire, and can be shifted by an amount of order \hbar/τ , which can be found using the uncertainty relation between time and energy: $\tau\delta E = \hbar$. Generalizing the sample size to an hypercube of size L^d Abrahams got:

$$\frac{\delta E}{dE(L)/dN} = \frac{2\hbar}{e^2} \sigma L^{d-2} = g(L), \quad (1.23)$$

where $g(L)$ is the generalized dimensionless conductance which is called ‘‘Thouless number’’. Abrahams then imagined combining many cubes of size L^d and computed the new Thouless number:

$$g(bL) = f(b, (L)), \quad (1.24)$$

which can be written as:

$$\frac{d \ln g(L)}{d \ln L} = \beta(g(L)), \quad (1.25)$$

where $\beta(g(L))$ is a scaling function. Abrahams then studied the limits of this function: for large g , where macroscopic theory of conduction is correct giving $G(L) = \sigma L^{d-2}$, Abrahams got:

$$\lim_{g \rightarrow \infty} \beta(g) = d - 2 \quad (1.26)$$

In the case of small g , localization occurs and therefore g falls off exponentially, giving $g(L) = g_0 \exp(-L/\xi)$:

$$\lim_{g \rightarrow 0} \beta(g) = \ln g - \ln g_0, \quad (1.27)$$

where g_0 is dimensionless ratio of order unity and ξ is the localization length. From the asymptotics of Eq. 1.26 and Eq. 1.27, Abrahams sketched the universal curve shown in Fig. 1.19 for $\beta(g)$ in $d = 1, 2$ and 3 dimensions.

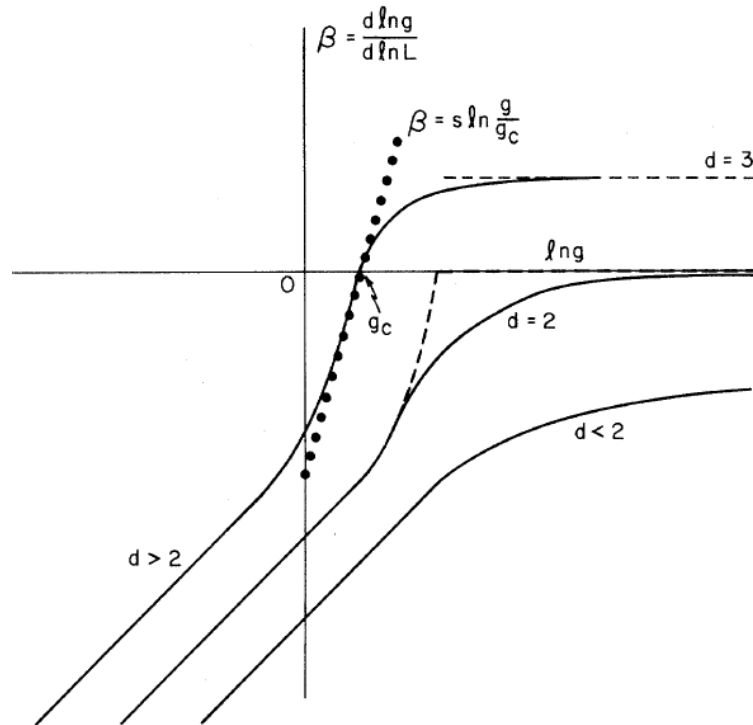


Figure 1.19: Plot of $\beta(g(L))$ vs $\ln(g)$ for $d=1,2$ and 3 dimensions.

In light of this results, it is shown that lower-dimension systems ($d < 3$) do not undergo a metal-insulator transition because the conductance always decreases with system size. Note that this theory does not involve electron-electron interactions nor weak localization.

1.3.6 Hopping transport

As we have seen previously, disorder induces a bandtail of localized states at the edges of the bands. We present here what happens to the d.c. conductivity when the Fermi energy lies in the range of energies where states are localized. Two mechanisms for conduction are then possible:

(i) Excitation of electrons to the bottom of the conduction band, or mobility edge E_c . The contribution to the conductivity is (neglecting interaction with phonons) [79]:

$$\sigma = \sigma_{\min} \exp\left(-\frac{\epsilon}{kT}\right), \quad (1.28)$$

where $\sigma_{\min} = 0.03e^2/ha$ is the value of the conductivity at $E = E_c$, $\epsilon = E_c - E_F$ and a is the average distance between defects. This kind of conduction dominates at high temperature or at small ϵ , and is often called thermally activated transport.

(ii) Thermally activated hopping of electrons between states near the Fermi energy. In this process, an electron hops from a filled state i to another empty state j . The two states

must be close to the Fermi energy, so their energy difference is not too high. The probability that this process occurs is the product of several factors [80]:

1. The Boltzmann factor $\exp(-\epsilon_{ji}/kT)$, where ϵ_{ji} is the difference between the energies of the two states;
2. A phonon rate ν_{ph} which depends on the strength of the interaction with phonons;
3. A factor which depends on the overlap of the wavefunctions for the two states. If the localization is very strong, as for hydrogenoid impurities or structural defects, this factor varies as $\exp(-2r_{ji}/\xi)$, where r_{ji} is the distance between the two states, and ξ is the spatial extension (the localization length) of these wavefunctions.

The hopping probability is then:

$$\nu_{\text{ph}} \exp\left(-\frac{2r_{ji}}{\xi} - \frac{\epsilon_{ji}}{kT}\right) \quad (1.29)$$

In a first approximation, Mott proposed one can assume that the total conductivity is well approximated by Eq. 1.29:

$$\sigma \sim \exp\left(-\frac{2r_{ji}}{\xi} - \frac{\epsilon_{ji}}{kT}\right) \quad (1.30)$$

Variable range hopping

Let us assume the the electron hops at a distance r , having $\pi r^2 \epsilon \text{DoS}$ available sites to hop to, where DoS is the density of states at E_F . Assuming at least one site available, this gives the minimal value for ϵ (the average spacing between energies):

$$\epsilon = \frac{1}{\pi r^2 \text{DoS}}, \quad (1.31)$$

and the conductivity is then given by:

$$\sigma \sim \exp\left(-\frac{2r}{\xi} - \frac{1}{\pi r^2 \text{DoS} kT}\right) \quad (1.32)$$

The derivation of the term in the exponential with respect to r gives the optimal hopping distance. One obtains:

$$\sigma \sim \exp\left[-\left(\frac{T_3}{T}\right)^{1/3}\right], \quad (1.33)$$

where:

$$T_3 = \frac{27}{\pi\xi^2\text{DoS}k_B} \quad (1.34)$$

$$r = \left(\frac{\xi}{\pi\text{DoS}k_B T} \right)^{1/3} = \frac{\xi}{3} \left(\frac{T_3}{T} \right)^{1/3} \quad (1.35)$$

$$\epsilon = \left(\frac{k_B^2 T^2}{\pi\text{DoS}\xi^2} \right)^{1/3} = \frac{1}{3} k_B (T_3 T^2)^{1/3} \quad (1.36)$$

Ambegaokar *et al.* [81] and Pollak [82] were the first to apply percolation theory to the hopping problem. They found a value of T_3 differing slightly from the value given in Eq. 1.34. In two dimensions, percolation theory gives:

$$T_3 = \frac{13.8}{\xi^2\text{DoS}(E_F)k_B} \quad (1.37)$$

Nearest neighbour hopping

If the localization length is too large, which is the case near the Anderson transition, one can neglect the first term in the exponential on Eq. 1.32, the result is:

$$\sigma \sim \exp \left[- \left(\frac{T_1}{T} \right) \right], \quad (1.38)$$

where $T_1 = (k_B a^2 \text{DoS})^{-1}$. This kind of transport is known as nearest neighbour hopping (NNH).

Efros-Schklovskii

The previous discussion neglects Coulomb interaction which may exist between the two sites if they correspond, for instance, to two donors. This discussion also assumed a constant density of states at the Fermi level being equal to DoS_0 . Efros and Shklovskii re-derived this law for electrons with Coulomb interactions [83]. The effect of the Coulomb interaction is to empty the density of states near the Fermi energy. In this case, the DoS varies with energy below a critical energy Δ from the Fermi level and vanishes at the Fermi level.

Consider the equilibrium case at temperature $T = 0$ K, where all states below the Fermi level are occupied and those above it are empty. Consider now two states i and j , which in the ground state are occupied and vacant respectively. The transfer of an electron from state i to state j should increase the energy of the system:

$$\epsilon_{ji} = \epsilon_j - \epsilon_i - \frac{e^2}{\kappa r_{ij}} > 0, \quad (1.39)$$

where κ is the dielectric of the system. We consider now a small energy interval ε centered at the Fermi level. According to 1.39, any two donors in this band with energies on opposite sides of the Fermi level must be separated by a distance r_{ij} not less than $e^2/\kappa\varepsilon$. Therefore the donor concentration $n(\varepsilon)$ in a band of width ε cannot exceed $\varepsilon^2\kappa^2/e^4$, and the density of states $\text{DoS}(\varepsilon) = dn(\varepsilon)/d\varepsilon$ must vanish when $\varepsilon \rightarrow 0$. In the 2D case, the density of states is:

$$\text{DoS}(\varepsilon) = \frac{2}{\pi} \frac{|\varepsilon|\kappa^2}{e^4} \quad (1.40)$$

Expression 1.40 is valid provided the energy ε is so small that the distance $r_{ij} = e^2/\kappa\varepsilon$ much exceeds the mean separation between donors or, equivalently, when $\text{DoS}(\varepsilon) \ll \text{DoS}_0$, where DoS_0 is the constant density of states used by Mott. The width of the Coulomb gap Δ is given by the equation $\text{DoS}(\Delta) = \text{DoS}_0$:

$$\Delta = \frac{\pi}{2} \frac{e^4}{\kappa^2} \text{DoS}_0 \quad (1.41)$$

Thus the density of state in 2 dimensions is then [84]:

$$\text{DoS}(\varepsilon) = \frac{2}{\pi} \left(\frac{\kappa^2}{e^4} \right) |\varepsilon| \text{ if } \varepsilon \ll \Delta \quad (1.42)$$

$$\text{DoS}(\varepsilon) = \text{DoS}_0 \text{ if } \varepsilon \gg \Delta \quad (1.43)$$

The gap size should be compared with the optimum band ϵ in Eq. 1.31. When the optimum band is much larger than Δ , the influence of the Coulomb gap can be safely neglected. At the opposite, when $\epsilon \ll \Delta$, the Coulomb gap must be taken into account. Eq. 1.30 then becomes:

$$\sigma \sim \exp \left(-\frac{2r}{\xi} - \frac{U}{rk_B T} \right), \quad (1.44)$$

where $U = e^2/\kappa$. Following the same approach as when deriving Eq. 1.38, we find the optimal hopping distance:

$$\sigma \sim \exp \left[-\left(\frac{T_2}{T} \right)^{1/2} \right], \quad (1.45)$$

where:

$$T_2 = \frac{8e^2}{\kappa\xi k_B} \quad (1.46)$$

$$r = \left(\frac{e^2\xi}{2k_B T} \right)^{1/2} = \frac{\xi}{4} \left(\frac{T_2}{T} \right)^{1/2} \quad (1.47)$$

A slightly different expression for T_2 has been found by numerical methods. It was found that $k_B T_2 = \beta e^2/\kappa\xi$, where β is a numerical coefficient which depends on the dimensionality of the system, and has been calculated by numerical methods [85]: $\beta = 6.2$ in two dimensions.

Hopping conduction in strong electric fields

In the low-temperature and strong electric field regime, an additional term, representing the energy that an electron gains with the electric field, appears in Eq. 1.30. The conduction is then driven by the electric field with a negligible thermal dependence. In the presence of the ES Coulomb gap, the field-driven conductivity in the insulating phase is described as [86–88]:

$$\sigma \sim \exp \left[- \left(\frac{E_{ES}}{E} \right)^{1/2} \right], \quad (1.48)$$

where E is the electric field and $E_{ES} = \frac{k_B T_2}{2e\xi}$, with T_2 given by Eq. 1.46. This electric-field-dependence conductivity leads to non-linear current-voltage curves, and it has been observed in monolayer graphene [89] and few layers of MoS₂ [5].

1.3.7 Percolation method

In the solution presented above, we neglected the fact that there is not only two impurities, but a network of sites on which the electrons can hop. Percolation theory applied to this problem gives a more rigorous treatment. In this approach, the hopping problem is transposed to the problem of percolation through a network of random spheres (in 3D) or discs (in 2D). Webman *et al.* [90] studied the MIT as a percolation problem by numerical simulations of a cubic resistor network, where the material is viewed as consisting of a random submicroscopic mixture of metallic and nonmetallic regions, with the parameter C being the fraction of the total volume which is metallic at the Fermi energy. If C is large then continuous metallic paths extend throughout the material, so that electrons at the Fermi energy are in extended states, whereas when C decreases to some critical value C^* , called the percolation threshold, extended metallic paths cease to exist, and the electrons become localized. Webman *et al.* were able to fit the conductivity data of metal-ammonia solutions and of alkali-tungsten bronzes (which undergo a MIT) with the expression $\sigma(C) = A(C - C^*)^\gamma$, finding values for $C = 0.13 - 0.25$ and $\gamma = 1.5 - 1.75$.

More recently, Das Sarma *et al.* [91–93] suggested that as the carrier density is lowered in a 2D system, screening becomes progressively weaker and strongly nonlinear, and eventually leads to a highly inhomogeneous 2D system as the electron gas becomes unable to screen the disorder potential. This gives rise to a random “hill-and-valley” potential landscape, as shown in Fig. 1.20, with the 2D carriers repelled from the potential hills and accumulating

at the potential valleys, in contrast to the high carrier density homogeneous situation. Once these potential hills are numerous enough to prevent percolating conducting paths to span the 2D system, an effective 2D MIT transition takes place with the system being an effective metal (insulator) for $n > (<) n_c$, where n_c is the critical percolation density. Das Sarma *et al.* were able to fit the low-temperature conductivity of GaAs/AlGaAs heterojunctions [91] and Si MOSFETs [92] with the expression $\sigma(n) = A(n - n_c)^\delta$, the results are summarized on the table 1.1.

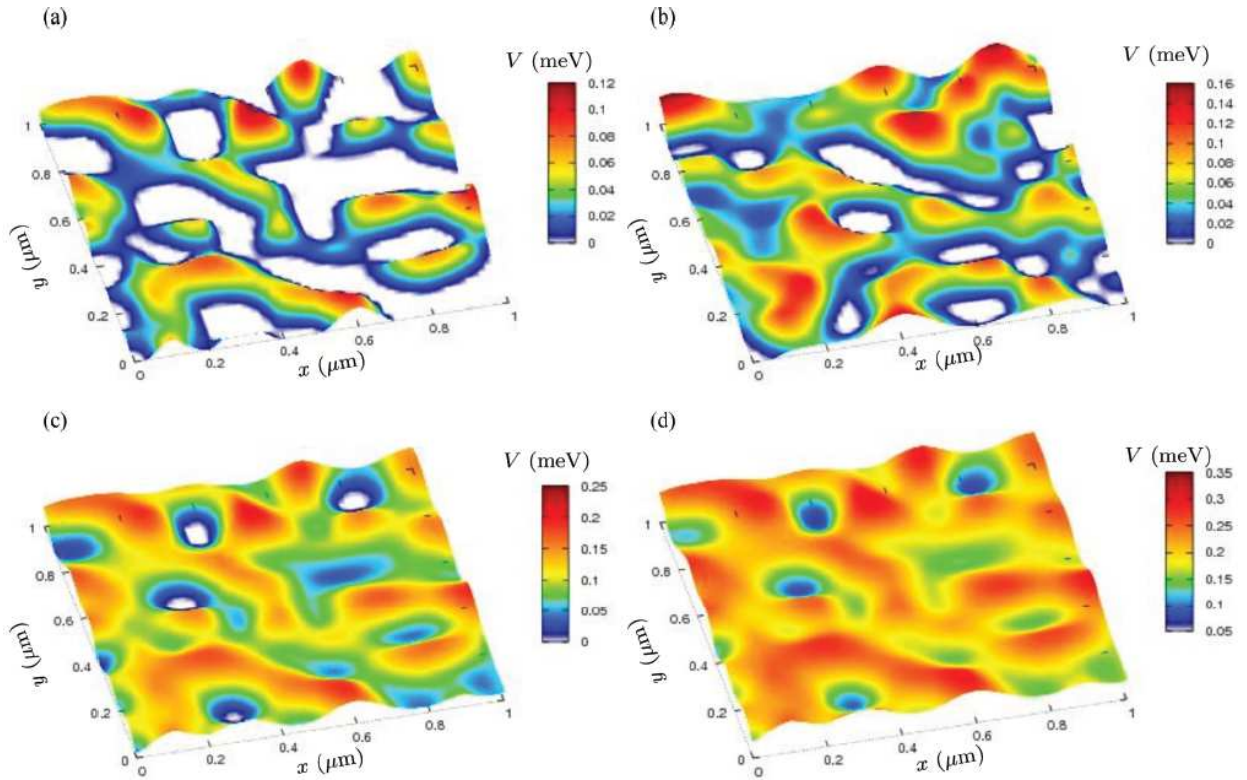


Figure 1.20: Schematic diagram of the potential landscape for a disorder strength of $s = 0.05$ meV at different Fermi levels: (a) $E_F = 0.01$ meV. (b) $E_F = 0.05$ meV. (c) $E_F = 0.1$ meV. (d) $E_F = 0.2$ meV. From [93].

| Sample | δ | n_c |
|-------------|-------------|--|
| Si | 1.20 – 1.24 | $1.2 - 2.0 \times 10^{11} \text{ cm}^{-2}$ |
| GaAs/AlGaAs | 1.4 – 1.5 | $1.8 - 2.8 \times 10^9 \text{ cm}^{-2}$ |

Table 1.1: Percolation fitting results from [91, 92].

All these transport mechanism will be used in Chapter 3 to describe the gate and temperature dependent electronic transport in monolayer MoS₂.

1.4 Metal-semiconductor interface: the Schottky barrier

As the monolayer MoS₂ is contacted with metal in order to perform electrical measurements, one needs to understand what happens at the semiconductor-MoS₂ interface. The electrical current flowing across such interface is usually non-linear against the applied bias voltage, as a result of the discontinuity of the energy of the electronic states responsible for conduction in the two materials. In Fig. 1.21, a band diagram of the interface is sketched to show this discontinuity. Delocalized electronic states around the Fermi level are responsible for electrical conduction in the metal, drawn on the left, but these states are not coupled to any delocalized electronic states in the semiconductor drawn on the right. The lowest-lying states for n-type semiconductor that can communicate with electrons in the metal are now at an energy Φ_B above the Fermi level, as shown in the figure. For electronic transport across the metal-semiconductor interface, this energy offset, known as Schottky barrier (SB), manifests itself as a potential energy barrier that leads to rectifying behavior between the metal and the n-type semiconductor, *i.e.*, the flow of electrons from the semiconductor to the metal is easier than conduction in the opposite direction [94]. A metal–semiconductor junction that conducts current in both directions without rectification is called an ohmic contact. A decrease in barrier height and width will improve the charge injection, which in turn will have significant impact in fabricating high-performance electronic devices.

Electric contacts are commonly of Schottky type on MoS₂ [13–15, 95, 96]. At the metal–MoS₂ contact (where a barrier is formed) the charge injection occurs either (i) as a result of thermionic emission over the top of the barrier due to the transfer of thermal energy or (ii) as a result of quantum mechanical tunneling of carriers across the barrier width. The tunneling behavior can be direct or Fowler–Nordheim (FN) type, depending on the shape and width of the barrier. The direct tunneling and the F–N tunneling are determined by the nature of the interfacial barrier, that is, the former occurs when the barrier is trapezoidal (wide) and the latter occurs when the barrier is triangular (thin). Those mechanisms are shown in Fig. 1.21b. Besides the SB, an interface barrier is also created at the interface, as schematically shown in Fig. 1.21a. The shape of this barrier is characterized for being rectangular, with the width depending on the distance between the metal and the semiconductor, or more precisely, the quantum overlapping between the electronics states at the metal with those at the semiconductor.

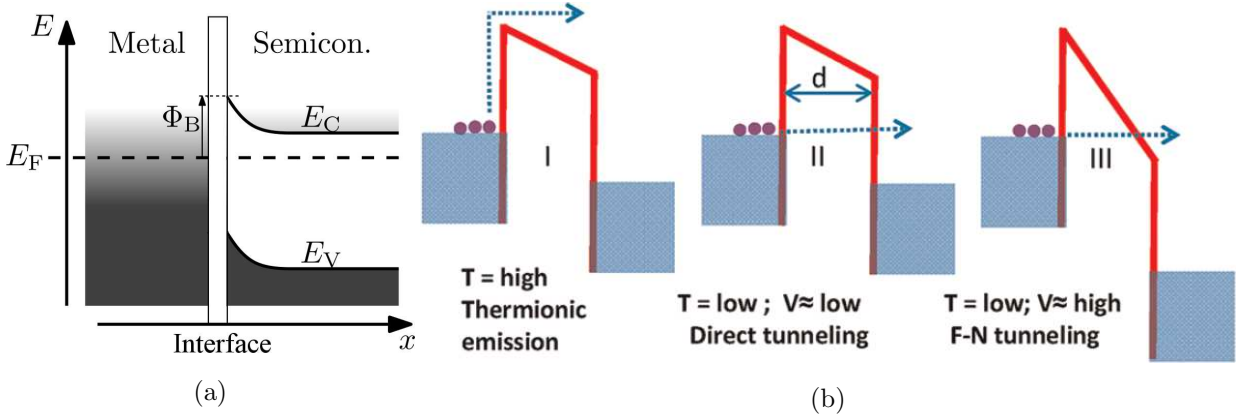


Figure 1.21: (a) Band diagram for n-type semiconductor Schottky barrier (SB). (b) Schematic diagram of a SB at different temperatures and voltages. The circles represent the charge carriers, and the arrow indicates the charge carrier injection processes: (I) thermionic emission, (II) direct tunneling, and (III) Fowler-Nordheim (F-N) tunneling. From [97].

1.4.1 Thermionic emission

In vacuum, thermionic emission is commonly known as the liberation of electrons from an electrode because of its thermal energy. This occurs because the thermal energy given to the charge carrier overcomes the work function of the material. In the case of contacted semiconductors, the electrons emitted by thermionic emission overcome the SB. Some of the earliest work on electron emission in vacuum from hot bodies were carried out by Richardson, naming the subject as “thermionics”. In 1901 [98], Richardson was able to show that each unit area of a platinum surface emitted a definite number of electrons per unit time, and that it was governed by the well-known law:

$$J = AT^2 \exp(-\omega/k_B T), \quad (1.49)$$

where T is the temperature of the emitter, ω is its work function, k_B is the Boltzmann constant and A is a constant. Originally, Richardson derived the Eq. 1.49 with an exponent on T of $1/2$ instead of 2 , and the Boltzmann constant wasn't present. The equation was later modified by Saul Dushman in 1923 [99]. The Nobel Prize in Physics 1928 was awarded to Owen Willans Richardson “for his work on the thermionic phenomenon and especially for the discovery of the law named after him” [100].

In semiconductors, the Eq. 1.49 takes the form:

$$J = AT^2 \exp(-q\Phi_B/k_B T) \exp(q\Delta\Phi_{img}/k_B T), \quad (1.50)$$

where Φ_B is the Schottky barrier height, A is the Richardson constant and Φ_{img} is the barrier lowering due to the image force. The Eq. 1.50 is usually used on 3D materials, but it was shown by Anwar *et al.* [101] that due to electron confinement and reduced DoS on 2D materials the equation for thermionic emission takes the form:

$$J = A^* T^{3/2} \exp(-q\Phi_B/k_B T) \exp(-qV/\eta k_B T), \quad (1.51)$$

where $A^* = q(8\pi k_B^3 m^*)^{1/2}/h^2$ and η is the ideality factor.

1.4.2 Tunneling

In 1963 Simmons derived an expression for the electric tunnel effect between similar electrodes separated by a thin insulating film. The purpose of this film is to introduce a potential barrier between the electrodes, impeding the flow of electrons between them [102]. Starting from the equilibrium conditions (the top of the energy gap of the insulator being positioned above the Fermi level of the electrodes), the electronic current can flow through the insulating region between the two electrodes if: (a) the electrons in the electrodes have enough thermal energy to surmount the potential barrier and flow in the conduction band (already discussed in the previous Section), or (b) the barrier is thin enough to permit its penetration by the electric tunnel effect. With this, Simmons was able to come up with the expression of the current flow through a generalized barrier:

$$J = J_0 \left(\tilde{\phi} e^{-A\tilde{\phi}^{1/2}} - (\tilde{\phi} + eV) e^{-A(\tilde{\phi} + eV)^{1/2}} \right), \quad (1.52)$$

where $J_0 = e/2\pi h(\beta d)^2$, $A = (4\pi\beta d/h)(2m^*)^{1/2}$, with e, h and d being the electron charge, Planck constant and width of the barrier respectively. β is a correction factor, defined in the appendix of Simmons work's, and $\tilde{\phi}$ is the mean barrier height above Fermi level.

Two regions can be studied: low and high source-drain voltage (V_{sd}). In Fig. 1.21b is shown the effect of V_{sd} on the barrier. In the low V_{sd} limit ($V \simeq 0$) the expression 1.52 takes the form shown in Eq. 1.53, while in the high V_{sd} limit ($V > \phi/e$) it takes the form shown in Eq. 1.54, which is called Fowler-Nordheim (F-N) tunneling, after their contribution to electronic emission under high electric fields [103].

$$J = \frac{3}{2d} (2m^* \phi_B)^{1/2} \left(\frac{e}{h} \right)^2 V_{sd} e^{-\frac{2d}{h} (2m^* \phi_B)^{1/2}} \quad (1.53)$$

$$J = \frac{2.2e^3}{8\pi h \phi_B d^2} V_{sd}^2 e^{-\frac{4d}{3e\hbar V} (2m^* \phi_B^3)^{1/2}} \quad (1.54)$$

Expression 1.53 is obtained assuming a rectangular SB shape, while expression 1.54 is obtained assuming a triangular SB shape. The work done by Simmons does not take into account the interfacial barrier that is sometimes created at the semiconductor-metal interface, however, those expressions can still work given a sufficiently thin interfacial layer.

1.5 Conclusion

In this Chapter we have reviewed the basic properties of TMDs, in particular those of monolayer MoS₂. The commonly known electronic transport models, through the material and at the semiconductor-metal interface, both classical and mesoscopic, has been also presented. Those models will be used in the next Chapters, but before presenting the main results, we will describe the devices and the experimental setup used to characterize them.

Chapter 2

Experimental techniques

In this Chapter, we first introduce a brief description of transistors and their working principle. Then, the growth process of MoS₂ and the fabrication methods for the different devices is presented. The general experimental setups used to characterize these devices is also presented. Finally, some typical preliminary results are shown, which illustrate the technical difficulties encountered. We detail how we made changes on the fabrication steps and the type of measurements we could perform to overcome these difficulties.

2.1 Device working principle

Here we present the transistor configuration used, the different shapes of the devices, and how we can extract intrinsic information of monolayer MoS₂.

2.1.1 Field effect transistor

A transistor is a semiconductor device used to amplify or switch electrical signals and power. It is composed of a semiconductor material, usually with at least three terminals for electrical connection to an electronic circuit, called source, drain, and gate. A voltage or current applied to the gate electrode controls the current injected between the source and drain terminals. Because the controlled (output) power can be higher than the controlling (input) power, a transistor can amplify a signal. A field effect transistor (FET) is a type of transistor that uses electric fields to modulate the current flow between the source and drain terminals. The Nobel Prize in Physics 1956 was awarded jointly to William Bradford Shockley, John Bardeen and Walter Houser Brattain “for their researches on semiconductors

and their discovery of the transistor effect” [104]. In Fig. 2.1 is shown a sketch of a FET and its working principle.

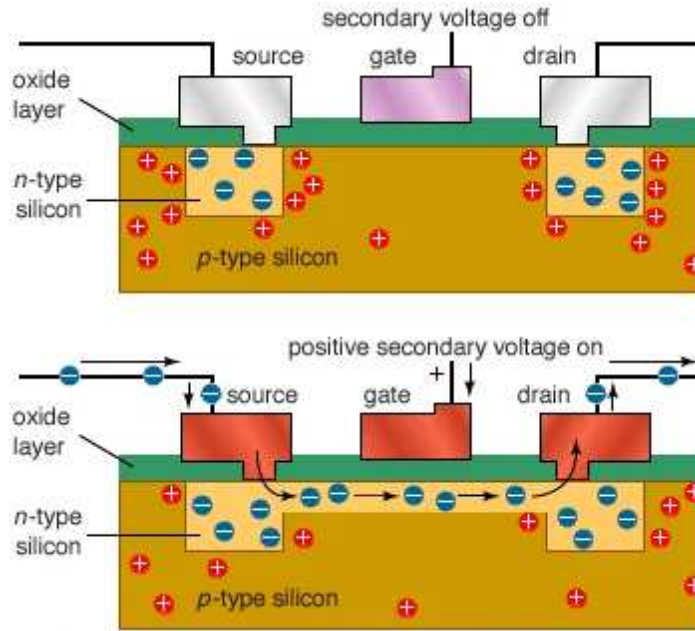


Figure 2.1: Sketch of a FET and its working principle. A negative-channel metal-oxide semiconductor employs a positive secondary voltage to switch a thin layer of p-type semiconductor material below the gate into n-type. From [105].

The ability to control the chemical potential of a material using electric fields is crucial in semiconductor electronics, and is a major degree of freedom in many experiments in solid state physics. Usually, in a FET, the gate is made up of a metal, but it is possible to use liquids and even light for gating. The electron density below the gate can hence be tuned with an electric field, and is usually approximated to a parallel plate capacitor: $\Delta n = C\Delta V_g$; where n , C and V_g are the electron density, capacitance and gate voltage respectively. Those types of transistors will be discussed in the following.

Ionic liquid gating

In conventional field-effect gating techniques using a solid gate dielectric, SiO_2 or high- κ dielectric, the charge carrier density accumulated is rather small, of the order of $1 \times 10^{13} \text{ cm}^{-2}$, a density that is far from what is expected to induce the desired electronic phase changes (See Section 1.1.3). A different route for carrier doping that has gained popularity in 2D materials is electrochemical doping with an electric field using ionic liquids. An ionic liquid is a salt containing separable and mobile cations and anions [106]. Under an externally applied

voltage, the ions in the liquid will separate and a layer of cations or anions accumulates near the sample surface, forming an electric double layer (EDL) that is essentially a capacitor with a gap of a few nanometers. When a voltage is applied to an ionic liquid, a huge electric field of the order of 10 MV/cm is generated at the solid/liquid interface due to the formation of an EDL. Owing to this extremely high electric field, EDL gating has the unique capability to push the charge density accumulation as high as a few 10^{14} cm $^{-2}$, with some electrolytes reaching 1×10^{15} cm $^{-2}$, determined by Hall effect measurements. This is well beyond the limitations of any solid gate dielectric [1, 19, 34, 35, 44–47].

Photogating

Photogating is a way of modulating the device channel conductance with light-induced gate voltage. Photogating can be ascribed to the prolonged excess carrier lifetime induced by defects and impurities. If one type of the photogenerated carriers is trapped and they have a certain spatial distribution, they can produce an additional electric field similar to the gate voltage, modulating then the channel conductance [107]. Photogating have been applied in TMDs and topological insulators as a tool to modify the sample's conductance [108, 109].

2.1.2 Devices geometries

Different devices were fabricated for specific purposes. The most common used and widely known is the Hall bar, but TLM and vdP geometries were also fabricated. In the following, we give a bit more details on these devices and their purpose.

Hall bar devices

One of the most common geometry used in electronics research is a Hall bar. This type of devices allows extracting the conductivity of the material by 4-probe measurements. As a consequence, if a magnetic field is applied perpendicular to the Hall bar plane, mobility and carrier density can be estimated via the Hall effect (see Section 1.2.2). A sketch of a Hall bar is shown in Fig. 2.2, and the resistivity can be obtained with the use of the following expression:

$$\rho_{xx} = \frac{V_x w}{I_{sd} l} \quad (2.1)$$

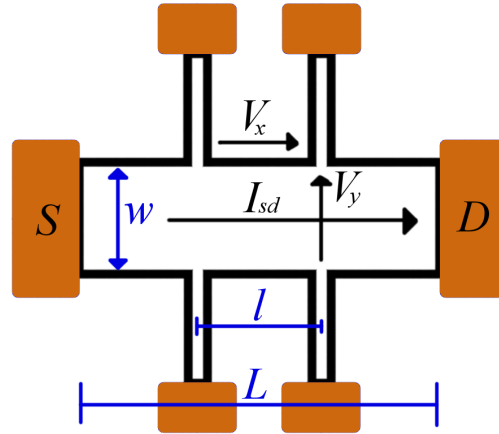


Figure 2.2: Sketch of a Hall bar showing the current and voltages that can be measured.

The van der Pauw method

The van der Pauw method is a technique used to measure the resistivity and the Hall coefficient of thin films with four contacts. Its power lies in its ability to measure the properties of a sample of any arbitrary shape, as long as the sample is homogeneous, approximately two-dimensional, does not contain any (geometrical) holes, and the electrodes are small and placed on its perimeter, as shown in Fig. 2.3 [110]. By applying a current i_{MN} between contacts M and N , measuring the potential difference $V_P - V_O$ and defining $R_{MN,OP} = \frac{V_P - V_O}{i_{MN}}$, the resistivity of the sample can be obtained using the following expression:

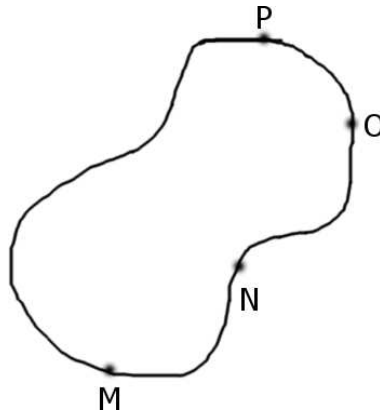


Figure 2.3: A flat lamella of arbitrary shape, with four contacts M,N,O and P placed on the periphery.

$$\rho = \frac{\pi d}{\ln 2} \frac{R_{MN,OP} + R_{NO,PM}}{2} f, \quad (2.2)$$

where d is the thickness of the sample, f is a factor which depends on the ratio $R_{MN,OP}/R_{NO,PM}$

and is given by the following equation:

$$\frac{R_{MN,OP} - R_{NO,PM}}{R_{MN,OP} + R_{NO,PM}} = f \cosh^{-1} \left(\frac{\exp(\ln 2/f)}{2} \right) \quad (2.3)$$

The Hall coefficient (R_H) can be also determined using this method. If we measure $R_{MO,NP}$ at zero magnetic field, and if $\Delta R_{MO,NP}$ is the change on resistance when turning on the magnetic field, the Hall coefficient can be calculated using the following expression:

$$R_H = \frac{d}{B} \Delta R_{MO,NP} \quad (2.4)$$

Transmission line measurement

Transmission line measurement (TLM) is a technique used to determine the contact resistance between a metal and a semiconductor. The technique involves making a series of metal–semiconductor contacts separated by various distances, as schematically shown in Fig. 2.4. Voltages are applied to pairs of adjacent contacts, measuring at the same time the current, and hence determining the resistance between them. The current flows from the first probe into the metal contact, across the metal–semiconductor junction, through the sheet of semiconductor, across the metal–semiconductor junction again (except this time in the other direction) into the second contact, and from there into the second probe and into the external circuit. The resistance measured is the sum of the two probes, the two contacts, and the sheet resistance of the semiconductor between the contacts. When several such measurements are made between pairs of contacts that are separated by different distances, a plot of resistance versus contact separation can be obtained, being linear if the contact resistance is homogeneous. The slope of the line corresponds to the sheet resistance, and the intercept of the line with the y -axis is two times the contact resistance. Thus, the sheet resistance as well as the contact resistance can be determined from this technique.

2.1.3 DC measurements

All the measurements were performed using DC power sources. Two different Keithleys source-measure units (SMUs), the 2400 and 2612B models, were used as power sources. Each SMU instrument is both, a stable DC power source and a 6.5-digit multimeter. The 2400 model, shown in Fig. 2.5a, have a voltage range of 100 μ V to 200 V and a current range of 10 pA to 1 A, while the model 2612B, shown in Fig. 2.5b, have similar voltage range but a current range of 1 pA to 10 A. A Hewlett Packard voltmeter is added to measure voltages

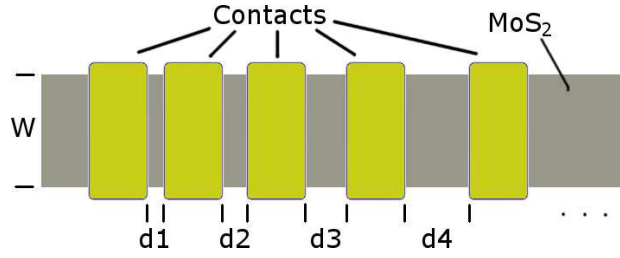


Figure 2.4: Simplified sketch of a TLM. The MoS_2 , shown in gray color, has a rectangular shape and is contacted on top with metal contacts, shown in yellow color. The distance between the contacts increases with the addition of new contacts.

in a 4-probe configuration, shown in Fig. 2.5c. It is a 6.5 digit voltmeter with two modes for input impedance, a lower one of $10\text{ M}\Omega$ and a higher one of $10\text{ G}\Omega$.

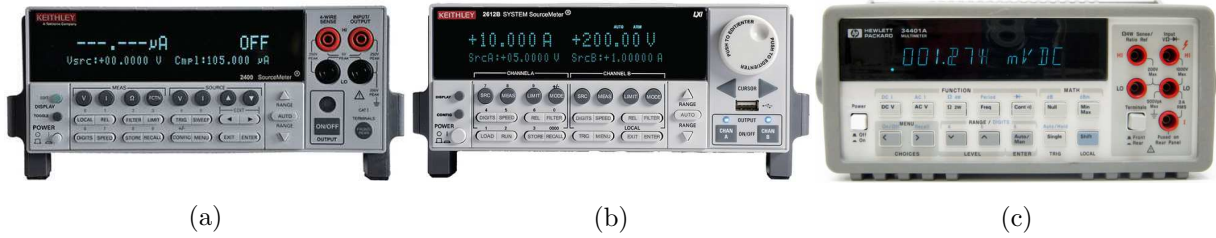


Figure 2.5: Power sources and voltmeters. (a) Keithley 2400 used as source-drain voltage power supply and source-drain current measurement. A second one was used for the back-gate. (b) Keithley 2612B used during ionic liquid measurements, the channel **a** was used as source-drain voltage input and channel **b** for the ionic liquid voltage. (c) Hewlett Packard voltmeter for measuring voltages in a 4-probe configuration.

The most common technique used for measuring the sample resistance is the 4-probe method. This technique involves using four probes to make electrical contacts with the material, as shown in Fig 2.6. The applied current I enters and leaves the sample via the outer probes, and flows through the sample. The voltage is then measured between the inner probes. Voltmeters with higher electrical impedance than the sample will prevent them from affecting the circuit being measured, meaning that no current will flow through the inner two probes. Therefore, the wire resistances R_{W2} and R_{W3} , and the contact resistances R_{C2} and R_{C3} do not contribute to the measurement. Any measured decrease in voltage (ΔV) will therefore arise entirely from the sample resistance R_{S2} [111].

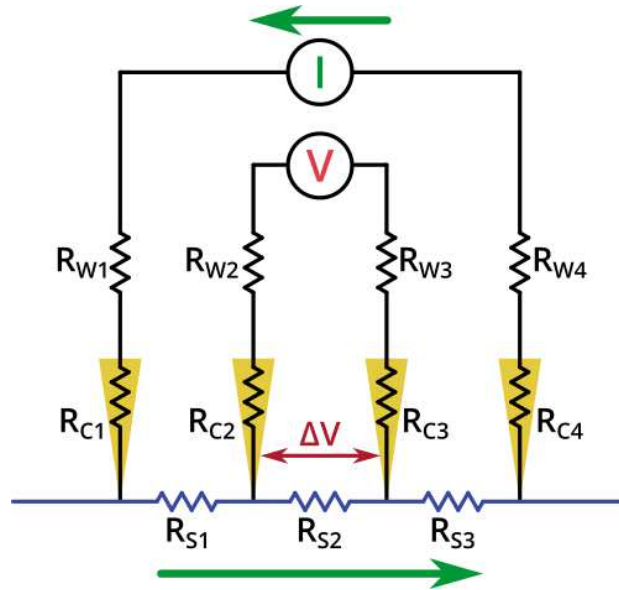


Figure 2.6: (a) Schematic diagram of a four-probe circuit. From [111].

2.2 Fabrication

2.2.1 MoS₂ grown by CVD

The emergence of mass production technologies has enabled scalable growth of polycrystalline monolayer MoS₂ by chemical vapour deposition (CVD), providing a commercially viable path towards MoS₂ electronics at low cost. CVD is a method that produces large areas, high-quality MoS₂ films, with uniform morphology and controllable size by the chemical reaction between molybdenum and sulfur sources at suitable temperature and gas flow. The CVD synthesis of monolayer MoS₂ can be performed by one of the following two routes shown in Fig. 2.7. The first is a two-step growth route, in which Mo-based precursors are initially deposited on a substrate and then sulphurised/decomposed into MoS₂ (route 1). The second is considered as a one-step growth, wherein gaseous Mo and S feedstocks are simultaneously introduced and react to form MoS₂ on the substrate (route 2) [112]. Some other gases, like H₂ and Ar, are used to control the rate of the reaction with varying degrees of crystallinity and number of layers.

The MoS₂ flakes used in this work were grown by CVD in SiO₂/Si(n++) substrate, following route 1. The growth was done at the University of Pennsylvania under the supervision of Charlie Johnson [113]. On Fig. 2.8 are shown some pictures of the MoS₂ flakes grown with this process. They have a triangular shape with size no larger than 150 μm. A small percentage of layers are not uniform, varying from monolayer up to bulk-like structures,

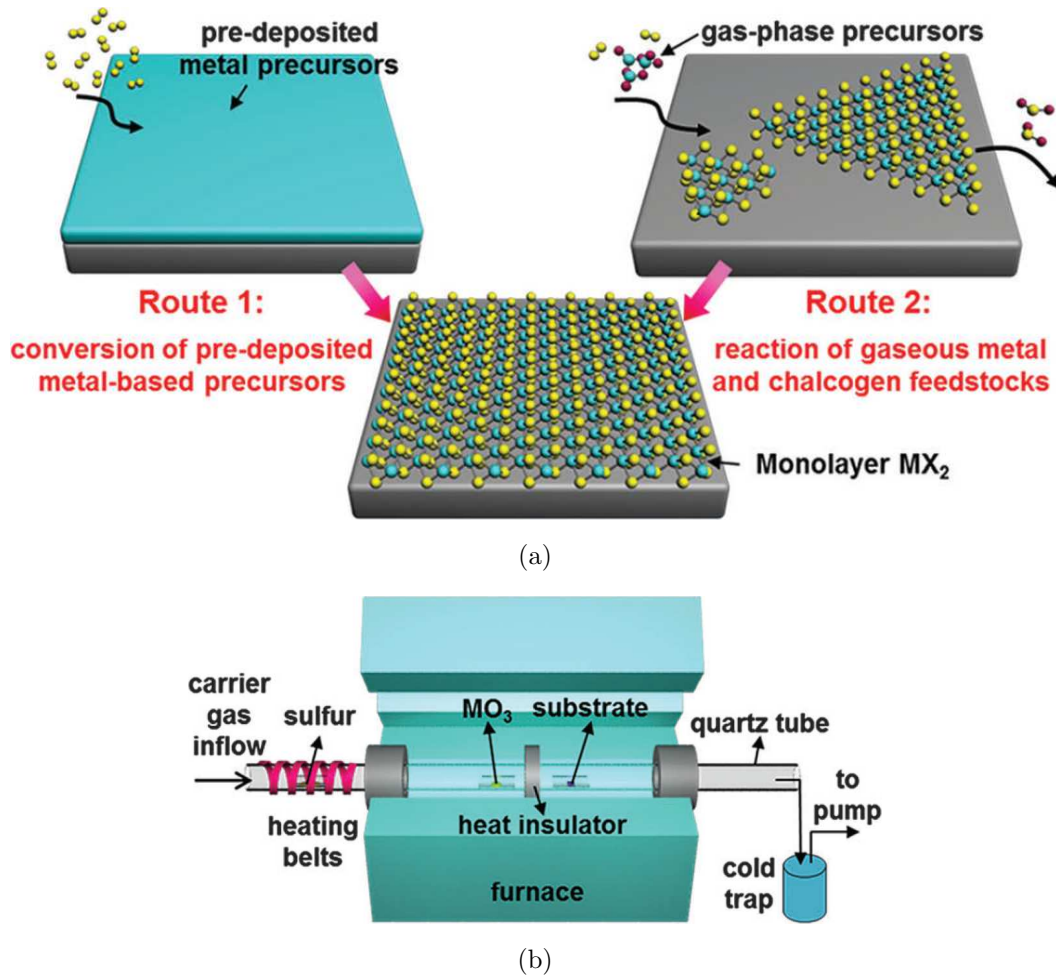


Figure 2.7: (a) Two routes for MX₂ synthesis. (b) Typical setup of a CVD systems. Adapted from [112].

with some of the flakes merging with others forming a random big non-uniform flake. Large, isolated monolayer flakes were commonly available, which has been used in fabricating the MoS₂ transistors.

2.2.2 Design of the devices

All the designs were done with the open source KLayout software [114]. KLayout is an viewer and editor of graphic data system files (GDS files). A GDS file contains information about the layout of a circuit, layers, geometric shapes, and text labels. GDS files are used as a standard format between integrated circuit design applications. The created GDS files were then transferred to the electron beam lithography system of the Centrale de Technologie de Montpellier (CTM), where all the devices have been fabricated. Ultraviolet lithography could no be used since the flakes are at random positions, it would have been required to make the physical mask for each growth sample.

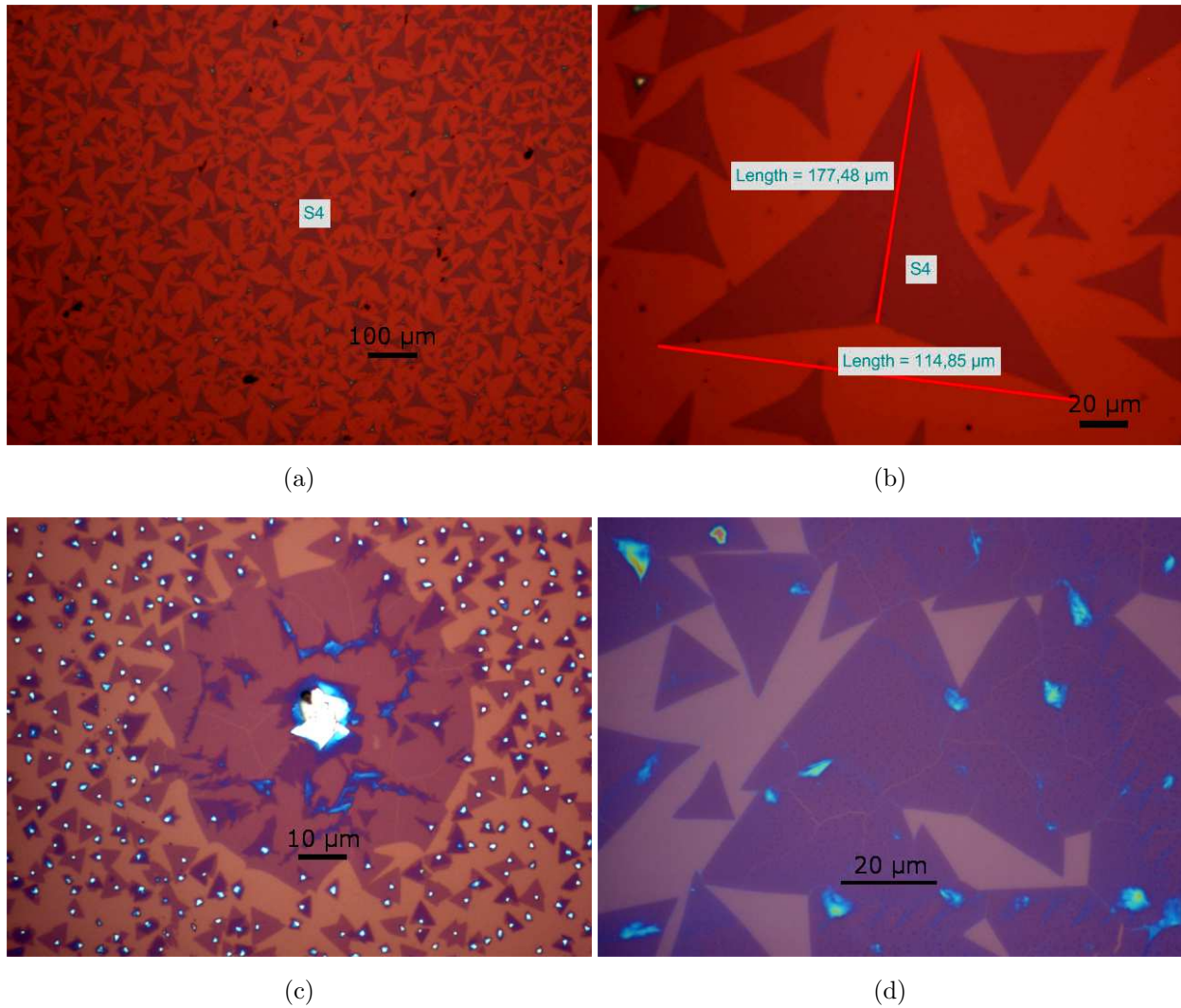


Figure 2.8: Usual triangular shape of two different CVD grown MoS_2 samples: Jjedi01 (a-c) and Jjedi06 (d). (a) Large field view. (b) close look at the triangular monolayer MoS_2 flakes. (c) Agglomeration of flakes into a big non-uniform structure. The white center is a bulk MoS_2 structure. (d) Triangular monolayer MoS_2 flakes.

In order to extract information about the MoS_2 electrical properties, several designs can be used. We have designed Hall bars (HB) and van der Pauw (vdP) devices for the measurement of resistivity, mobility and Hall effect. We have also designed transmission length method (TLM) devices to get both resistivity and contact resistance. Those designs are shown in Fig. 2.9. Two different versions of Hall bars, shown in Fig. 2.9a and Fig. 2.9d, were used to test the effect of contact size and contact shape on contact resistance.

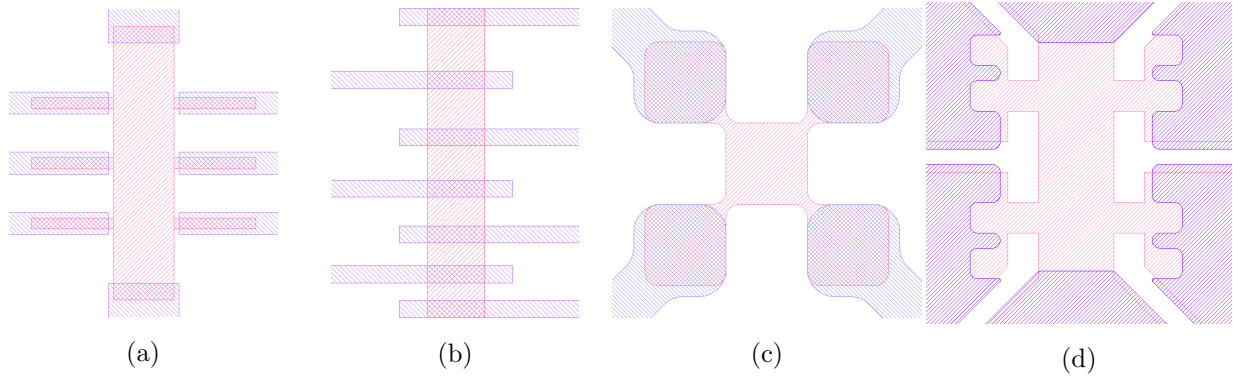


Figure 2.9: Masks of the different devices. The MoS₂ is represented by pink color and the metal contacts by blue color. (a) A simple Hall Bar (HB). (b) Transmission length method (TLM). (c) van der Pauw (vdP) square. (d) A second generation of Hall bars.

2.2.3 Electron beam lithography (EBL)

The process of shaping MoS₂ flakes into any desired form is carried out using electron beam lithography (EBL). The process is summarised in Fig. 2.10. The typical process is the following: first, two thin film of PMMA are uniformly deposited on the substrate by spin coating and separately baked at 170 °C for 5 min. Then, part of the resist is chemically modified by exposing it to an electron beam (EB). Finally, the sample is put in a solvent called “developer”, which consist of a mix of Methyl isobutyl ketone (MIBK) and isopropanol (IPA). The MIBK/IPA ratio used is 1:3, and it will remove the exposed or unexposed parts of the resist if positive or negative development is used:

- Positive resist: The resist is exposed with the EB where the underlying material is to be removed. In these resists, exposure to the EB changes the chemical structure of the resist so that it becomes more soluble in the developer. The exposed resist is then washed away by the developer solution.
- Negative resist: When exposed to the EB, the negative resist becomes crosslinked/polymerized and less soluble in the developer. Therefore, the negative resist remains on the surface of the substrate where it is exposed, and the developer solution removes only the unexposed areas. We have used this method to minimize the exposure of the MoS₂ to the EB.

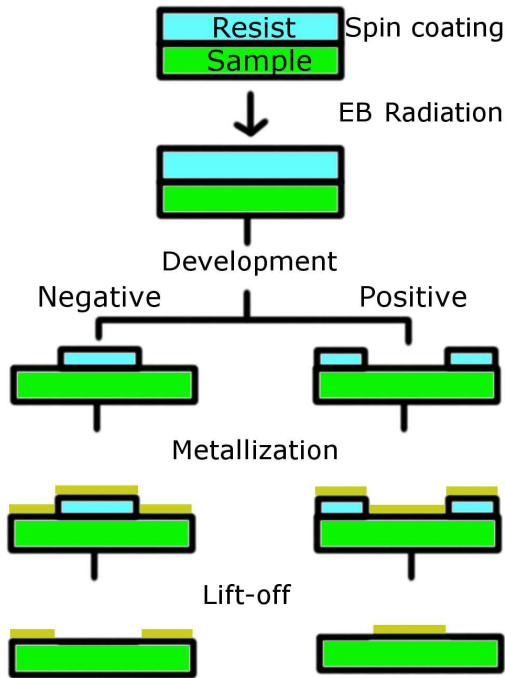


Figure 2.10: Illustration of a EBL process: resist deposition by spin coating; electron beam exposure; development carried out with MIBK/IPA with a ratio of 1:3; metallization; and lift-off. Positive resist has been used during the full fabrication process.

2.2.4 Plasma etching

In order to shape the MoS₂ flakes into any form, CHF₃ plasma is used. The plasma is generated by radio frequency (RF) at a pressure of 10 mTorr with a power of 20 W. The gases flowing into the plasma are: 10 sccm of argon, 20 sccm of oxygen and 60 sccm of CHF₃. With this low power plasma, the time required to etch a few layers is on the order of a few minutes. Below we show one of the plasma etching tests on PMMA and SiO₂, which was performed before making the real devices. In Fig. 2.11 is shown a PMMA Hall bar made by EBL using the design shown in Fig. 2.9a. After 5 min of plasma etching, the lateral size reduction is around 200–300 nm. The thickness of the PMMA is also reduced by ~ 100 nm, as measured with a profilometer. After etching, the remaining PMMA can be easily removed using acetone. The SiO₂ is also etched with this kind of plasma at a rate of 2–3 nm/min, as measured with the reflectometry technique.

2.2.5 Description of the lithography process

The process of shaping the MoS₂ consists of three levels (**S1**, **S2** and **S3**), each of them divided into several sub-levels (**a**, **b**, **c**,...). Positive EBL is used during the lithography process.

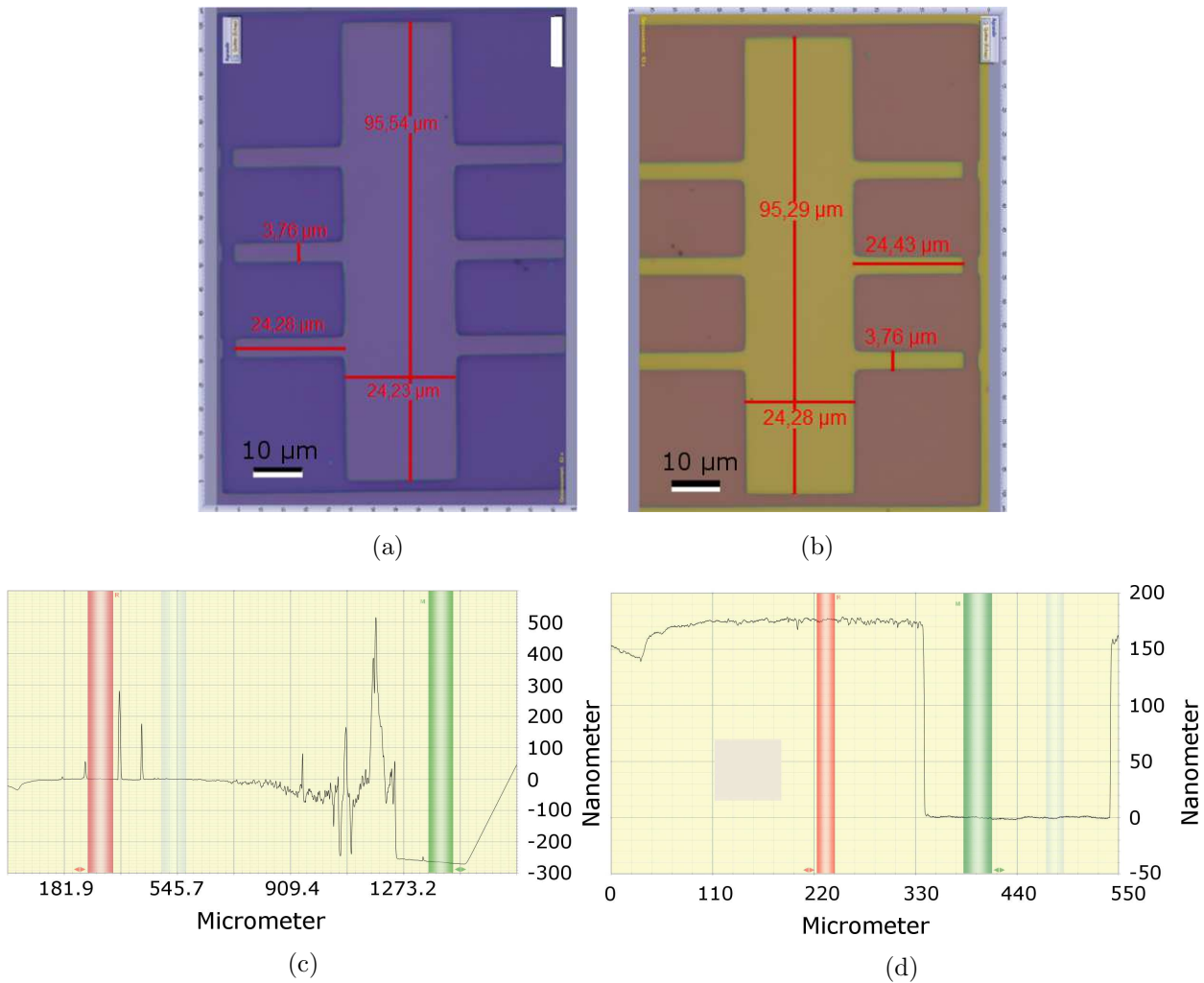


Figure 2.11: (a) and (b) PMMA Hall bar before and after plasma etching. A close analysis reveals a lateral reduction of a 200–300 nm on the PMMA layer. (c) and (d) profilometer results before and after plasma etching showing ~ 100 nm of thickness reduction on the PMMA.

All the levels are explained in the following, and shown in Fig. 2.12.

S1 Markers level.

S1a Resist: A layer of electron-sensitive resist PMMA4 is spin coated on the sample's surface. This layer is then baked at 170 $^{\circ}\text{C}$ for 5 min. Two layers of resist are used, each of them separately baked, just to have a thick ~ 400 nm layer of resist.

S1b EBL: This level consist of irradiating small areas of the resist with a cross pattern. These pattern will be used in the alignment of the next levels, and to precisely locate the MoS_2 flakes.

S1c Development: It is carried out using MIKB/IPA 1:3 for 30 s. This chemical mix

dissolves the exposed resist leaving behind the unexposed areas. In this way, we have resist everywhere except on the exposed parts.

S1d Metallization: Metal is deposited on the sample by EB sputtering. The contacts are mainly gold (Au) but a small layer of titanium (Ti) metal is used to have a better adhesion to the SiO₂ surface. On this step, the thickness of the metals deposited is not important as long as they are visible optically with a microscope and with a scanning electron microscope, since the markers are used only for alignment.

S1e Lift-off: The excess of metal is removed using hot acetone, leaving the exposed areas untouched, and hence, the crosses are transferred to the sample. In Fig. 2.12a is shown the result of markers level.

S2 Plasma etching level.

S2a Resist: Again, two layers of PMMA4 are separately spin coated and baked.

S2b EBL: The area needed to be etched away is exposed since only positive resist is used. The large pads for bonding the devices and the paths connecting them are also exposed in this step. This is done to avoid any shortcut within contacts or with other devices when there are many MoS₂ flakes.

S2c Development: As before, MIKB/IPA 1:3 is used for the development. After developing, we have resist everywhere except around the desired pattern. In Fig. 2.12b is shown the the exposed area to be etched.

S2c Plasma etching: The sample is then exposed to CHF₃ plasma, already presented in Section 2.2.4.

S3 Contacts level.

S3a Resist: As usual, two layers of PMMA4 are separately spin coated and baked.

S3b EBL: The exposed areas of the sample are where the metal for electrical contacts is desired.

S3c Development: As before, MIKB/IPA 1:3 is used for the development. After developing, the pads and paths ready for metallization. In Fig. 2.12c is shown the exposed area where the metal will be deposited.

S3d Metallization: As with the markers, Ti/Au is deposited on the sample by EB sputtering. In this step, the thickness of the metals deposited are important, since they are contacting the MoS₂. Different thickness has been tried, they will be described at the end of the current Section.

S3e Lift-off: The excess of metal is removed using hot acetone. This is the final step of the fabrication process, Fig. 2.12d shows a fabricated device.

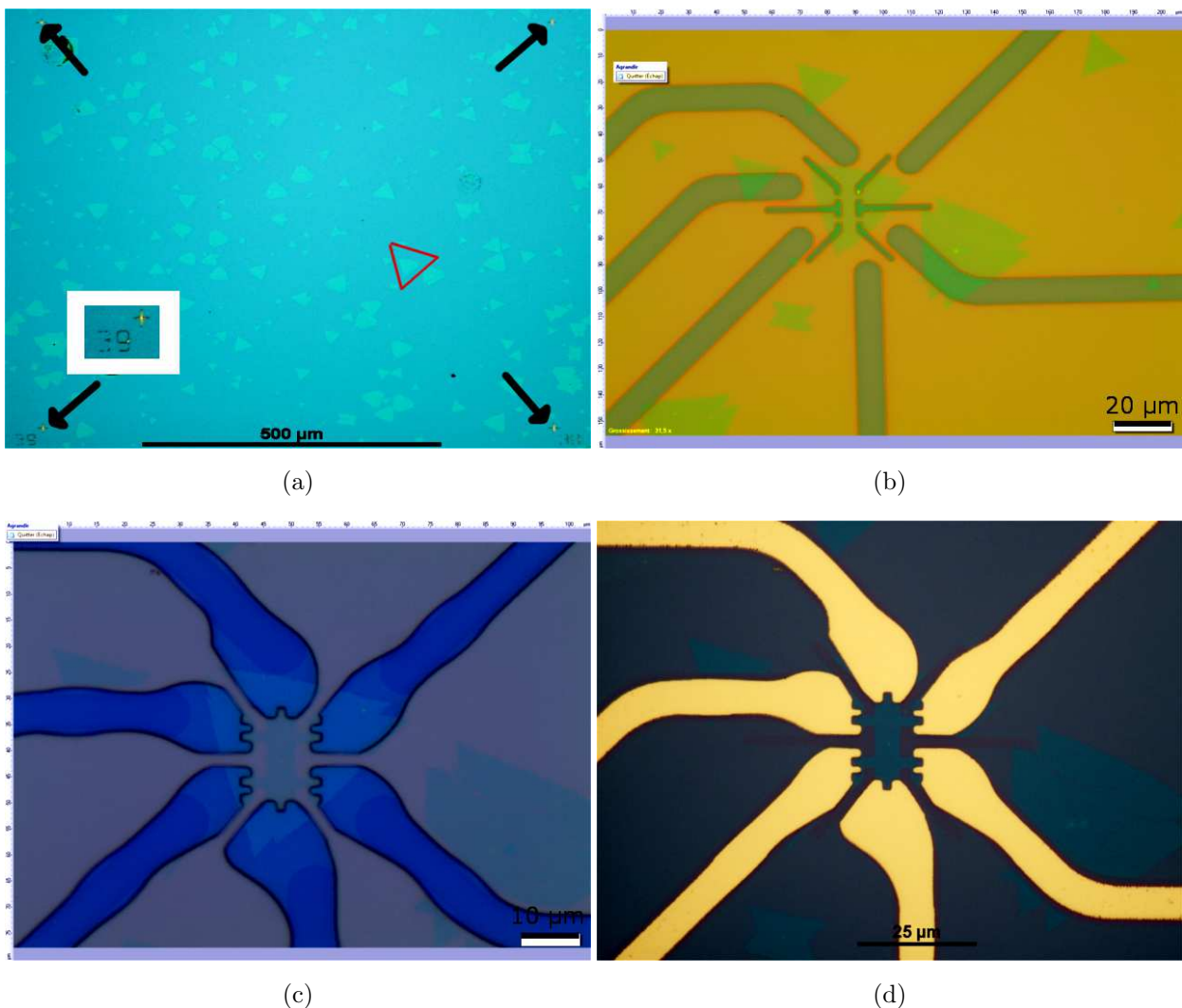


Figure 2.12: Shaping a MoS₂ flake into a Hall bar by EBL. The device is named J339 (the name follows a notation that will be explained later). (a) Step S1e: markers. There are four crosses forming a square of length 860 μm, indicated by black arrows. The red triangle shows the flake used for the EBL. The insert shows a closer look at the marker. (b) Step S2c plasma-etching. (c) Step S3c: contacts. (d) Step S3e: metallization of contacts.

2.2.6 Fabricated devices

The devices were fabricated on 3 different CVD grown MoS₂ samples, and 1 CVD grown WSSe sample. All those samples were grown on top of silicon dioxide, with highly doped silicon acting as the back-gate (SiO₂/Si(n++)). The 4 different samples fabricated are named Jjedi01, Jjedi03, Jjedi04 and Jjedi06, and are shown in Fig. 2.13, 2.14, 2.15, and 2.16, respectively. As those samples come from different CVD growths, they were fabricated at different times, with the exception of Jjedi03 and Jjedi04 which were fabricated together.

Each sample is divided into small squares called writing fields (WFs). Each side of the WF is 1 mm length, and contains up to 2 different devices. A labeling in the horizontal and vertical axis was used in order to label each WF. The notation used to identify each device is presented in the following. The letter “J”, being the name of the project: Jjedi; the number representing the sample: 1, 3, 4 or 6; and finally, two characters indicating the WF on the sample. Those characters are the numbers or letters from the labeling used on the vertical and horizontal axis, with the first character indicating the row and the second one indicating the column. Let us look at the following example: J162 is a device in Jjedi01 in the row number 6 and column number 2. The device J162 is marked by a red circle in Fig. 2.13.

A closer look into a few WFs for the different samples are shown in Fig. 2.17, 2.18, 2.19, and 2.20, for samples Jjedi01, Jjedi03, Jjedi04, and Jjedi06 respectively. Close to 200 devices were fabricated. Fig. 2.21 shows a few of them.

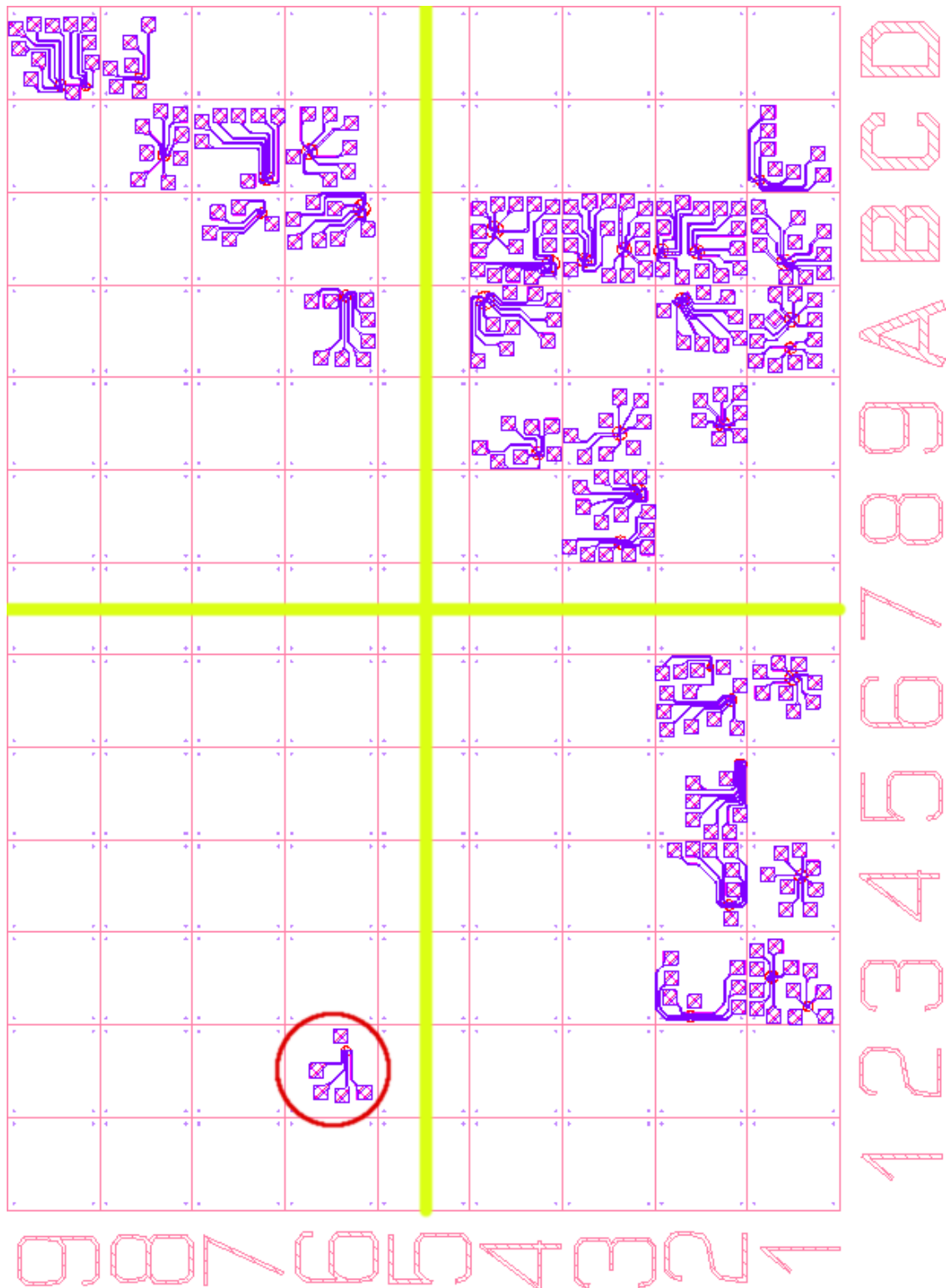


Figure 2.13: Jjedi01. The red circle marks the device J162. A total of 28 HBs and 7 vdP shapes were fabricated on this sample. This sample was cut into 4 parts on column 7 and row 5, indicated by the yellow lines.



Figure 2.14: Jjedi03. A total of 58 HBs and 15 TLM shapes were fabricated on this sample. This sample was cut into two parts on column 6, indicated by the yellow line.

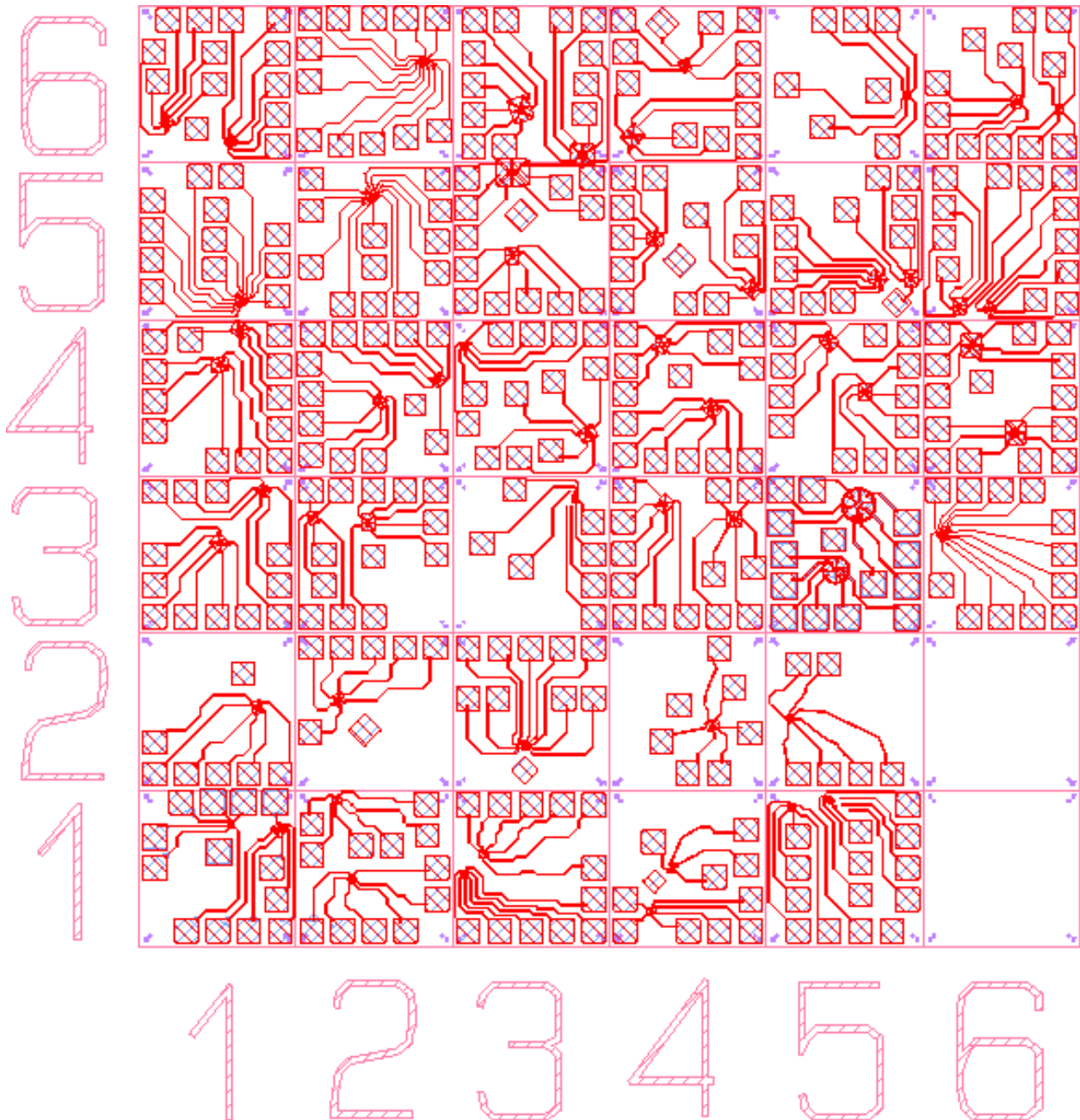


Figure 2.15: Jjedi04. A total of 47 HBs, 7 TLM and 1 vdP shapes were fabricated on this sample.

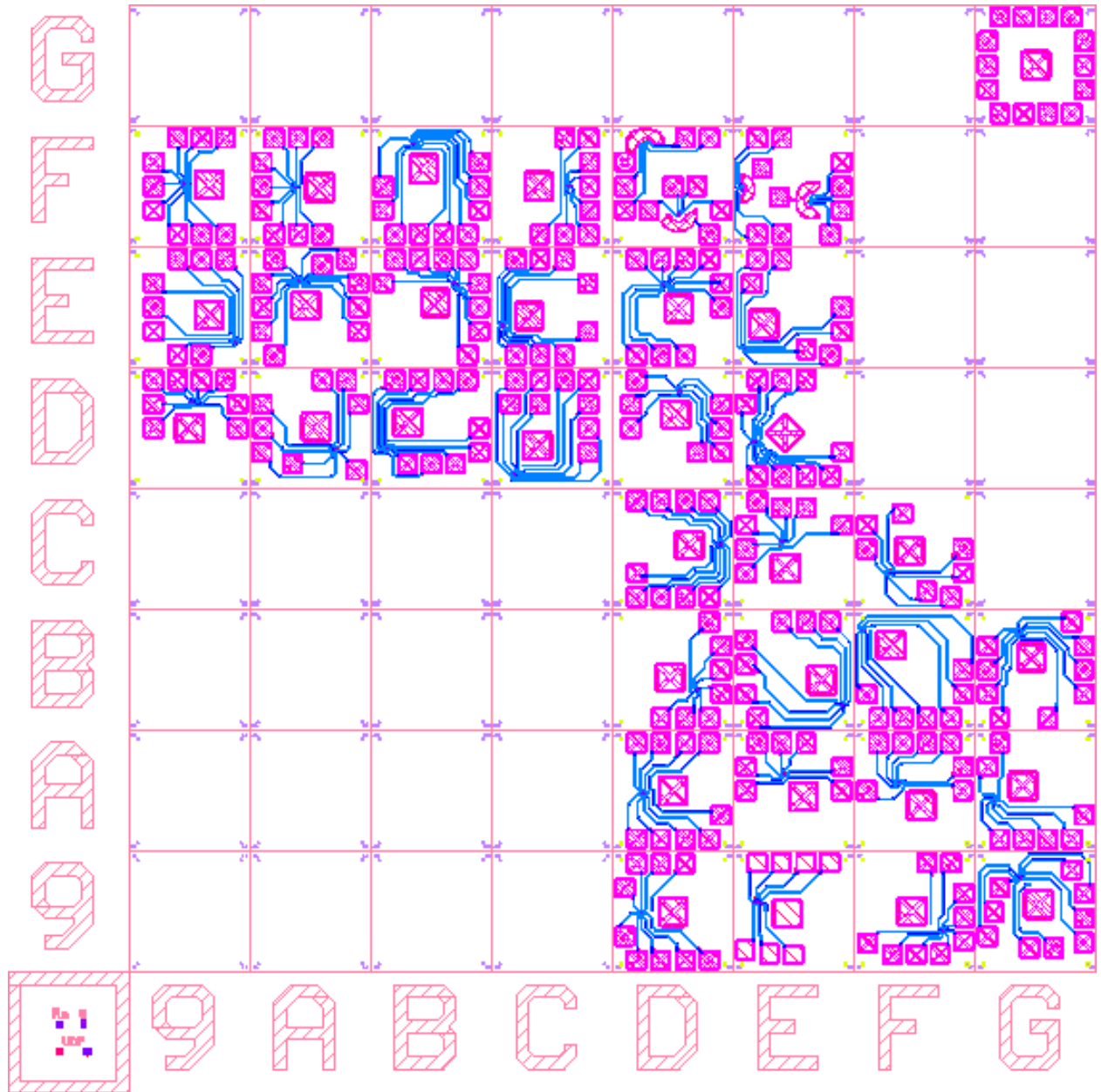


Figure 2.16: Jjedi06. A total of 30 HBs and 4 vdP shapes were fabricated on this sample.

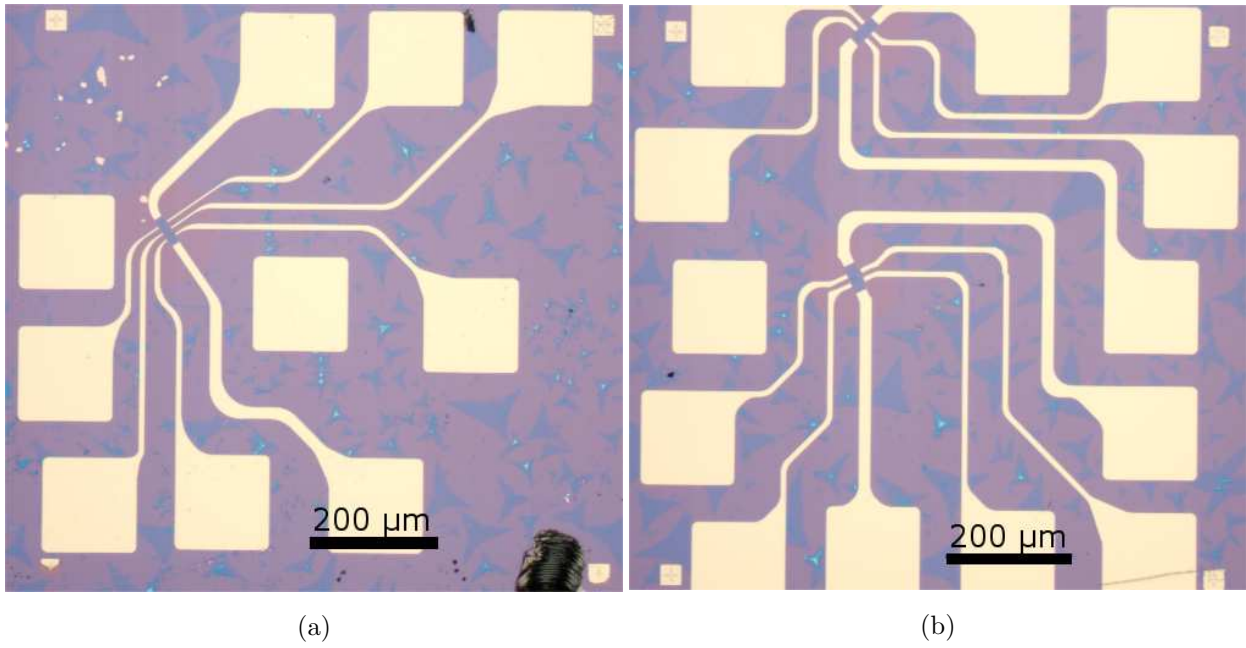


Figure 2.17: Two different WFs of Jjedi01. (a) J11B with a single HB. (b) J12B with 2 HBs.

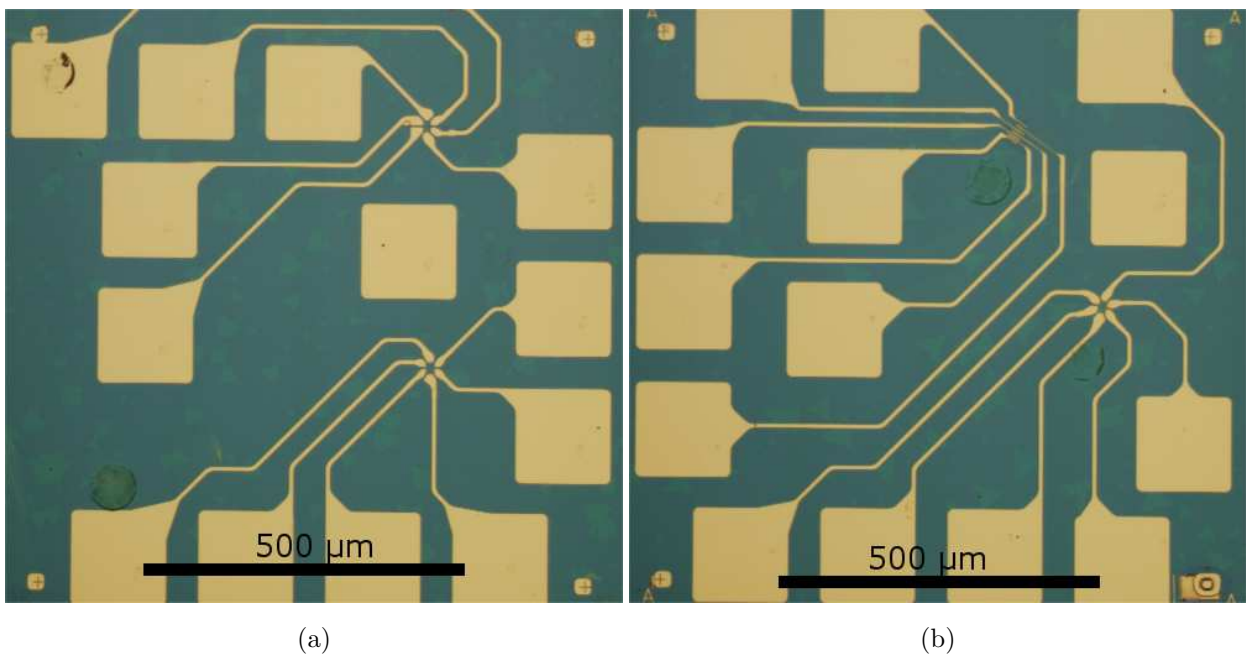


Figure 2.18: Two different WFs of Jjedi03. (a) J339 with 2 HBs. (b) J31A with a HB and a TLM.

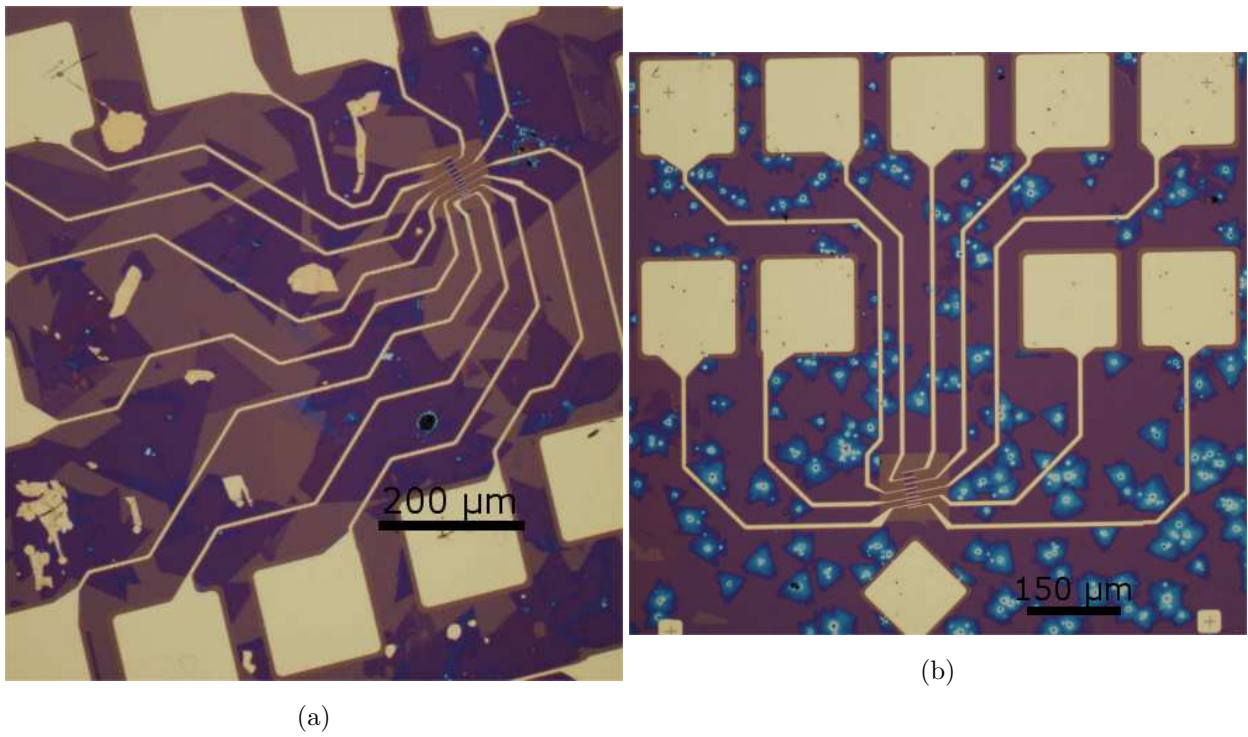


Figure 2.19: Two different WFs of sample Jjedi04. (a) J462 with a single TLM. (b) J423 also with a single TLM.

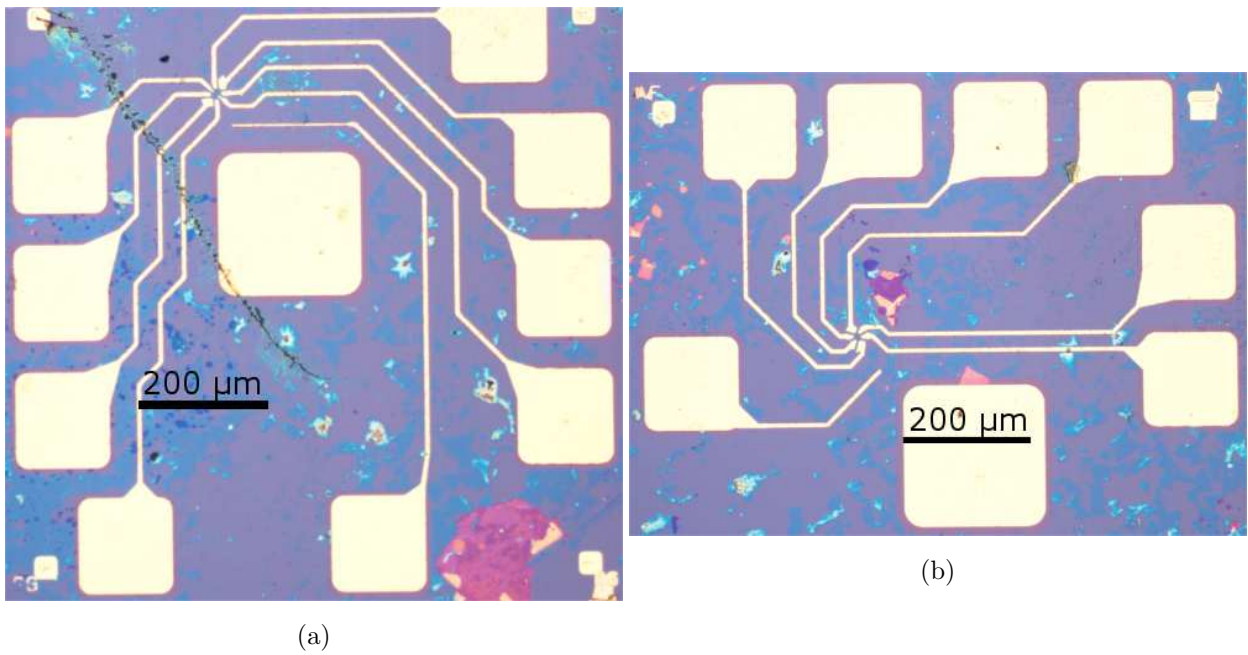


Figure 2.20: Two different WFs of Jjedi06. (a) J6BG with a single HB. (b) J6AF also with a single HB.

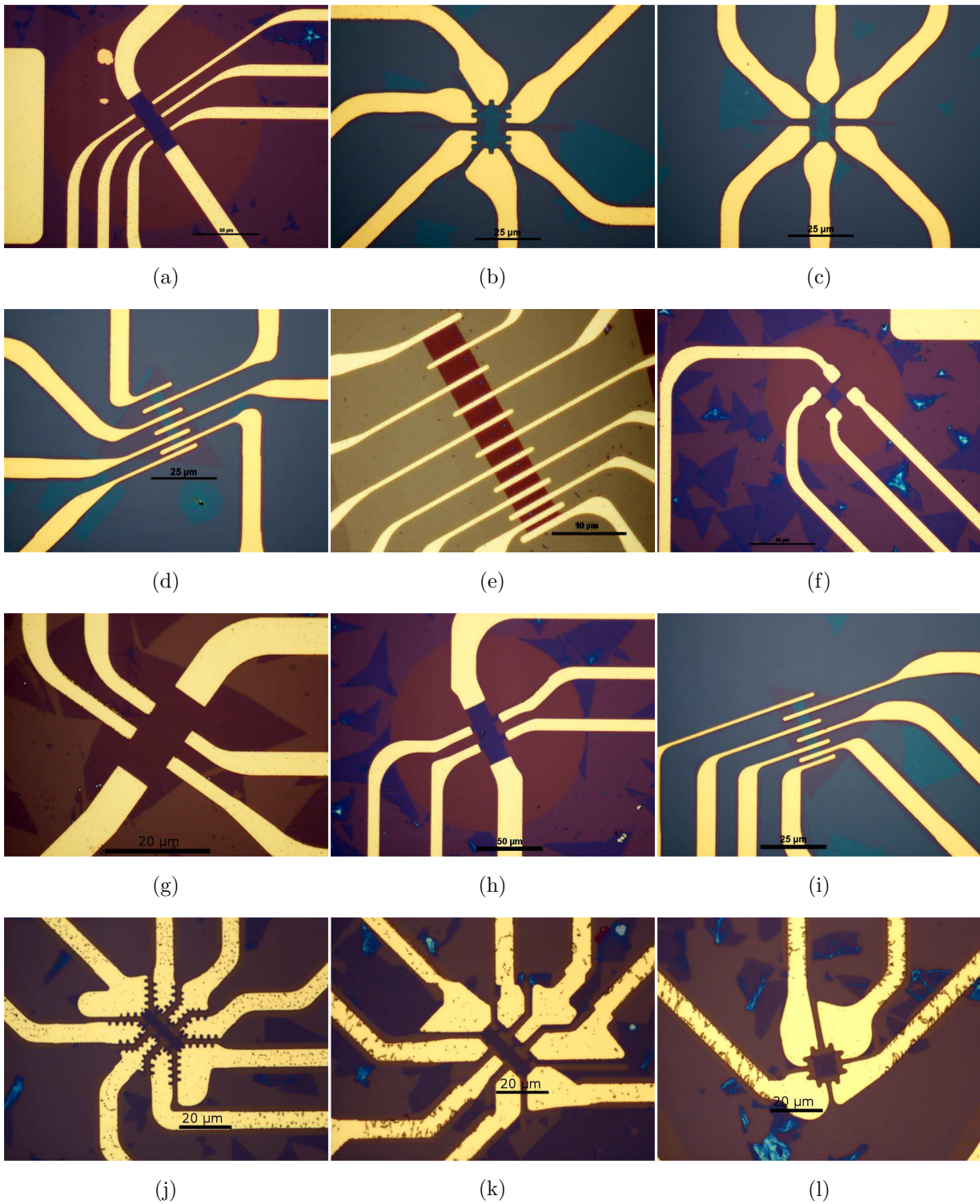


Figure 2.21: Some of the fabricated devices: (a) HB J11B. (b) HB J339. (c) HB J338. (d) TLM J335. (e) TLM J462. (f) vdP J17B. (g) HB J16A. (h) HB J12B. (i) TLM J349. (j) HB J6DC. (k) HB J69G. (l) vdP J6FD.

2.3 Experimental setups

Before showing the measurement results, we present here the setup used for the different characterizations. Some of those has been performed on MoS₂ flakes prior and after fabricating the devices.

2.3.1 Raman spectroscopy

Raman spectroscopy is a spectroscopic technique used to determine vibrational modes of molecules, although rotational and other low-frequency modes of systems may also be observed. It is a light scattering technique, where molecules scatter incident light coming from a source. Most of the scattered light is at the same wavelength as the incident light, and does not provide useful information. However, a small amount of light is scattered at different wavelengths which depend on the chemical structure of the sample, this is called Raman Scattering [115]. The Nobel Prize in Physics in 1930 was awarded to Sir Chandrasekhara Venkata Raman “for his work on the scattering of light and for the discovery of the effect named after him” [116]. A sketch of the energy levels involved on the scattering light is shown in Fig. 2.22a. Typically, these measurements are performed with the setup shown in Fig. 2.22b. This setup uses a laser of known wavelength which is focused onto the sample surface. The scattered light is then collected by the microscope objective and sent to a spectrometer.

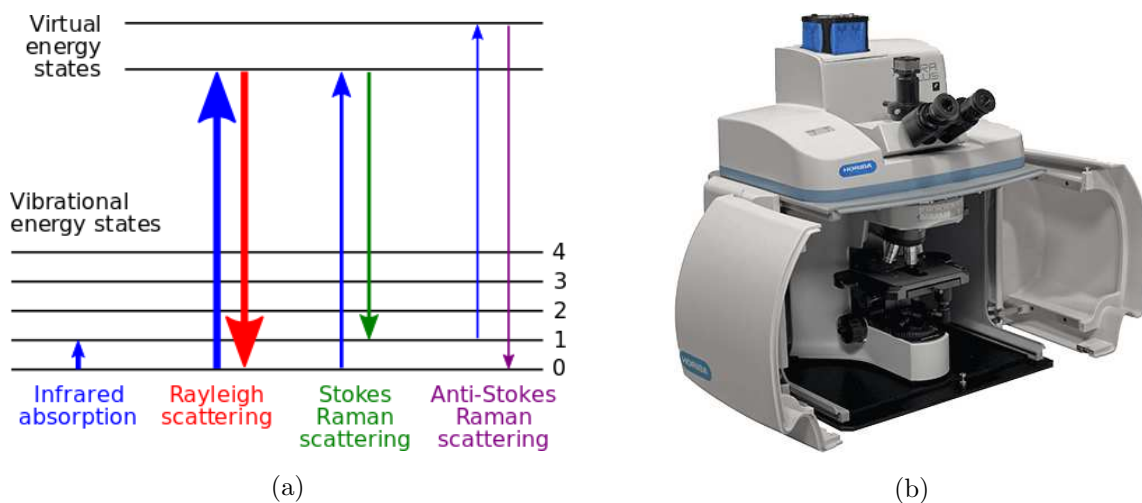


Figure 2.22: (a) Energy-level diagram showing the states involved in Raman spectra. (b) A modern Raman microscope system.

The MoS₂ has two characteristic Raman peaks or modes called E_{2g}^1 and A_{1g} and they

exhibit sensitive thickness dependence. The E_{2g}^1 is an in-plane vibrational mode and A_{1g} is an out-of-plane vibrational mode. The distance in frequency between those peaks increases with the number of layers in MoS₂, which provides a convenient and reliable mean for determining layer thickness with atomic-level precision [117]. Raman spectroscopy has been used to evaluate the thickness of the flakes before the EBL process using an Horiba commercial micro-Raman. A home-made system from the group has been used for more accurate studies.

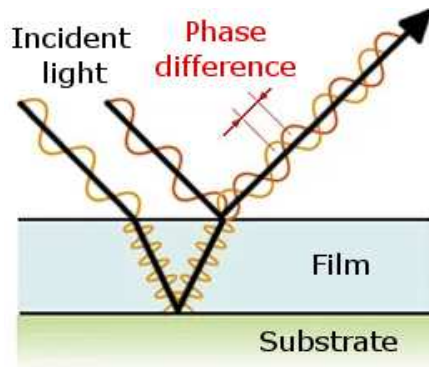
2.3.2 Reflectometry

Reflectometry uses the reflection of light at surfaces and interfaces to measure characteristics such as film thickness and index of refraction. The main components of a reflectometer are a broadband white light source, focused onto the sample's surface via an microscope objective (see Fig. 2.23b). The reflected light is collected by the same objective and sent to a spectrometer. The working principle is described in the following [118]:

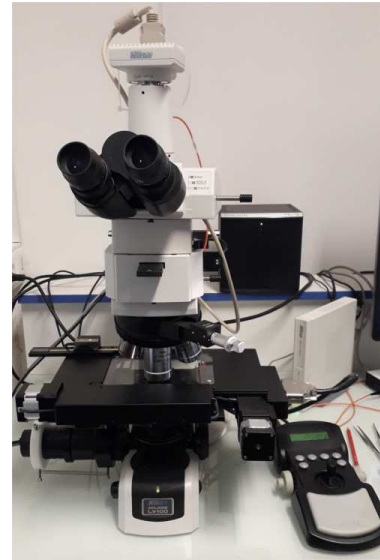
- A source of stable intensity light is used to illuminate a spot on the sample.
- Some light is reflected from the top surface of the sample and some is transmitted into it. There is another reflection when the transmitted light reaches the bottom interface of the sample. The light from each of these reflections recombines to generate varying levels of constructive or destructive interference depending on the wavelength of light and the optical distance the light travels (see Fig. 2.23a).
- A model is used to fit the reflected intensity versus wavelength data to extract the sample thickness. This model uses the Fresnel coefficients, the optical indices of thin film and of the substrate. These fixed values are stored beforehand.
- This technique gives access to the SiO₂ thickness through the interference pattern, as well as the MoS₂ thickness through its absorption coefficient. It can only solve for layer thicknesses, from one layer up to a few layers in the case of MoS₂.

2.3.3 Ball bonding

Ball bonding is a common type of wire bonding used to make electrical connections between small devices and the sample holder. This process is carried out using the microscopic



(a)



(b)

Figure 2.23: (a) Illustration of reflectometry principle. (b) The microscope Nikon eclipse LV100 used for the reflectometry measurements.

bonding machine shown in Fig. 2.24. Its working principle is described in the following. There is a small capillary through which the wire is delivered. A high-voltage electric discharge is applied to the wire, melting its tip and forming a ball because of the surface tension. Finally, the capillary is lowered to the surface of the sample, which is typically heated until 100 °C, and ultrasound is applied to the wire in contact with the metallic pad of the sample. The combined heat, pressure, and ultrasound create a weld between the ball and the contact pad. The wire is then brought to the sample holder and the process is repeated, this time with higher strength, forming the second bond and cutting the wire. This process is resumed in Fig. 2.25a.

A series of small crosses or markers were used to test the bonding parameters prior fabricating the devices. The markers were done by EBL and are made of Ti/Au 10/75 nm. The ball bonding creates a circular gold contact on the surface with 150 μm of diameter, and does not break the 300 nm of SiO_2 , which was tested by applying a voltage between the marker and the back-gate. The bonding parameters used are shown in Fig. 2.25b, where Bond1 and Bond2 are, respectively, the bonding done on the device, and the one done on the sample holder.

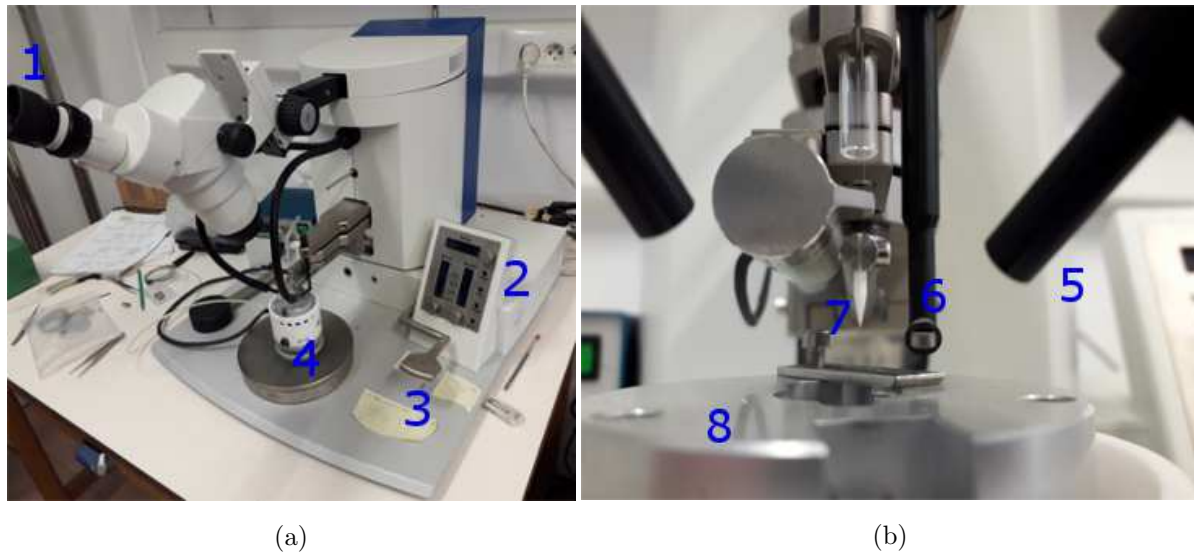


Figure 2.24: Ball bonding machine.. (a) Full view of the bonding machine. The labels are: 1) binoculars to look at the sample; 2) interface to view and change bonding parameters such as ultrasonic time and force; 3) handle to lower the capillary with the gold wire to make the bond; 4) Sample holder. (b) Close view at the capillary. The labels are: 5) light source; 6) high voltage discharge wire; 7) capillary; 8) surface of the sample holder that can be heated up to 100 °C.

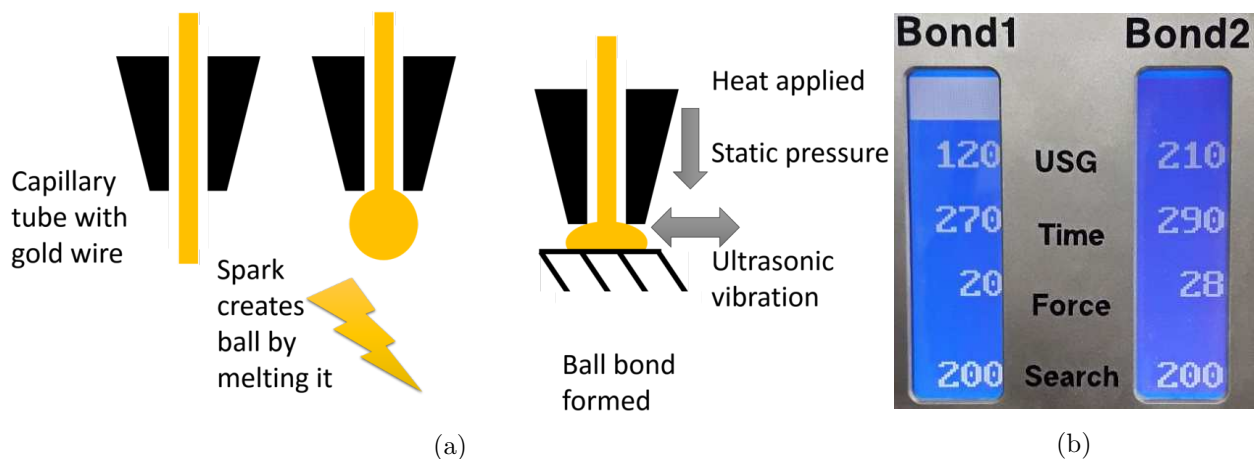


Figure 2.25: (a) Ball bonding processes: the gold wire is fed through the capillary tube, a ball is formed using high voltage discharge, and finally the bond is formed by pressing the ball onto the hot surface. (b) Bonding parameter used to bond the devices. Bond1 and Bond2 are first bonding (usually performed on the device) and second bonding (usually performed on the sample holder), respectively. USG, Time and Force, stand for Ultrasonic power, ultrasonic time and bond force (static pressure), respectively.

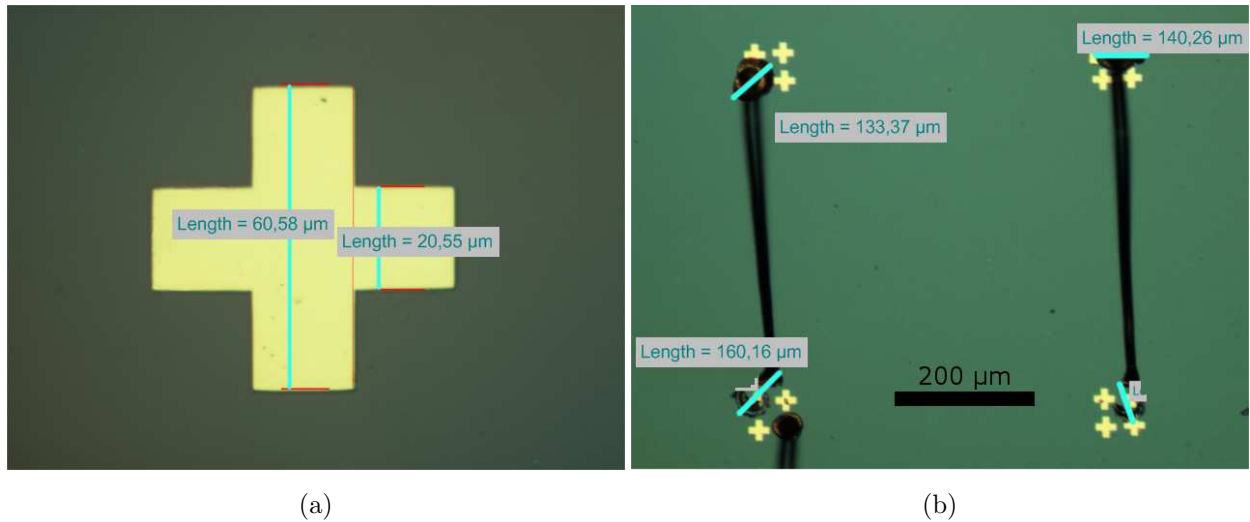


Figure 2.26: (a) Marker used to test the ball bonding (b) Markers successfully bonded without breaking the SiO_2 . The contact pad for the bonding must have at least $150 \mu\text{m}$ of size.

2.3.4 Probe Station

After finishing the fabrication process in the clean room, the first step is to check which devices are working properly, i.e, they are conducting, and the back-gate is not leaking. For this step a probe station, shown in Fig. 2.27, is used. The probe station is used to electrically test a device before and after bonding wires on it. It utilizes micrometer screws to allow precise positioning of thin metal needles on the device's surface, with the force applied to the contacts being a controllable parameter. The material of the needles used were copper and tungsten, having a tip diameter of $150 \mu\text{m}$ and $7 \mu\text{m}$ respectively. These needles are connected to coaxial cables.

2.3.5 Doping control

The doping was controlled using mainly the back-gate of the devices, which consists of highly doped silicon. It was electrically connected by pasting the sample with conductive epoxy. The voltage was applied with a SMU in the range $-100 \text{ V} - 100 \text{ V}$, which is close to the maximum that 300 nm of SiO_2 can hold. The current leakage was also systematically monitored to prevent breakdowns.

Two other ways of controlling doping were also tested: the ionic liquid Diethylmethyl(2-methoxyethyl)ammonium bis(trifluoromethylsulfonyl)imide, shown in Fig. 2.28a, and photogating with an UV light emitting diode (LED), shown in Fig 2.28b.

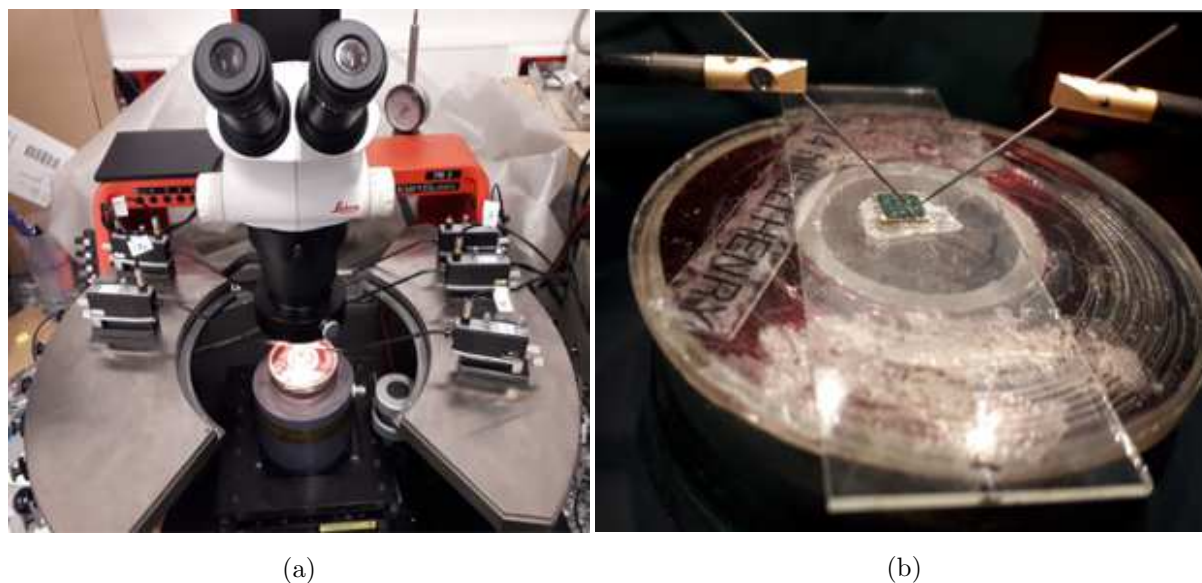


Figure 2.27: Probe station Karl Suss PM5. (a) Full view of the probe station. Five controllers are visible (2 on the left and 3 on the right). They are used to control 5 different metal needles. (b) Close view of 2 needles electrically contacting a 5×5 mm sample.



Figure 2.28: Different tools used for doping control. (a) Ionic liquid Diethylmethyl(2-methoxyethyl)ammonium bis(trifluoromethylsulfonyl)imide. (b) UV LED of wavelength $\lambda = 375$ nm.

2.3.6 He free cryostat

A Janis helium-free cryostat, shown in Fig. 2.29, with a temperature range of 10 K – 800 K was used to test the effect of thermal annealing on the samples. Most of the electrical measurements were performed on this setup, at high and low temperatures. The high temperatures are reached under low ($\sim 10^{-3}$ mTorr) primary pump vacuum. This setup uses helium gas in a closed loop to lower the temperature, meaning efficient recycling of the helium gas. With this setup, it is also possible to apply a magnetic field up to 1 T, using water cooled electro magnets.

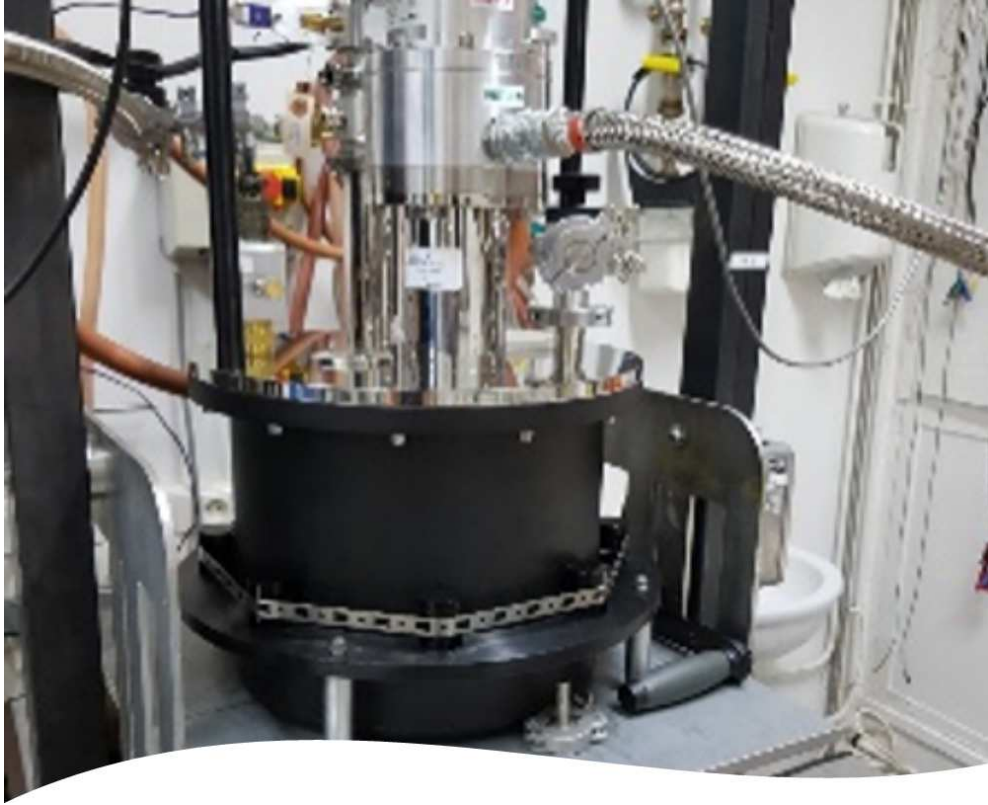


Figure 2.29: The high-temperature Janis Helium-free cryostat used for most of the measurements done with a controlled temperature.

2.3.7 Low Temperature & High Magnetic Field

Some of the electrical transport measurements at low temperature were carried out in a liquid helium cryostat from Cryogenic Limited, shown in Fig. 2.30. It consists mainly of a helium-4 vessel, isolated from ambient air by high vacuum (an insulator), a liquid nitrogen vessel and another insulator. Inside the helium vessel there is a superconducting magnet which can reach up to 13 T. The temperature is controlled with a Variable Temperature Insert (VTI). The VTI is a cylindrical, tubular structure, that is inserted into the bore of the superconducting magnet. The samples are mounted on a removable rod placed inside the VTI. The cylindrical structure separates the sample from the surrounding liquid helium environment. The temperature of the sample can be varied by circulating liquid or cold vapor helium through a needle valve and by direct heating from an integrated heater. A Lakeshore cryogenic temperature controller is supplied with the VTI and allows a fine tuning of the temperature, from 1.7 K up to 300 K with a precision of the order of 1 K at room temperature, and 5 mK at low temperature.

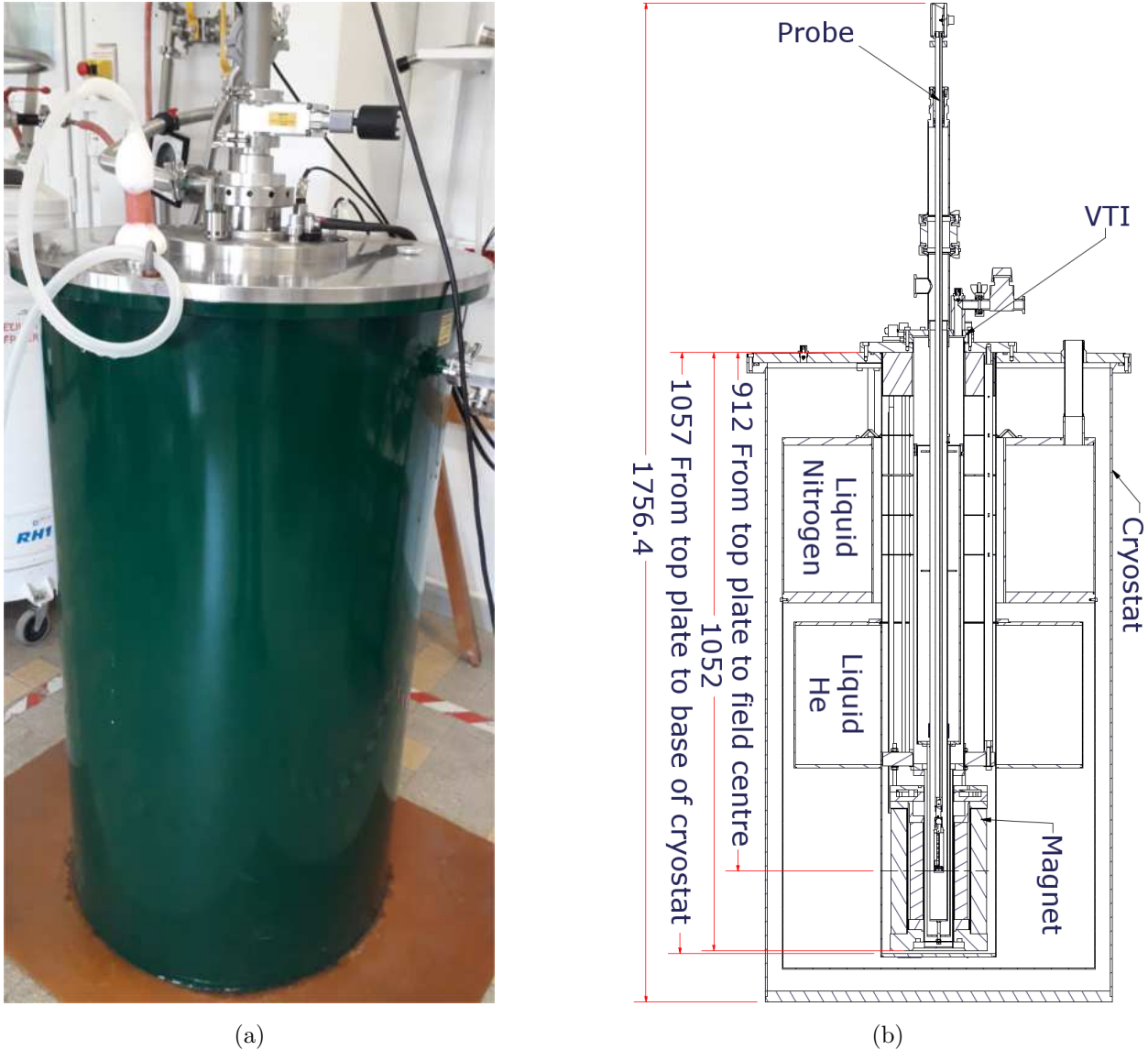


Figure 2.30: Liquid helium-4 cryostat. (a) Optical picture. (b) Diagram indicating the main parts. Distances are given in millimeters.

2.4 Device Performance

In this Section we present a few preliminary results that show the difficulties encountered. Before and after transport measurement, device thickness and/or homogeneity has been checked by optical means. All the fabricated devices has been tested in the probe station, bonding the ones that worked. All of the working devices exhibited high, non-linear 2-probe resistance and low doping, even at high back gate voltages. We will present here the various attempt to improve in-situ those devices, with the thermal annealing being the most favorable given our setup.

2.4.1 Reflectometry and Raman spectra

The typical reflectometry fit window is shown in Fig. 2.31a, where the ratio between the reference light and the reflected light from the sample is plotted against their wavelength. The region of interest is between 450 nm and 900 nm. The reflected light, both from the MoS₂ flake (red dots) and from the SiO₂ (white dots) are fitted, and the number of layers of the MoS₂ flake is then obtained. In Fig. 2.31b are shown the reflectometry results for various regions on the same MoS₂ flake, named S9. The results are offset by 0.5 per flake, giving a value 1.5 for monolayer and 3 for bilayer. Inhomogeneous MoS₂ flakes like the one shown in Fig. 2.31b helped us to tell the number of layers by optical contrast.

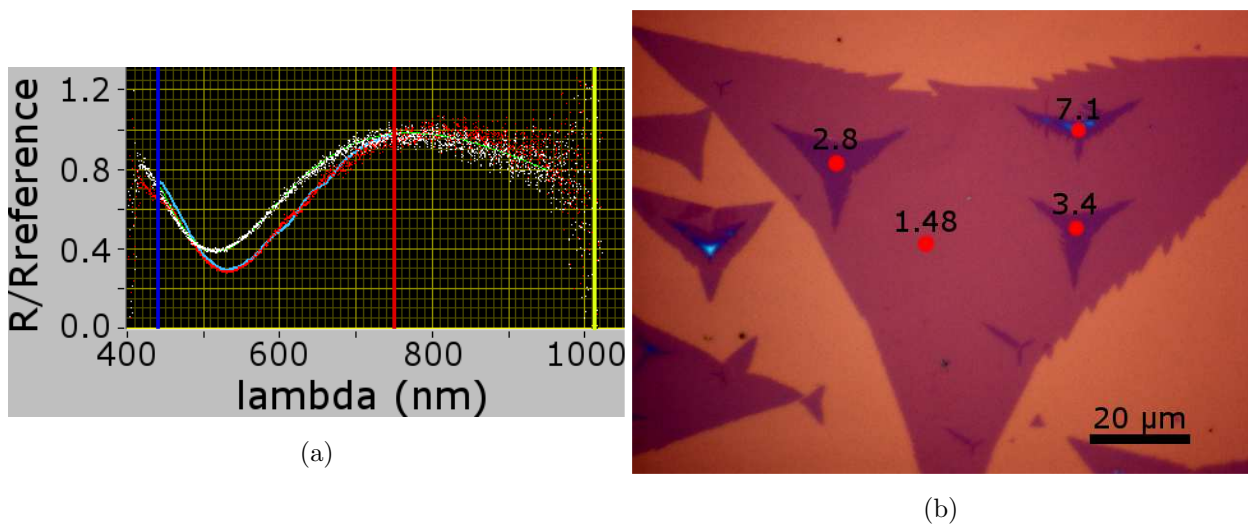


Figure 2.31: (a) Typical reflectometry fit window. The vertical blue and yellow lines correspond to the limit of the fitting in wave length λ , while the vertical red line shows the maximum of the reflected light. The red and white dots correspond to the measured reflected light from the MoS₂ flake and the SiO₂ respectively, which are being fitted by the blue and green line respectively. (b) Number of layers given by reflectometry on different spots within the flake S9. The spots are indicated by a red dot, and the corresponding number of layers is written just above it.

On Fig. 2.32 are shown the Raman spectroscopy results for two different MoS₂ flakes prior to the EBL fabrication. Some of the flakes are not uniform, having small areas forming multilayer MoS₂. In Fig. 2.32a and Fig. 2.32b are shown two different flakes, named S7 (monolayer) and S8 (big bilayer region) respectively. A single Raman spectra was obtained from a point close to the center, and the results are shown in Fig. 2.32c. The results do not show a clear distinction between monolayer and bilayer since the Raman setup used does not have the sufficient resolution. The expected distance change between peaks is around

1 cm^{-1} , while the setup resolution is $\sim 4 \text{ cm}^{-1}$. This issue was addressed with a different Raman setup, but for already fabricated devices.

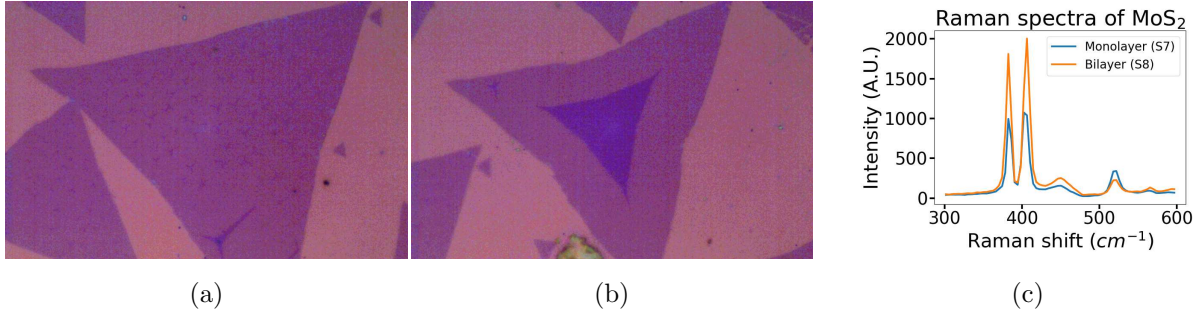


Figure 2.32: (a) and (b) MoS₂ flakes, namely S7 and S8 respectively. (c) Raman spectra obtained for flakes S7 and S8, in a region close to the center of each flake. The spectra show the E_{2g}^1 mode at $\simeq 380 \text{ cm}^{-1}$ and the A_{1g} mode at $\simeq 405 \text{ cm}^{-1}$.

A more thorough and detailed mapping of two devices, namely J339 and J12B, shown in Fig. 2.33a and 2.33b respectively, has been done after they were electrically tested (the electrical measurement result of those device will be shown in the next Chapters). These Raman measurements were realized with a laser of optical wavelength of 532 nm and a spot size $\sim 1 \mu\text{m}$, allowing a complete spatial mapping of the device. In Fig. 2.33c is shown a color map plot of the frequency difference $\delta = \omega(A_{1g}) - \omega(E_{2g}^1)$ measured on device J339. The energy difference δ is very homogeneous over the entire MoS₂ surface. It is centered around 20 cm^{-1} , with a full width at half maximum of less than 0.8 cm^{-1} . Such a peaked frequency dispersion is the signature of a homogeneous MoS₂ monolayer [117].

Similar results were obtained on device J12B, where, however, a few additional MoS₂ bilayer patches were also evidenced covering less than 1% of the total surface. These patches were also visible with optical and SEM images, confirming this low coverage. Fig. 2.33d and 2.33e show some typical Raman spectra obtained in devices J339 and J12B. The spectrum of an additional sample, obtained by exfoliation of a MoS₂ monolayer, is also shown for comparison. Fig. 2.33d focuses on the two A_{1g} and E_{2g}^1 modes, whereas Fig. 2.33e evidences the presence of additional modes at lower frequencies. Among these modes, the most prominent is the $LA(M)$ peak around 227 cm^{-1} . Its intensity is proportional to the density of defects n_D . Following Mignuzzi *et al.* [119], the average inter-defect distance L_D can be evaluated from the ratio \mathcal{R} of the integrated intensities of the $LA(M)$ and A_{1g} mode. For device J339, $\mathcal{R} \sim 0.044$ gives a $L_D = 3\text{--}4 \text{ nm}$, meaning a density of defects of $n_D = (2\text{--}3.5) \times 10^{12} \text{ cm}^{-2}$, calculated as $n_D = (\pi L_D^2)^{-1}$, assuming a random defect distribution. Device J339 hosts a

typically large number of defects, whereas, by comparison, device J12B appears to be less defective, being below the detection limit of this approach, with $\mathcal{R} < 0.005$, $L_D > 10$ nm and $n_D \leq 3 \times 10^{11}$ cm⁻². Those values will be compared to the density of defects obtained in transport measurements in the next Chapter.

2.4.2 Probe Station

Just after the fabrication, the devices were systematically characterized electrically with a probe station. The transport property has been characterized by connecting the source-drain electrodes to a SMU, which supplies the source-drain voltage (V_{sd}) and measures the source-drain current (I_{sd}). A second SMU applies a back-gate voltage (V_g) and measures the leakage current (I_g).

Two tests were carried out: 2-probe current-voltage measurements (IV) and transfer measurements. With IV measurements, V_g is fixed while V_{sd} is varied, measuring at the same time the source-drain current. In the case of transfer measurements, V_{sd} is fixed while V_g is varied, measuring at the same time the source-drain current. Fig. 2.34 shows some typical characteristic behaviors, obtained with device J114. The device has a high resistance, in the order of G Ω s, non-ohmic contacts, and a large (~ 10 V) back-gate hysteresis.

The flakes that were not shaped into Hall bars had lower electrical resistances, probably because of lower contact resistance, as can be seen in Fig. 2.35, where the results obtained with the J16A device are shown. This motivated us to change the design of the contacts, and to maximize the size of the interface between MoS₂ and metal. The transfer curves shows a ~ 10 V hysteresis for all pair of contacts.

All fabricated devices showed non-linear IVs, because of non-ohmic/Schottky contacts (discussed on Chapter 4), and big (10-20 V) back-gate hysteresis under ambient conditions. Those topics will be discussed in the following Sections.

2.4.3 Current annealing

Passing a high current density through the samples have been shown to be an effective way for improving device's quality [120]. In the lattice, the electron scattering is mostly elastic in nature, however, the scattering is high at the defects where the electrons lose their momentum, developing atomic scale force known as the "electron wind force" [121]. The electron wind force could make migrate the vacancies, enhancing the sample's mobil-

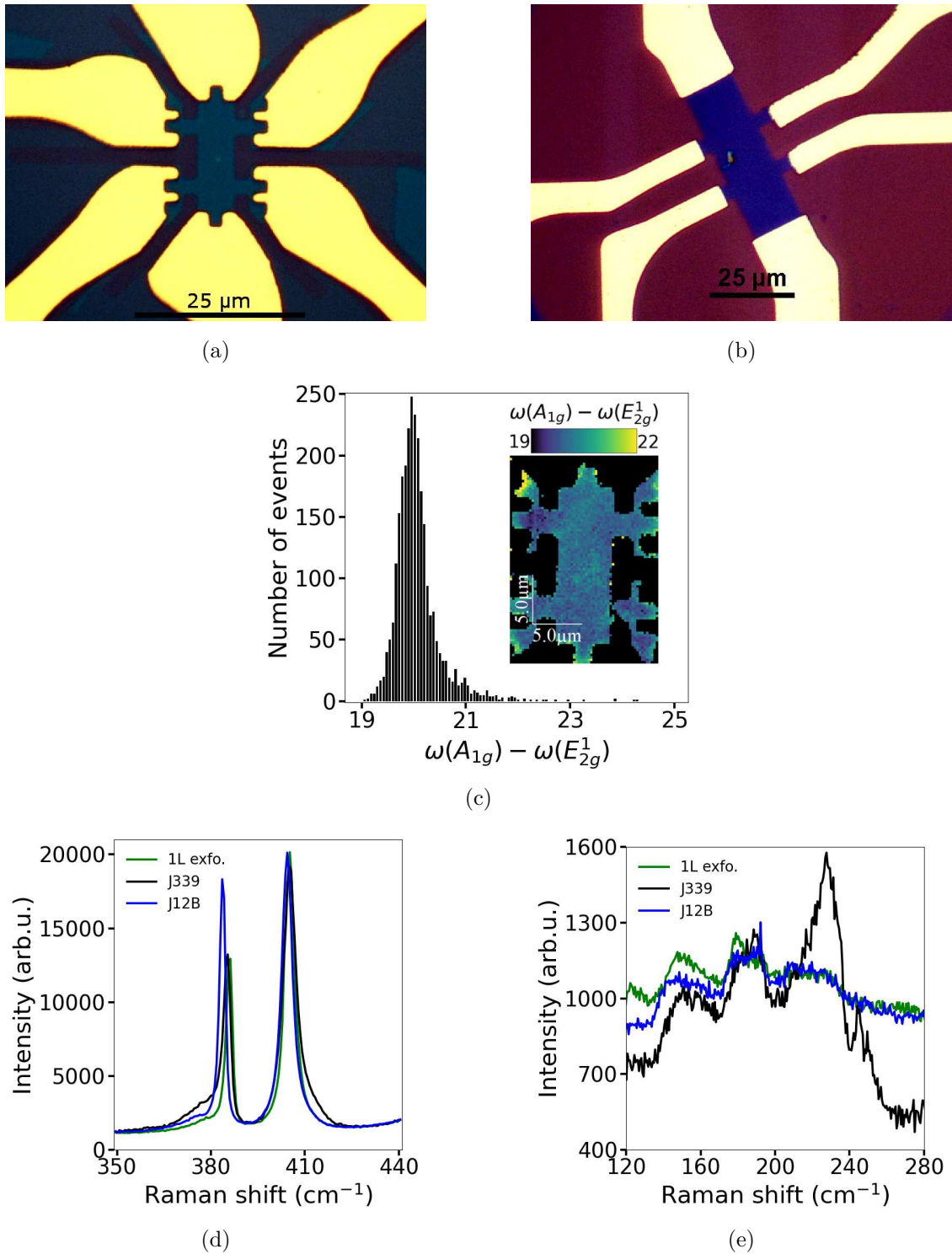


Figure 2.33: (a) and (b) Optical pictures of J339 and J12B respectively. (c) Histogram of the frequency difference $\delta = \omega(A_{1g}) - \omega(E_{2g}^1)$, extracted from the map analysis shown in the inset (device J339). (d) Three Raman spectra: from device J339, device J12B, and from an exfoliated monolayer MoS₂ reference. The spectra show the E_{2g}^1 mode at $\simeq 380$ cm⁻¹ and the A_{1g} mode at $\simeq 405$ cm⁻¹. (e) Raman spectra as in panel d but at lower frequencies, showing the LA mode centered around 240 cm⁻¹.

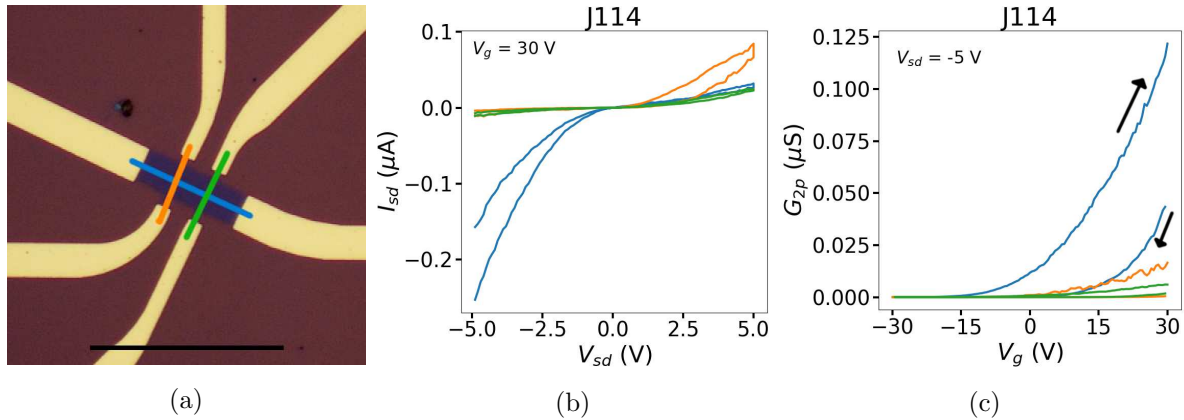


Figure 2.34: Usual IV and transfer curves of Hall bar shaped MoS₂ flakes. (a) Device J114, scale bar = 50 μm . (b) IV curves at fixed gate voltage for the different pairs of contacts indicated by color lines in panel (a). (c) Transfer curves at fixed source-drain voltage. Similar to the previous panel, the colored curves were obtained using the pairs of contacts indicated in (a). The black arrows show the cycle of the transfer measurements: $V_g = 30 \text{ V} \rightarrow -30 \text{ V} \rightarrow 30 \text{ V}$.

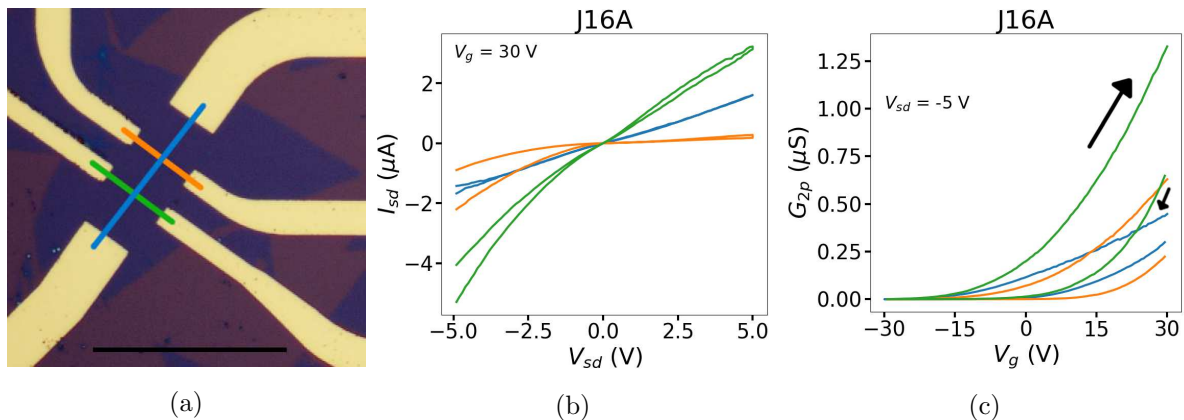


Figure 2.35: Usual IV and transfer curves of non-shaped MoS₂ flakes. (a) Device J16A, scale bar = 50 μm . (b) IV curves at fixed gate voltage for the different pairs of contacts indicated by color lines in panel (a). (c) Transfer curves at fixed source-drain voltage. Similar to the previous panel, the colored curves were obtained using the pairs of contacts indicated in (a). The black arrows show the cycle of the transfer measurements: $V_g = 30 \text{ V} \rightarrow -30 \text{ V} \rightarrow 30 \text{ V}$.

ity. Additionally, a high current density could locally increase the temperature, desorb the molecules attached to the sample's surface, and reduce the amount of those defects.

A moderate current density of 3.4 A/m was passed through a few devices, all of them giving similar results. Below we present the data for a single device, namely J113, as shown in Fig. 2.36a. The IVs measurements were performed in the following cycle: $V_{sd} = 0 \text{ V} \rightarrow 16 \text{ V} \rightarrow -10 \text{ V} \rightarrow 0 \text{ V}$, and has been performed under primary vacuum at $T = 130 \text{ K}$. The sample shows instability when $V_{sd} > 5 \text{ V}$, but becomes stable as the annealing takes

effect. This is evident at negative V_{sd} , once the current annealing at positive V_{sd} takes effect, as can be seen in Fig. 2.36b. Passing a higher current damaged the contacts, as shown in Fig. 2.36c. Therefore, this approach for quality enhancement was abandoned.

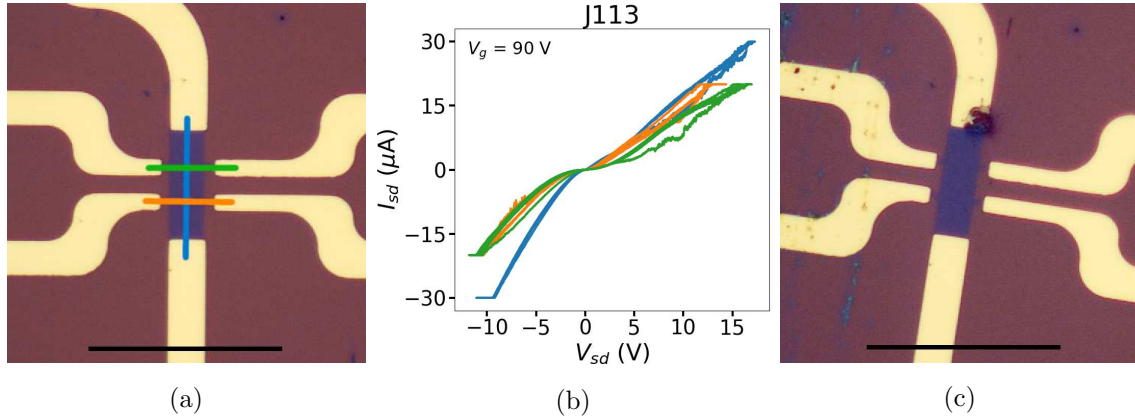


Figure 2.36: Current annealing of J113. (a) Device J113, scale bar = $50 \mu\text{m}$. (b) IV curves at high V_{sd} for the different pairs of contacts indicated by color lines in panel (a). (c) Optical picture after current annealing, evidencing the contact burned.

2.4.4 Ionic liquid gating

One of the first ionic liquid (IL) drops was placed on top of device J124. As the droplet was quite big, it covered and disabled other devices around, as can be seen in Fig. 2.37a. After placing the IL drop, the sample was electrically tested at room temperature, performing IVs and transfer curves with the back-gate before performing them with the IL gate. The results at room temperature are shown in Fig. 2.37b and Fig. 2.37c for IV and transfer curves respectively. Although the temperature was not stable during the measurements, the behaviour was usual, with non-linear IVs, and a bit of gate hysteresis. The cycle of the transfer measurements with the back-gate is the following: $V_{bg} = 0 \text{ V} \rightarrow 30 \text{ V} \rightarrow -30 \text{ V} \rightarrow 0 \text{ V}$. The contacts used for the measurements are shown in Fig. 2.38c and are labeled as ‘S’ and ‘D’.

After knowing that the back-gate was working, the IL gate (ILG) was tested, but nothing could be measured, as shown in Fig. 2.38. It turned out that the sample was destroyed during the previous measurements because of the high V_{sd} which was also applied to the IL, resulting in a degradation of the device, as shown in Fig. 2.38c.

Another device, J126, was tested with the IL trying to overcome some of the mistakes made on the previous device. A small “spoon” was made by using a piece of $25 \mu\text{m}$ diameter

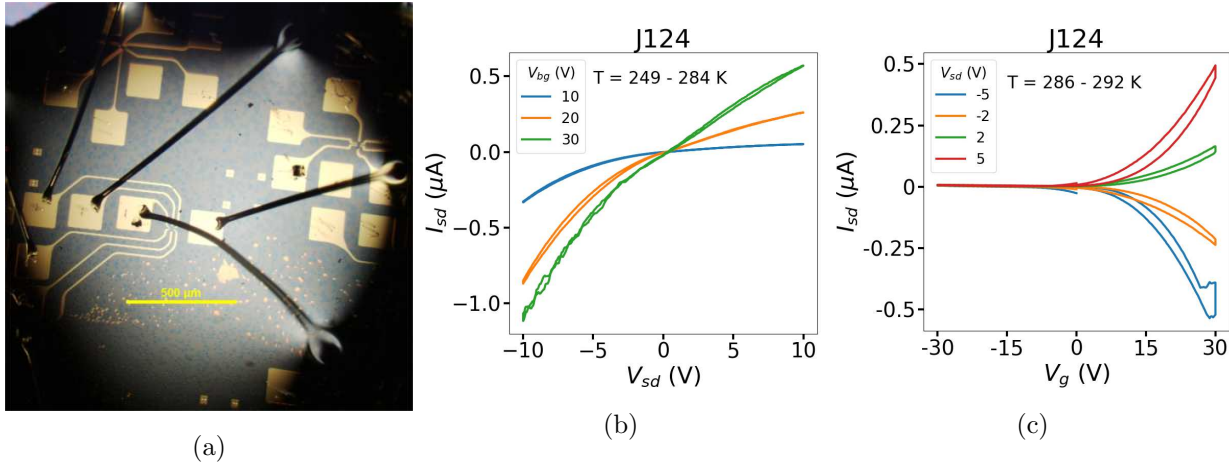


Figure 2.37: Test of the back-gate with IL on top of J124. (a) J124 covered with the IL. (b) IV curves at different V_{bg} . (c) Transfer curves at different V_{sd} . Positive and negative values has been used to look at the symmetry of the curves.

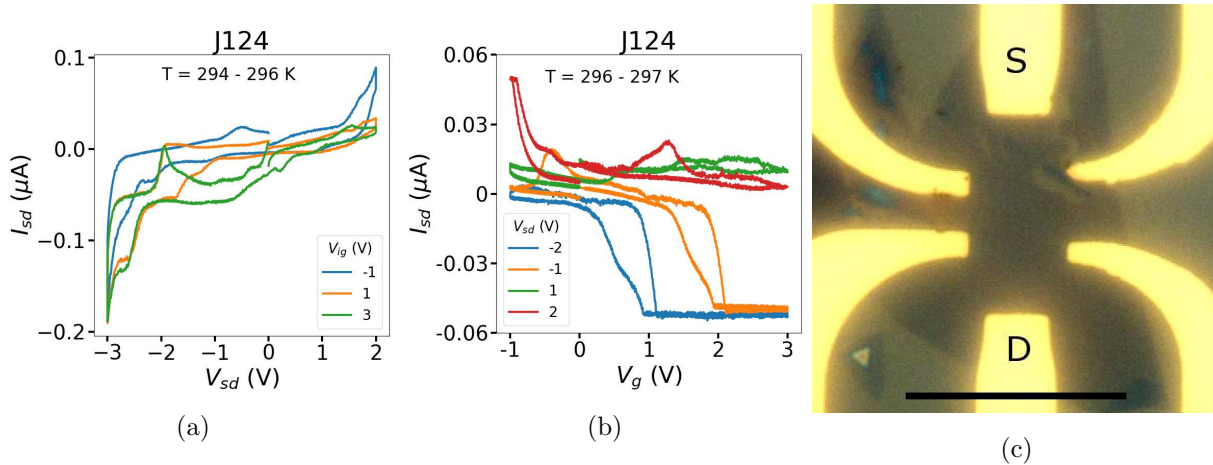


Figure 2.38: Ionic liquid gating of J124, IL voltage rate = 20 mV/s. (a) IV curves at different ionic gate voltages. (b) Transfer curves with the ionic gate at different V_{sd} . (c) Optical picture of J124 after measurements, scale bar = 25 μm .

gold wire, and twisting the end of it forming a loop. With this handmade tool it was possible to take a small drop of IL and to place it on top of the desired device. In Fig. 2.39a is shown a picture of J126 with the IL on top.

As with the previous device, the back-gate was tested prior to the ILG, and a high V_{sd} was applied. The IVs and transfer measurement results are shown in Fig. 2.39b and Fig. 2.39c respectively. This time, the operating temperature was kept stable at $T = 275$ K. The cycle of the transfer measurements with the back-gate is the following: $V_{bg} = 0$ V \rightarrow 80 V \rightarrow -80 V \rightarrow 0 V. Luckily, after the back-gate test, the device was still operating and we could effectively control the electron density with the ILG, as show in Fig. 2.40a.

Unfortunately, the device stopped working after the transfer measurement, and the IV curves made afterwards were meaningless, as can be seen in Fig. 2.40b.

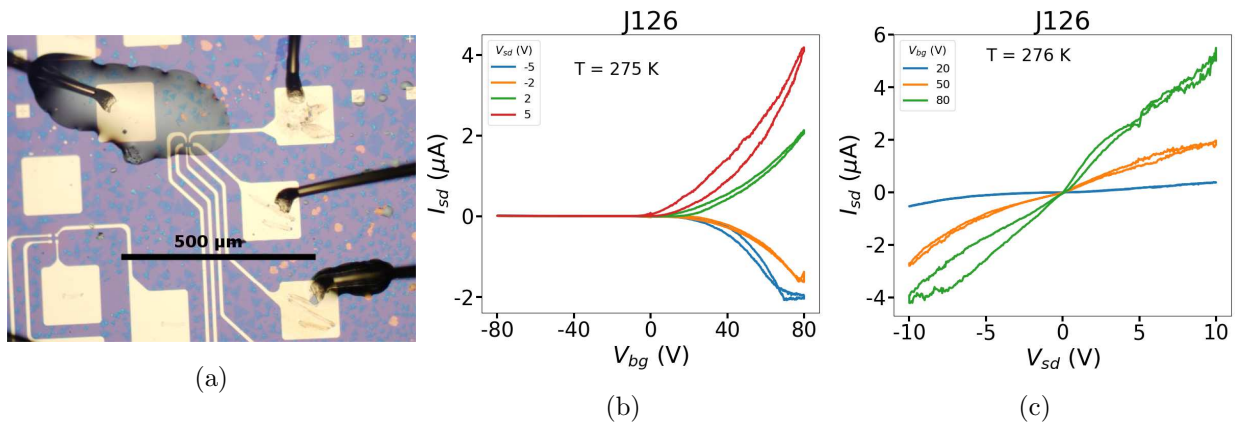


Figure 2.39: Test of the back-gate with IL on top of J126. (a) J126 covered with a small drop of IL. (b) Transfer curves at different V_{sd} . Positive and negative values has been used to look at the symmetry of the curves. (c) IV curves at different V_{bg} .

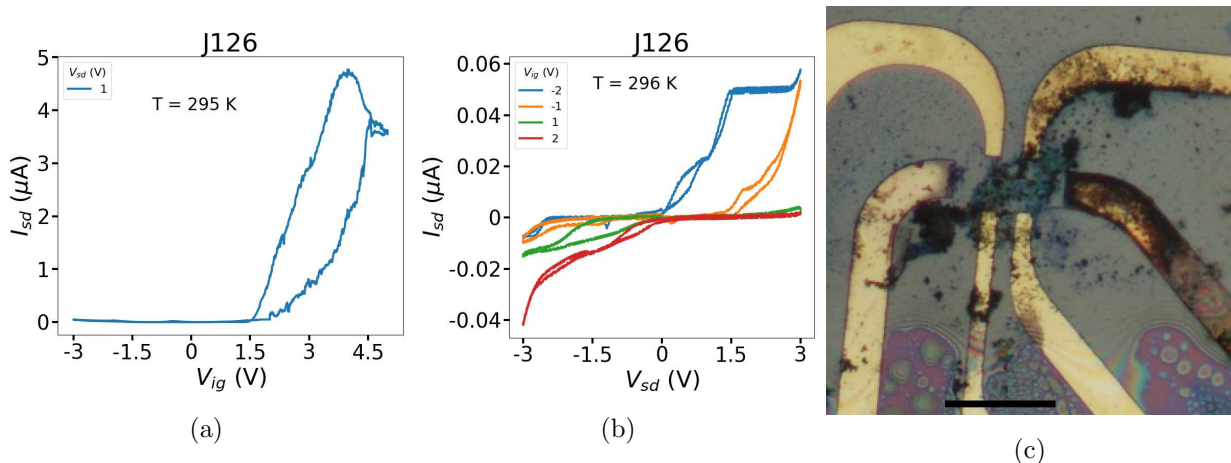


Figure 2.40: Ionic liquid gating of J126, IL voltage rate = 40 mV/s. (a) Transfer curves with the ionic gate. (b) IV curves at different ionic gate voltages. (c) Optical picture of J126 after measurements, scale bar = 25 μm .

As with J124 (Fig. 2.38c), J126 (Fig. 2.40c) also appears to be dissolved in the IL. Initially, it was thought that a too high ILG voltage rate and too high V_{sd} were the causes of this dissolution. We reduced the ILG voltage rate and reduced the maximal V_{sd} on subsequent devices but still the MoS₂ seemed to be dissolved by IL.

Following the work of Lezama *et al.* [122], the ILG was trained by sweeping it slowly over a small range of voltages, increasing this range gradually. A few devices were tested with this approach and all of them showed similar results. We present the data for one of them, called

J6AF, as shown in Fig. 2.41. Unfortunately, we could not perform 4-probe measurements on this device because the metallization of contacts at the end of the fabrication process was not uniform, as can be seen on Fig. 2.41b, making difficult the bonding of the contacts pads. The next discussion will then be on the results obtained with 2-probe measurements only. The notation for back-gate voltage and ionic liquid gate voltage are, respectively, V_{bg} and V_{tg} .

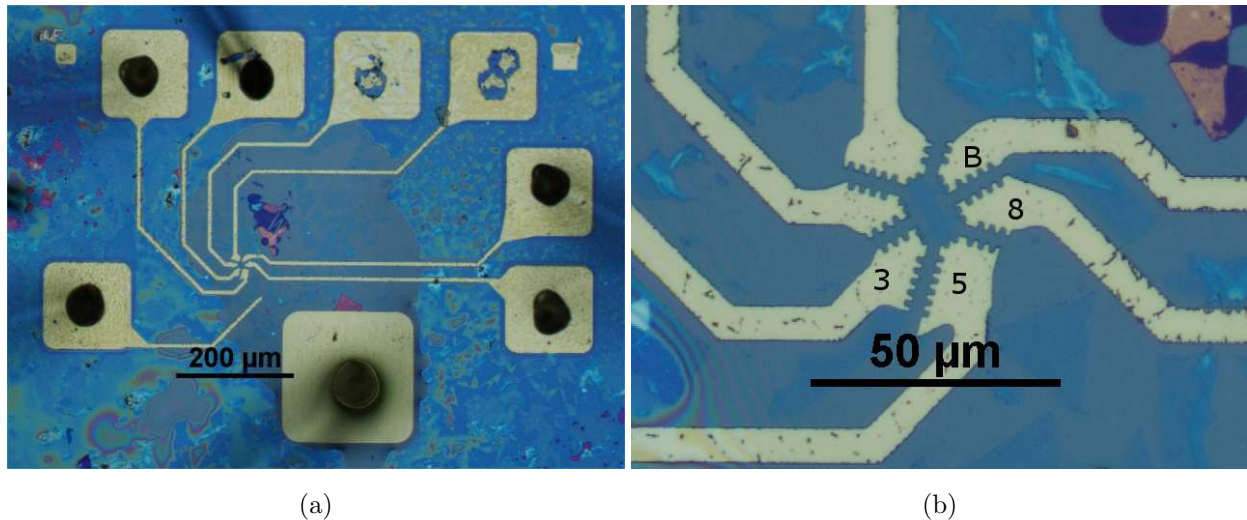


Figure 2.41: Device J6AF with IL drop on top. (a) Large area image. The biggest contact pad is the ILG pad. (b) Closer look at the Hall bar, the contacts used are labelled.

During operation, the ILG leakage needs to be kept negligibly small by sweeping the ILG voltage slowly (the leakage increases with the sweeping rate). A rapid increase of leakage upon increasing ILG voltage may be indicative of chemical reactions that can cause device degradation and should, therefore, be avoided. Environment conditions like temperature and pressure also play a role on the ILG performance, with the ILG leakage increasing with temperature.

In Fig. 2.42 is shown the “ILG training” at room temperature and high vacuum ($\sim 10^{-6}$ mBarr): transfer measurements with the ILG, increasing voltage range gradually. A small V_{sd} voltage of 10 mV was applied in order to know if the training was taking place. A color bar has been included to indicate the time during the measurements, since, as mentioned before, the sweep is performed over a small range of voltages which is increased over time. The ILG sweep range starts with an amplitude of 0.5 V and is increased in steps of 0.2 V after completing a full cycle. For instance, the ILG cycle at the beginning of the training is the following: $V_{tg} = 0 \text{ V} \rightarrow 0.5 \text{ V} \rightarrow -0.5 \text{ V} \rightarrow 0.7 \text{ V} \rightarrow -0.7 \text{ V} \rightarrow 0.9 \text{ V} \dots$, and so on. The

ILG goes from positive to negative and then back to positive with the added voltage step.

As shown in Fig. 2.42a, the IL effectively gates the sample. The ILG voltage at which a noticeable current is measured is lower as the training takes place, starting from $V_{tg} \sim 1$ V at the beginning of the training and decreasing down to $V_{tg} \sim 0.5$ V at the end. Also, the slope of the $I_{sd} - V_{tg}$ curves becomes steeper as the training takes place, meaning the ILG efficiency is increased with the training.

A maximum in the current is reached around $V_{tg} \sim 2$ V, attributed to the Q valley which also starts to be filled once the Fermi level is high enough [24, 106]. As discussed in Section 1.1.2, monolayer MoS₂ has a direct gap at the K-points, but there is a local minimum at the Q-point with an indirect gap. The electron density at the Q-valley is estimated to be 1×10^{13} cm⁻² [24].

Fig. 2.42b shows the 2-probe conductance, defined as I_{sd}/V_{sd} and measured between contacts 5-B. A wide region of low conductance ($G < 10^{-7}$ S, between V_{tg} : -2.5 V – -0.5 V) is observed, and the hole conduction band is not reached, indicating that the efficiency of the ILG was not good enough, or that a extremely large impurity band is present on this device. In Fig. 2.42c is shown the ILG leakage, which increases with the sweeping range and shows peaks in both, positive and negative V_{tg} , which may be signs of occurring irreversible chemical reactions [123].

After the ILG training, we stopped the ILG voltage at 2.5 V, close to the peak in conductance, and measured the current over time. In Fig. 2.42d, we can see that the conductance decreases over time, which we attribute to a decrease in electron density, possibly due to the ions in the IL still rearranging themselves.

Then, an ILG voltage of $V_{tg} = 3$ V (past the peak on conductance) was set and the device was cooled down to liquid He temperature and electrically tested. Transfer and IV measurements were performed, this time on a different pair of contacts: 3-8, as shown in Fig. 2.41b. The results are shown in Fig. 2.43. It is worth noting that the conductance increases when decreasing the back-gate voltage (reducing the electron density) which is apparent since we are past the maximum in conductance shown in Fig. 2.42b. The IV curves, shown in Fig. 2.43b, are strongly non-linear, which could be a contact issue (high Schottky barrier) or VRH transport mechanism taking place, which can not be discriminated by 2-probe measurements. Unfortunately, no Hall effect could be detected because the electron density and mobility of the device gives a theoretical Hall voltage value on the order of μ V,

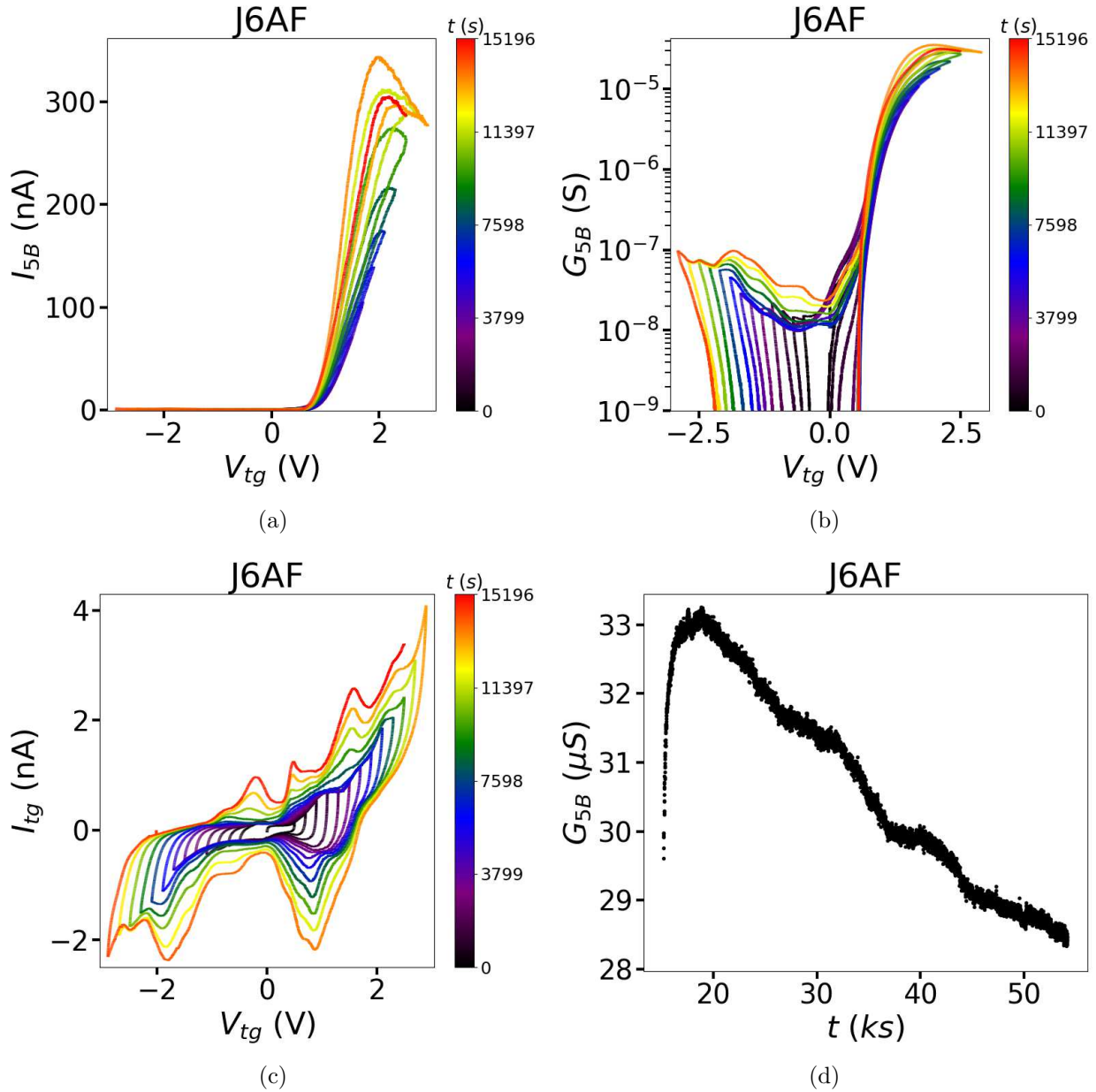


Figure 2.42: ILG transfer curves for device J6AF on contacts 5-B. IL rate = 6 mV/s, $V_{sd} = 10$ mV and room temperature. (a) Source-drain current in linear scale. (b) 2-Probe conductance curves in semilog scale. A peak is reached around $V_{tg} = 2$ V, possibly because the Q-point starts to be filled. (c) ILG leakage. (d) Stability of conductance over time. ILG voltage fixed at $V_{tg} = 2.5$ V.

surpassed by the noise.

After the previous IVs and transfer measurements, the device was warmed up to room temperature in order to apply a different V_{tg} , training the IL before that, and cooled down to He liquid temperature to be electrically tested again. This process was repeated a couple of times, resulting in a higher resistance of the device each time, regardless of the V_{tg} applied. A total of 3 cooling downs at different ILG voltages has been performed on this device; the first

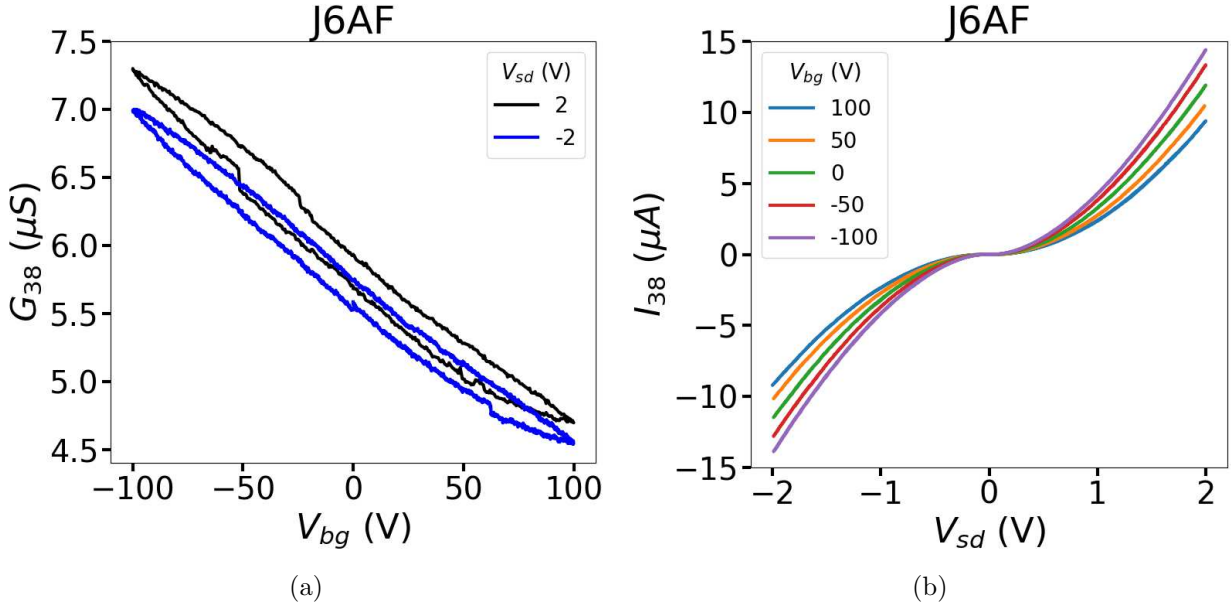


Figure 2.43: Measurements performed at $T = 4.2$ K on contacts 3-8. $V_{tg} = 3$ V. (a) Transfer curves with the back-gate at different V_{sd} . (b) IV curves at different back-gate voltages.

a $V_{tg} = 3$ V, the second a $V_{tg} = 6$ V and the third a $V_{tg} = 2$ V. The extracted conductance during each cooling down is shown in Fig. 2.44a, in a Efros-Shklovskii plot. In some regions of temperatures, the data follows very well the Efros-Shklovskii VRH transport mechanism, as seen by the linearity of the data in that plot, although, as mentioned before, we can not be conclusive with 2-probe data. This transport mechanism will be studied in more detail in the next Chapter.

During the first cooling down (blue curve), the conductance was significantly higher than the other two since the device degraded with each cycle of cooling down, warming up and ILG training. After the third cool down, the device stopped working and no I_{sd} could be measured at low temperature. It turned out the device got damaged because of unwanted chemical reactions caused by the IL, as shown in Fig. 2.44b and Fig. 2.44c. We attribute this chemical reaction to the temperature at which the IL's training was performed (room temperature). A low temperature of slightly above 220 K (the freezing point of the IL), is recommended for operating the ILG in order to avoid chemical reactions.

Ionic liquid gating is a promising approach if high electron densities are desired. However, controlling it requires technique and very specific conditions. We could reach the Q-point, which is estimated to happen at a density of $1 \times 10^{13} \text{ cm}^{-2}$, but with consequent cycles of warming ups and cooling downs the device got damaged.

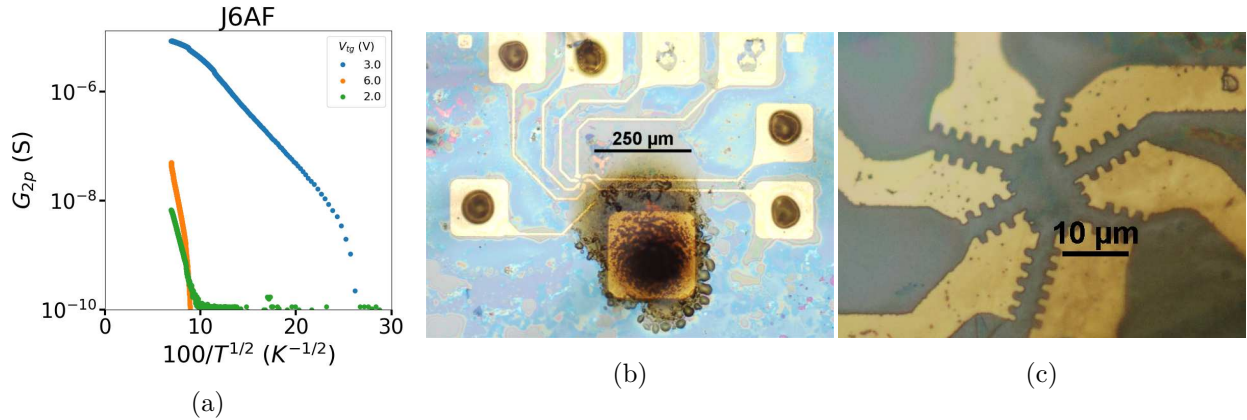


Figure 2.44: (a) Cooling downs of device J6AF at different V_{tg} in a Efron-Shklovskii plot. (b) and (c) Optical pictures of the device after measurements.

2.4.5 Photogating

Series of timed exposures to UV light ($\lambda = 375$ nm) interspersed with dark periods (LED switched off) has been performed to demonstrate the optical gating effect of UV light. The measurements were performed in primary vacuum at room temperature. The UV LED was placed close to the device in such a way that, when turned on, it illuminates the whole device, as shown in the schematics in Fig. 2.45a. The results are shown in Fig. 2.45b. The moment when the LED is switched ON or OFF is indicated in blue color. With each exposure, the conductivity increases, possibly as a consequence of increase in doping and the creation of excited states into the conduction band. When switched OFF, the conductivity drops sharply, since there are no more excited states. Additionally to the LED, a small power heater was also used, with the maximum temperature reached being estimated around $T = 350$ K, which is not enough for a thermal annealing (as will be shown in the next Section). At $t = 5000$ s the heater is switched ON, the conductivity falls and then slowly recover until $t = 6500$ s when both the heater and LED are switched OFF. This drop in conductivity could be related to an outgassing of the MoS_2 , since the vacuum meter recorded a pressure increase. There is not a clear constant value of conductivity with the use of LED gating, reaching a different maximum with each consequent UV illumination.

IV and transfer measurements under different LED conditions have also been performed, and are shown in Fig. 2.46. Three different LED states were tested: OFF, ON at low LED power (LED current = 15 mA) and ON at high LED power (LED current = 90 mA). The IV curves, shown in Fig. 2.46a, reveal a high resistance and Schottky contacts that are

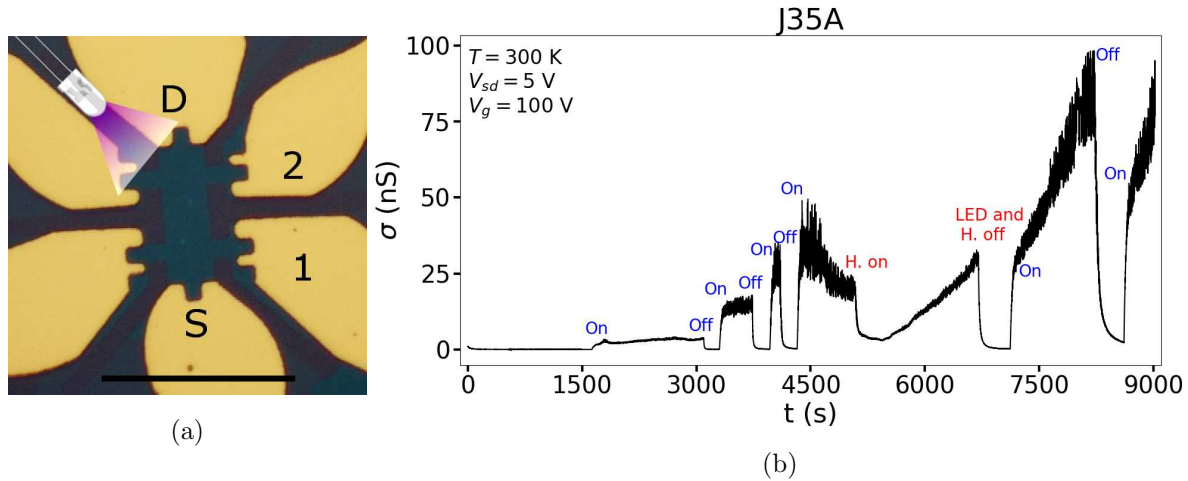


Figure 2.45: Photogating of device J35A. (a) Schematic of the UV illumination and measurements. Scale bar = 25 μm . (b) 4-probe conductivity as a function of time during UV illumination.

probably dominating the device's performance. It also shows that the resistance decreases with increasing LED power. The transfer curves, shown in Fig. 2.46b, reveals big hysteresis, which makes it difficult to estimate the variation of the doping under LED illumination.

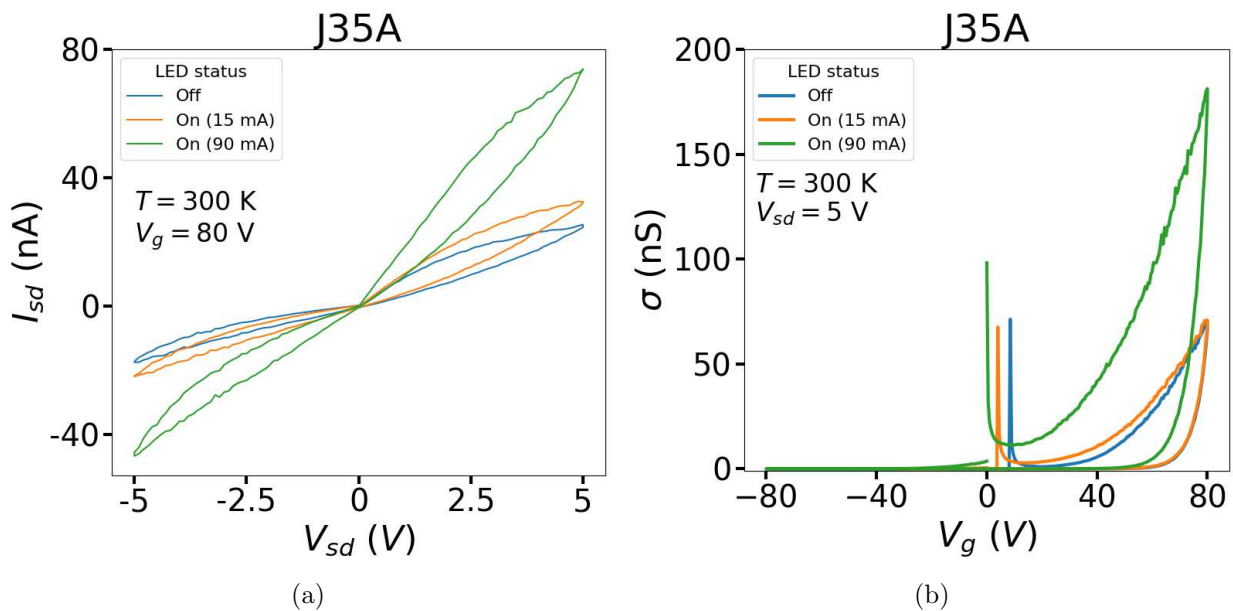


Figure 2.46: IV (a) and transfer (b) measurements for different LED conditions: LED OFF (blue curves), LED ON at low power (Orange curve), and LED ON at high power (green curve).

The LED gating showed not reproducibility, making it hard to be used as a tool for efficient doping control. As a consequence, this way of controlling doping was discontinued.

2.4.6 Thermal annealing

Vacuum thermal annealing is commonly used to improve the contact quality and achieve enhanced device performance [124]. In our case, we performed annealing with the Janis cryostat shown in Fig. 2.29 under primary vacuum, without further exposure to air. This method was the only one that allowed us to obtain reproducible results and several complete data sets as a function of temperature. A detailed analysis of these data will be presented in the next Chapters. Below we simply present this method, and the first results obtained.

J11B was the first device measured at high temperature. For this device, the measurements were performed in order of increasing temperature from 300 K up to 600 K, with a noticeable change in the device performance above $T = 500$ K. The annealing times and temperatures are: 87.6 min at 500 K, 37.5 min at 550 K and 37.5 min at 600 K. In Fig. 2.47 are compared the IV and transfer data obtained at $T = 300$ K before and after annealing. It is clear from the results that the total resistance decreases, as seen by the higher current at the same V_{sd} . Also, the doping increases, as seen by the change in threshold voltage V_{Th} on the transfer curves. Following [125], a linear fit on the transfer curve was performed in order to determine V_{Th} , as shown by the dashed line in the insert of Fig. 2.47c. This gives a value of $V_{Th} \sim 40$ V before annealing, but an unknown value for after annealing. The annealing changed the V_{Th} to negative values on the gate voltage, meaning that the device got n doped and a negative gate voltage is needed in order to deplete it.

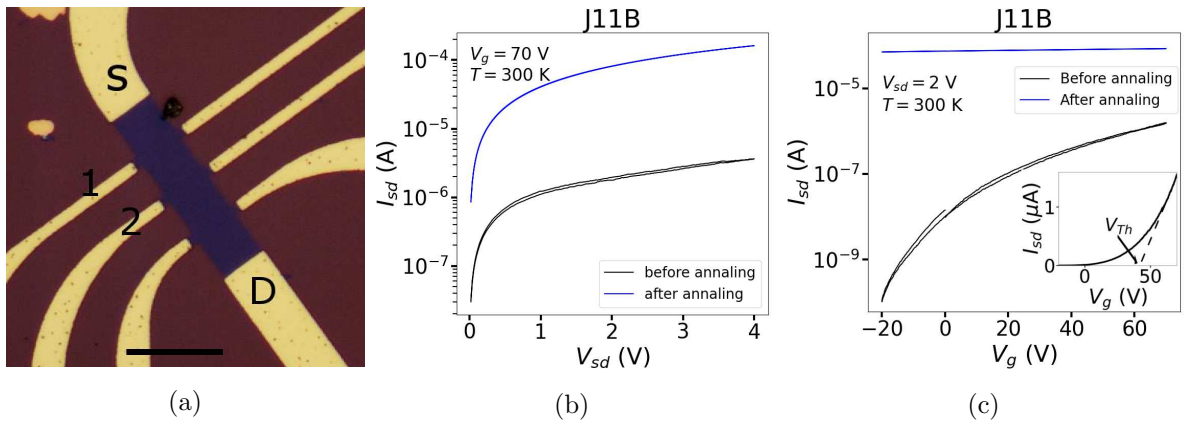


Figure 2.47: J11B before and after thermal annealing. (a) Device J11B showing the contacts used for the measurements. Scale bar = 25 μ m. (b) and (c) IV and transfer results before (in black color) and after (blue color) thermal annealing at $T = 600$ K.

After the thermal annealing, the contact resistance is negligible compared to the MoS_2 resistance, as can be seen from the 2-probe and 4-probe results at $T = 500$ K, shown in

Fig. 2.48, and at $T = 300$ K, shown in Fig. 2.49. V_{sd} is 4 times V_x , with the distance between contacts used in the 4-probe configuration being roughly 1/4 the distance between source-drain contacts, meaning there is a negligible (compared to the MoS₂ resistance) voltage drop at the contacts.

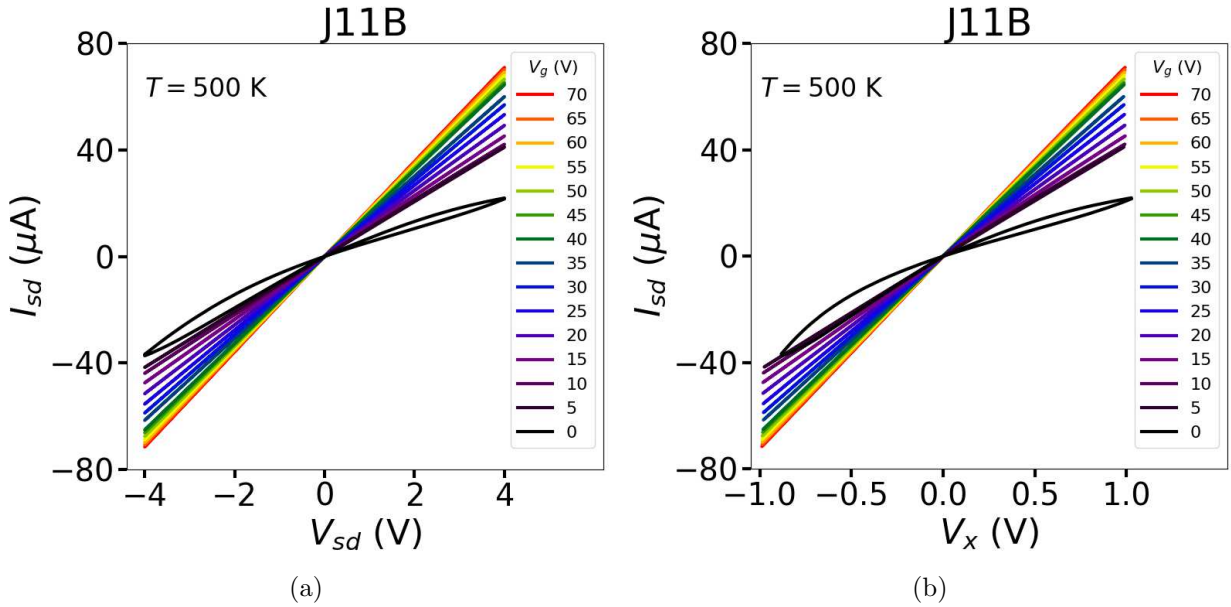


Figure 2.48: J11B IV plots at $T = 500$ K. (a) 2-probe results (b) 4-probe results.

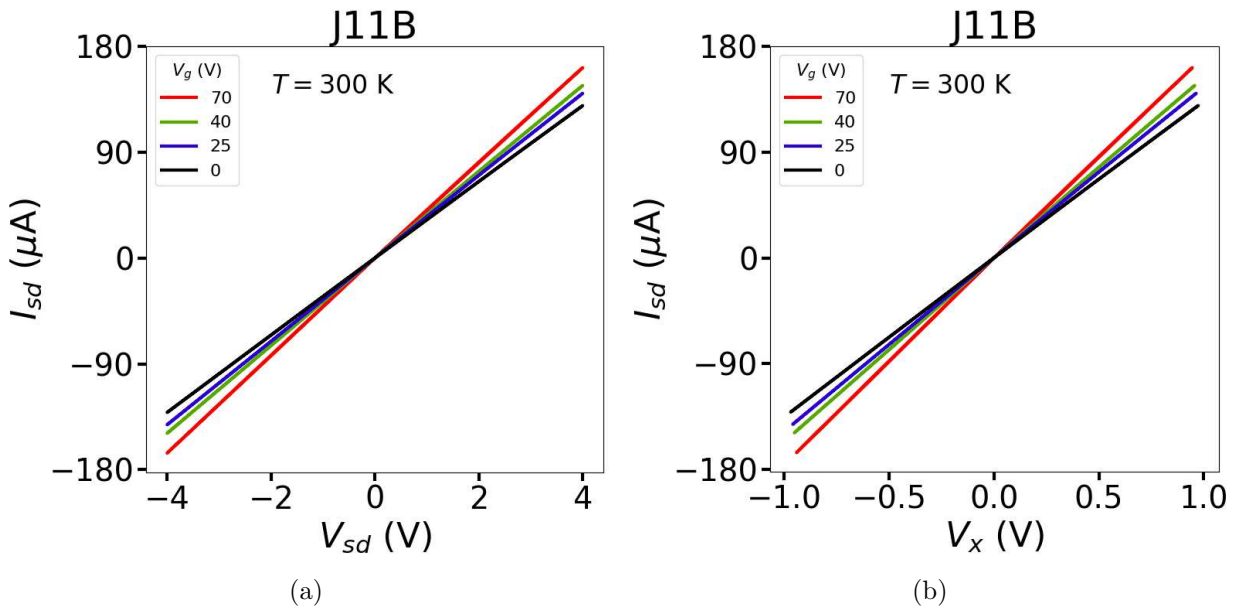


Figure 2.49: J11B IV plots at $T = 300$ K. (a) and (b) 2-probe and 4-probe results respectively.

Similar results were obtained for several other devices. In Fig. 2.50 are shown the annealing results for devices J31A and J339. The estimated change of V_{Th} with annealing

is ~ 120 V, or equivalently, an electron density increase of around $n = 8 \times 10^{12}$ cm $^{-2}$, estimated using the capacitive model: $n = C_g(V_g - V_{Th})/e$, where e is the electron charge and $C_g = 1.04 \times 10^{-8}$ F/cm $^{-2}$ is the geometric capacitance for 300 nm thickness of SiO $_2$. This increase in doping with annealing has been already documented [12, 74, 124], and a possible explanation could be that the annealing is desorbing molecules from the MoS $_2$ surface, exposing the (sulphur) vacancies which in turn acts as electron donors [4, 9]. The fact that there is a noticeable difference in doping when the sample is on ambient air or in vacuum, as shown by the black and blue curves in Fig. 2.50, supports this explanation of desorbing molecules from the surface [126].

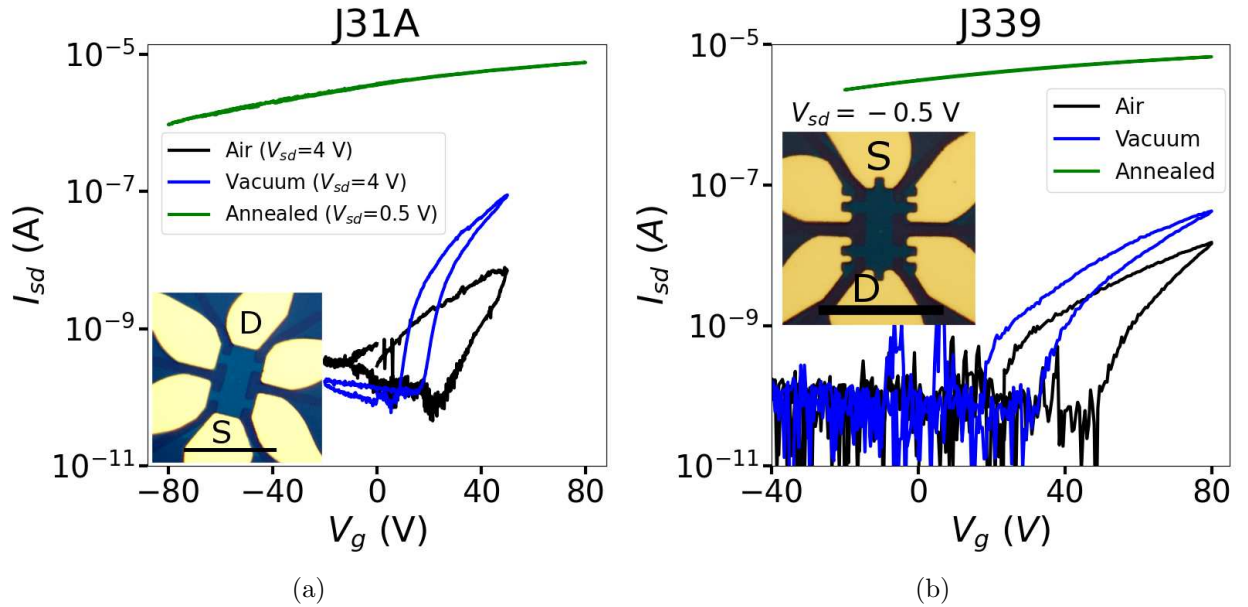


Figure 2.50: Change in doping with annealing for different devices. (a) Device J31A. (b) Device J339. The insert shows the device with the contacts used marked. The scale bar for both devices is $25 \mu\text{m}$.

Different annealing temperatures and consecutive annealings have also been studied. A temperature of $T = 500$ K is not sufficient (but induces already noticeable changes) while consecutive annealings at $T = 600$ K negatively affect the device performance. This study was performed in several devices, but here we show the results for a single one, named J348. Transfer measurements, shown in Fig. 2.51, were performed at $T = 400$ K after annealing the device at different temperatures: at $T = 520$ K for 30 min (blue curve), at $T = 600$ K for 30 min (orange curve), and finally, at $T = 600$ K for 20 min (green curve), in that order. The device's conductivity changes by almost 1 order of magnitude after being annealed at $T = 600$ K compared to the effect of annealing at $T = 520$ K, indicating that temperatures close to 500 K are not sufficient for a proper thermal annealing. However,

consecutive annealing at high temperature are detrimental for the devices. After a second annealing at $T = 600$ K, the conductivity dropped by almost 1 order of magnitude (green curve) compared to the first annealing at $T = 600$ K (orange curve).

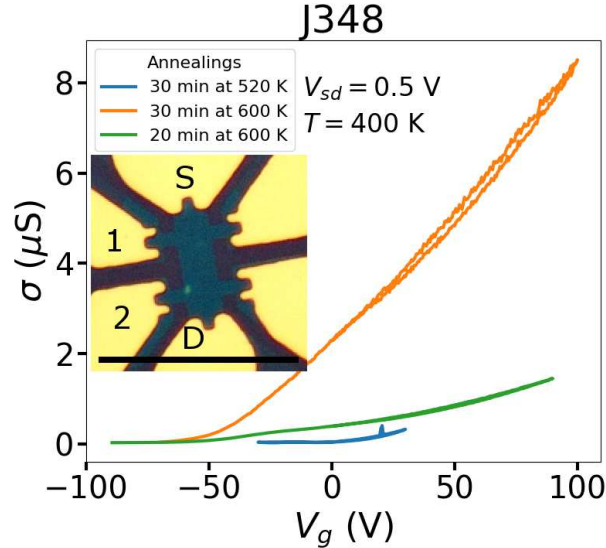


Figure 2.51: Effect of different annealing temperature and consecutive high temperature annealing. Device J348, scale bar = $25 \mu\text{m}$. All the measurements were performed at $T = 400$ K after performing the annealing. The temperatures and times of the thermal annealing are: $T = 520$ K for 30 min (blue curve), $T = 600$ K for 30 min (orange curve), and $T = 600$ K for 20 min (green curve), measured in that order.

Of all devices that were thermally annealed, all of them had varying degrees of doping change, with some of them breaking during the annealing. The magnitude of the impact that the annealing will have on the device, such as the change in doping and the device's resistance to the annealing (meaning the device doesn't break during the annealing) can not be known *a priori*, since it is strongly device-dependent.

2.4.7 Hysteresis

Hysteresis is a bistability in the operational transistor current. It appears as a difference in the source-drain current values observed during forward and backward sweeps of the gate voltage. Hysteresis is useful in nonvolatile memory devices but it is generally avoided in standard integrated circuits [127–129]. The hysteresis behavior is schematically depicted in Fig. 2.52, where it shows on cyclic transfer curves, I_{sd} vs. V_g , with I_{sd} depending on the sweep direction of V_g . Depending on the microscopic effect, the hysteresis of the full transfer cycle can result in clockwise or anti-clockwise direction. In Fig. 2.52a and Fig. 2.52b are shown both directions for n-doped semiconductors. For n-type FETs, a clockwise hysteresis is

attributed to charge carrier trapping close to the channel, whereas anti-clockwise hysteresis is usually caused by mobile ions in the dielectric, or by (ferroelectric) polarization of the dielectric [130].

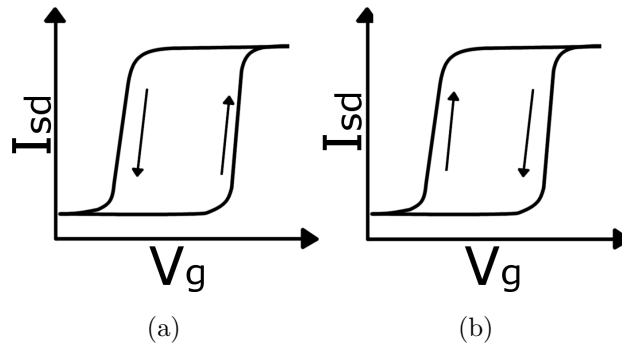


Figure 2.52: Schematic of transfer curves with hysteresis for n-type FETs. (a) and (b) shows anti-clockwise and clockwise respectively. Adapted from [130].

All of our devices showed anti-clockwise hysteresis at temperatures above $T = 300$ K. Figure 2.53 shows the characteristic transfer data of four devices. Each device was annealed at $T = 600$ K for about 3.8 min, 10.6 min, 20 min and 15 min for devices J339, J338, J12B-bot and J12B-top respectively. After the thermal annealing, the transfer measurements were performed starting at $T = 500$ K down to $T = 300$ K, where the hysteresis starts to be negligible for almost all devices. The sweeping of the gate voltage V_g is from 0 V up to the maximum V_g , then to the minimum V_g and finally back to 0 V. For instance, for device J339, shown in Fig. 2.53e, the transfer cycle is the following: $0 \text{ V} \rightarrow 80 \text{ V} \rightarrow -20 \text{ V} \rightarrow 0 \text{ V}$. As we can see from the results, the magnitude and behavior of the hysteresis is sample dependent: for devices from the sample Jjedi03, the hysteresis decreases with decreasing temperature, as shown in Fig. 2.53e and 2.53f, while for devices from sample Jjedi01 the opposite occurs, but only above $T = 300$ K, as shown in Fig. 2.53g and 2.53h. This behavior can be explained by considering V_{Th} higher than the V_g range used, with the later increased as the temperature was lowered.

All devices showed counterclockwise BSC hysteresis, possibly due to oxide traps close to MoS₂-SiO₂ interface [128, 130]. Some other authors have reported a transition from clockwise to anti-clockwise as temperature increases [128]. However, the origin of the increase of hysteresis when decreasing the temperature, as observed on devices from sample Jjedi01, is unclear.

The typical hysteresis for device J339 at $T = 400$ K is $\Delta V_T \sim 10 - 20$ V, which allows

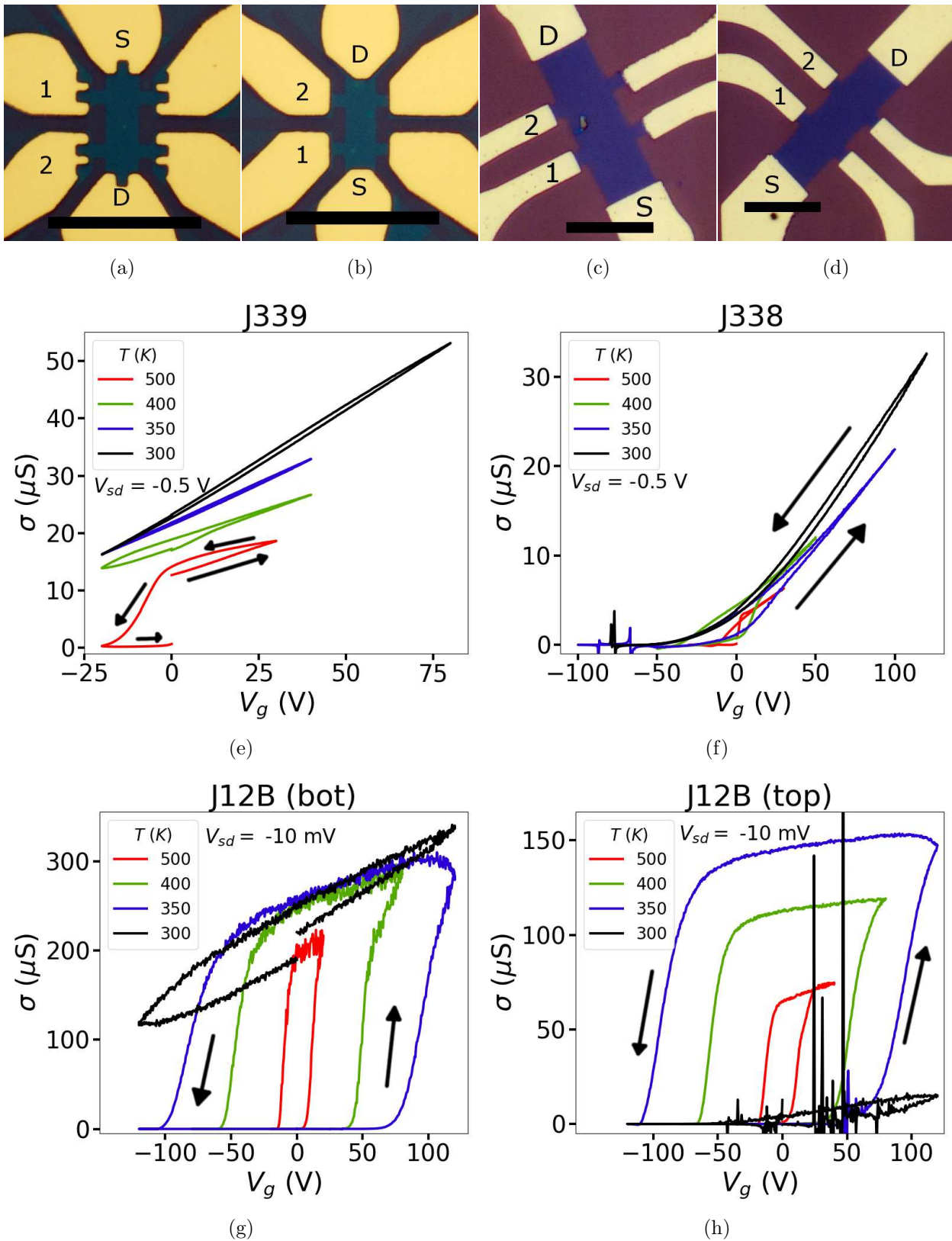


Figure 2.53: (a), (b), (c) and (d) Devices J339, J338, J12B (bot) and J12B (top) respectively. Scale bar = 25 μm . (e), (f), (g) and (h) Transfer curves showing hysteresis for the aforementioned devices. The black arrows shows the back-gate sweeping direction. The hysteresis is noticeable above $T = 300$ K.

us to estimate a lower value for J339's doping inhomogeneity of $N_T \gtrsim 10^{12} \text{ cm}^{-2}$, using a simple capacitive model: $N_T > \Delta N_T \geq \Delta V_T * C_{ox}/e$. This value will be compared to the density of defects calculated in the next Chapter.

2.5 Conclusion

In this Chapter we have introduced the fabrication process of the different devices, the setup used to characterize them, and a few preliminary measurements that helped us to understand the electronic transport mechanism on MoS₂. Several of those measurements resulted in damages of the samples (current annealing, ionic liquid gating) while some others give us hints on what to change on the device itself and the type of measurements we could perform without damaging the sample. The ionic liquid gating is a delicate technique that requires a fine control over the temperature, the sweeping voltage rate and the current leakage. The temperature should be as low as possible while keeping mobile ions, which is around 220 K. Hall effect measurements have been tried but the mobility of the samples was not adequate to measure any significant signal. Thermally annealing the devices resulted in a big change of doping, more than what the SiO₂ back gate could change, pushing the Fermi level close to the conduction band. With this method, the electronic transport has been successfully studied, as will be shown in the next Chapters.

Chapter 3

Electronic transport through the MoS₂

This Chapter is devoted to the low-temperature electronic transport measurements performed on devices J339, J338 and J12B. The three devices are shown in Fig. 3.1, with a label on the contacts that were used in 2-probe and 4-probe measurements.

Those measurements were performed on the Janis He-free cryostat presented in Section 2.3.6. The DC two-terminal and four-terminal current-voltage ($I - V$) characteristics were recorded as a function of the back gate voltage, and as function of the source-drain voltage at different temperatures. As mentioned in Section 2.4.2, after fabrication, all measured devices were extremely resistive with resistances of the order of $G\Omega$, and electron conduction merely accessible at high positive gate voltages. To reduce the electric resistance, the devices were annealed at 600 K in primary vacuum ($\sim 10^{-3}$ mbar) before the measurements. Devices J339, J338 and J12B were annealed during 4 min., 11 min. and 15 min. respectively. The measurements were performed starting at 500 K, measured at fixed T , and progressively cooling down to 20 K without any further exposure to ambient air. Devices J339 and J338 have been measured in primary vacuum down to 300 K, and at low pressure He gas afterwards; whereas device J12B has been measured in primary vacuum down to 108 K, and at low pressure He gas afterwards.

For each measurement, V_{sd} and V_g were sourced, while the current I_{sd} , the 4-probe voltage $V_x = V_{12}$, and the gate leakage I_g were recorded. Two set of measurements has been performed: sweeping V_{sd} at fixed V_g (IV measurements), and sweeping V_g at fixed V_{sd} (transfer measurements).

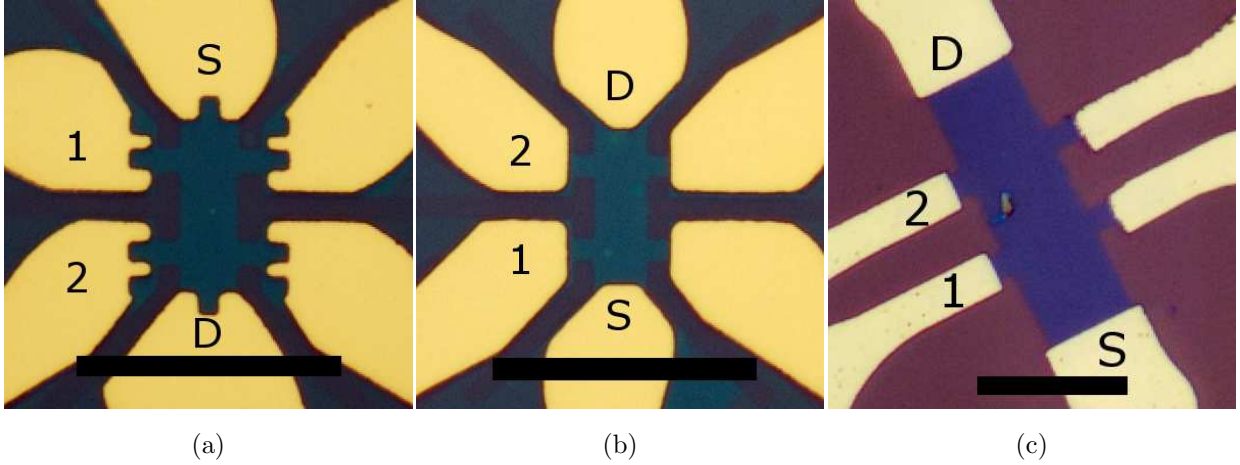


Figure 3.1: Optical pictures of J339 (a), J338 (b), and J12B (c). Scale bar = $25 \mu\text{m}$. **S** and **D** stand for source and drain respectively. The contacts 1 and 2 were used to measure voltage in a 4-probe configuration.

3.1 2- and 4-probe I-V

The *in-situ* thermal annealing considerably doped the devices with n-type carriers, shifting the threshold voltage V_T by ~ 120 V towards negative values for device J339, as already discussed in Section 2.4.6. This increase in doping with thermal annealing has been already documented [12, 74, 124], and it is thought to be caused by the desorption of molecules in the vicinity of MoS_2 and, in particular, near sulfur vacancies which will then act as electron donors [4, 9]. This results in a large increase of both carrier density and conductivity. The gate dependent conductivity curves exhibited hysteresis at temperatures above ~ 350 K, as discussed in Section 2.4.7. At $T \leq 300$ K, the amplitude of the hysteresis is negligible for the three devices.

Figure 3.2 shows the 2-probe and 4-probe curves at different temperatures and fixed gate voltage (V_g) for J339, J338 and J12B devices. Here, I_{sd} and V_{sd} correspond to the current and voltage between the source and the drain, and V_x is the local voltage measured in the four probe configuration. As we can see from the figure, the four-probe curves are linear, while the two-probe curves are not. This is especially obvious for device J338. The non-linearity is induced in the vicinity of the contacts by Schottky barriers, as will be discussed in the next Chapter. As the I_{sd} current is limited by the blocking Schottky contact, the superlinear behavior (in the 2-probe data) may be due to Schottky contacts as will be discussed on the next Chapter.

The measured $I_{sd} - V_x$ curves are straight lines, which ensures that the properties of the

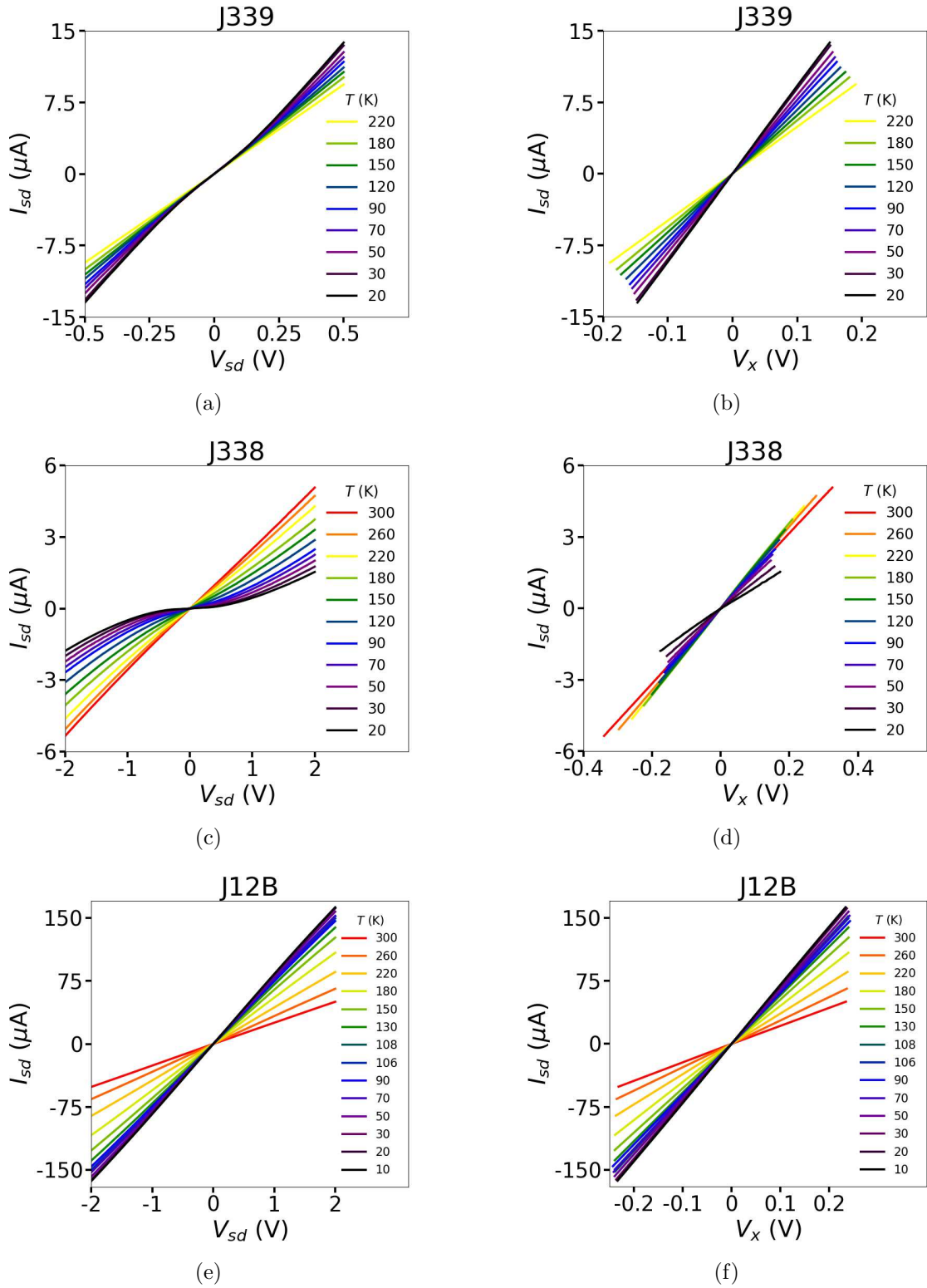


Figure 3.2: Two-probe ((a), (c) and (e)) and four-probe ((b), (d) and (f)) curves for J339, J338 and J12B devices respectively. $V_g = 100$ V for J339 and J338 devices, while $V_g = 120$ V for device J12B.

MoS₂ can be extracted from the 4-probe measurements. Thus, in the following, we use only the 4-probe data, and we restrict the analysis to the domain in which the gate hysteresis is negligible ($T \leq 300$ K), to ensure that the resistivity of the MoS₂ is extracted correctly.

3.2 Conductivity: Metallic and insulating behavior

Given the linearity of the 4-probe data shown earlier, the conductivity is then confidently extracted as $\sigma = I_{sd}/V_x$ at fixed V_{sd} while sweeping V_g , *i.e.*, using the transfer data. Figure 3.3 shows the conductivity σ of the three devices as a function of backgate voltage at different temperatures, and as a function of temperature at different backgate voltages. The conductivity is vanishingly small at low V_g for devices J339 and J338, and steadily increases with V_g . In the case of J339 (see Fig. 3.3a), for $V_g < 45$ V, the conductivity decreases with T , indicating a clear insulating behavior. At the opposite, for $V_g > 45$ V, the conductivity decreases with increasing temperatures, indicating a metallic behavior. The crossover between the two regimes can be associated to a crossing point between the $\sigma(V_g)$ curves taken at low temperatures. In the temperature range $T = 20 - 120$ K, the crossing point marking this transition is remarkably temperature-independent and is located at $V_c = V_g \simeq 45$ V, where V_c is the gate voltage at the crossover. At higher temperatures, the crossing point shifts slowly from $V_g \simeq 45$ V at $T = 20 - 120$ K down to $V_g \simeq 0$ V at $T = 300$ K. For comparison, Fig. 3.3c shows the conductivity of device J338, the onset of the apparent crossover is visible at $V_g \simeq 120$ V. As in device J339, $\sigma_c \simeq 1.4e^2/h = 55 \mu\text{S}$ at the transition, and the apparent crossover shifts progressively to lower gate voltages when T increases. We recall that $e^2/h \simeq 39 \mu\text{S}$.

Device J12B, shown in Fig. 3.3e, was considerably more doped than J339 and J338 and only the metallic region could be observed, with σ in the range 100-700 μS . For this device, the measurements were performed under low vacuum down to $T = 108$ K. At lower T , the chamber was filled with He at low pressure. This had a negative effect on the device performance, as shown in Fig. 3.3f, where the asterisk (*) marks the temperature at which the chamber was filled. Below this point, the conductivity is much more noisy and with an apparent thermal-dependence suppression. This phenomena will be discussed on appendix B. For this device, the data for temperatures above 108 K will be considered for further analysis.

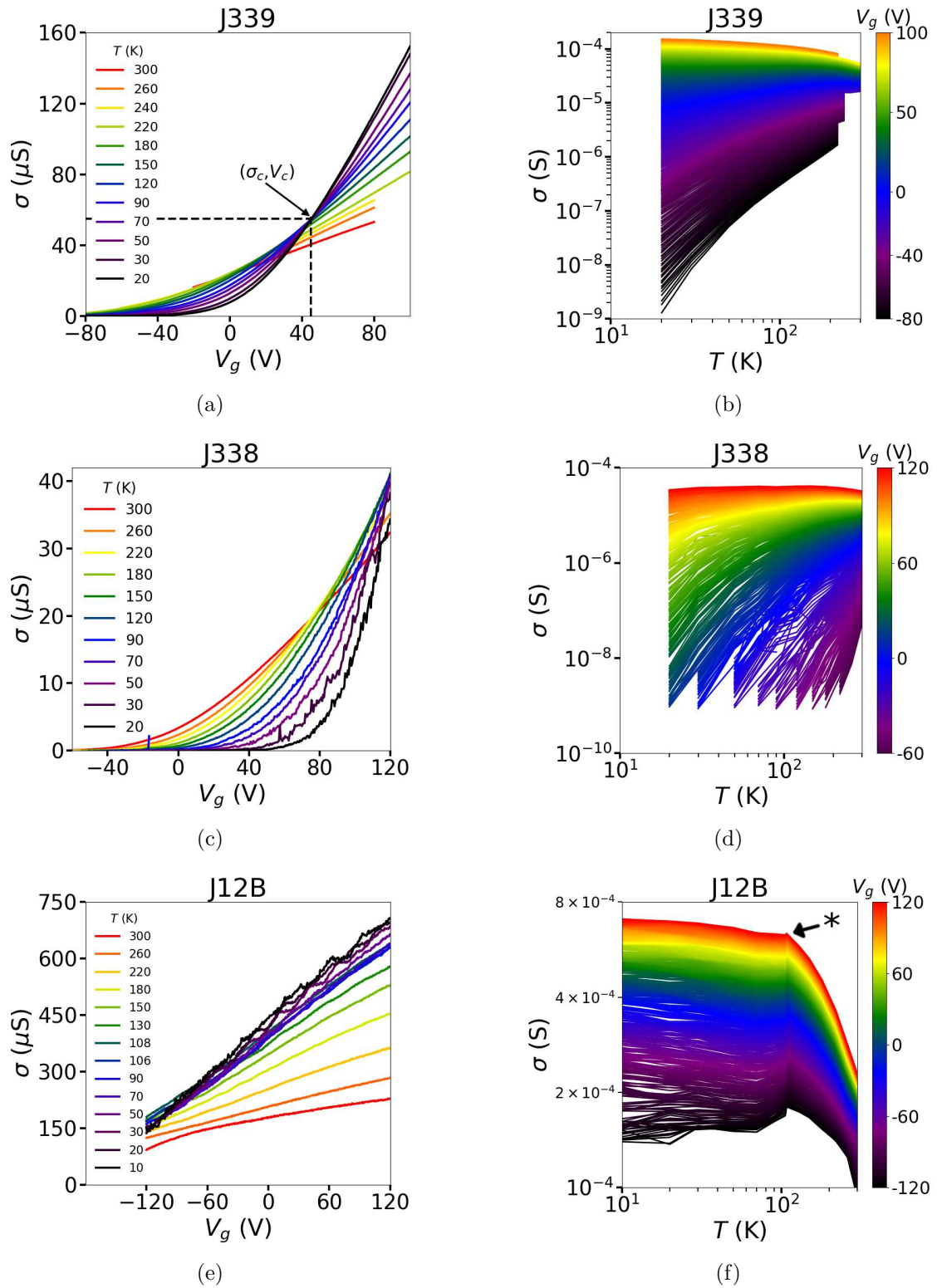


Figure 3.3: Four-probe conductivity of devices J339 (a and b), J338 (c and d), and J12B (e and f), as a function of gate voltage and temperature. In panel (a) is shown the the critical conductivity $\sigma_c \simeq 55 \mu\text{S}$, and the critical gate voltage $V_c = 45 \text{ V}$. For the data of device J12B shown in panel (f), the asterisk marks the temperature below which the sample's chamber was filled with Helium at low pressure.

This apparent two-dimensional metal-insulator transition (2D MIT) was first observed in MoS_2 monolayer by Radisavlevic and Kis [75], and later by Baugher *et al.* [74], Schmidt *et al.* [12], Yu *et al.* [10] and more recently by Moon *et al.* [5]. The experimental ubiquity of this MIT, systematically observed with a critical conductivity around e^2/h in various samples, has not been elucidated yet. It was suggested that this phenomena originates from percolation [131], as already observed in two dimensional electron gases [91, 93], or from a genuine 2D MIT induced by interaction [5, 132, 133]. It should also be noted that the term ‘‘MIT’’ is often used ambiguously. In some papers, it is used to indicate the presence of a genuine phase transition. In other works [10, 12], it is purely phenomenological, and refers to a transition between metallic and insulator as a function of doping. In our case, as a real phase transition can not be demonstrated, we refer to the MIT as ‘‘apparent MIT’’.

As introduced in Section 1.3, the scaling theory predicts that a non-interacting 2D electron gas (2DEG) is always an insulator, and cannot have a genuine 2D MIT. However, it could be induced by another phenomenon, for example the crossing between weak and strong localization [73]. In the strong localization regime, the conductivity falls exponentially with temperature because the carriers become exponentially localized. In the weak localization regime, the metallic behaviour comes from the temperature-dependence of phonons and screened impurities scattering. The Ioffe-Regel criteria for the wave localization in disordered media could be used to study such a crossover. It stipulates that an Anderson phase crossover from weak to strong localization [73] occurs in a 2DEG when $k_F l_e \simeq 1$. Here, $k_F = \sqrt{2\pi n_{2D}}$ is the wavevector at the Fermi energy, n_{2D} is the electron concentration, $l_e = \hbar k_F \sigma / n_{2D} e^2$ is the mean free path of the electrons and e is the electron charge. In two dimensions, neglecting screening, the Ioffe-Regel criteria gives a conductivity σ_c at the crossover independent of the charge concentration:

$$\sigma_{c,IR} = \frac{g_s g_v e^2}{2 h}, \quad (3.1)$$

where g_s and g_v are the spin and valley degeneracies respectively. For MoS_2 , $g_s = 2$ and $g_v = 2$, thus $\sigma_{c,IR} = 2e^2/h \simeq 80 \mu\text{S}$.

As the system is confined in two dimensions, Coulomb interactions between electrons become important. To tell if our system have important electron-electron interactions we look at the parameter r_s , which is the ratio between potential (Coulomb, E_C) and kinetic

(Fermi, E_F) energies:

$$r_s = \frac{E_C}{E_F} = \frac{g_v}{a_B^* \sqrt{\pi n_{2D}}} = m^* e^2 g_v / 4\pi \epsilon_r \epsilon_0 \hbar^2 \sqrt{\pi n_{2D}}, \quad (3.2)$$

where $a_B^* = (4\pi \epsilon_r \epsilon_0) / (m^* e^2)$ is the effective Bohr radius, $m^* = 0.45$ is the effective electron mass for monolayer MoS₂ [134, 135], and ϵ_r is the relative dielectric constant of the system, which we evaluate by the Keldysh formula [136]:

$$\epsilon_r = (\epsilon_r(\text{SiO}_2) + \epsilon_r(\text{air})) / 2 + dq(\epsilon_r(\text{MoS}_2) - 1) / 2, \quad (3.3)$$

where d is the MoS₂ thickness, and q is the in-plane reciprocal lattice vector of the screening particles. In the insulator regime, all electrons are localized and the last term can be safely neglected, thus, $\epsilon_r = (3.9 + 1) / 2 \simeq 2.5$.

The carrier density at any V_g can be obtained using the capacitive model: $n_{2D} = C_g(V_g - V_{Th}) / e$, where e is the electron charge, $C_g = 1.04 \times 10^{-8} \text{ F/cm}^{-2}$ is the geometric capacitance, and V_{Th} is the threshold voltage, above which conduction starts to take place through the conduction band. Following [125], V_{Th} is extracted by finding the intercept with the V_g axis of the linear extrapolation of the $\sigma - V_g$ curves at high V_g , as illustrated in Fig. 3.4a. At $T = 20 \text{ K}$ we get $V_{Th} \simeq 18 \text{ V}$ and $V_{Th} \simeq 87 \text{ V}$ for device J339 and J338 respectively. For J338, V_{Th} is probably underestimated because the conductivity curves are not perfectly linear, even at the highest V_g . It is worth mentioning that V_{Th} should be extracted at the lowest temperature possible in order to precisely locate the bottom of the conduction band. When T is increased, in-gap states contribute to the conductance through hopping and thermal activation, and artificially decrease the threshold voltage, see Fig. 3.4b. The change of V_{Th} occurs because of trapping/detrapping electrons from the impurities or disorder [137]. Disorder states are occupied or unoccupied depending if the FL is above or below their energy. Decreasing temperature traps electrons since they no longer have the thermal energy to be activated and participate in the conduction. Hence, electron trapping results in a positive shift of V_{Th} with decreasing temperature.

As the crossover voltage takes place at $V_c - V_{Th} \simeq 27 \text{ V}$ for devices J339 and J338, the crossover charge density is $n_c \simeq 27 \times C_g / e \simeq 1.7 \times 10^{12} \text{ cm}^{-2}$ for both devices. Using Eq. 3.2, with the obtained n_c , ones get $r_s \simeq 20$. Even if we use the value $\epsilon_r = 7.3$ calculated for monolayer MoS₂ [138], we still get $r_s \simeq 8$. In both cases, such a high interaction parameter ($r_s \gg 1$) points toward systems where electron-electron interactions cannot be neglected to describe transport mechanisms [5, 75]. Thus, the MIT might be a real transition coming

from $e - e$ interactions. With this value of n_c , we can estimate the mean free path at the crossover: $l_c = \hbar\sqrt{2\pi}/\sqrt{n_c e^2} \simeq 3$ nm. This value is close to the average defect distance in device J339 deduced from the Raman analysis presented in Section 2.4.1. It is also similar to the substrate-induced doping inhomogeneity estimated from the width of the hysteresis at high temperature, see Section 2.4.7.

Before studying the transition itself, we will look into more details at the models describing these insulating and metallic regimes.

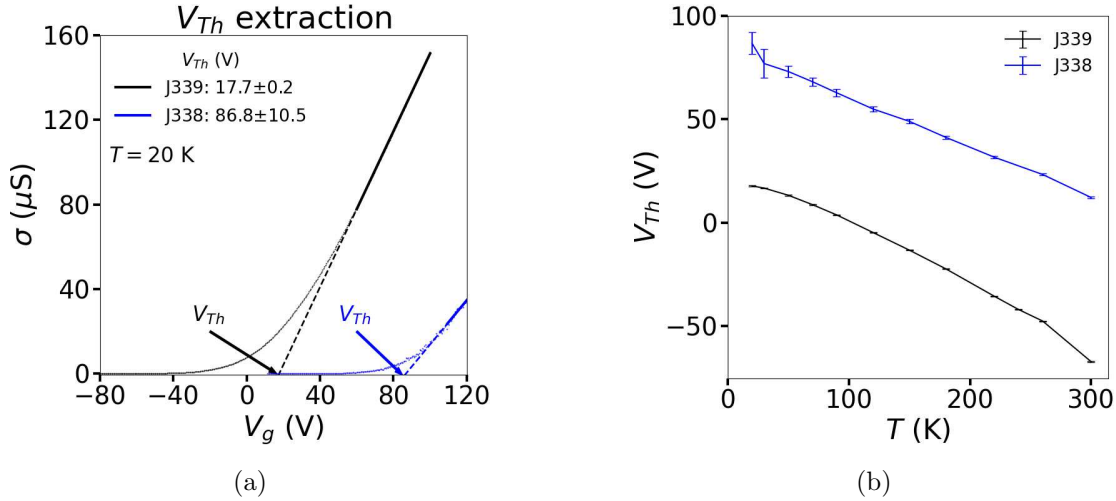


Figure 3.4: Threshold voltage (V_{Th}) of devices J339 (black color) and J338 (blue color). (a) V_{Th} extraction at $T = 20$ K. (b) V_{Th} as a function of temperature.

3.3 Transport mechanisms in the insulating regime

In the insulating regime, the carrier transport on MoS_2 can take place *via* thermal activation at relatively high temperatures and *via* variable-range hopping (VRH) at low but finite temperatures [4, 139]. Whichever the transport mechanism, it can be modelled by Eq. 3.4

$$\sigma = C_p \exp \left[- \left(\frac{T_p}{T} \right)^{\frac{1}{p}} \right], \quad (3.4)$$

where C_p is a constant of proportionality and T_p is the characteristic temperature. The exponent p depends on the transport regime: $p = 1$ when the transport is dominated by thermal activation, $p = d + 1$ for Mott VRH (d is the dimension of the system, $d = 2$ in our case) and $p = 2$ for Efros-Shklovskii (ES) VRH. Those transport mechanism were presented in Section 1.3, and will be discussed in the following.

3.3.1 Thermally activated transport

The Arrhenius plot ($p = 1$) of conductivity at different gate voltages is shown in Fig. 3.5 for devices J339 and J338. The fit is performed on the temperature range 220–150 K and 300–220 K for J339 and J338 respectively. Unfortunately, for both samples, we could fit only three temperature points. The higher the gate voltage, the closer is the Fermi level (FL) to the bottom of the conduction band E_c , and the lower is the temperature needed to thermally activate carriers into the extended states. As a result, the activation energy E_a should decrease to zero when approaching E_c .

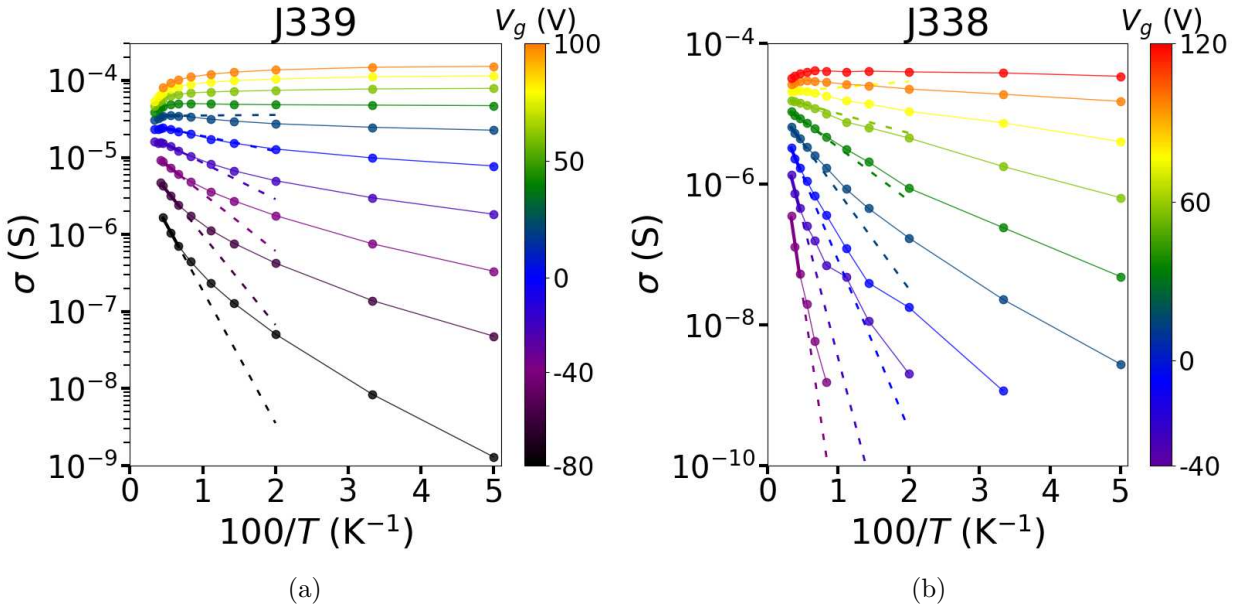


Figure 3.5: (a) and (b) Arrhenius plot of conductivity for J339 and J338 respectively. The data is shown by dots joined by thin solid lines, and the fitting results by thermally activated model are shown by solid thick lines. The dashed lines are extrapolations of the fit to show the deviation at lower temperatures.

Assuming that E_a is the energy difference between E_F and E_c , we get the relation (valid at $T = 0$ but commonly used at $T \neq 0$) [139, 140]:

$$-\frac{dE_a}{dV_g} = \frac{dE_F}{dV_g} = \frac{eC_g}{C_g + C_q}, \quad (3.5)$$

where $C_q = e^2 \text{DoS}(E_F)$ is the quantum capacitance and $\text{DoS}(E)$ is the density of states at the energy E . From the Arrhenius fit, one gets $E_a(V_g)$, which in turns allows us to reconstruct the DoS with the help of Eq. 3.5. In Fig. 3.6 is shown the extracted E_a from the Arrhenius fit, and the computed DoS from Eq. 3.5. The activation energy depends exponentially on V_g for negative values of V_g (see Fig. 3.6a), and $E_a \rightarrow 0$ when $V_g \rightarrow V_{Th}$, reinforcing the

idea that this point indeed correspond to E_c . We assume that $E_a = E_c - E_F$, and that the increasing of gate voltage moves E_F closer to E_c , eventually vanishing E_a .

We find that $\text{DoS}(V_g = V_{Th}) \sim 3 \times 10^{14} \text{ eV}^{-1}\text{cm}^{-2}$ (shown by the dashed lines in Fig. 3.6b), which is the expected DoS value for pristine or ideal MoS_2 with a parabolic band and an effective mass $m^* = 0.45m_0$. This result further confirms that, above $T = 100 \text{ K}$, the temperature dependence of the conductivity indeed corresponds to the thermal activation from localized states to the bottom of the conduction band.

Our range of gate voltages for device J339 was not enough to look deep below the bottom of conduction band E_c , reaching a maximum of 30 meV below E_c . However, the situation is different for device J338, where E_a goes up to 240 meV. We notice that in the range -80 – -60 meV the DoS is not properly computed because of a small bump on the activation energy for J338 (the DoS extraction involves numerical differentiation, a bump introduces diverging points). We also notice that the DoS does not fall quickly but instead seems to reach a plateau.

One of the main results of this analysis is that below E_c , the DoS decreases exponentially on an energy scale $s \sim 25 \text{ meV}$: $\text{DoS}(E - E_c) = \text{DoS}(E = E_c) \times \exp[(E - E_c)/s] + \text{DoS}_0$, where $\text{DoS}_0 \simeq 10^{13} \text{ eV}^{-1}\text{cm}^{-2}$ is an additional constant contribution. This exponential decay, together with the constant term, are indicated in Fig. 3.6b by a red solid line. It is consistent with spatial doping fluctuations encountered in 2D materials on SiO_2 [2]. This residual DoS_0 is in the same order of magnitude than the density of defects found by Raman analysis (see Section 2.4.1). Moreover, in Section 2.4.7, we attributed the hysteresis observed at $T > 350 \text{ K}$ to traps in SiO_2 . The energy scale $s \sim 25 \text{ meV}$ is roughly quantitatively consistent with this explanation. Indeed, $\text{DoS}(V_g = V_{Th}) \times s \simeq 7.5 \times 10^{12} \text{ cm}^{-2}$, is in good agreement with the residual DoS_0 found.

3.3.2 Variable Range Hopping

At lower temperature, there is a departure from the thermal activation model, as seen in Fig. 3.5, where the data can no longer be fitted by straight lines. Usually, in disordered semiconductors, $\sigma(T)$ can be very well modeled in terms of variable range hopping (VRH), which have two expressions: $p = 2$ or $p = 3$ in Eq. 3.4 [4, 5, 132, 139]. As detailed in Section 1.3.6, the value of p depends on the exact form of the VRH mechanism. When electron-electron interactions can be neglected, the exponent is given by the Mott's law and $p = 3$ in

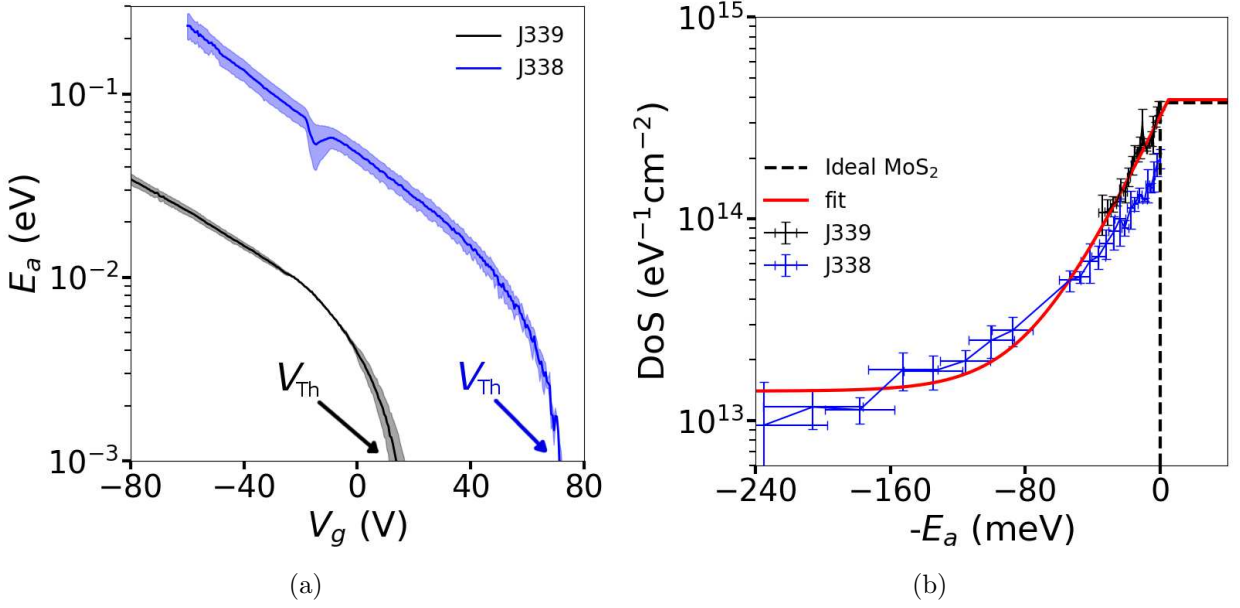


Figure 3.6: (a) Extracted activation energy as a function of gate voltage. The bottom of the conduction band is reached at $V_g = V_{Th}$, where the conduction band starts to be populated and there are not more thermally activated electrons. (b) Computed density of states (DoS) as a function of activation energy. The DoS reaches the expected value for pristine or ideal MoS₂ at the bottom of the conduction band.

two dimensions. However, when screening is poor, Coulomb interaction must be included. This corresponds to the Efros-Schklovskii (ES) VRH regime and $p = 2$ in any dimensions.

Previous studies in semiconductors unveiled two possible distinct behaviors for the prefactor C_p : a constant prefactor $C_p = e^2/h$, and a temperature-dependent prefactor $C_p = AT^{-m}$. For monolayer graphene, a temperature-dependent prefactor has been reported [141]. For GaAs/AlGaAs heterostructures, both cases have been reported: a temperature dependent factor, with $m = 1$ in the quantum Hall regime [142] or $m = 0.8$ with or without magnetic field [143], and a constant prefactor with the value e^2/h [144, 145]. This remarkable universal prefactor e^2/h has also been observed in Si metal-oxide semiconductor field-effect transistors [146], and in insulating Si:B [147]. In these experiments, the temperature invariance of the prefactor implied that the hopping in these systems is not mediated by phonons, as originally assumed in the VRH model [148, 149]. The possibility of variable-range hopping involving electron-electron interactions, instead of the usual electron-phonon mechanism, has been considered theoretically by a number of authors [150–153].

Interestingly, the importance of the prefactor C_p and its temperature dependence have not been studied in monolayer MoS₂. In most experimental studies of MoS₂ thin films, a T -independent prefactor has been used [4–6, 139], while in some others, $C_p \propto T^{-0.8}$ [2, 3,

[154] has been used to fit the conductivity, without further justification.

Furthermore, Mott [2–4] and ES [5, 6] expressions for VRH are both commonly used in monolayer MoS_2 , without a clear distinction between them. Xue *et al.* [139] was able to discriminate between the two VRH expressions by looking at the change of magnetoresistance with magnetic field. In some other materials, a transition from ES to Mott has been reported. For AlGaAs/GaAs heterostructures, this transition can be magnetic field dependent [143], or doping and temperature-dependent [144]. For graphene in the quantum hall regime, the transition occurs depending on the filling factor [141]. This motivates us to have a closer look into the different VRH mechanisms.

To identify which VRH mechanism is at play, we introduce the parameter $W = T^{-1} \partial \ln \rho(T) / \partial T^{-1}$. If Eq. 3.4 is satisfied, and if the temperature dependence of C_p is weak or non-existent, one finds:

$$\ln W = -\frac{1}{p} \ln T + \text{const.}, \quad (3.6)$$

and the slope of W on a double logarithmic scale ($\ln(W)$ vs. $\ln(T)$) gives directly the exponent $1/p$ of Eq. 3.4. Fig. 3.7 shows the plot of W vs T in a log-log scale at different gate voltages, and three dashed lines show the slope for the three different transport regimes. For device J339, shown in Fig. 3.7a, the value of p is very close to 2 for gate voltages less than -20 V and temperatures less than 100 K. By contrast, $p = 3$ would give a too moderate slope, and the steeper slope for $p = 1$ indeed starts to appear at $T > 100$ K. In the case of device J338, shown in Fig. 3.7b, it seems not to follow any regime to the letter, with p between 2 and 1. A fit on the W vs T plots has been performed in order to extract p as a function of gate voltage, the results are shown in Fig. 3.8. As mentioned before, the value of p for device J339 is close to 2, while $p \sim 1.3$ in the case of device J338.

As the index $p = 2$ has been determined for J339 device, we can plot the logarithm of the conductivity in units of e^2/h as a function of $T^{-1/2}$, as shown in Fig. 3.9. The experimental data are very well fitted by straight lines over large domains of gate voltages and temperatures. J338 device has been also fitted with $p = 2$ for comparison. The fit is extrapolated to $T^{-1} = 0$, as shown by the dashed lines. In the case of J339 device, the extrapolated fit almost converges at $T^{-1} = 0$, giving a value of $C_p = 0.8 \pm 0.2 e^2/h$. In the case of J338 device, it gives $C_p = 3.3 \pm 1.5 e^2/h$. The discrepancy of the C_p value between J339 and J338 devices comes from the fact that the ES VRH model does not describe well the transport mechanism on J338, as shown by the extracted p value, and the poor ES fit.

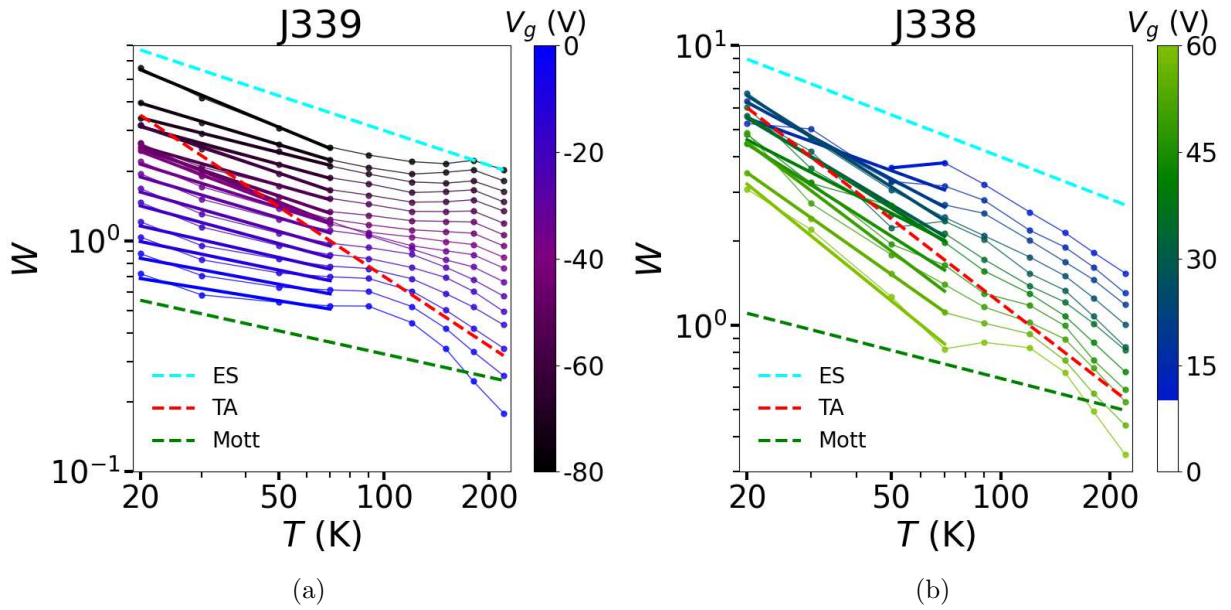


Figure 3.7: Parameter $W = T^{-1}\partial \ln \rho(T)/\partial T^{-1}$ on a double logarithmic plot. The thick solid lines are the linear fits, and the dashed lines correspond to different transport mechanisms, each with its corresponding p value (Eq. 3.4). Thermally activated transport (TA) with $p = 1$, Efros-Shklovskii (ES) VRH with $p = 2$, and Mott VRH with $p = 3$. (a) and (b) J339 and J338 respectively.

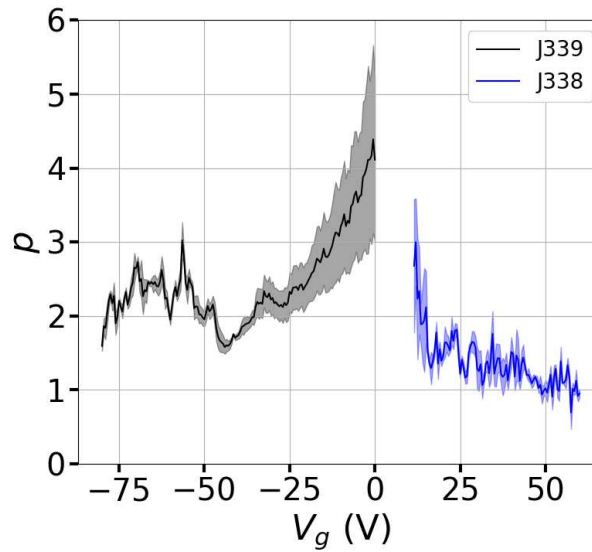


Figure 3.8: Extracted p from the linear fit performed on the W plots shown in Fig. 3.7.

Nonetheless, from the fits we extracted the temperature coefficient T_2 for both devices.

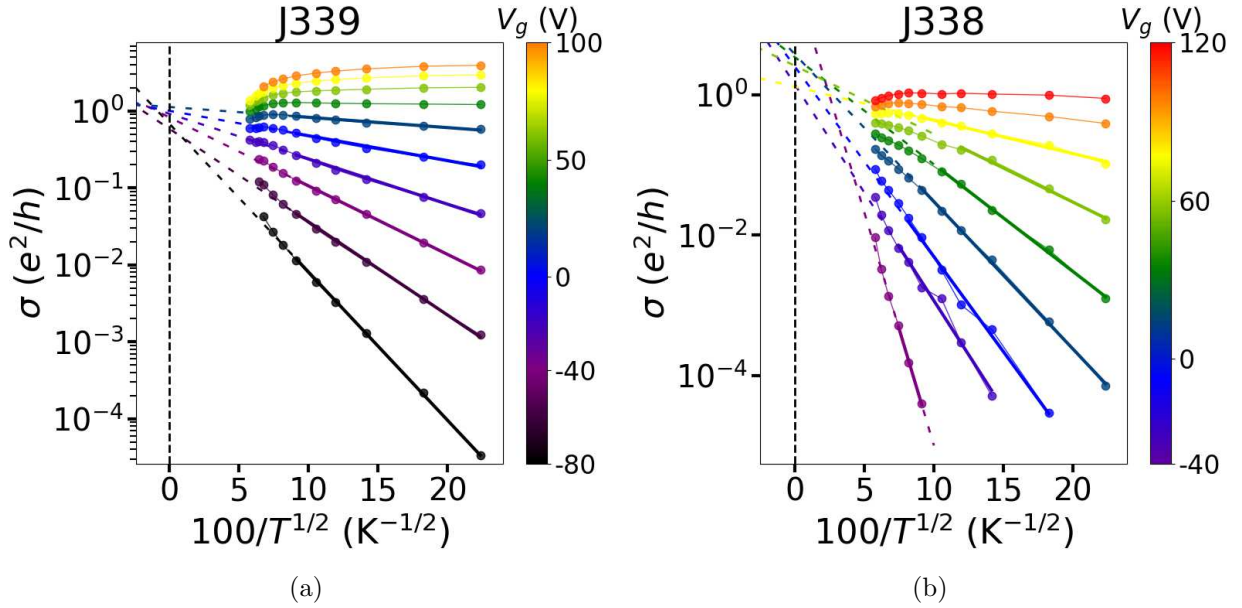


Figure 3.9: Temperature dependence of the conductivity versus $T^{-1/2}$ (ES plot). Only a reduced data set is indicated for clarity, represented by points joined with thin solid lines. The thick lines are the fitting results using the ES model. (a) Device J339. The data below $T = 120$ K and $V_g = 20$ V have been fitted. (b) Device J338. The fitting temperature region varies depending on the gate voltage. The fit is extrapolated to $T^{-1} = 0$ to extract the C_p coefficient.

The universality of the prefactor C_p is better seen in Fig. 3.10, where the conductivity in units of e^2/h is plotted as a function of $(T/T_2)^{-1/2}$. For device J339, all the data collapse onto the same straight line. The extrapolation to $T^{-1} = 0$ of the the linear fit confirms that the value of the prefactor is very close to e^2/h . The small residual discrepancy can be easily explained, *e.g.* by a slightly incorrect geometric factor w/l when computing the conductivity with the inverse of Eq. 2.1. However, for device J338, the data is highly scattered, and the extrapolation gives a value of $C_p = 3.2 \pm 1.9 e^2/h$.

For ES VRH, the localization length is related to the characteristic temperature T_2 by:

$$\xi = C_{ES} \frac{e^2}{4\pi\epsilon_r\epsilon_0 T_2}, \quad (3.7)$$

where the prefactor $C_{ES} \simeq 6.2$ in two dimensions [85] (see Section 1.3.6). Figure 3.11 shows the T_2 temperature and localization length as extracted from Eq. 3.7, as a function of gate voltage. One can see that $T_2 \rightarrow 0$ when approaching E_c , while ξ increases to large values signaling delocalization. Device J339 has very large values of ξ at V_g values close to V_{Th} . If ϵ_r is constant as defined by the Keldysh formula shown in Eq. 3.3 ($\epsilon_r \sim 2.5$), then $\xi \sim 1.7 \mu\text{m}$

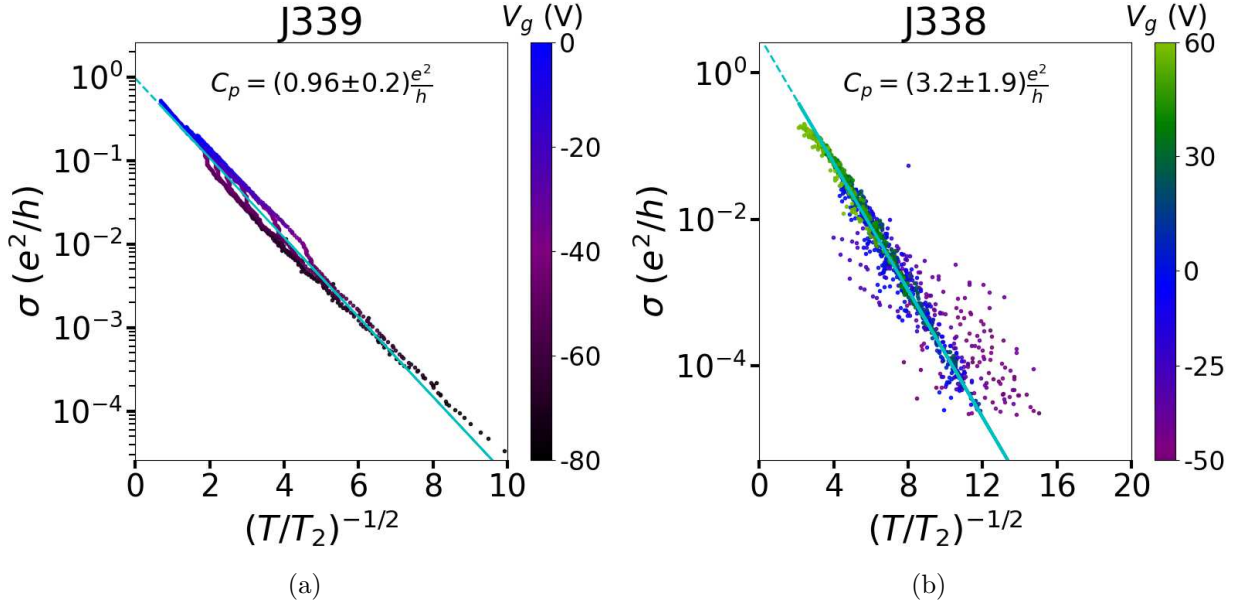


Figure 3.10: Dimensionless conductivity σ as a function of $(T/T_2)^{-1/2}$. The linear fit is indicated by a cyan line, which is extrapolated to $T^{-1} = 0$ and intercepted with the y -axis. This intersection gives a value close to the quantum conductance e^2/h for device J339 (a), while the data is highly scattered for device J338 (b).

at $V_g = 10$ V, and $\xi \sim 4.4$ μm at $V_g = 20$ V. These ξ values are unrealistically high, as they become comparable to the size of the device. This discrepancy was already experimentally observed by Mason *et al.* [146] and Khondaker *et al.* [145]. It was suggested that the C_{ES} quoted above ($C_{ES} = 6.2$) is too large by a factor of 10, as numerical calculations of a Coulomb glass with multi-electron hopping gave a much lower value $C_{ES} \simeq 0.62$ [155]. Keuls *et al.* also suggested a lower value of $C_{ES} = 0.64$ by assuming that their smallest measured values of ξ must be greater than the 2D Bohr radius of 5 nm [143].

As mentioned before, the two VRH models are commonly used to fit the conductivity data of MoS₂. Just for comparison, we fitted our conductivity data with the Mott model ($p = 3$ in Eq. 3.4) as well. The fitting results are shown in Fig. 3.12. As we can see from these plots, the Mott model also fits very well the data, even over a wider range of temperatures than the ES model. For device J338, similar as with the ES model, the fit is poor, meaning that the transport mechanism for this device is not described by either model. Nonetheless, the characteristic temperature T_3 and the corresponding localization length ξ , as extracted from Eq. 3.8, are shown in Fig. 3.13.

$$\xi = \left(\frac{13.8}{\text{DoS}(E_F)k_B T_3} \right)^{1/2} \quad (3.8)$$

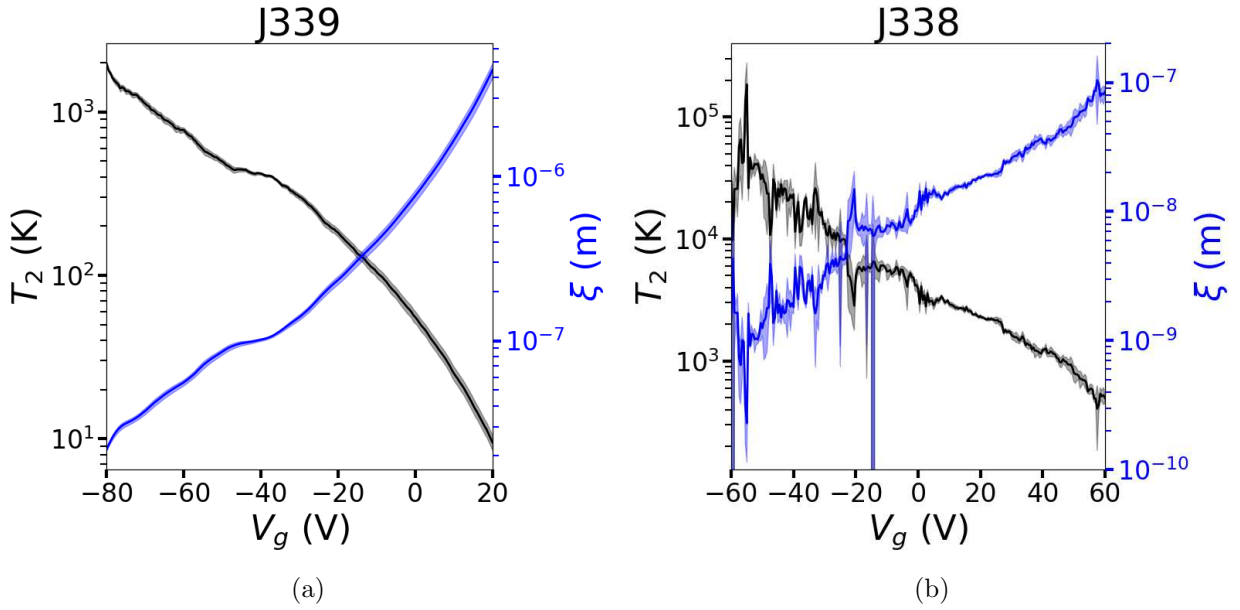


Figure 3.11: Temperature T_2 (black color) extracted from the ES VRH fit and its corresponding localization length (blue color) as computed using Eq. 3.7, for devices J339 (a) and J338 (b).

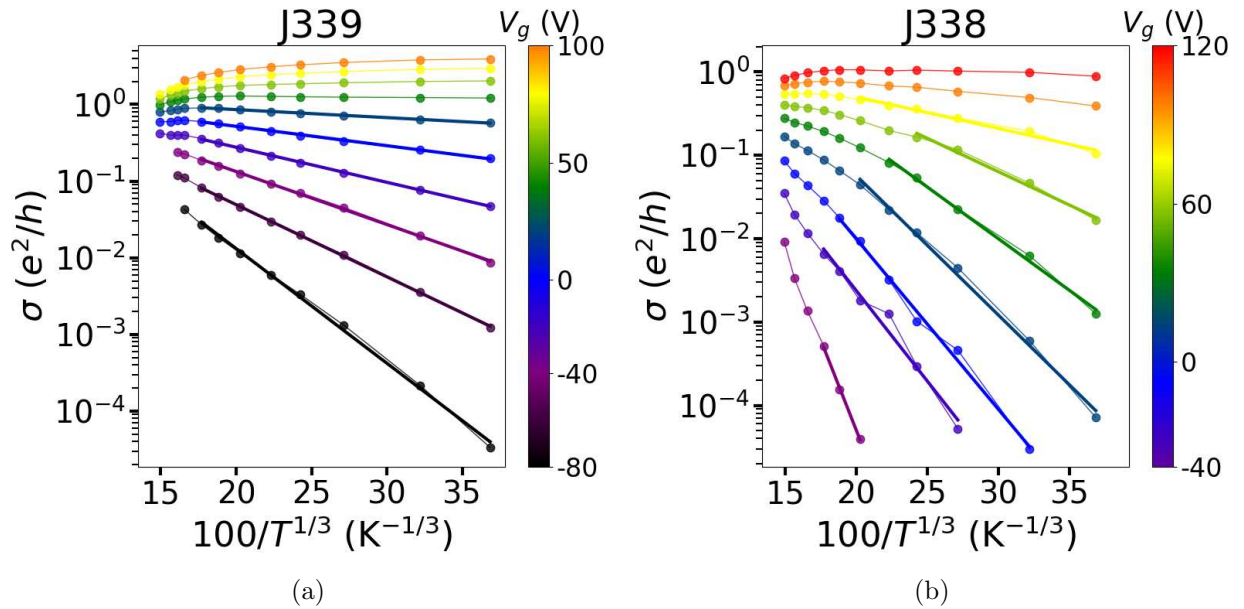


Figure 3.12: Temperature dependence of the conductivity versus $T^{-1/3}$ (Mott plot). Only a reduced data set is indicated for clarity, represented by points joined with thin solid lines. The thick lines are the fitting results using the Mott model. (a) Device J339. The data below $T = 180$ K and $V_g = 20$ V have been fitted. (b) Device J338. The fitting temperature region varies depending on the gate voltage.

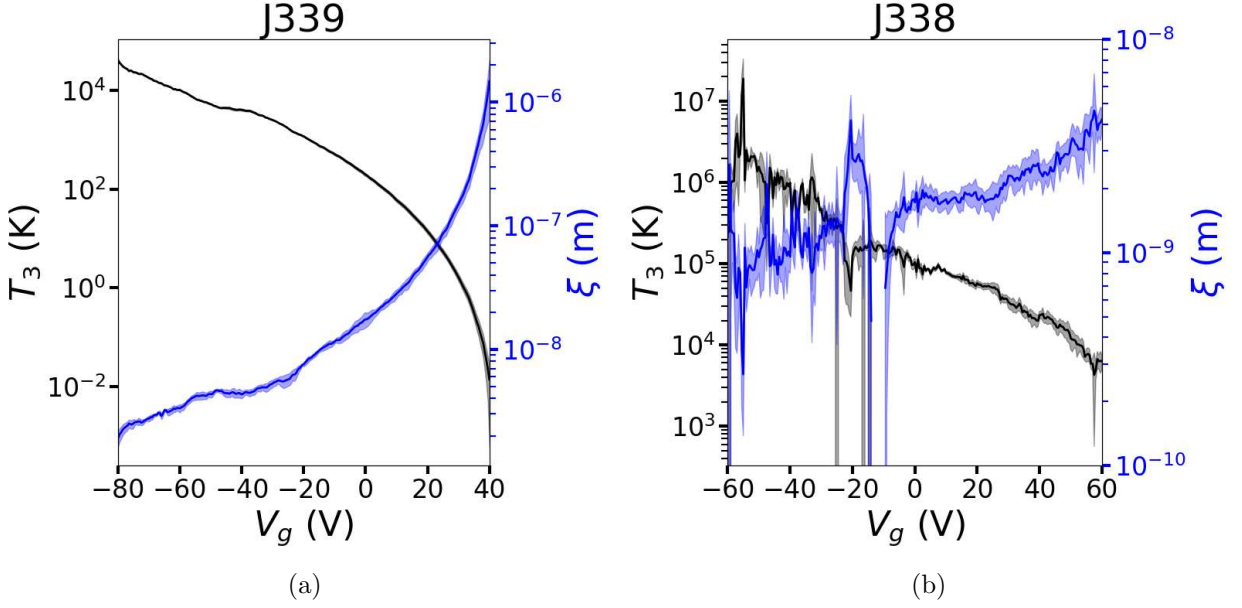


Figure 3.13: Temperature T_3 (black color) extracted from the Mott VRH fit and its corresponding localization length (blue color) as computed using Eq. 3.8, for devices J339 (a) and J338 (b).

The fitting results from the ES (Fig. 3.9) and Mott (Fig. 3.12) models show that just the quality of the fitting is not sufficient to discriminate which VRH transport is at play. Therefore, the VRH type must be crosschecked by other means, *e.g.*, the parameter W , which was shown in Fig. 3.7. We introduce another way of discriminating between those models, by looking at the energy gap $\Delta = \frac{\pi}{2} \frac{e^4}{\kappa^2} \text{DoS}$ in the ES model (Eq. 1.41), and compare it to the average spacing between energies $\epsilon = \frac{1}{3} k_B (T_3 T^2)^{1/3}$ in the Mott model (Eq. 1.36). As the ES model was deduced assuming $\Delta \gg \epsilon$, while the Mott model was deduced assuming $\Delta \ll \epsilon$, we then look at the dimensionless energy ratio Δ/ϵ . The results are shown in Fig. 3.14. $\Delta/\epsilon \gg 1$ means that the electronic transport mechanism is governed by the ES model, whereas $\Delta/\epsilon \ll 1$ means it is governed by the Mott model. The result shows that the electronic transport for device J339 is effectively dominated by ES VRH, whereas for device J338 it is neither Mott nor ES. Those VRH models were obtained under the assumption of the gap Δ being much greater or much smaller than the Mott average energy spacing ϵ , and device J338 does not meet any of those assumptions, except for $V_g > 60$ V where $\Delta/\epsilon > 10$.

It is evident that neither Mott nor ES model fits well the conductivity data of J338, and since the ES/Mott ratio gives values around 1, it means that the assumptions made to derive Mott and ES models are not valid. A revision on the derivation of the VRH models has been done by the doctorant on Appendix A, where no assumptions on the energy Δ and ϵ are made, and both terms are included in the transport equation. The result is an intermediate

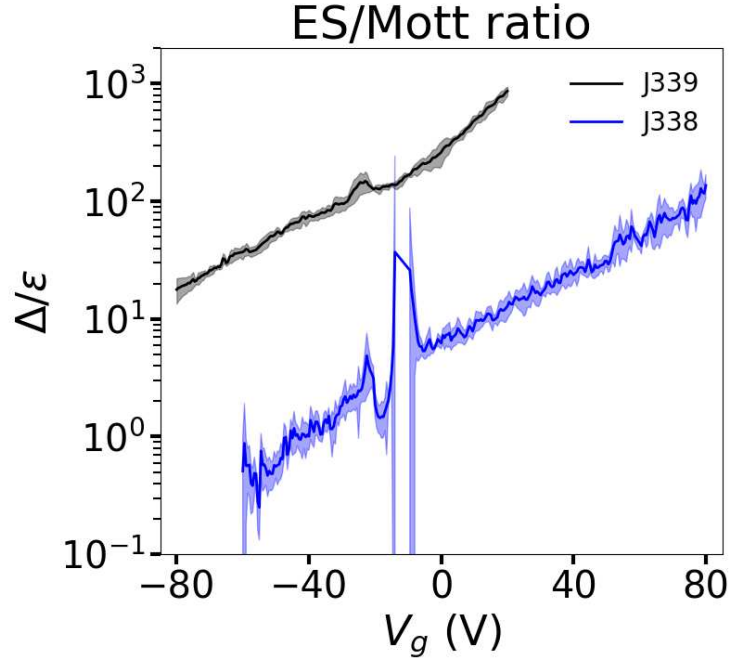


Figure 3.14: Dimensionless energy ratio for device J339 (black color) and J338 (blue color) at $T = 180$ K.

VRH regime with a p value of $3/2$. This new model fits very well the conductivity data of J338, and the corresponding characteristic temperature and localization length are extracted and discussed.

3.4 Effective mobility, effective doping and metallic regime

In this Section, a discussion on the mobility, doping and electronic transport in the conduction band is given. Since we could not perform Hall measurements to extract those parameters, we resort to numerical derivation of the conductivity.

3.4.1 FET & effective mobilities

In 2012, Kaasbjerg *et al.* [156] showed that, from first principles, the phonon-limited mobility in pristine monolayer MoS_2 is weakly dependent on the carrier density, and depends on temperature as $\mu \sim T^{-\gamma}$ for $T > 100$ K, where the damping factor $\gamma \sim 1.7$. They also predicted a theoretical value at room temperature of $\sim 410 \text{ cm}^2\text{V}^{-1}\text{s}^{-1}$. Those studies were performed taking into account only electron-phonon interactions, without considering any other type of electron scattering. A few years later, in 2019, Kaasbjerg *et al.* [9] addressed the problem again but this time on disordered monolayer MoS_2 , with impurities such as

sulphur vacancies acting as both, short-range and long-range scatterers. Their results are quite different from their first work, with the Coulomb scattering being the main scattering mechanism. The dominance of Coulomb disorder scattering gives rise to a strong temperature and density dependence of the mobility, which arise from the temperature and density dependent screening of the Coulomb potential [157]. Kaasbjerg *et al.* also showed that the damping factor does not have a fixed value but depends on temperature and carrier density, as commonly found in experiments [3, 10–12, 74, 75]. Thus, having multiple scattering mechanisms modifies the damping factor. It has been suggested that a change in the dielectric environment by using high- κ dielectrics on top of the samples can improve the mobility by attenuating the Coulomb scattering on charged impurities [158], and it has been successfully implemented in the literature [56, 75].

From the conductivity data presented in Fig. 3.3, we extracted the field-effect mobility (μ_{FET}) using the expression $\mu_{\text{FET}} = [\Delta\sigma/\Delta V_g] \times [1/C]$, where the linear fit $[\Delta\sigma/\Delta V_g]$ is performed in the linear region of the σ vs V_g curves at high gate voltage. Figure 3.15 shows the temperature dependence of the extracted FET mobility in a log-log scale, from where we observe a monotonous increase of the mobility as the temperature is decreased, with a saturation at low temperatures. The fitting on the conductivity curves for device J338 is not quite accurate since, as mentioned before, the transfer curves at low temperature are not linear, and because of this we might be underestimating the mobility. The extracted FET mobility, shown in Fig. 3.15, hardly shows linearity against temperature in a log-log plot. Nonetheless, a linear fit was performed on the high temperature region and a value for the damping factor was extracted for each device. We find large differences between devices, with J338 having the lowest value of damping factor ($\gamma = 1.1$) while J12B having the highest ($\gamma = 2.4$).

In order to take a closer look at the damping factor, we introduce the “effective mobility” (μ_{eff}) defined as $\mu_{\text{eff}} = d\sigma/CdV_g$, and numerically computed over the entire range of gate voltages and temperatures. The gate-dependent μ_{eff} at different temperatures is shown in Fig. 3.16. It shows low values at large negative gate voltages (low doping) and increases as the electron density increases, reaching a plateau at high gate voltages in the case of J339 (see Fig. 3.16a). We can distinguish three different transport regimes for device J339: gate voltages below -40 V, μ_{eff} slowly increases with doping, and the transport is dominated by variable range hopping; at gate voltages between -40 V and 40 V, μ_{eff} increases quickly with

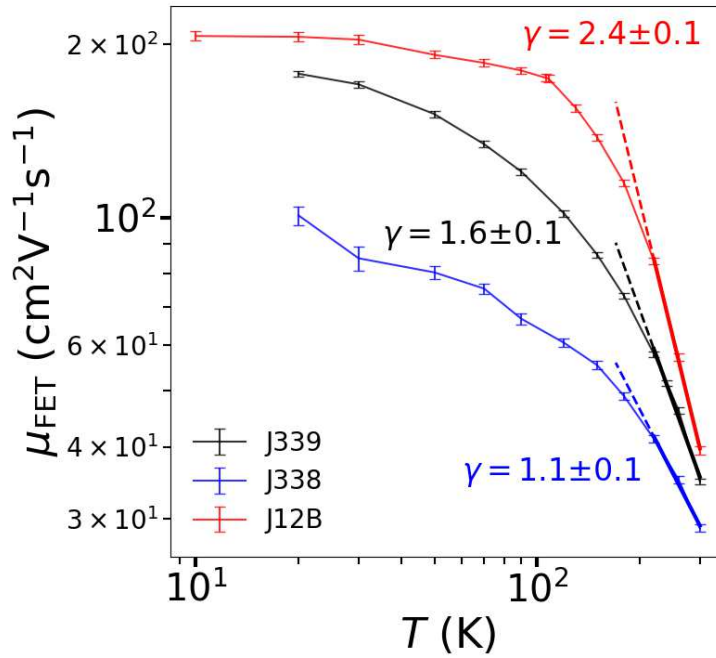


Figure 3.15: Extracted FET mobility (μ_{FET}) from the linear fit of conductivity at high gate voltage. The high temperature region was fitted and the damping factor was then extracted.

gate voltage, indicating screening of charged impurities; and for high positive gate voltages, the transport is metallic and reveals an upper limit of mobility, becoming almost doping independent. This saturation of mobility with temperature as well as with charge carrier density is a signature of short-range scattering limiting the device performance [10, 12]. The mobility of device J338 (see Fig. 3.16b) does not reach a saturation, indicating poor screening due to low (high) doping (density of defects), showing only the VRH and screening regions. In the case of device J112B (see Fig. 3.16c), only the metallic region is observed, with μ_{eff} being almost doping-independent.

The damping factor γ is then extracted from the effective mobility and is shown in Fig. 3.16d for device J339. It decreases over the entire range of temperature (in agreement with Kaasbjerg *et al.* [9]), and there is little change with V_g for values above the critical voltage V_c .

The low mobilities usually found in the literature are because those devices have low electron density, falling in the VRH region. The mobility should then be obtained once the metallic regime is reached, where the electrons are conducting because of the conduction band, and not because the impurity band.

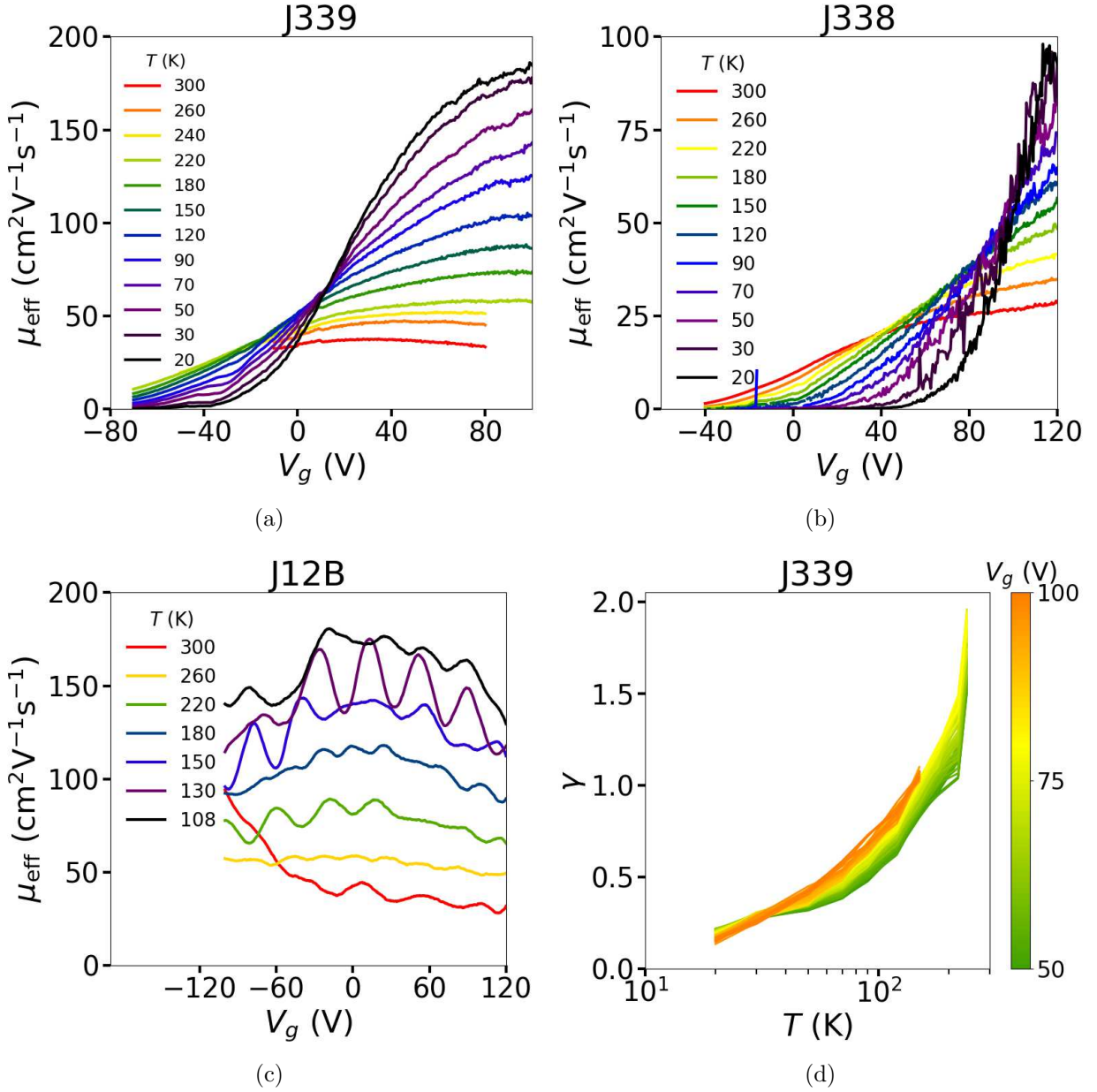


Figure 3.16: (a), (b) and (c) Gate dependent of effective mobility for devices J339, J338 and J12B respectively. For device J12B, the μ_{eff} is computed only above $T = 108$ K, since at lower temperatures the data is very noisy. (d) Damping factor of device J339 extracted from the effective mobility (μ_{eff}) as $\gamma = d\log\mu_{\text{eff}}/d\log T$, for gate voltages above V_c (in the metallic regime).

3.4.2 Capacitive & effective doping

With the conductivity data and the effective mobility defined in the previous Section, we now define the effective doping as $n_{\text{eff}} = \sigma/(e\mu_{\text{eff}})$. Since we could not perform Hall measurements to extract the doping, our only options were to compute the doping using the capacitive model (n_C) and the effective doping defined before.

In the extraction of n_C , the temperature dependent threshold voltage, shown in Fig. 3.4b,

has been used. In Fig. 3.17 is shown the similarities between n_{eff} (solid lines) and n_C (dashed lines) for device J339 in the metallic regime. As can be seen in the figure, the two models gives similar doping results, with noticeable deviation at low gate voltage, close to the MIT. This deviation occurs because there is still a large part of VRH conduction at play, given the relatively high thermal broadening.

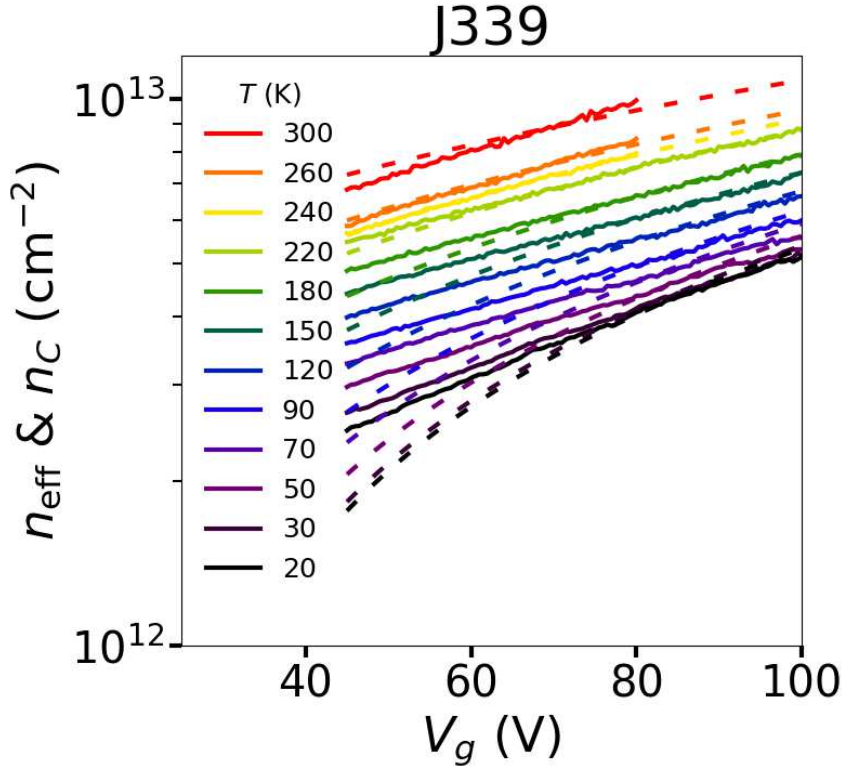


Figure 3.17: Electron densities extracted from two different ways for device J339. Solid lines correspond to n_{eff} while dashed lines correspond to n_C .

3.4.3 Metallic conduction

In the following, we focus on the metallic part of the conductivity data, at temperatures above 90 K and gate voltages above V_c . There, VRH hopping is not the main electronic transport mechanism, and it is possible to show that the data are reasonably well fitted by the usual single-particle models, when phonon scattering and impurity scattering are considered in a single electron picture. More precisely, the theoretical conductivity is simulated by considering electron scattering with phonons and charged point defects with a full energy- and momentum-dependent Boltzmann transport equation. Electron-phonon interactions are computed *ab initio* using density functional perturbation theory, and charge screening

is included for both types of scattering. This work has been done in collaboration with Thibault Sohler at Laboratoire Charles Coulomb.

In Fig. 3.18 is shown the fit on conductivity and effective mobility. The experimental data is shown by thin solid lines with error bars, while the fit is shown by thick solid lines. The conductivity for each device is obtained at four different doping values, with the error bars showing the conductivity between a 10% error on doping.

It appears from Fig. 3.18d that the combination of these two scatterings give a fair fit of the mobility versus carrier concentration for J339 and J12B devices, except at low doping $n < 2 \times 10^{12} \text{ cm}^{-2}$. J338 is not well described by this model because it does not reach the metallic regime. These observations are consistent with the presence of a impurity DoS and thermal broadening which makes the actual band carrier concentration more poorly defined.

For a finer analysis, Fig. 3.18 shows the fitted experimental conductivities for the three devices. The individual adjustment of the defect density for each device is enough to obtain fair fits for the 3 devices, confirming the validity of this approach. The defect density is $n_D = 1.0 \times 10^{12}, 1.5 \times 10^{12}, 1.2 \times 10^{12} \text{ cm}^{-2}$ for devices J339, J338 and J12B respectively. These values cannot be directly related to the defect densities observed by Raman spectroscopy, since the Raman spectra was obtained after the electrical measurements under ambient air and may have absorbed impurities. Nevertheless, one can note that the agreement is fairly good for device J339, while the discrepancy in J12B could be explained either by a less good approximation of doping, or the uncertainties in the position in energy of the local band minimum at the Q-point, which introduces newer scattering paths at dopings above $\sim 10^{13} \text{ cm}^{-2}$.

This model of phonons and charged point defect scattering describe well the conductivity in the conduction band, at sufficiently high doping and temperatures. However, the transition from an insulator regime where VRH transport dominate, to a metallic regime where phonons and impurity scattering transport dominates, is still an open issue as we will see in the next Section.

3.5 A genuine MIT?

From these previous analysis, it still appears reasonable to investigate the existence of a possible scaling function, *i.e.*, a function that collapses all the conductivity curves

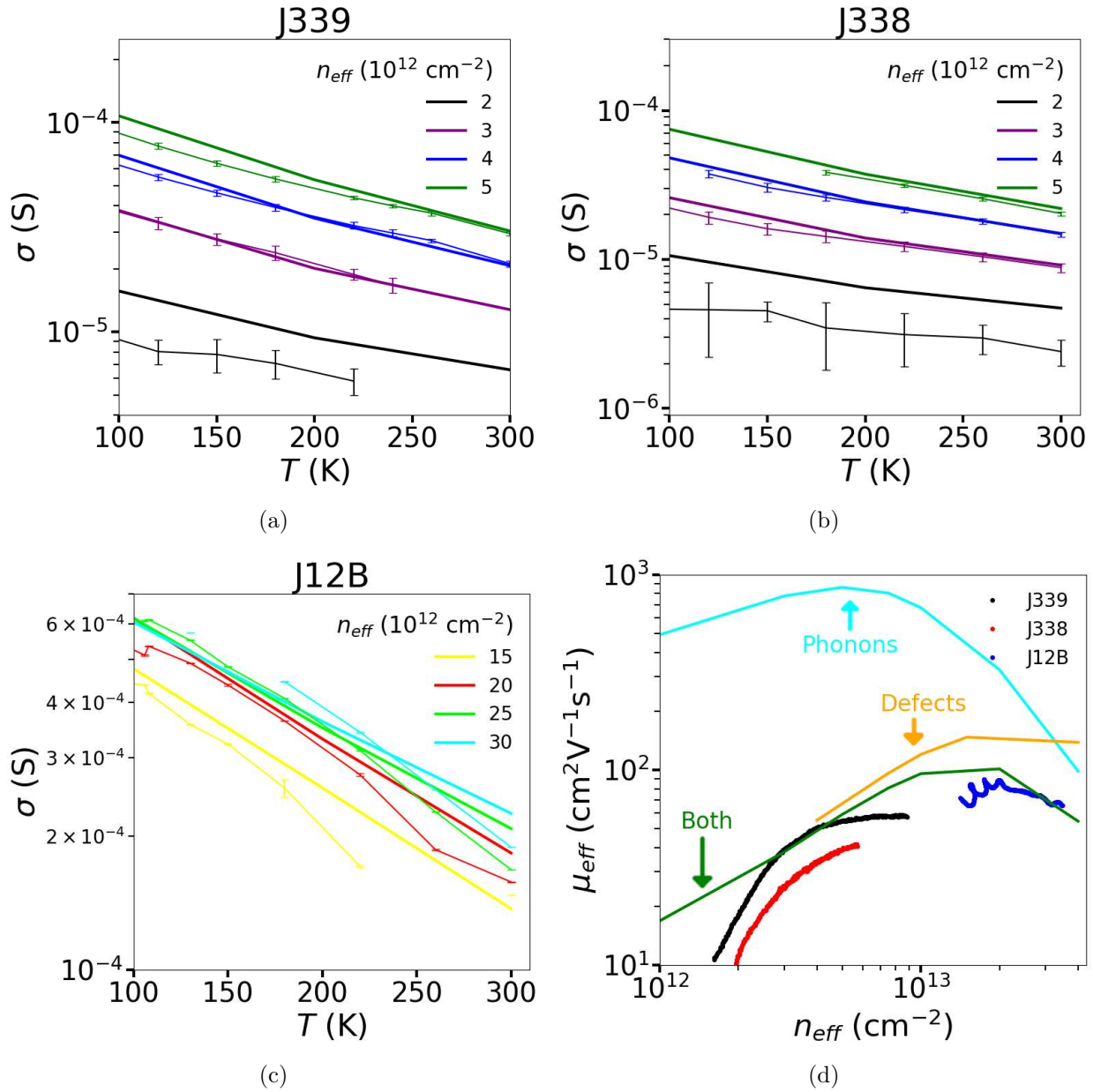


Figure 3.18: (a), (b) and (c) Conductivity versus temperature at different carrier concentrations for devices J339, J338 and J12B respectively. The experimental data are shown as colored dots and the best theoretical fits are indicated by solid lines. The best fit parameters are $n_D = 1.0 \times 10^{12}$, 1.5×10^{12} , $1.2 \times 10^{12} \text{ cm}^{-2}$ for devices J339, J338 and J12B respectively. (d) Effective mobility of the three devices, J339 (black dots), J338 (red dots), and J12B (blue dots), at $T = 220 \text{ K}$. The theoretical mobility is shown for phonon scattering only (cyan curve), impurity scattering only (orange curve), and both type of scatterings (green curve).

shown in Fig. 3.3 onto a single one. Such function is usually used to test the validity of a real quantum phase transition. This function has the form $\sigma = \sigma_c(T)f(|x - x_c(T)|t(T))$, where σ_c is the conductivity at the limit $x \rightarrow x_c$, f is the scaling function, x is the tuning parameter which in our case is the gate voltage, $t(T) = T^{-1/z\nu}$ is the scaling factor with z and ν being the dynamical and correlation length exponents respectively [159]. The critical conductivity together with the scaling factor encode the nature of the MIT transition [5, 7, 8]. Furthermore, ξ is expected to diverge close to the transition as $\xi \sim |n_{2D} - n_c|^{-\nu}$. Fig. 3.19a shows the results of the scaling on conductivity for device J339. We were able to collapse all the conductivity curves for temperatures below 90 K, where the critical voltage V_c and conductivity σ_c are independent of the temperature, into two branches: the upper and lower branches containing the conductivity data above and below the MIT respectively. The collapse has been performed using the parameter $t = T^{-1/z\nu}$ with $z\nu = 4.16$. Fig. 3.19b shows the results of the scaling on ξ for the same device, giving a value of $\nu = 2.96 \pm 0.01$. This leads to a value of the dynamical exponent of $z = 1.4$, which is supposed to be equal to 1 in the case of strongly interacting electrons [160].

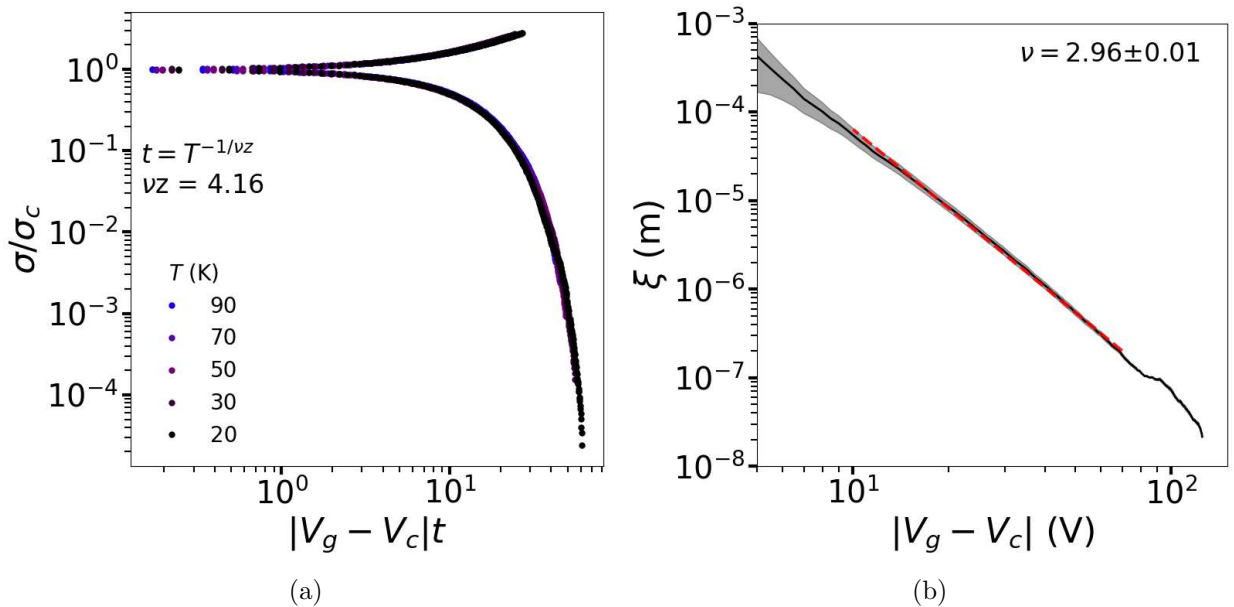


Figure 3.19: MIT of device J339. (a) Scaling on conductivity. (b) Scaling on localization length.

Although the presented scaling theory has been developed for superconductors [159], it has been applied in the literature on different sample materials, with some of them showing superconductor-insulator transitions [7, 161] and some others showing metal-insulator transitions [5, 8, 162]. Different values of the critical exponent $z\nu$ can be found, usually in the

range 0.6 – 4, with $z\nu$ values being low the more symmetric are the two scaled conductivity branches. It has been suggested that low values of the critical exponent correspond to low disordered samples [5].

While we can successfully apply the scaling theory suggesting a quantum phase transition, we can't rule out the possibility of this being a classical phonon-related phenomena. Following Das Sarma 2D screening work [157], three characteristic temperatures, namely Fermi T_F , Bloch-Grüneisen T_{BG} and Dingle T_D temperatures suffice to tell if phonons still plays a role in the observed MIT, or if the metallic temperature dependence in the conductivity arises purely from electronic effects. The Fermi temperature T_F defines the intrinsic quantum temperature scale for the 2D electrons, and when T_F is very large there cannot be any temperature dependence in the metallic conductivity at low temperatures arising from intrinsic electronic effects. The Bloch-Grüneisen temperature T_{BG} defines the characteristic temperature scale for phonon scattering effects to become important in the 2D metallic conductivity. The Dingle temperature T_D acts as a lower cutoff, suppressing the temperature dependence in conductivity for $T < T_D$. This is because the strong temperature dependence of carrier screening is cutoff for $T < T_D$ by impurity disorder effects parametrized by the Dingle temperature. Thus, we end up with the condition shown in Eq. 3.12 for intrinsic 2D electronic effects, with $T_{BG} > T_F$ guaranteeing that phonon scattering would not play a role in the 2D MIT physics, and $T_D < T$ guaranteeing that disorder is not restraining the temperature dependence of conductivity [157]. Those characteristic temperatures are shown in Eqs. 3.9, 3.10 and 3.11.

$$k_B T_F = \frac{\hbar^2 k_F^2}{2m^*} = \frac{\hbar^2}{2m^*} \left(\frac{4\pi n}{g_s g_v} \right) \quad (3.9)$$

$$k_B T_{BG} = 2\hbar k_F v_{ph} = 2\hbar v_{ph} \left(\frac{4\pi n}{g_s g_v} \right)^{1/2} \quad (3.10)$$

$$k_B T_D = \frac{\hbar}{2} \left(\frac{e}{m^* \mu} \right) \quad (3.11)$$

$$T_D < T < T_F < T_{BG} \quad (3.12)$$

T_{BG} depends on the phonon velocity v_{ph} which, considering acoustic phonons for MoS_2 [156], is equal to $v_{ph} = 6.7 \times 10^3$ m/s. As T_F and T_{BG} depend on the electron density n , we use the n obtained by the capacitive model ($n = C_g(V_g - V_{Th})/e$) for any $V_g > V_{Th}$, where $V_{Th} = 18$ V is the threshold voltage obtained at $T = 20$ K (explained in Section 3.2). In the case of T_D , the mobility used is $\mu_{\text{eff}}(T = 20 \text{ K})$, which depends on the electron density.

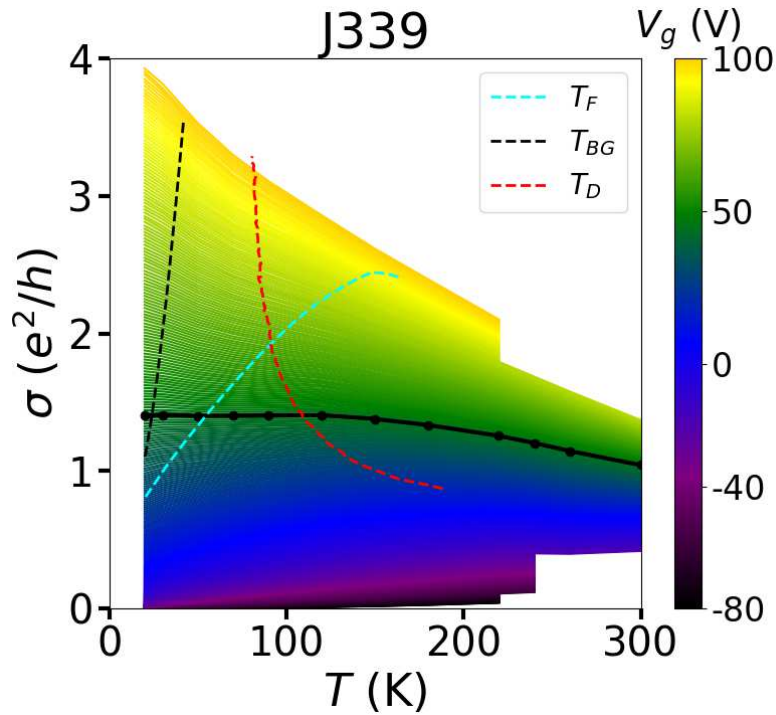


Figure 3.20: Conductivity with the three characteristic temperatures shown by colored dashed lines. The black solid line with dots is the curve used in the scaling analysis shown in Fig. 3.19a.

We end up then with the three characteristic temperatures being doping dependent that, for simplicity, is translated to a gate voltage dependence. We then interpolate the conductivity data for temperatures between (20 K, 220 K), and find the value of the interpolated $\sigma(V_g, T_s)$ for any $V_g > V_{Th}$ and T_s , where T_s is any of the characteristic temperatures. With this we were able to show, in the conductivity plot, the three characteristic temperatures, as shown in Fig. 3.20.

The Bloch-Grüneisen temperature (green dashed line) is on the order of the lowest experimental temperature at the critical point $T_{BG}(n_c) \simeq 24$ K, meaning that phonon plays a role in almost the entire temperature region. The Dingle temperature (cyan dashed line) is also high, meaning that the temperature dependence of conductivity is being suppressed by disorder. The black solid line with dots is the conductivity σ_c at the critical voltage V_c : $\sigma_c = \sigma(V_g = V_c)$. For $T \leq 90$ K, σ_c is temperature-independent and equal to $\sim 1.4e^2/h$.

The condition shown in Eq. 3.12 is not met by device J339, therefore the possibility of the MIT being a classical phonon-related phenomena cannot be ruled out. The existence of a 2D MIT should be crosschecked with additional measurements in other materials [7, 8], at temperatures lower than T_{BG} , and as a function of the source-drain electric field [132]. The

MIT can be observed intuitively by the combination of (i) the increase in mobility and (ii) positive V_{Th} shift with decreasing the temperature, as already pointed out by Nan Fang and Kosuke Nagashio [163]. The mobility increases with decreasing temperature due to suppression of phonon scattering, while the change of V_{Th} occurs because of trapping/detrapping electrons from the impurities or disorder. Thus, while we can successfully apply the scaling theory suggesting a quantum phase transition, we can't rule out the possibility of this being a classical phonon-related phenomena.

3.6 Conclusion

We have performed IVs and transfer measurements on three different devices after thermally annealing them at $T = 600$ K. The increase of doping with the annealing pushed the Fermi level deeper into the conduction band, after which it was varied with the back gate, resulting in the observation of both, the metallic and insulator regimes. The insulator regime has been studied as a function of temperature and gate voltages, showing TA and VRH transport mechanisms, with a possible existence of an intermediate VRH transport mechanism. The metallic regime has been modeled with electrons experiencing phonons and impurity scattering. The long-debated MIT phenomena has been studied in terms of a QPT, although the analysis could be performed only on a single device, with the conditions not being the optimal to be conclusive.

We were able to model the conductivity of monolayer MoS_2 in the metallic regime, as well as in the insulating regime. A small overview summarizing the transport mechanism found is shown in the Fig 3.21. The conductivity depends on temperature and electron density. At low doping and low temperature, all the data enclosed by the red box, VRH takes place. At low doping and high temperature, all the data enclosed by the green box, thermally activated transport takes place. At high doping and high temperature, all the data enclosed by the black box, electrons are delocalized and band-like conduction takes place. A quantum phase transition might be occurring at temperatures below 100 K, corresponding to all the data enclosed by the cyan color box.

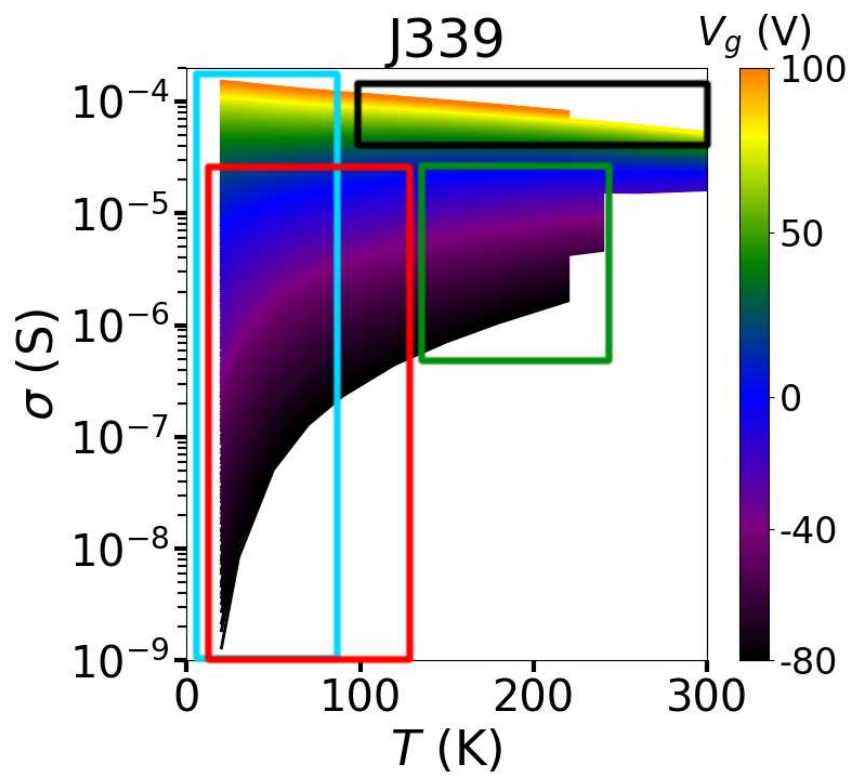


Figure 3.21: Conductivity of device J339. Colored boxes are enclosing different regions with their particular electronic transport mechanism.

Chapter 4

Transport at the MoS₂-contact interface

This Chapter is devoted to the analysis of the 2-probe electronic transport data before and after thermal annealing. The devices were connected as shown in Fig. 4.1a, with the outer contacts (S and D) serving as the current source - drain, and two inner contacts as the voltage probes. The DC two-terminal and four-terminal IV characteristics were recorded simultaneously as a function of back gate voltage and source-drain voltage, at different temperatures. We will show that the contact resistance is high, in the order of tens of $\text{k}\Omega \cdot \mu\text{m}$ up to hundreds of $\text{M}\Omega \cdot \mu\text{m}$, depending on temperature and gate voltage. We show that those contacts are of a Schottky type limiting the device performance. We then study thermionic emission over the top of the Schottky barrier, and quantum tunneling of carriers across it.

4.1 Contact inhomogeneity

4.1.1 Transmission line measurement

Two TLM devices were electrically tested to extract the contact resistance after thermal annealing at $T = 600$ K. Here we present the results for only one TLM device since the two of them showed similar behaviour. The TLM device is named J31A and is shown in the inset of Fig. 4.2b, with a label for each contact. The IV and transfer curves are shown in Fig. 4.2a and 4.2b respectively. Each IV or transfer curve represents two-probe measurements between different combinations of pairs of contacts. For instance, the black curve shows the

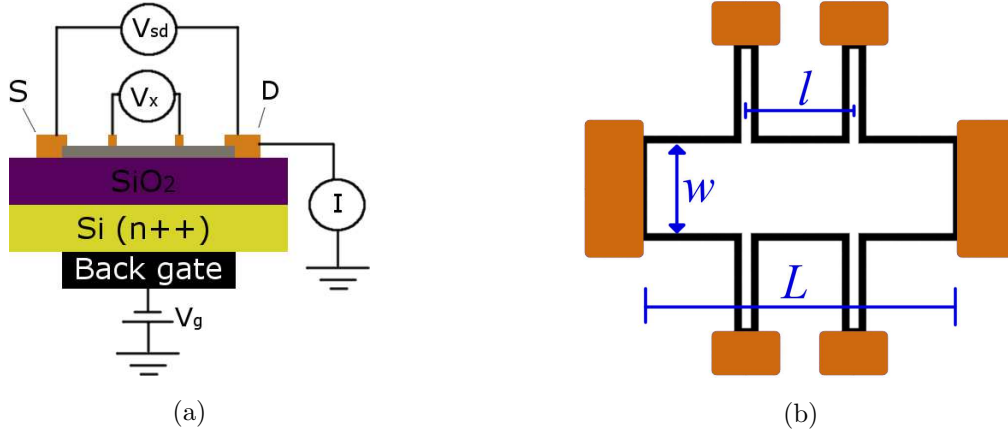


Figure 4.1: Schematic of the 2- and 4-probe measurements. (a) side view: S and D stand for Source and Drain respectively and are the outer electrodes contacting the MoS_2 (in gray color). (b) top view showing the width w , external length L and internal length l of a Hall bar shape.

results obtained during the 2-probe test of contacts F and A. Some combinations of contacts included a floating contact in-between, and they are marked with an asterisk symbol (*) in the labels, *i.e.*, the 2-probe measurements performed with contacts DA have an asterisk because between contacts D and A there is the contact F, which was floating when measuring DA contacts.

The measurements were performed at different back-gate voltages and a temperature of $T = 350$ K, after annealing the device at $T = 600$ K for 42 min. A linear fit is performed on the IV curves, for V_{sd} values between $-0.1 \text{ V} < V_{sd} < 0.1 \text{ V}$, in order to extract the resistance of each pair of contacts. The extracted resistance is then plotted against the distance between the contacts, and the result is shown in Fig. 4.2c. In theory, this method should give a linear dependence $R_L = \rho \times (L/w) + 2R_c$, and then the contact resistance is extracted from the y -intercept, extrapolating to zero distance. Our TLM devices showed strongly non-linear IVs, and large inhomogeneities on the contacts resistance. Thus, as the inhomogeneities dominated the total resistance, it was impossible to extract a mean contact resistance value. A 4-probe measurement was also performed giving non-linear results, as shown in Fig. 4.2d, which could be a sign of VRH transport. In this case, four different contacts combination has been used for the 4-probe measurements. For instance, the black curve shows the results obtained using B and H as 2-probe contacts with G and C as the 4-probe contacts.

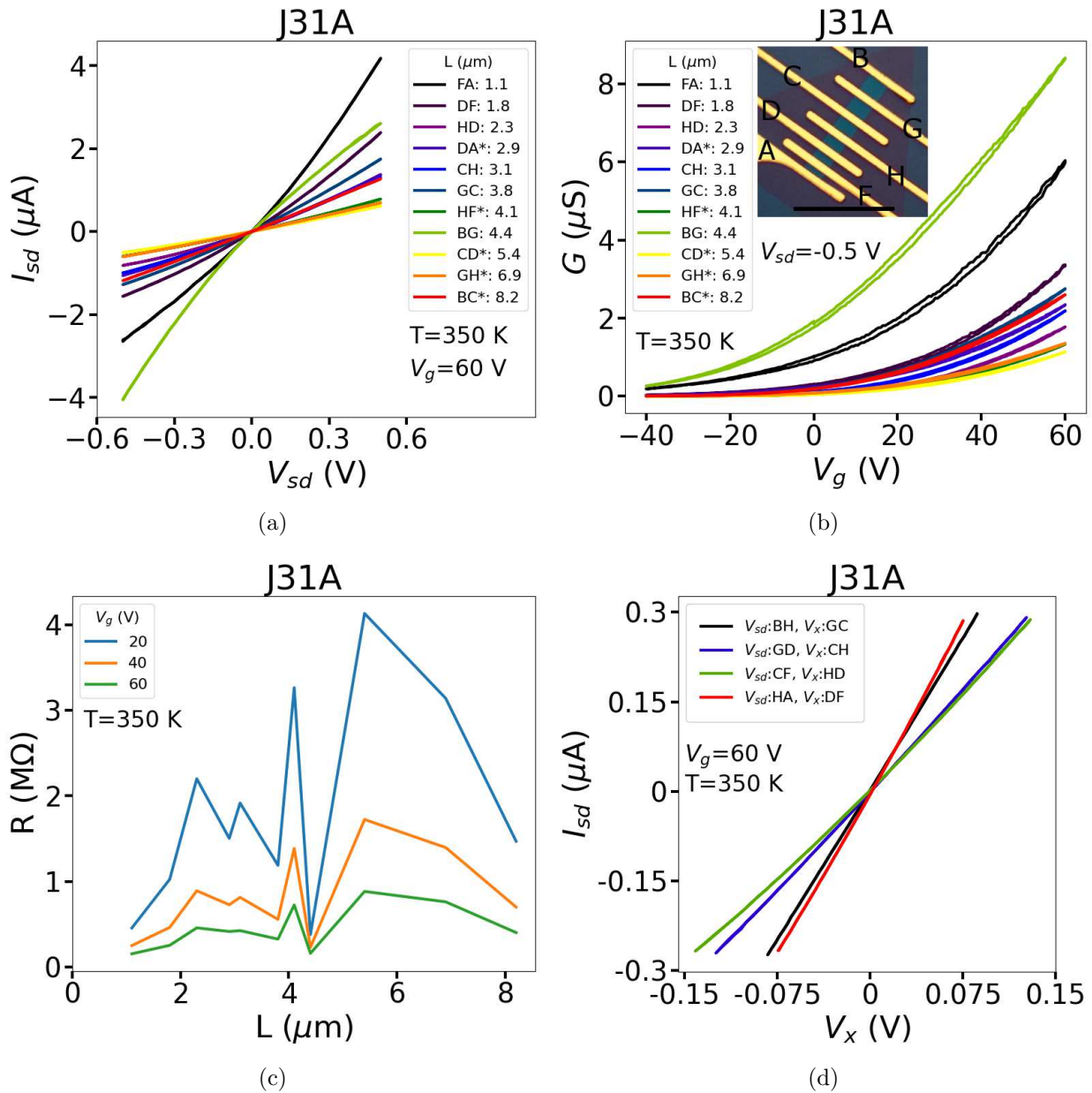


Figure 4.2: TLM technique on device J31A. The measurements were performed at $T = 350\text{ K}$ after annealing at $T = 600\text{ K}$ for about 42 min. (a) and (b) IV and transfer curves respectively. The colored curves represent different pair of contacts. The insert of (b) shows the TLM device with a label for each contact, the scale bar is $25\ \mu\text{m}$. The distance between the contacts is on the labels. (c) extracted contact resistance from fitting the IV curves. (d) 4-Probe measurements for a few contacts showing a non-linear behaviour.

4.1.2 Non linear IVs

Non-linear 2-probe IVs were the usual results in all devices just after fabrication, with some devices showing non-linearity on the 4-probe measurements. This non-linear 4-probe behavior could be a sign of variable range hopping conduction, or an impedance mismatch issue with the voltmeter used. Here we present the results of using a high input impedance preamplifier (HIP). The device used is J11B, which was already presented in the thermal annealing Section 2.4.6, although the data shown here were taken before the annealing. J11B device is shown again in Fig. 4.3, before and after metallization of contacts. S and D labels indicate the Source and Drain contacts respectively, while V_{x1} and V_{x2} labels indicate the 2 pairs of contacts used for DC 4-probe measurements. V_{x1} was measured with the HIP of $10 \text{ T}\Omega$ and Hewlett Packard Voltmeter, while V_{x2} was measured directly with another Hewlett Packard Voltmeter with a $10 \text{ G}\Omega$ input impedance.

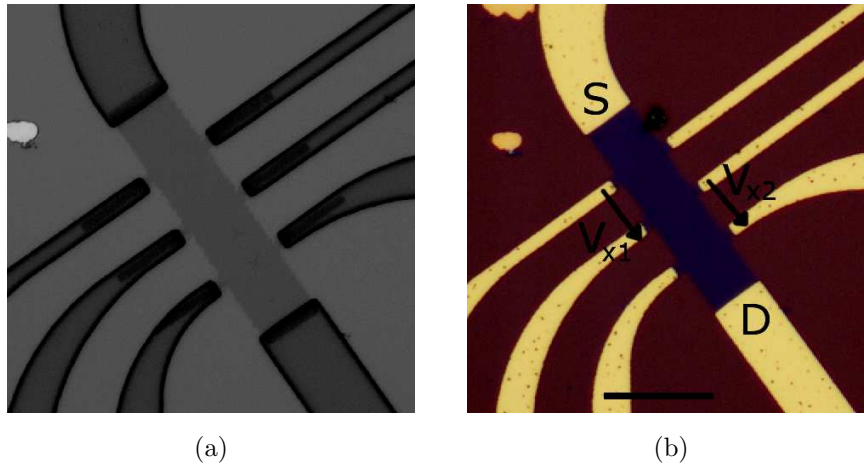


Figure 4.3: J11B before (a) and after (b) metallization. Scale bar = $50 \mu\text{m}$. S and D labels indicate the Source and Drain contacts respectively, while V_{x1} and V_{x2} labels indicate the 2 pair of contacts used for DC 4-probe measurements. V_{x1} was measured with the help of the HIP.

Figure 4.4 shows the 2-probe and 4-probe IVs data obtained at different gate voltages and temperatures. As we can see on Fig. 4.4a and 4.4b, the 2-probe IVs curves are not linear (non-ohmic contacts) caused by barriers between the metal contact and MoS_2 . The non linearity even persist in the 4-probe measurements, especially at low temperatures, as shown in Fig. 4.4c and 4.4e. The data obtained in the 4-probe configuration with (Fig. 4.4c and 4.4d) and without (Fig. 4.4e and 4.4f) the HIP are noticeably different. All the V_{x2} curves are shifted (not centered at zero) with the shift being temperature and doping dependent, and making no sense at low gate voltages, as can be seen in Fig. 4.4f. This happens because at low

gate voltages the sample resistance becomes comparable to the instrument input impedance, and a current can start circulating in the voltmeter, giving a wrong voltage measurement. By contrast, the data obtained with the HIP are linear at high temperature, as shown in Fig. 4.4d, but lose their linearity at low temperature, as shown in Fig. 4.4c. However, the non-linearity on the 4-probe data could also be a sign of VRH transport.

The non-linearity of IV curves might come from an impedance mismatch or because VRH transport is at play. Nonetheless, having an input impedance higher than $10 \text{ G}\Omega$ is desirable when measuring MoS_2 transistors at low doping & temperatures.

4.1.3 Contact resistance

This Section is devoted to the analysis of the 2-probe electronic transport data of devices J339, J338 and J12B. The three devices were presented in the previous Chapter, where the 4-probe data has been studied. The 2-probe set of data presented here has been obtained at the same time as the 4-probe data. The three devices are shown again in Fig. 4.5, with a label on the contacts that were used in 2-probe and 4-probe measurements.

To extract the contact resistance (R_c), the devices were connected as shown in Fig. 4.1a, with the outer contacts (S and D) serving as the current source - drain, and two inner contacts as the voltage probes. The contact resistance was then computed from the resistivity as $R_c = w(V_{sd}/I_{sd} - \rho(L/w))$, where L and w are the full sample length and width, respectively (see Fig. 4.1b), and $\rho = (V_x/I_{sd})(w/l)$, with l being the length between the inner contacts in the 4-probe configuration. It is usually given in terms of the width the transistor channel, in units of $\Omega \cdot \mu\text{m}$, to take into account the sample width.

The extracted contact resistance as a function of gate voltage at different temperatures is shown in Fig. 4.6 for the three devices. As can be seen from the figures, R_c decreases as V_g increases. This happens because the Fermi level is increasing, decreasing the effective Schottky barrier. This phenomena will be discussed in the next Section. A low R_c of $\sim 90 \text{ k}\Omega \cdot \mu\text{m}$, $\sim 2 \text{ M}\Omega \cdot \mu\text{m}$ and $\sim 115 \text{ k}\Omega \cdot \mu\text{m}$, has been achieved at high densities for devices J339, J338 and J12B respectively.

For device J339 the contact resistance could not be reliably extracted at low doping ($V_g < 0 \text{ V}$), where the contact resistance drops quickly to zero, which is absurd. This could be caused by an incorrect measurement of the length L , since the source and drain contacts have a saw-tooth shape, as can be seen in Fig. 4.5a. This saw-tooth shape also increases

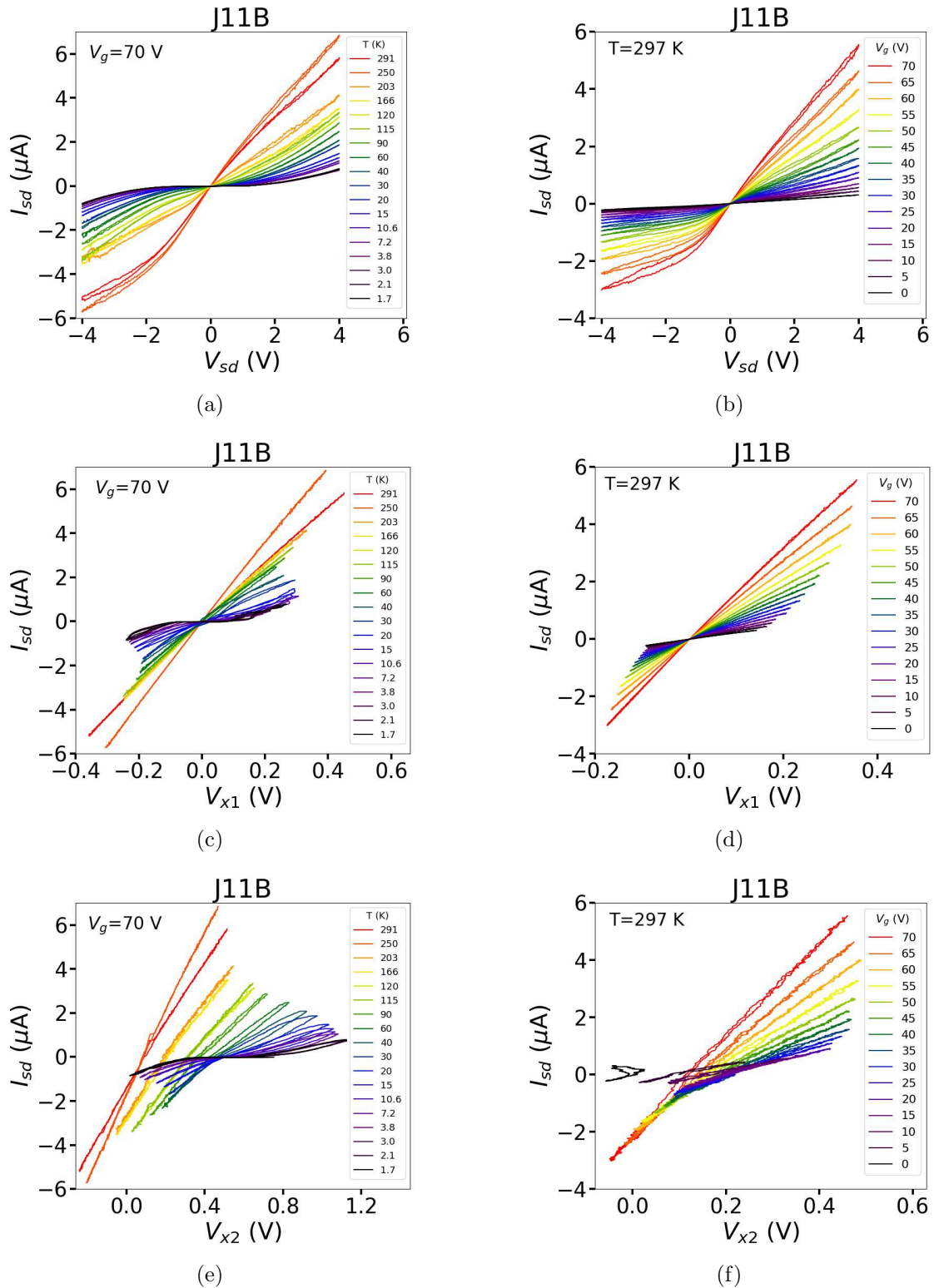


Figure 4.4: IVs curves for device J11B at (a,c,e) different temperatures for fixed V_g , and (b,d,f) different V_g for fixed temperature. V_{x1} is measured with a HIP of $10 \text{ T}\Omega$ input impedance and a Hewlett Packard Voltmeter, while V_{x2} is measured directly with another Hewlett Packard Voltmeter with $10 \text{ G}\Omega$ input impedance.

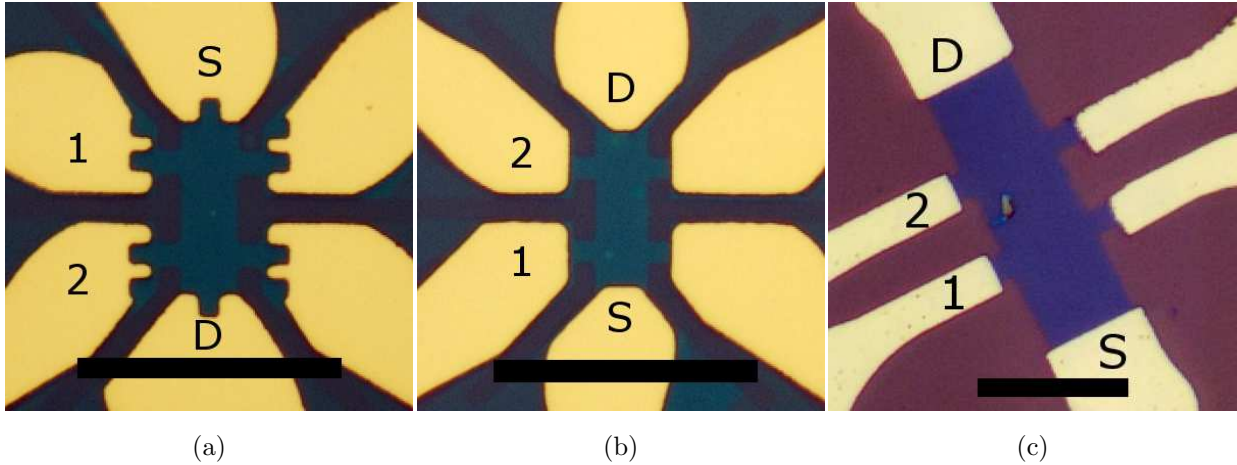


Figure 4.5: Optical pictures of J339 (a), J338 (b), and J12B (c). Scale bar = 25 μm . **S** and **D** stand for source and drain respectively. The contacts 1 and 2 were used to measure voltage in a 4-probe configuration.

the possibility of having field electron emission from the tips, making the electron injection non-uniform through the width of the Hall bar.

The contact resistance also varies with the temperature, increasing when T is lowered in devices J339 and J338 but having the opposite effect in device J12B. This behavior could be caused by the differences in the contacts between J1 and J3 devices: for J3 devices, the contacts are made of Ti/Au 2/150 nm; while for J1 devices, they are made of Ti/Au 15/75 nm. As a consequence, the contacts from J1 devices behave more like Ti contacts, while those from J3 sample behave more like a Au contacts. This phenomenon could also be related to electron density. Device J339 shows a R_c that decreases with T , but in a small region at $V_g > 70$ V and $T < 120$ K; while J12B shows a R_c that increases when decreasing T , in the region $V_g < 0$ V and $T < 108$ K. Thus, at low doping, R_c increases when decreasing T , but the opposite occurs at high doping. This could be related to a transition from thermionic emission at low doping to “ohmic” contact or tunneling dominated transport at high doping, as we will discuss in the next Sections.

4.2 Electronic transport and Schottky barrier

Electric contacts are commonly of Schottky type on MoS₂ [13–15, 95, 96, 164]. At the metal–MoS₂ contact (where a barrier is formed) the charge injection occurs either (i) as a result of thermionic emission over the top of the barrier due to the transfer of thermal energy or (ii) as a result of quantum mechanical tunneling of carriers across the barrier

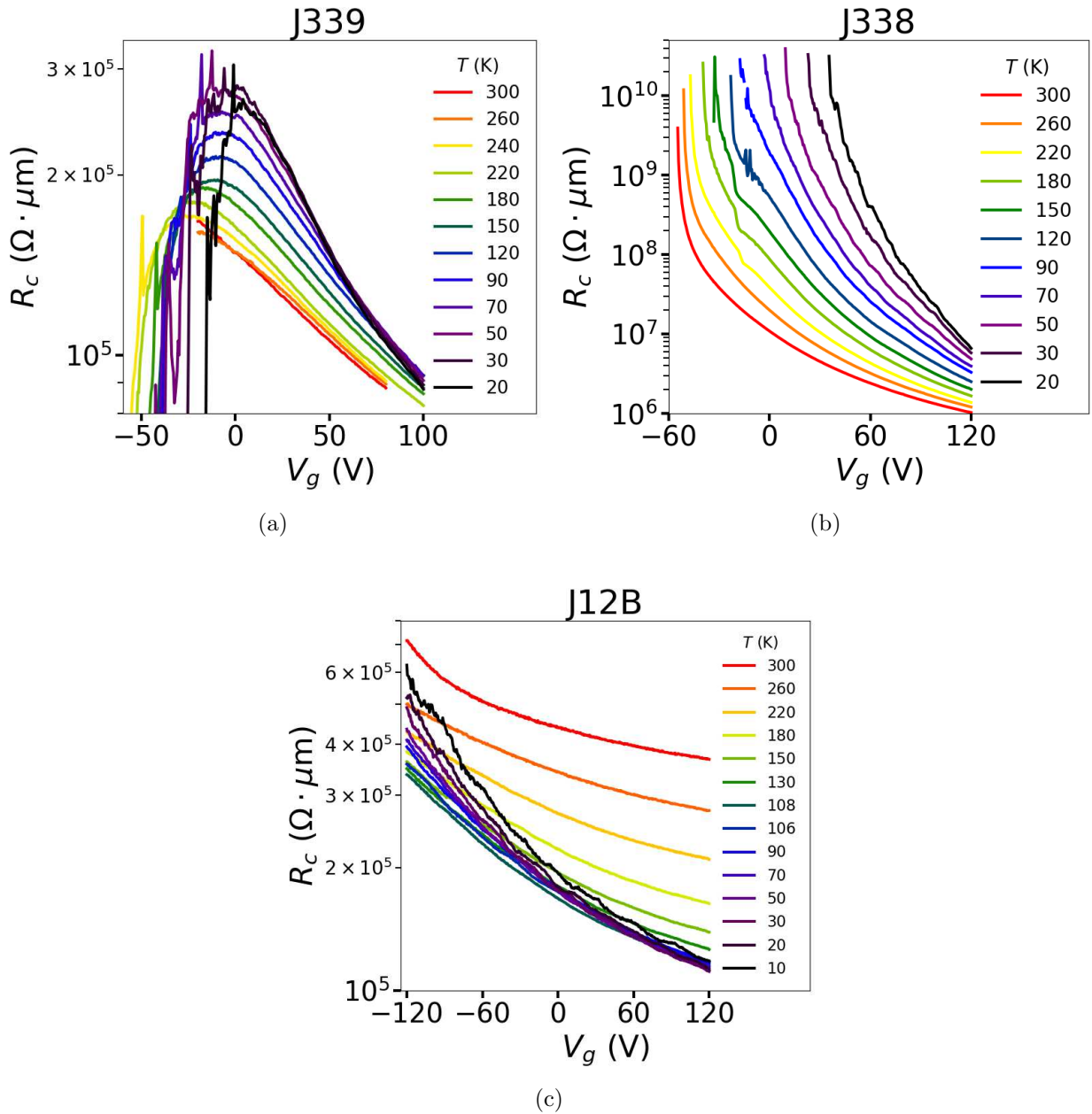


Figure 4.6: Contact resistance as a function of gate voltage at different temperatures for devices J339 (a), J338 (b), and J12B (c). The contact resistance R_c increases when decreasing V_g for all devices, with J339 being the exception where it decreases for $V_g < 0$ V. Decreasing the temperature resulted in an increase on R_c for devices J339 and J338 but with the opposite effect for device J12B.

width, as schematically shown in Fig. 4.8c. In the following Sections, those charge injections mechanism will be discussed.

4.2.1 Schottky barrier

All of our devices exhibited Schottky contacts, especially at low temperature and gate voltages, when the thermal energy is small, and the Fermi level is far away from the conduction band. Here, we present the data for a single device, called J35A, which showed a relationship between the area of MoS₂ below the contact and its resistance. Optical pictures of device J35A, before and after metallization of contacts, are shown in Fig. 4.7a and Fig. 4.7b. In Fig. 4.7b are shown the source (S) and drain (D) contacts. The *high* of the SMU was connected to contact S and the *low* was connected to contact D. In Fig. 4.7a are shown the S and D contacts as two back-to-back connected Schottky diodes, but this configuration can be treated as a single Schottky diode [165], where the transport is dominated by the blocking diode at high V_{sd} . As can be seen in Fig. 4.7a, there is significant difference of MoS₂ area below S and D contacts, and this has an effect on the contact resistance as we will show in the following.

The 2-probe and 4-probe IV results are shown in Fig. 4.7c and 4.7d respectively. It is clear from the results that the device conducts better for positive V_{sd} bias than for negative bias, given the higher current magnitude reached under positive bias than negative bias. With positive V_{sd} the current flows from D1 to D2 and the resistance is dominated by D2. But with negative V_{sd} the resistance is dominated by D1, which has a higher resistance. The small contacted MoS₂ area in contact S manifest itself as a higher resistance for electrons when going from the metal contact to the MoS₂, showing that the contacted area is important when fabricating low resistance contacts.

4.2.2 Thermionic emission

To understand the nature of the electron transmission at the Schottky barrier (SB), we investigate the two-probe data as a function of the inverse of temperature at various gate voltages, in the range $300 \text{ K} < T < 150 \text{ K}$. Electrical transport across a Schottky contact into a 2D material can be described by the 2D thermionic emission equation [101]:

$$I_{sd} = AA_{2D}^* T^{3/2} \exp \left[-\frac{e}{k_B T} \left(\phi_B - \frac{V_{sd}}{\eta} \right) \right] \quad (4.1)$$

where A is contact area of junction, A_{2D}^* is the two-dimensional equivalent Richardson constant, e is the magnitude of the electron charge, ϕ_B is the Schottky barrier height, k_B is the Boltzmann constant and η is the ideality factor.

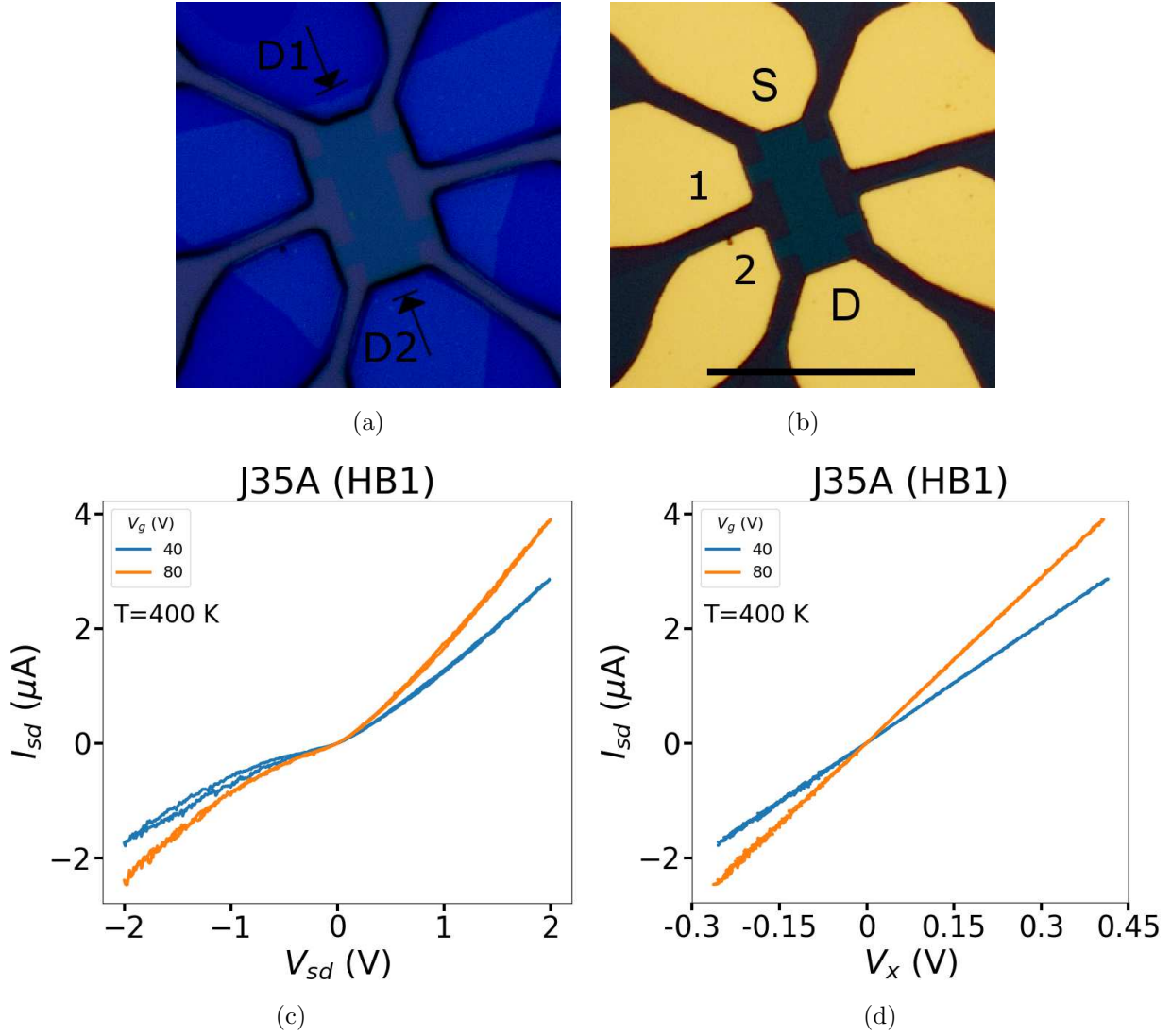


Figure 4.7: Device J35A before (a) and after (b) metallization. Scale bar 25 μm . (c) and (d) 2-probe and 4-probe IV results respectively. Negative bias have a higher resistance than positive bias, and this behaviour could be related to the area of MoS_2 below the contact.

The Schottky barrier is then extracted from the linear fit of $\ln(I_{sd}/T^{3/2})$ as a function of $1/T$ at different V_g , using equation 4.1, and the results are shown in Fig. 4.9. In the extraction of the SB height, the transfer data has been used, and the term $\exp[eV_{sd}/k_B T \eta]$ was omitted for simplicity. A V_{sd} value of ± 0.5 V has been used on devices J339 and J338, but $V_{sd} = \pm 0.01$ V for device J12B (the data's average between positive and negative V_{sd} was used, with the error bars being the difference).

For devices J339 and J12B, the fit was not performed since the data does not show any linearity and the current decreases as the temperature increases, being opposite to what happens with thermionic emission. This happens because those devices are so highly doped

that the Fermi level lies deep in the conduction band, and the transport is of a tunneling nature, as will be discussed in the next Section. However, for device J338, as the temperature increases so does the measured current. Thus, for this device, the SB height ϕ_B , could be extracted for gate voltages below 60 V, and is shown in Fig. 4.9d.

If carrier transport is dominated by thermionic emission, for low doping $\phi(V_g)$ varies in a linear fashion until the flat band voltage (V_{FB}) is reached. This situation is schematically shown in Fig. 4.8, and increasing V_g corresponds to a continuous change from the situation shown in Fig. 4.8a to the one shown in Fig. 4.8b. Thus, the SB height obtained at the endpoint of the linearity (at $V_g = V_{FB}$), ϕ_{FB} , indicates the true SB height between a 2D semiconductor and a metal [15]. For $V_g > V_{FB}$, the change in SB height is no longer linear because the carriers can tunnel through the SB, and their transport is no longer described by thermionic emission alone, and tunneling becomes more and more important. This situation is shown in Fig. 4.8c, and will be subject of the next Section.

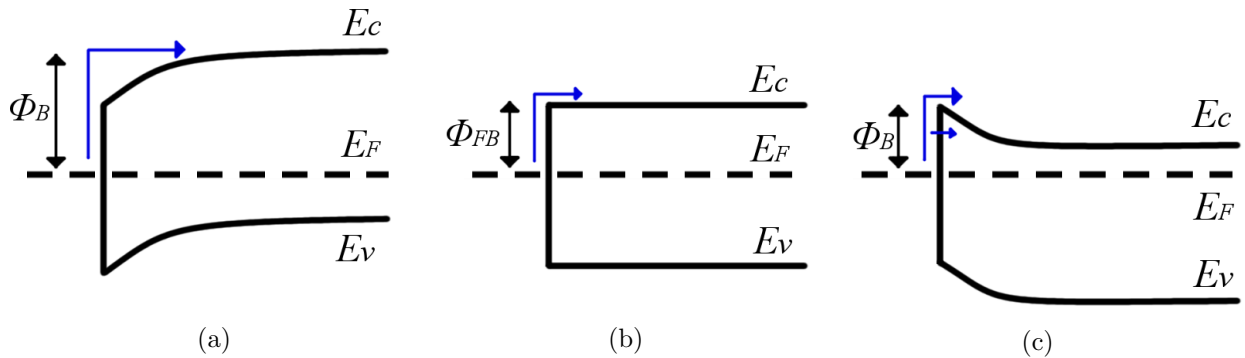


Figure 4.8: Energy band bending when changing the Fermi energy E_F . The electron injection into the band is indicated by the blue arrows. (a), (b) and (c) correspond to $V_g < V_{FB}$, $V_g = V_{FB}$ and $V_g > V_{FB}$, respectively.

In order to avoid making assumptions on the ideality factor η and the effect of V_{sd} , the Schottky barrier has also been extracted using the $I_{sd}(V_{sd})$ measurements. The results are shown in Fig. 4.10. The fit is done using the same equation 4.1 and the slope obtained is then plotted against V_{sd} , with the interception with y -axis being proportional to the SB [95, 164]. As before, devices J339 and J12B show the opposite behavior to what happens with thermionic emission because of their high doping. However, for device J338 at $V_g = 50$ V, a SB $\phi_B \sim 7 \pm 2$ meV is obtained. This value is consistent with the one obtained with transfer measurements, $\phi_B \sim 7.1 \pm 0.7$ meV, as shown by the black dashed lines in Fig. 4.9d.

Such small SB could come from the fact that the devices are highly doped, with the

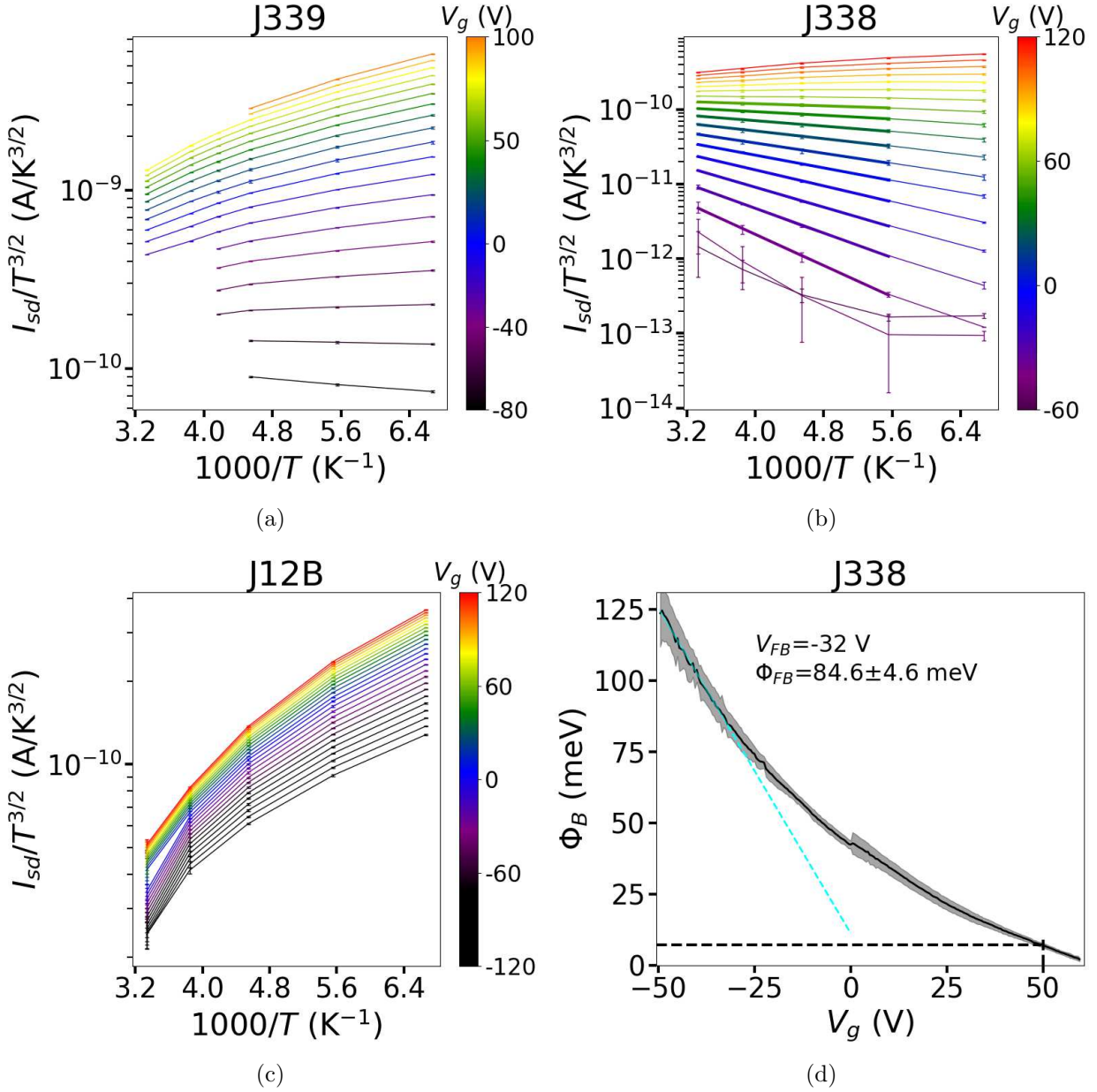


Figure 4.9: 2D Richardson plots for device J339 (a), J338 (b) and J12B (c). The dots represent the data which are joined by thin solid lines as a guide for the eye. The thick solid lines are the linear fits, performed only on device J338. (d) Extracted Schottky barrier Φ_B for device J338 as a function of V_g . V_{FB} is the gate voltage at which the flat band condition is reached.

Fermi level close to the bottom or deep into the conduction band. This comes from the fact that the fitting is done on a temperature range not high enough, underestimating the SB due to the weak thermionic emission at low temperatures [15]. In such case, the thermionic emission model does not apply very well because electron tunneling across the barrier becomes important, as we will see in the next Section. The image force due to the high V_{sd} used could also affect the SB value extracted with the transfer data [166].

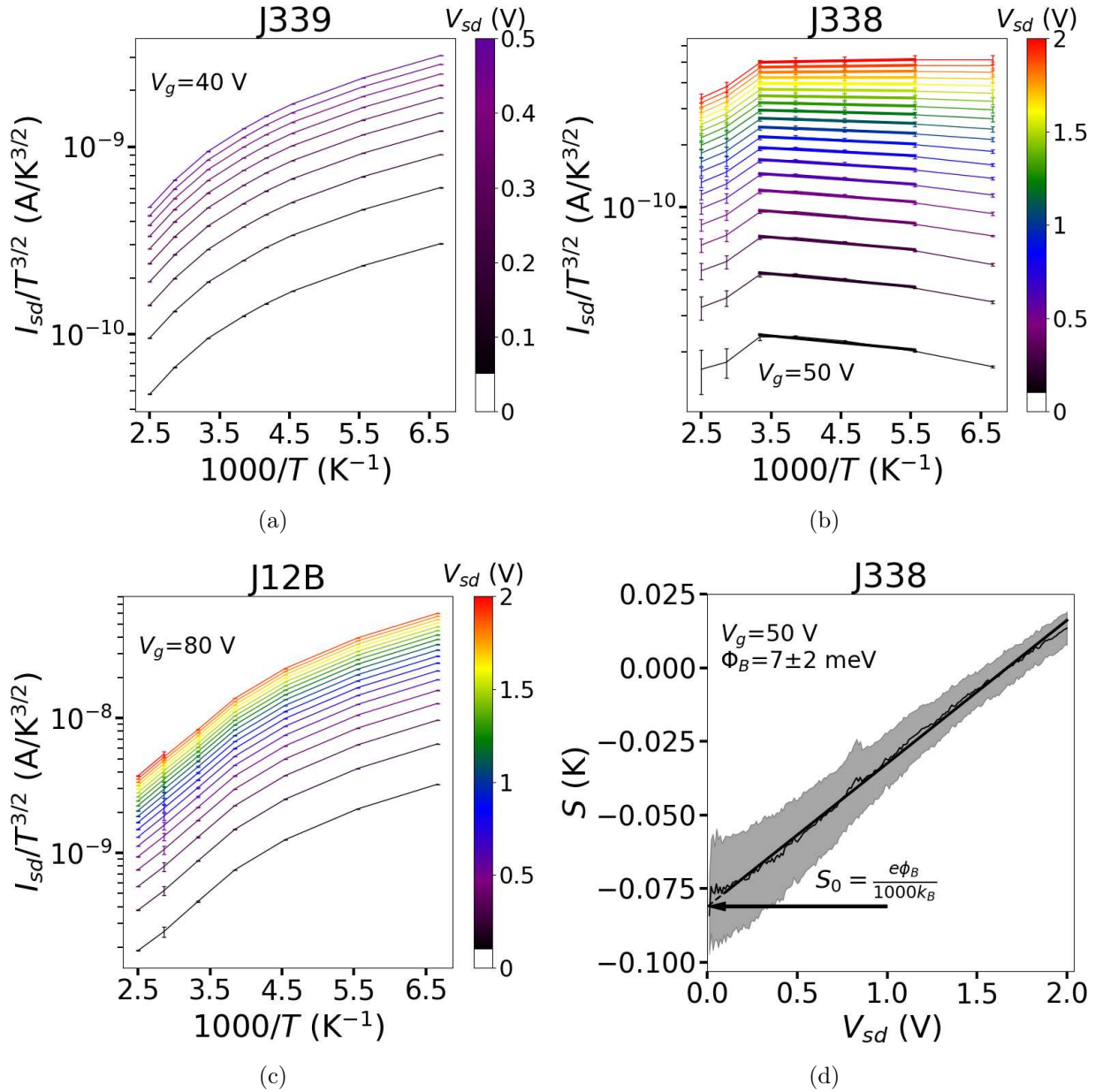


Figure 4.10: 2D Richardson plots at fixed V_g for device J339 (a), J338 (b) and J12B (c). The dots represent the data which are joined by thin solid lines as a guide for the eye. The thick solid lines are the linear fits, performed only on device J338. (d) Slopes extracted from (b) as a function of V_{sd} . The Schottky barrier (Φ_B) is derived from the y-intercept, S_0 .

4.2.3 Tunneling

The tunneling behavior can be of two different types: direct or Fowler–Nordheim (FN) depending on the shape and width of the barrier. The direct tunneling and the F–N tunneling are determined by the nature of the interfacial barrier, that is, the former occurs when the barrier is trapezoidal (wide) and the latter occurs when the barrier is triangular (thin), as already discussed in Section 1.4.

The equations governing both type of transport can be rewritten as equation 4.2 for direct tunneling, and equation 4.3 for FN tunneling:

$$I \propto V_{sd} \exp \left[-\frac{2d\sqrt{2m^*\phi}}{\hbar} \right] \quad (4.2)$$

$$I \propto V_{sd}^2 \exp \left[-\frac{4d\sqrt{2m^*\phi^3}}{3\hbar e V_{sd}} \right] \quad (4.3)$$

where d , ϕ , m^* , e and \hbar are the SB width, SB high, effective mass, electron charge, and the reduced Planck constant, respectively.

In the following, (I_{sd}/V_{sd}^2) vs $1/V_{sd}$ plots are presented in semi-log and log-log scales. If the plot in semi-log scale shows linearity, then F–N tunneling is expected to occur, whereas when the plot in log-log scale shows linearity, direct tunneling is thought to occur. A high V_g has been used in order to push the Fermi level deep into the conduction band, bending it, at least, as shown in Fig. 4.8c. In this scenario, tunneling transport is more likely to occur.

In Fig. 4.11, the tunneling plots for the three devices are shown. The F-N plots for the three devices are not linear, as can be seen in Fig. 4.11a, 4.11c and 4.11e, meaning that the V_{sd} used is not high enough to bend the barrier [166], or F-N tunneling simply does not occur. However, the direct plots show linearity in almost the entire range of V_{sd} for devices J339 and J12B, as shown in Fig. 4.11b and 4.11f, but partially for J338 device, as can be seen in Fig. 4.11d. This deviation from direct tunneling on device J338 could be a transition to F-N tunneling caused by high enough V_{sd} [14, 97, 167].

The linearity shown in all Direct tunneling plots from devices J339 and J12B, regardless of the temperature, happens because the contacts are of ohmic-like nature. In those devices, the Fermi level is deep in the conduction band and the SB does not affect the electronic transport. Moreover, they show similar Direct tunneling behaviour, considering their different metal-contact thickness. This shows that there is no difference between 2/150 nm and 15/75 nm Ti/Au at this range of doping and temperatures. The apparent transition to F-N tunneling on device J338 disappears when increasing temperature where thermionic emission occurs, since tunneling current is dominant mainly in the low temperature regime.

4.3 Conclusion

The results presented in this Chapter suggest that the charge carrier injection from the metal to the MoS₂ is dominated by direct tunneling at low temperature, and thermionic

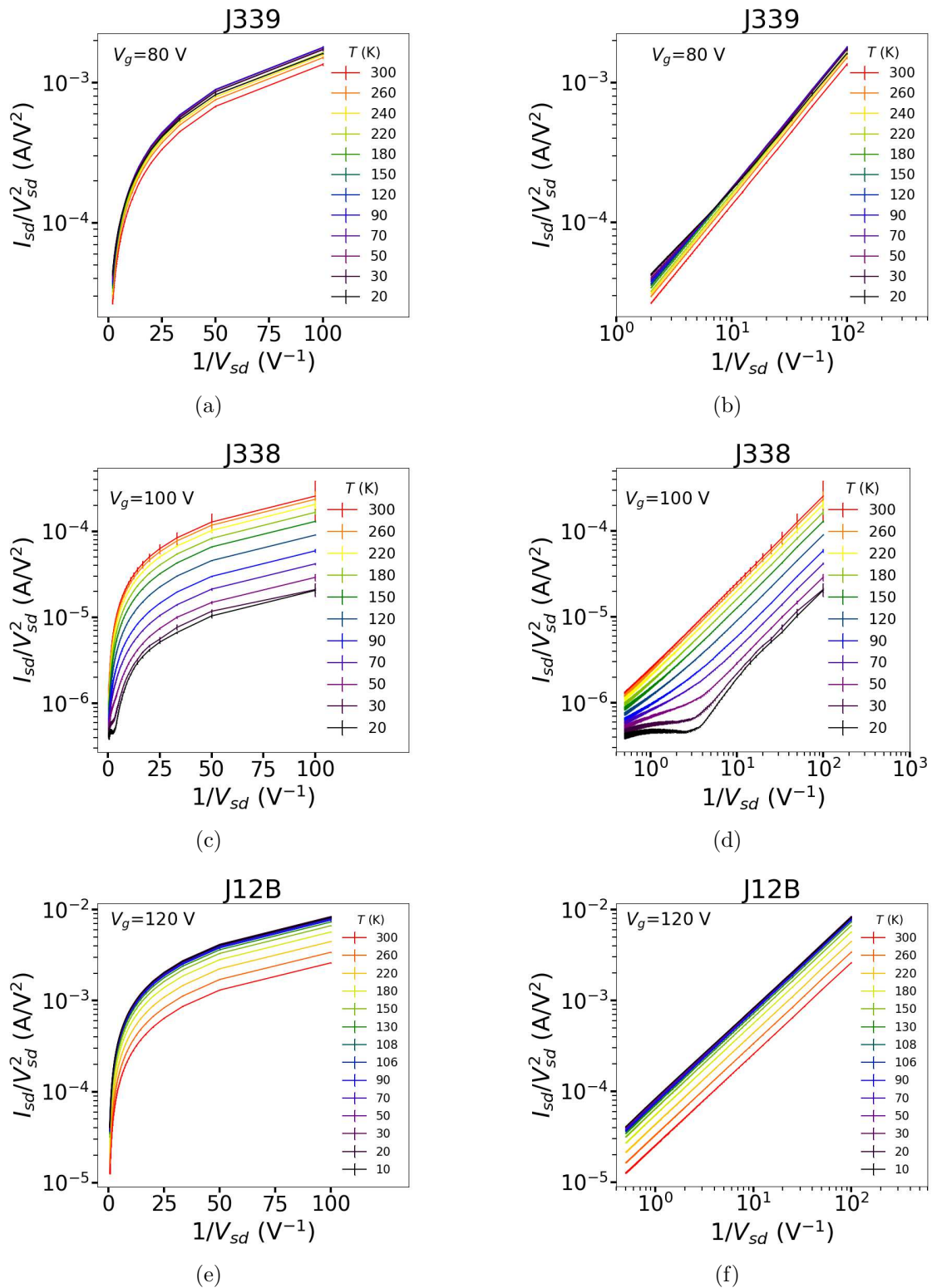


Figure 4.11: I_{sd}/V_{sd} plotted vs. the inverse of the drain bias ($1/V_{sd}$) for different temperatures and fixed gate voltage: (a), (b) and (c) Direct-like plots and (d), (e) and (f) FN-like plots for devices J339, J338 and J12B respectively.

emission at high temperature. The extracted Schottky barrier for device J338 is being underestimated for two reasons: the electrons are tunneling through the barrier, and the temperature range used in its extraction is not the adequate. However, a flat band SB $\phi_{FB} = 84.6$ meV has been extracted, and is commonly found in the literature. Ohmic contacts can be realized at sufficiently high doping as in the case of device J12B, but also depending on the shape of the contacts, as in the case of J339. A contact resistance as low as ~ 82.5 $\text{k}\Omega \cdot \mu\text{m}$ has been achieved, which is commonly reported in the literature.

Conclusion & Outlook

The discovery of graphene by Novoselov and Geim in 2004 has opened a new field of research on 2D materials. The properties of these materials range from zero-gap, like in graphene, to finite gaps, of 1–2 eV in semiconducting TMDs. Of all TMDs, MoS₂ has been the most studied because of its abundance, and since it has been used as dry lubricant since the 60s.

Nowadays, monolayer MoS₂ is studied for its electronic and optical properties. One of the most important electronic property is that it can transition from an insulating to a metallic state, even reaching a superconducting state, depending on its electron density. However, at the fundamental level, these interesting transitions are not fully understood yet. Within this thesis we studied the transport mechanism of MoS₂ in the insulating and metallic regimes, hopefully shedding some light into this transition that still remains debated for 2D materials. We also discussed some of the features of metal-MoS₂ contact, and the electronic transport occurring at this interface.

Our MoS₂ samples were grown by CVD in Pennsylvania University, under the supervision of Charlie Johnson. The number of layers of the MoS₂ flakes has been determined by Raman spectroscopy and reflectometry. Electron beam lithography was used in the fabrication of close to 200 different devices, with different metals deposited for the contacts. The MoS₂ flakes have been shaped into any desired shape with the use of our own plasma recipe.

Different techniques for controlling the electron density and improving the quality of the sample have been explored, with the *in-situ* thermal annealing at $T = 600$ K being the most favorable, and the only reliable method with which complete data-sets could be obtained. The mobility of our MoS₂ devices after thermal annealing is one of the largest reported for CVD grown MoS₂, reaching values $\sim 200 \text{ cm}^2\text{V}^{-1}\text{s}^{-1}$. The thermal annealing also increased the electron density of the samples, pushing the Fermi level deep into the conduction band where the metal-insulator transition (MIT) could be observed.

The electron conduction in the insulating side can be well described by variable range hopping models. It is found that the prefactor of the VRH models is a constant, which points to a hopping mechanism which is not assisted by phonons, contrary to the common belief. The hopping mechanism is then thought to be assisted by electron-electron interaction, which is demonstrated to be high in our samples, as commonly found in 2D materials. There are two commonly known VRH models: Efros-Shklovskii and Mott models, which have different power law in the temperature-dependent conductivity. An intermediate VRH mechanism seems to occur on device J338, where neither the Efros-Shklovskii nor Mott models can describe the conductivity. An attempt to derive a complete model, working on the ideas already developed by Efros and Shklovskii, is presented in the appendix. The new derived model describe very well the conductivity of J338, suggesting that this transport mechanism could be real.

The conductivity in the metallic regime seems to be of a classical nature. A model of phonons and charged point defect scattering describe very well the conductivity in the conduction band, a sufficiently high doping and temperatures. Regarding the transition itself, a scaling on the conductivity and the localization length has been performed, suggesting that this phenomena is a transition of second order, and a quantum phase transition is occurring. However, we could not rule out the possibility of this transition being a classical phenomena, or even just an artifact. Classically, the MIT can be observed intuitively by the combination of (i) the increase in mobility and (ii) positive threshold voltage shift with decreasing the temperature. If a correction of doping or threshold voltage on the conductivity is performed, the MIT is no longer visible, suggesting that the MIT could even be an artifact.

The analysis of the 2-probe data showed that, after the thermal annealing at $T = 600$ K, the contact resistance drops significantly, reducing also the Schottky barrier. The shape of the contacts also affects the Schottky barrier, with the “saw-tooth” contact shape having a low Schottky barrier. Altogether, the contacts become ohmic and the intrinsic quantities such as mobility and sheet resistance can be reliably extracted. The transport at the metal-MoS₂ interface is then dominated by thermionic emission at high temperatures, and by Direct tunneling at low temperatures.

In this PhD study, we have made progress in the fabrication process of MoS₂ transistors with ohmic contacts, and in the understanding of the electronic transport at different temperatures and electron density. This progress constitutes an important step towards future

studies on MoS₂, in particular for the Jjedi project. The goal of the project was to build a tunable Josephson junction, with important sub-goals as making the proper design, fabricating working transistors, knowing the operation limits of those transistors, and how stable they are over time. Although the tunable Josephson junction could not be build, important progress has been done in the fabrication of functioning devices, and in the understanding of its electronic properties.

Appendix A

Variable range hopping

A more complete picture of variable range hopping (VRH) must include the average energy spacing and the coulomb interaction. Once both terms are included, a different VRH model can be derived. The result is a value of $p = 3/2$ in Eq. A.1.

$$\sigma = C_p \exp \left[- \left(\frac{T_p}{T} \right)^{\frac{1}{p}} \right], \quad (\text{A.1})$$

The derivation is shown below, starting with the conductivity shown in Eq. A.2:

$$\sigma \sim \exp \left(- \frac{2r}{\xi} - \frac{1}{\pi r^2 \text{DoS} k_B T} - \frac{e^2}{r \kappa k_B T} \right) \quad (\text{A.2})$$

The term $\frac{-2r}{\xi}$ correspond to a tunneling probability between impurities; the term $\frac{-1}{\pi \text{DoS} k_B T}$ corresponds to the average energy between impurities states, with a density of impurities depending on energy given by $\text{DoS}(E_F)$; the last term, $\frac{-e^2}{r \kappa k_B T}$, corresponds to the Coulomb interaction between states.

The optimal hopping distance is then obtained by finding the maximum of the previous expression, i.e. differentiating against r and equating to zero:

$$-\frac{2}{\xi} + \frac{2}{\pi r^3 \text{DoS} k_B T} + \frac{e^2}{r^2 \kappa k_B T} = 0 \quad (\text{A.3})$$

which can be rewritten as:

$$-Ar^3 + Cr + B = 0 \quad (\text{A.4})$$

where $A = 2/\xi$, $B = 2/\pi \text{DoS} k_B T$ and $C = e^2/\kappa k_B T$. The Eq. A.4 was solved with the use of Wolfram Alpha [168], and it have only one real root:

$$r = \frac{\sqrt[3]{2/3C}}{\sqrt[3]{9A^2B + \sqrt{3}\sqrt{27A^4B^2 - 4A^3C^3}}} + \frac{\sqrt[3]{9A^2B + \sqrt{3}\sqrt{27A^4B^2 - 4A^3C^3}}}{\sqrt[3]{2}\sqrt[3]{3^2A}} \quad (\text{A.5})$$

At sufficient low DoS ($< 1 \times 10^{17} \text{ eV}^{-1} \text{ m}^{-2}$) and low ξ ($< 1 \times 10^{-9} \text{ m}$), the term $27A^4B^2 \gg 4A^3C^3$, hence the term $4A^3C^3$ on Eq. A.5 can be omitted and the expression is reduced to:

$$r = \frac{\sqrt[3]{2/3}C}{\sqrt[3]{18A^2B}} + \frac{\sqrt[3]{18A^2B}}{\sqrt[3]{2}\sqrt[3]{3^2A}} \quad (\text{A.6})$$

$$r = \frac{3\sqrt[3]{AB^2} + C}{3\sqrt[3]{A^2B}} \quad (\text{A.7})$$

Using the same condition as before (low DoS and low ξ), the term $3\sqrt[3]{AB^2} \gg C$, then the Eq. A.7 can be further reduced to:

$$r = \sqrt[3]{\frac{B}{A}} \quad (\text{A.8})$$

We have then found the optimal hopping distance r . This value of r is now reintroduced into the exponent of Eq. A.2:

$$-Ar - \frac{B}{2r^2} - \frac{C}{r} \quad (\text{A.9})$$

$$-\frac{3}{2}\sqrt[3]{A^2B} - C\sqrt[3]{\frac{A}{B}} \quad (\text{A.10})$$

$$-\frac{3}{2}\sqrt[3]{\frac{2^2}{\xi^2} \frac{2}{\pi \text{DoS} k_B T}} - \frac{e^2}{\kappa k_B T} \sqrt[3]{\frac{2\pi \text{DoS} k_B T}{\xi}} \quad (\text{A.11})$$

$$-\frac{3}{\sqrt[3]{\xi^2 \pi \text{DoS} k_B T}} - \frac{e^2}{\kappa} \sqrt[3]{\frac{\pi \text{DoS}}{\xi (k_B T)^2}} \quad (\text{A.12})$$

$$\frac{-\sqrt[3]{\pi^2 \frac{e^2}{\kappa} \sqrt[3]{\text{DoS}^2 \xi}} - 3\sqrt[3]{k_B T}}{\sqrt[3]{\pi} \sqrt[3]{\text{DoS} \xi^2} \sqrt[3]{(k_B T)^2}} \quad (\text{A.13})$$

At sufficient low T , the term $3\sqrt[3]{k_B T}$ in Eq. A.13 can be omitted, reducing the expression to:

$$\left(\frac{1}{k_B T} \sqrt{\frac{e^6 \pi \text{DoS}}{\kappa^3 \xi}} \right)^{2/3} \quad (\text{A.14})$$

We now define the characteristic temperature $T_{3/2}$ and localization length ξ :

$$T_{3/2} = \frac{1}{k_B} \sqrt{\frac{e^6 \pi \text{DoS}}{\kappa^3 \xi}} \quad (\text{A.15})$$

$$\xi = \frac{e^6 \pi \text{DoS}}{\kappa^3 (k_B T_{3/2})^2} \quad (\text{A.16})$$

Finally, Eq. A.2 can be rewritten as:

$$\sigma \sim \exp \left[- \left(\frac{T_{3/2}}{T} \right)^{2/3} \right] \quad (\text{A.17})$$

We then proceed to fit the conductivity data of J338 with the Eq. A.1 and with $p = 3/2$, the results are shown in Fig. A.1. The conductivity data for this device follows very well the model with $p = 3/2$, and the fitting is done over a wide range of temperatures, from $T = 180$ K down to $T = 20$ K. The characteristic temperature $T_{3/2}$ extracted from the fit, and its corresponding localization length computed with the help of Eq. A.16 are shown in Fig. A.1b. The localization length is large, higher than the assumption made in order to derive the $p = 3/2$ model. A possible explanation to this issue is the fact that the computed localization length using the ES model alone is also high, probably by a not fully correct Coulomb interaction, as discussed in Chapter 3. As the present model uses the same coulomb interaction used by ES, it is expected to have large, overestimated ξ .

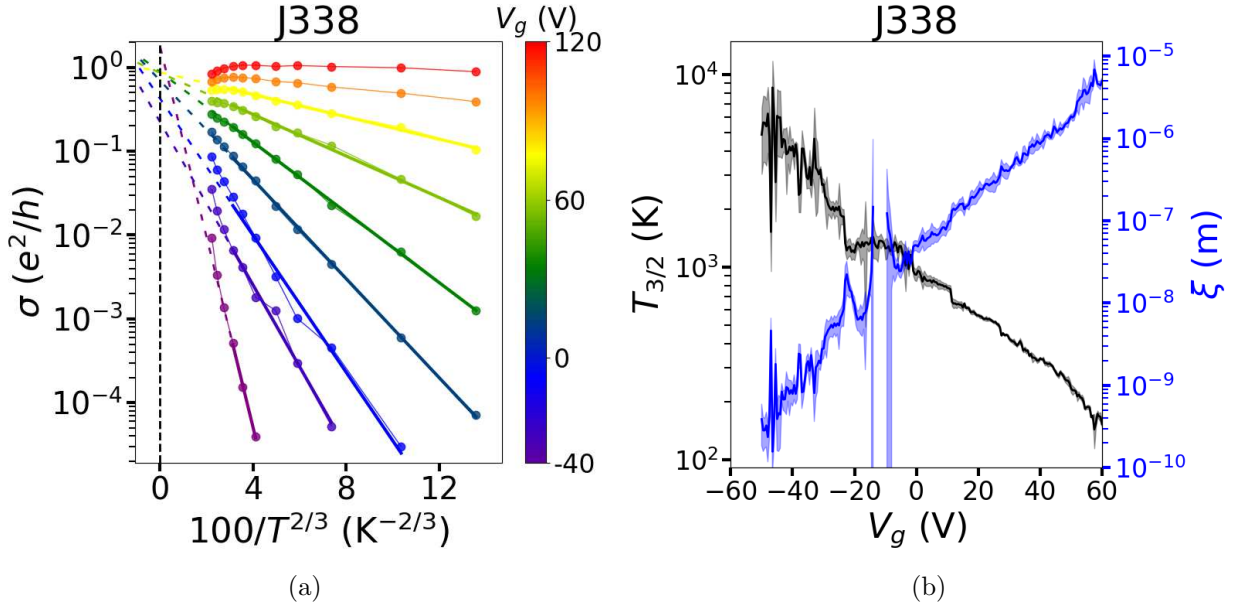


Figure A.1: Conductivity fitting results of device J338 with $p = 3/2$. (a) Temperature dependence of the conductivity versus $T^{-2/3}$ (VRH plot). Only a reduced data set is shown for clarity, represented by points. The thick lines are the fitting results using the VRH model. (b) Temperature $T_{3/2}$ (black color) extracted from the VRH fit and its corresponding localization length (blue color).

The prefactor C_p is then extracted, giving a value of $C_p = 0.92 \pm 0.5 e^2/h$ from the fit performed on Fig. A.1a. The universality of the prefactor is better seen in Fig. A.2, where the conductivity in units of e^2/h is plotted as a function of $(T/T_{3/2})^{-2/3}$. A linear fit is performed on the data shown in Fig. A.2, extrapolated to $T^{-2/3} = 0$, and from the y -intercept another value value for C_p is extracted: $C_p = 0.93 \pm 0.24 e^2/h$. This two values of C_p are closer to the unity in terms of the quantum conductivity and with a lower error compared to the ES fitting results.

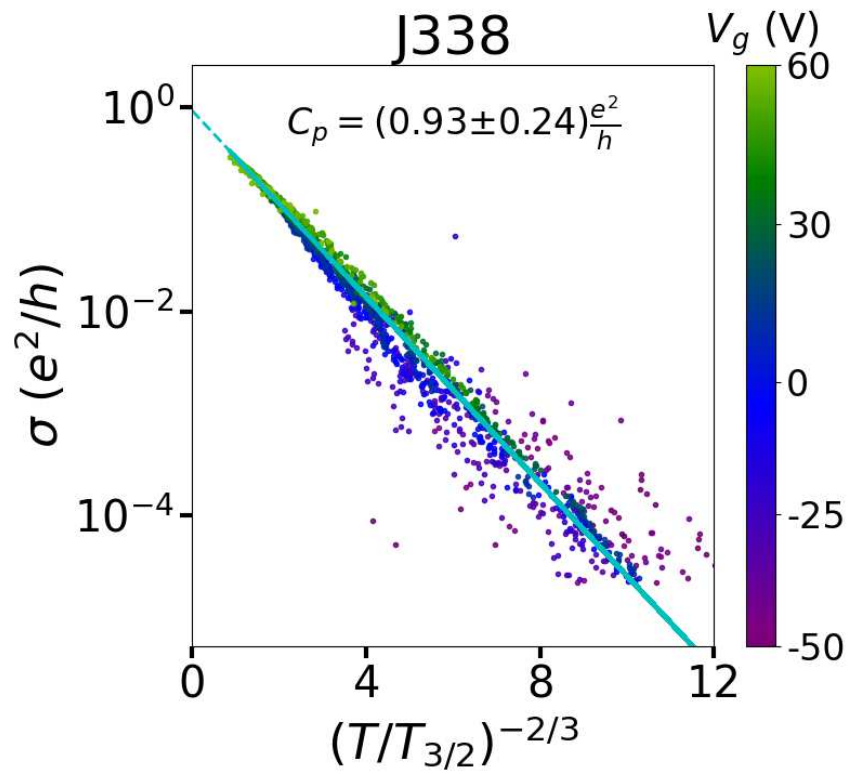


Figure A.2: Dimensionless J338's conductivity σ as a function of $(T/T_{3/2})^{-2/3}$. The linear fit is indicated by a cyan line, which is extrapolated to $T^{-2/3} = 0$ and intercepted with the y -axis. This intersection gives a value close to the quantum conductance e^2/h .

Appendix B

On the presence of Helium gas at atmospheric pressure

An unexpected phenomenon occurred with J12B-top at $T = 300$ K, as shown by the black curve in Fig. 2.53h. All the data presented in Fig. 2.52 were taken in primary vacuum ($\sim 10^{-3}$ mbar) except for this single voltage sweep, where the chamber was filled with He at near atmospheric pressure. This phenomenon was studied in more detail on another device, namely J35A, and shown in Fig. B.1. J35A was annealed at $T = 600$ K in vacuum twice, for 16.2 min and 28.4 min the first and second time respectively. The data shown in Fig. B.1b was obtained after the second annealing, before and after introducing helium in the chamber. The blue curve was obtained under vacuum and the orange curve was obtained with the chamber full of helium. As we can see, the resistance of the device increased under Helium atmosphere. The return to vacuum did not reverse the effect, as shown by the green curve. This phenomenon has been observed in different devices, with Jjedi01 devices being the most affected ones. Either there is a helium intercalation between the MoS₂ and the contacts, or the residual impurities present in the helium gas react strongly with the MoS₂ device.

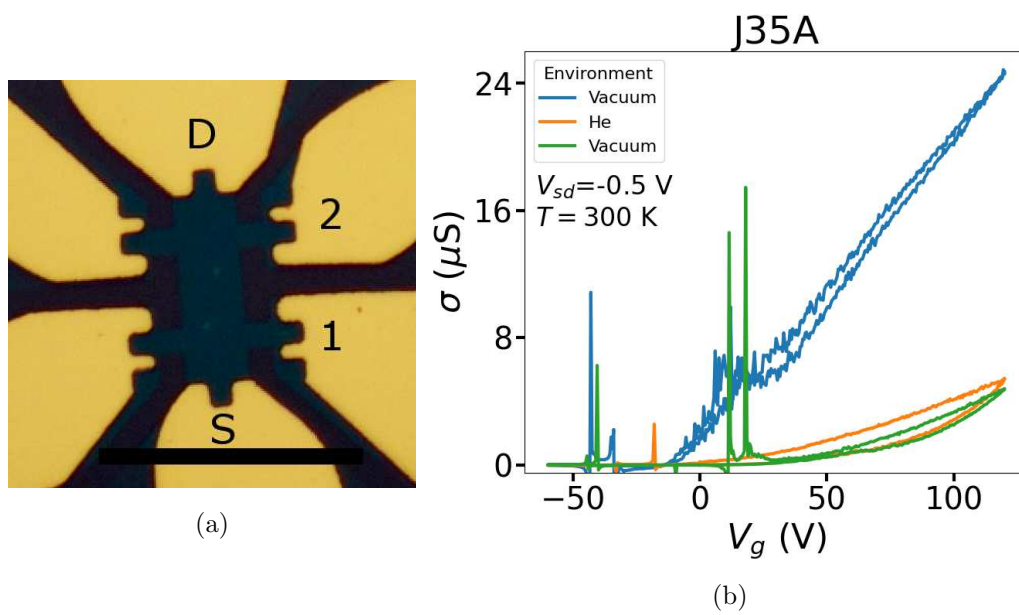


Figure B.1: Effect of pressure on device's performance. (a) Device J35A, scale bar = 25 μm . (b) Transfer curves taken same electrical conditions but different ambient conditions: under vacuum (blue curve), under He at close atmospheric pressure (orange curve), and going back to vacuum (green curve). Going back to vacuum after exposing the sample to He does not reverse its effect.

Bibliography

- [1] J. T. Ye et al. “Superconducting Dome in a Gate-Tuned Band Insulator”. In: *Science* 338.6111 (2012), pp. 1193–1196. DOI: [10.1126/science.1228006](https://doi.org/10.1126/science.1228006).
- [2] Subhamoy Ghatak, Atindra Nath Pal, and Arindam Ghosh. “Nature of Electronic States in Atomically Thin MoS₂ Field-Effect Transistors”. In: *ACS Nano* 5.10 (Sept. 2011), pp. 7707–7712. DOI: [10.1021/nm202852j](https://doi.org/10.1021/nm202852j).
- [3] Deep Jariwala et al. “Band-like transport in high mobility unencapsulated single-layer MoS₂ transistors”. In: *Applied Physics Letters* 102.17 (Apr. 2013), p. 173107. DOI: [10.1063/1.4803920](https://doi.org/10.1063/1.4803920).
- [4] Hao Qiu et al. “Hopping transport through defect-induced localized states in molybdenum disulphide”. In: *Nature Communications* 4.1 (Oct. 2013), p. 2642. ISSN: 2041-1723. DOI: [10.1038/ncomms3642](https://doi.org/10.1038/ncomms3642).
- [5] Byoung Hee Moon et al. “Soft Coulomb gap and asymmetric scaling towards metal-insulator quantum criticality in multilayer MoS₂”. In: *Nature Communications* 9.1 (May 2018), p. 2052. ISSN: 2041-1723. DOI: [10.1038/s41467-018-04474-4](https://doi.org/10.1038/s41467-018-04474-4).
- [6] N. Papadopoulos, G. A. Steele, and H. S. J. van der Zant. “Efros-Shklovskii variable range hopping and nonlinear transport in 1T/1T'-MoS₂”. In: *Physical Review B* 96.23 (Dec. 2017), p. 235436. DOI: [10.1103/physrevb.96.235436](https://doi.org/10.1103/physrevb.96.235436).
- [7] Fang Wang et al. “Superconductor-insulator transition in space charge doped one unit cell Bi_{2.1}Sr_{1.9}CaCu₂O_{8+x}”. In: *Nature Communications* 12.1 (May 2021), p. 2926. ISSN: 2041-1723. DOI: [10.1038/s41467-021-23183-z](https://doi.org/10.1038/s41467-021-23183-z).
- [8] Nihar R. Pradhan et al. “Metal to Insulator Quantum-Phase Transition in Few-Layered ReS₂”. In: *Nano Letters* 15.12 (Nov. 2015), pp. 8377–8384. DOI: [10.1021/acs.nanolett.5b04100](https://doi.org/10.1021/acs.nanolett.5b04100).
- [9] Kristen Kaasbjerg, Tony Low, and Antti-Pekka Jauho. “Electron and hole transport in disordered monolayer MoS₂: Atomic vacancy induced short-range and Coulomb disorder scattering”. In: *Phys. Rev. B* 100 (11 Sept. 2019), p. 115409. DOI: [10.1103/PhysRevB.100.115409](https://doi.org/10.1103/PhysRevB.100.115409).
- [10] Zhihao Yu et al. “Towards intrinsic charge transport in monolayer molybdenum disulfide by defect and interface engineering”. In: *Nature Communications* 5.1 (Oct. 2014), p. 5290. ISSN: 2041-1723. DOI: [10.1038/ncomms6290](https://doi.org/10.1038/ncomms6290).
- [11] Wenjuan Zhu et al. “Electronic transport and device prospects of monolayer molybdenum disulphide grown by chemical vapour deposition”. In: *Nature Communications* 5.1 (Jan. 2014), p. 3087. ISSN: 2041-1723. DOI: [10.1038/ncomms4087](https://doi.org/10.1038/ncomms4087).
- [12] Hennrik Schmidt et al. “Transport Properties of Monolayer MoS₂ Grown by Chemical Vapor Deposition”. In: *Nano Letters* 14.4 (2014). PMID: 24640984, pp. 1909–1913. DOI: [10.1021/nl4046922](https://doi.org/10.1021/nl4046922).

- [13] Yuanyuan Pan et al. “Reexamination of the Schottky Barrier Heights in Monolayer MoS₂ Field-Effect Transistors”. In: *ACS Applied Nano Materials* 2.8 (July 2019), pp. 4717–4726. DOI: [10.1021/acsanm.9b00200](https://doi.org/10.1021/acsanm.9b00200).
- [14] Faisal Ahmed et al. “Carrier transport at the metal–MoS₂ interface”. In: *Nanoscale* 7 (20 2015), pp. 9222–9228. DOI: [10.1039/C5NR01044F](https://doi.org/10.1039/C5NR01044F).
- [15] Changsik Kim et al. “Fermi Level Pinning at Electrical Metal Contacts of Monolayer Molybdenum Dichalcogenides”. In: *ACS Nano* 11.2 (2017), pp. 1588–1596. DOI: [10.1021/acsnano.6b07159](https://doi.org/10.1021/acsnano.6b07159).
- [16] Alexander V. Kolobov and Junji Tominaga. In: *Two-Dimensional Transition-Metal Dichalcogenides*. Cham: Springer International Publishing, 2016, pp. 1–5. DOI: [10.1007/978-3-319-31450-1_1](https://doi.org/10.1007/978-3-319-31450-1_1).
- [17] Shang-Chun Lu and Jean-Pierre Leburton. “Electronic structures of defects and magnetic impurities in MoS₂ monolayers”. In: *Nanoscale Research Letters* 9.1 (Dec. 2014), p. 676. DOI: [10.1186/1556-276X-9-676](https://doi.org/10.1186/1556-276X-9-676).
- [18] Kin Fai Mak et al. “Atomically Thin MoS₂: A New Direct-Gap Semiconductor”. In: *Phys. Rev. Lett.* 105 (13 Sept. 2010), p. 136805. DOI: [10.1103/PhysRevLett.105.136805](https://doi.org/10.1103/PhysRevLett.105.136805).
- [19] Wu Shi et al. “Superconductivity Series in Transition Metal Dichalcogenides by Ionic Gating”. In: *Scientific Reports* 5.1 (Aug. 2015), p. 12534. DOI: [10.1038/srep12534](https://doi.org/10.1038/srep12534).
- [20] Na Li et al. “Large-scale flexible and transparent electronics based on monolayer molybdenum disulfide field-effect transistors”. In: *Nature Electronics* 3.11 (Nov. 2020), pp. 711–717. DOI: [10.1038/s41928-020-00475-8](https://doi.org/10.1038/s41928-020-00475-8).
- [21] Eric Singh et al. “Flexible Molybdenum Disulfide (MoS₂) Atomic Layers for Wearable Electronics and Optoelectronics”. In: *ACS Applied Materials & Interfaces* 11.12 (2019), pp. 11061–11105. DOI: [10.1021/acsam.8b19859](https://doi.org/10.1021/acsam.8b19859).
- [22] *Molybdenum Disulfide (MoS₂): Theory & Applications*. <https://www.ossila.com/en-eu/pages/molybdenum-disulfide-MoS2>. Accessed: 2022-05-26.
- [23] E. Ridolfi et al. “A tight-binding model for MoS₂ monolayers”. In: *Journal of Physics: Condensed Matter* 27.36 (Aug. 2015), p. 365501. DOI: [10.1088/0953-8984/27/36/365501](https://doi.org/10.1088/0953-8984/27/36/365501).
- [24] Erik Piatti et al. “Multi-Valley Superconductivity in Ion-Gated MoS₂ Layers”. In: *Nano Letters* 18.8 (2018), pp. 4821–4830. DOI: [10.1021/acs.nanolett.8b01390](https://doi.org/10.1021/acs.nanolett.8b01390).
- [25] Katsuyoshi Kobayashi and Jun Yamauchi. “Electronic structure and scanning-tunneling-microscopy image of molybdenum dichalcogenide surfaces”. In: *Phys. Rev. B* 51 (23 June 1995), pp. 17085–17095. DOI: [10.1103/PhysRevB.51.17085](https://doi.org/10.1103/PhysRevB.51.17085).
- [26] Andrea Splendiani et al. “Emerging Photoluminescence in Monolayer MoS₂”. In: *Nano Letters* 10.4 (2010), pp. 1271–1275. DOI: [10.1021/nl903868w](https://doi.org/10.1021/nl903868w).
- [27] Fang Wang et al. “Superconductor-insulator transition in space charge doped one unit cell Bi_{2.1}Sr_{1.9}CaCu₂O_{8+x}”. In: *Nature Communications* 12.1 (May 2021), p. 2926. ISSN: 2041-1723. DOI: [10.1038/s41467-021-23183-z](https://doi.org/10.1038/s41467-021-23183-z).
- [28] Gui-Bin Liu et al. “Three-band tight-binding model for monolayers of group-VIB transition metal dichalcogenides”. In: *Phys. Rev. B* 88 (8 Aug. 2013), p. 085433. DOI: [10.1103/PhysRevB.88.085433](https://doi.org/10.1103/PhysRevB.88.085433).

- [29] Z. Y. Zhu, Y. C. Cheng, and U. Schwingenschlögl. “Giant spin-orbit-induced spin splitting in two-dimensional transition-metal dichalcogenide semiconductors”. In: *Phys. Rev. B* 84 (15 Oct. 2011), p. 153402. DOI: [10.1103/PhysRevB.84.153402](https://doi.org/10.1103/PhysRevB.84.153402).
- [30] Di Xiao et al. “Coupled Spin and Valley Physics in Monolayers of MoS₂ and Other Group-VI Dichalcogenides”. In: *Phys. Rev. Lett.* 108 (19 May 2012), p. 196802. DOI: [10.1103/PhysRevLett.108.196802](https://doi.org/10.1103/PhysRevLett.108.196802).
- [31] Dirk van Delft and Peter Kes. “The discovery of superconductivity”. In: *Physics Today* 63.9 (2010), pp. 38–43. DOI: [10.1063/1.3490499](https://doi.org/10.1063/1.3490499).
- [32] J. Bardeen, L. N. Cooper, and J. R. Schrieffer. “Microscopic Theory of Superconductivity”. In: *Phys. Rev.* 106 (1 Apr. 1957), pp. 162–164. DOI: [10.1103/PhysRev.106.162](https://doi.org/10.1103/PhysRev.106.162).
- [33] Nobel Foundation. *The Nobel Prize in Physics*. 1972. URL: <https://www.nobelprize.org/prizes/physics/1972/summary/>.
- [34] J. M. Lu et al. “Evidence for two-dimensional Ising superconductivity in gated MoS₂”. In: *Science* 350.6266 (Dec. 2015), pp. 1353–1357. DOI: [10.1126/science.aab2277](https://doi.org/10.1126/science.aab2277).
- [35] Yu Saito et al. “Superconductivity protected by spin–valley locking in ion-gated MoS₂”. In: *Nature Physics* 12.2 (Feb. 2016), pp. 144–149. ISSN: 1745-2481. DOI: [10.1038/nphys3580](https://doi.org/10.1038/nphys3580).
- [36] Benjamin T. Zhou et al. “Ising superconductivity and Majorana fermions in transition-metal dichalcogenides”. In: *Phys. Rev. B* 93 (18 May 2016), p. 180501. DOI: [10.1103/PhysRevB.93.180501](https://doi.org/10.1103/PhysRevB.93.180501).
- [37] B.D. Josephson. “Possible new effects in superconductive tunnelling”. In: *Physics Letters* 1.7 (1962), pp. 251–253. ISSN: 0031-9163. DOI: [https://doi.org/10.1016/0031-9163\(62\)91369-0](https://doi.org/10.1016/0031-9163(62)91369-0).
- [38] Nobel Foundation. *The Nobel Prize in Physics*. 1973. URL: <https://www.nobelprize.org/prizes/physics/1973/summary/>.
- [39] I. Sochnikov, D. Davino, and B. Kalisky. “dc SQUID Design with Femtotesla Sensitivity for Quantum-Ready Readouts”. In: *Phys. Rev. Applied* 14 (1 July 2020), p. 014020. DOI: [10.1103/PhysRevApplied.14.014020](https://doi.org/10.1103/PhysRevApplied.14.014020).
- [40] S. Kono et al. “Breaking the trade-off between fast control and long lifetime of a superconducting qubit”. In: *Nature Communications* 11.1 (July 2020), p. 3683. ISSN: 2041-1723. DOI: [10.1038/s41467-020-17511-y](https://doi.org/10.1038/s41467-020-17511-y).
- [41] Chad Rigetti et al. “Superconducting qubit in a waveguide cavity with a coherence time approaching 0.1 ms”. In: *Phys. Rev. B* 86 (10 Sept. 2012), p. 100506. DOI: [10.1103/PhysRevB.86.100506](https://doi.org/10.1103/PhysRevB.86.100506).
- [42] B. Dimov et al. “The asynchronous rapid single-flux quantum electronics - a promising alternative for the development of high-performance digital circuits”. In: *Advances in Radio Science* 6 (2008), pp. 165–173. DOI: [10.5194/ars-6-165-2008](https://doi.org/10.5194/ars-6-165-2008).
- [43] Sujay B. Desai et al. “MoS₂ transistors with 1-nanometer gate lengths”. In: *Science* 354.6308 (2016), pp. 99–102. DOI: [10.1126/science.aah4698](https://doi.org/10.1126/science.aah4698).
- [44] Davide Costanzo et al. “Gate-induced superconductivity in atomically thin MoS₂ crystals”. In: *Nature Nanotechnology* 11.4 (Apr. 2016), pp. 339–344. ISSN: 1748-3395. DOI: [10.1038/nnano.2015.314](https://doi.org/10.1038/nnano.2015.314).

- [45] Masaro Yoshida et al. “Electrostatic and electrochemical tuning of superconductivity in two-dimensional NbSe₂ crystals”. In: *Applied Physics Letters* 108.20 (2016), p. 202602. DOI: [10.1063/1.4950804](https://doi.org/10.1063/1.4950804).
- [46] Sanghyun Jo et al. “Electrostatically Induced Superconductivity at the Surface of WS₂”. In: *Nano Letters* 15.2 (2015), pp. 1197–1202. DOI: [10.1021/nl504314c](https://doi.org/10.1021/nl504314c).
- [47] Junwen Zeng et al. “Gate-Induced Interfacial Superconductivity in 1T-SnSe₂”. In: *Nano Letters* 18.2 (2018), pp. 1410–1415. DOI: [10.1021/acs.nanolett.7b05157](https://doi.org/10.1021/acs.nanolett.7b05157).
- [48] V. Mourik et al. “Signatures of Majorana Fermions in Hybrid Superconductor-Semiconductor Nanowire Devices”. In: *Science* 336.6084 (2012), pp. 1003–1007. DOI: [10.1126/science.1222360](https://doi.org/10.1126/science.1222360).
- [49] Yuxuan Wang et al. “Topological superconducting phases from inversion symmetry breaking order in spin-orbit-coupled systems”. In: *Phys. Rev. B* 93 (13 Apr. 2016), p. 134512. DOI: [10.1103/PhysRevB.93.134512](https://doi.org/10.1103/PhysRevB.93.134512).
- [50] Rui-Lin Chu et al. “Spin-orbit-coupled quantum wires and Majorana fermions on zigzag edges of monolayer transition-metal dichalcogenides”. In: *Phys. Rev. B* 89 (15 Apr. 2014), p. 155317. DOI: [10.1103/PhysRevB.89.155317](https://doi.org/10.1103/PhysRevB.89.155317).
- [51] Peng Zhang et al. “Observation of topological superconductivity on the surface of an iron-based superconductor”. In: *Science* 360.6385 (2018), pp. 182–186. DOI: [10.1126/science.aan4596](https://doi.org/10.1126/science.aan4596).
- [52] Sidney Shapiro. “Josephson Currents in Superconducting Tunneling: The Effect of Microwaves and Other Observations”. In: *Phys. Rev. Lett.* 11 (2 July 1963), pp. 80–82. DOI: [10.1103/PhysRevLett.11.80](https://doi.org/10.1103/PhysRevLett.11.80).
- [53] *A Primary Voltage Standard for the Whole World*. <https://www.nist.gov/news-events/news/2013/04/primary-voltage-standard-whole-world>. Accessed: 2022-07-26.
- [54] Roberta Caruso et al. “Properties of Ferromagnetic Josephson Junctions for Memory Applications”. In: *IEEE Transactions on Applied Superconductivity* 28.7 (2018), pp. 1–6. DOI: [10.1109/TASC.2018.2836979](https://doi.org/10.1109/TASC.2018.2836979).
- [55] K. S. Novoselov et al. “Two-dimensional atomic crystals”. In: *Proceedings of the National Academy of Sciences* 102.30 (2005), pp. 10451–10453. DOI: [10.1073/pnas.0502848102](https://doi.org/10.1073/pnas.0502848102).
- [56] B. Radisavljevic et al. “Single-layer MoS₂ transistors”. In: *Nature Nanotechnology* 6.3 (Mar. 2011), pp. 147–150. ISSN: 1748-3395. DOI: [10.1038/nnano.2010.279](https://doi.org/10.1038/nnano.2010.279).
- [57] Chunlan Wang, Yongle Song, and Hao Huang. “Evolution Application of Two-Dimensional MoS₂-Based Field-Effect Transistors”. In: *Nanomaterials* 12.18 (2022). ISSN: 2079-4991. DOI: [10.3390/nano12183233](https://doi.org/10.3390/nano12183233).
- [58] P. Drude. “Zur Elektronentheorie der Metalle”. In: *Annalen der Physik* 306.3 (1900), pp. 566–613. DOI: [10.1002/andp.19003060312](https://doi.org/10.1002/andp.19003060312).
- [59] H. A. Lorentz. “Ergebnisse und Probleme der Elektronentheorie”. In: (1879). DOI: [10.1007/978-3-642-91915-2](https://doi.org/10.1007/978-3-642-91915-2).
- [60] E. H. Hall. “On a New Action of the Magnet on Electric Currents”. In: *American Journal of Mathematics* 2.3 (1879), pp. 287–292. ISSN: 00029327, 10806377. URL: <http://www.jstor.org/stable/2369245>.

- [61] P. W. Anderson. “Absence of Diffusion in Certain Random Lattices”. In: *Physical Review* 109.5 (Mar. 1958), pp. 1492–1505. DOI: [10.1103/physrev.109.1492](https://doi.org/10.1103/physrev.109.1492).
- [62] N. F. Mott. “The transition to the metallic state”. In: *The Philosophical Magazine: A Journal of Theoretical Experimental and Applied Physics* 6.62 (1961), pp. 287–309. DOI: [10.1080/14786436108243318](https://doi.org/10.1080/14786436108243318).
- [63] Nobel Foundation. *The Nobel Prize in Physics*. 1977. URL: <https://www.nobelprize.org/prizes/physics/1977/summary/>.
- [64] Boris I. Shklovskii and Alex L. Efros. *Electronic Properties of Doped Semiconductors*. Springer Berlin Heidelberg, 1984. DOI: [10.1007/978-3-662-02403-4](https://doi.org/10.1007/978-3-662-02403-4).
- [65] Nevill Francis Mott. *Metal-Insulator Transitions*. CRC Press, 1990. ISBN: 9781466576452.
- [66] Ferdinand Evers and Alexander D. Mirlin. “Anderson transitions”. In: *Rev. Mod. Phys.* 80 (4 Oct. 2008), pp. 1355–1417. DOI: [10.1103/RevModPhys.80.1355](https://doi.org/10.1103/RevModPhys.80.1355).
- [67] N. F. MOTT. “Metal-Insulator Transition”. In: *Rev. Mod. Phys.* 40 (4 Oct. 1968), pp. 677–683. DOI: [10.1103/RevModPhys.40.677](https://doi.org/10.1103/RevModPhys.40.677).
- [68] Peter Phillip Edwards and Michell J. Sienko. “Universality aspects of the metal-nonmetal transition in condensed media”. In: *Phys. Rev. B* 17 (6 Mar. 1978), pp. 2575–2581. DOI: [10.1103/PhysRevB.17.2575](https://doi.org/10.1103/PhysRevB.17.2575).
- [69] N. F. Mott. “The electrical properties of liquid mercury”. In: *The Philosophical Magazine: A Journal of Theoretical Experimental and Applied Physics* 13.125 (1966), pp. 989–1014. DOI: [10.1080/14786436608213149](https://doi.org/10.1080/14786436608213149).
- [70] Morrel H. Cohen, H. Fritzsche, and S. R. Ovshinsky. “Simple Band Model for Amorphous Semiconducting Alloys”. In: *Phys. Rev. Lett.* 22 (20 May 1969), pp. 1065–1068. DOI: [10.1103/PhysRevLett.22.1065](https://doi.org/10.1103/PhysRevLett.22.1065).
- [71] N. F. Mott. “The conductivity near a mobility edge”. In: *Philosophical Magazine B* 49.6 (1984), pp. L75–L82. DOI: [10.1080/13642818408227643](https://doi.org/10.1080/13642818408227643).
- [72] A. F. Ioffe and A. R. Regel. “Progress in Semiconductors”. In: *London: Heywood* (1960), pp. 239–87.
- [73] S. Das Sarma and E. H. Hwang. “Two-dimensional metal-insulator transition as a strong localization induced crossover phenomenon”. In: *Physical Review B* 89.23 (June 2014), p. 235423. DOI: [10.1103/physrevb.89.235423](https://doi.org/10.1103/physrevb.89.235423).
- [74] Britton W. H. Baugher et al. “Intrinsic Electronic Transport Properties of High-Quality Monolayer and Bilayer MoS₂”. In: *Nano Letters* 13.9 (2013). PMID: 23930826, pp. 4212–4216. DOI: [10.1021/nl401916s](https://doi.org/10.1021/nl401916s).
- [75] Branimir Radisavljevic and Andras Kis. “Mobility engineering and a metal–insulator transition in monolayer MoS₂”. In: *Nature Materials* 12.9 (Sept. 2013), pp. 815–820. ISSN: 1476-4660. DOI: [10.1038/nmat3687](https://doi.org/10.1038/nmat3687).
- [76] Dmitry Ovchinnikov et al. “Electrical Transport Properties of Single-Layer WS₂”. In: *ACS Nano* 8.8 (July 2014), pp. 8174–8181. DOI: [10.1021/nn502362b](https://doi.org/10.1021/nn502362b).
- [77] E. Abrahams et al. “Scaling Theory of Localization: Absence of Quantum Diffusion in Two Dimensions”. In: *Physical Review Letters* 42.10 (Mar. 1979), pp. 673–676. DOI: [10.1103/physrevlett.42.673](https://doi.org/10.1103/physrevlett.42.673).
- [78] D. J. Thouless. “Maximum Metallic Resistance in Thin Wires”. In: *Phys. Rev. Lett.* 39 (18 Oct. 1977), pp. 1167–1169. DOI: [10.1103/PhysRevLett.39.1167](https://doi.org/10.1103/PhysRevLett.39.1167).

- [79] Nevill Francis Mott. *Metal-Insulator Transitions*. CRC Press, 1990, p. 51. ISBN: 9781466576452.
- [80] N.F. Mott. “Conduction in glasses containing transition metal ions”. In: *Journal of Non-Crystalline Solids* 1.1 (Dec. 1968), pp. 1–17. ISSN: 0022-3093. DOI: [https://doi.org/10.1016/0022-3093\(68\)90002-1](https://doi.org/10.1016/0022-3093(68)90002-1).
- [81] Vinay Ambegaokar, B. I. Halperin, and J. S. Langer. “Hopping Conductivity in Disordered Systems”. In: *Phys. Rev. B* 4 (8 Oct. 1971), pp. 2612–2620. DOI: [10.1103/PhysRevB.4.2612](https://doi.org/10.1103/PhysRevB.4.2612).
- [82] M. Pollak. “A percolation treatment of dc hopping conduction”. In: *Journal of Non-Crystalline Solids* 11.1 (1972), pp. 1–24. ISSN: 0022-3093. DOI: [https://doi.org/10.1016/0022-3093\(72\)90304-3](https://doi.org/10.1016/0022-3093(72)90304-3).
- [83] A. L. Efros and B. I. Shklovskii. “Coulomb gap and low temperature conductivity of disordered systems”. In: *Journal of Physics C: Solid State Physics* 8.4 (Feb. 1975), pp. L49–L51. DOI: [10.1088/0022-3719/8/4/003](https://doi.org/10.1088/0022-3719/8/4/003).
- [84] Boris Isaakovich Shklovskii and Alex L. Efros. “Electronic properties of doped semiconductors”. In: Springer-Verlag Berlin Heidelberg New York, 1984. DOI: [10.1007/978-3-662-02403-4](https://doi.org/10.1007/978-3-662-02403-4).
- [85] V. L. Nguen. “Two-Dimensional Hopping Conduction in a Magnetic Field”. In: *Fizika i Tekhnika Poluprovodnikov* 18.2 (1984), pp. 335–339.
- [86] Nguyen Van Lien and B.I. Shklovskii. “Hopping conduction in strong electric fields and directed percolation”. In: *Solid State Communications* 38.2 (1981), pp. 99–102. ISSN: 0038-1098. DOI: [https://doi.org/10.1016/0038-1098\(81\)90798-5](https://doi.org/10.1016/0038-1098(81)90798-5).
- [87] I. Zavaritskaya. “Hopping conductivity of germanium bicrystals in strong electric fields at $T < 1$ K”. In: *American Institute of Physics* 41.6 (1985), p. 279.
- [88] A. V. Nenashev et al. “Hopping conduction in strong electric fields: Negative differential conductivity”. In: *Phys. Rev. B* 78 (16 2008), p. 165207. DOI: [10.1103/PhysRevB.78.165207](https://doi.org/10.1103/PhysRevB.78.165207).
- [89] Chieh-I Liu et al. “Variable range hopping and nonlinear transport in monolayer epitaxial graphene grown on SiC”. In: *Semiconductor Science and Technology* 31.10 (2016), p. 105008. DOI: [10.1088/0268-1242/31/10/105008](https://doi.org/10.1088/0268-1242/31/10/105008).
- [90] Itzhak Webman, Joshua Jortner, and Morrel H. Cohen. “Numerical simulation of electrical conductivity in microscopically inhomogeneous materials”. In: *Phys. Rev. B* 11 (8 Apr. 1975), pp. 2885–2892. DOI: [10.1103/PhysRevB.11.2885](https://doi.org/10.1103/PhysRevB.11.2885).
- [91] S. Das Sarma et al. “Two-Dimensional Metal-Insulator Transition as a Percolation Transition in a High-Mobility Electron System”. In: *Physical Review Letters* 94.13 (Apr. 2005), p. 136401. DOI: [10.1103/physrevlett.94.136401](https://doi.org/10.1103/physrevlett.94.136401).
- [92] L. A. Tracy et al. “Observation of percolation-induced two-dimensional metal-insulator transition in a Si MOSFET”. In: *Phys. Rev. B* 79 (23 June 2009), p. 235307. DOI: [10.1103/PhysRevB.79.235307](https://doi.org/10.1103/PhysRevB.79.235307).
- [93] S. Das Sarma, E. H. Hwang, and Qiuzi Li. “Two-dimensional metal-insulator transition as a potential fluctuation driven semiclassical transport phenomenon”. In: *Physical Review B* 88.15 (Oct. 2013), p. 155310. DOI: [10.1103/physrevb.88.155310](https://doi.org/10.1103/physrevb.88.155310).
- [94] Raymond T. Tung. “The physics and chemistry of the Schottky barrier height”. In: *Applied Physics Reviews* 1.1 (2014), p. 011304. DOI: [10.1063/1.4858400](https://doi.org/10.1063/1.4858400).

- [95] Jen-Ru Chen et al. “Control of Schottky Barriers in Single Layer MoS₂ Transistors with Ferromagnetic Contacts”. In: *Nano Letters* 13.7 (June 2013), pp. 3106–3110. DOI: [10.1021/nl4010157](https://doi.org/10.1021/nl4010157).
- [96] Yuan Liu et al. “Approaching the Schottky–Mott limit in van der Waals metal–semiconductor junctions”. In: *Nature* 557.7707 (May 2018), pp. 696–700. ISSN: 1476-4687. DOI: [10.1038/s41586-018-0129-8](https://doi.org/10.1038/s41586-018-0129-8).
- [97] Biddut K. Sarker and Saiful I. Khondaker. “Thermionic Emission and Tunneling at Carbon Nanotube–Organic Semiconductor Interface”. In: *ACS Nano* 6.6 (2012), pp. 4993–4999. DOI: [10.1021/nm300544v](https://doi.org/10.1021/nm300544v).
- [98] O. W. Richardson. *On the Negative Radiation from Hot Platinum*. Vol. 11. Proceedings - Cambridge Philosophical Society, 1900, pp. 286–295. URL: <https://www.biodiversitylibrary.org/item/108210>.
- [99] Saul Dushman. “Electron Emission from Metals as a Function of Temperature”. In: *Phys. Rev.* 21 (6 June 1923), pp. 623–636. DOI: [10.1103/PhysRev.21.623](https://doi.org/10.1103/PhysRev.21.623).
- [100] Nobel Foundation. *The Nobel Prize in Physics*. 1928. URL: <https://www.nobelprize.org/prizes/physics/1928/summary/>.
- [101] Amro Anwar et al. “Effects of electron confinement on thermionic emission current in a modulation doped heterostructure”. In: *Journal of Applied Physics* 85.5 (1999), pp. 2663–2666. DOI: [10.1063/1.369627](https://doi.org/10.1063/1.369627).
- [102] John G. Simmons. “Generalized Formula for the Electric Tunnel Effect between Similar Electrodes Separated by a Thin Insulating Film”. In: *Journal of Applied Physics* 34.6 (1963), pp. 1793–1803. DOI: [10.1063/1.1702682](https://doi.org/10.1063/1.1702682).
- [103] Ralph Howard Fowler and L. Nordheim. “Electron emission in intense electric fields”. In: *Proceedings of the Royal Society of London. Series A, Containing Papers of a Mathematical and Physical Character* 119.781 (1928), pp. 173–181. DOI: [10.1098/rspa.1928.0091](https://doi.org/10.1098/rspa.1928.0091).
- [104] Nobel Foundation. *The Nobel Prize in Physics*. 1956. URL: <https://www.nobelprize.org/prizes/physics/1956/summary/>.
- [105] Britannica. *Transistor*. URL: <https://www.britannica.com/technology/transistor/>.
- [106] Daniel Vaquero et al. “Ionic-Liquid Gating in Two-Dimensional TMDs: The Operation Principles and Spectroscopic Capabilities”. In: *Micromachines* 12.12 (2021). ISSN: 2072-666X. DOI: [10.3390/mi12121576](https://doi.org/10.3390/mi12121576).
- [107] Hehai Fang and Weida Hu. “Photogating in Low Dimensional Photodetectors”. In: *Advanced Science* 4.12 (2017), p. 1700323. DOI: <https://doi.org/10.1002/advs.201700323>.
- [108] Enxiu Wu et al. “Dynamically controllable polarity modulation of MoTe₂ field-effect transistors through ultraviolet light and electrostatic activation”. In: *Science Advances* 5.5 (2019), eaav3430. DOI: [10.1126/sciadv.aav3430](https://doi.org/10.1126/sciadv.aav3430).
- [109] Yu Yeats Andrew L. and Pan et al. “Persistent optical gating of a topological insulator”. eng. In: *Science advances* 1.9 (Oct. 2015), e1500640–e1500640. ISSN: 2375-2548. DOI: [10.1126/sciadv.1500640](https://doi.org/10.1126/sciadv.1500640).

- [110] L. J. van der PAUW. “A METHOD OF MEASURING SPECIFIC RESISTIVITY AND HALL EFFECT OF DISCS OF ARBITRARY SHAPE”. In: *Philips Research Reports* 13.1 (Feb. 1958), pp. 1–9. URL: https://aki.issp.u-tokyo.ac.jp/okano/WalWiki/etc/VDP_PRR_13_1.pdf.
- [111] Ossila. *Sheet Resistance Measurements of Thin Films*. URL: <https://www.ossila.com/en-eu/pages/sheet-resistance-theory/>.
- [112] Qingqing Ji et al. “Chemical vapour deposition of group-VIB metal dichalcogenide monolayers: engineered substrates from amorphous to single crystalline”. In: *Chem. Soc. Rev.* 44 (9 2015), pp. 2587–2602. DOI: [10.1039/C4CS00258J](https://doi.org/10.1039/C4CS00258J).
- [113] A.T. Charlie Johnson. <https://directory.seas.upenn.edu/a-t-charlie-johnson/>. Accessed: 2022-08-11.
- [114] KLayout. <https://www.klayout.de/intro.html>. Accessed: 2022-07-05.
- [115] Horiba scientific. *Raman spectroscopy*. URL: <https://www.horiba.com/esp/scientific/technologies/raman-imaging-and-spectroscopy/raman-spectroscopy/>.
- [116] Nobel Foundation. *The Nobel Prize in Physics*. 1930. URL: <https://www.nobelprize.org/prizes/physics/1930/summary/>.
- [117] Changgu Lee et al. “Anomalous Lattice Vibrations of Single- and Few-Layer MoS₂”. In: *ACS Nano* 4.5 (Apr. 2010), pp. 2695–2700. DOI: [10.1021/nm1003937](https://doi.org/10.1021/nm1003937).
- [118] Lurie Nanofabrication Facility Wiki. *Spectroscopic reflectometry*. URL: https://lnf-wiki.eecs.umich.edu/wiki/Spectroscopic_reflectometry/.
- [119] Sandro Mignuzzi et al. “Effect of disorder on Raman scattering of single-layer MoS₂”. In: *Physical Review B* 91.19 (May 2015), p. 195411. DOI: [10.1103/physrevb.91.195411](https://doi.org/10.1103/physrevb.91.195411).
- [120] Zahabul Islam et al. “Quality enhancement of low temperature metal organic chemical vapor deposited MoS₂: an experimental and computational investigation”. In: *Nanotechnology* 30.39 (July 2019), p. 395402. DOI: [10.1088/1361-6528/ab2c3a](https://doi.org/10.1088/1361-6528/ab2c3a).
- [121] H. Conrad et al. “Electroplasticity—the effect of electricity on the mechanical properties of metals”. In: *JOM* 42.9 (Sept. 1990), pp. 28–33. ISSN: 1543-1851. DOI: [10.1007/BF03221075](https://doi.org/10.1007/BF03221075).
- [122] Ignacio Gutiérrez-Lezama et al. “Ionic gate spectroscopy of 2D semiconductors”. In: *Nature Reviews Physics* 3.7 (July 2021), pp. 508–519. ISSN: 2522-5820. DOI: [10.1038/s42254-021-00317-2](https://doi.org/10.1038/s42254-021-00317-2).
- [123] Ulderico Ulissi et al. “Low-Polarization Lithium–Oxygen Battery Using [DEME][TFSI] Ionic Liquid Electrolyte”. In: *ChemSusChem* 11.1 (2018), pp. 229–236. DOI: <https://doi.org/10.1002/cssc.201701696>.
- [124] Rui Yang et al. “Multilayer MoS₂ transistors enabled by a facile dry-transfer technique and thermal annealing”. In: *Journal of Vacuum Science and Technology B: Nanotechnology and Microelectronics* 32 (Nov. 2014). DOI: [10.1116/1.4898117](https://doi.org/10.1116/1.4898117).
- [125] Adelmo Ortiz-Conde et al. “Revisiting MOSFET threshold voltage extraction methods”. In: *Microelectronics Reliability* 53.1 (2013), pp. 90–104. ISSN: 0026-2714. DOI: [10.1016/j.microrel.2012.09.015](https://doi.org/10.1016/j.microrel.2012.09.015).
- [126] Hyuk-Jun Kwon et al. “Electrical characteristics of multilayer MoS₂ transistors at real operating temperatures with different ambient conditions”. In: *Applied Physics Letters* 105.15 (2014), p. 152105. DOI: [10.1063/1.4898584](https://doi.org/10.1063/1.4898584).

- [127] G. He et al. “Thermally Assisted Nonvolatile Memory in Monolayer MoS₂ Transistors”. In: *Nano Letters* 16.10 (2016), pp. 6445–6451. ISSN: 15306992. DOI: [10.1021/acs.nanolett.6b02905](https://doi.org/10.1021/acs.nanolett.6b02905).
- [128] Naveen Kaushik et al. “Reversible hysteresis inversion in MoS₂ field effect transistors”. In: *npj 2D Materials and Applications* 1.1 (Oct. 2017), p. 34. ISSN: 2397-7132. DOI: [10.1038/s41699-017-0038-y](https://doi.org/10.1038/s41699-017-0038-y).
- [129] Jiawei Shu et al. “The intrinsic origin of hysteresis in MoS₂ field effect transistors”. In: *Nanoscale* 8.5 (2016), pp. 3049–3056. ISSN: 20403372. DOI: [10.1039/c5nr07336g](https://doi.org/10.1039/c5nr07336g).
- [130] Martin Egginger et al. “Current versus gate voltage hysteresis in organic field effect transistors”. In: *Monatshefte für Chemie - Chemical Monthly* 140.7 (July 2009), pp. 735–750. ISSN: 1434-4475. DOI: [10.1007/s00706-009-0149-z](https://doi.org/10.1007/s00706-009-0149-z).
- [131] Xiaolong Chen et al. “Electrically tunable physical properties of two-dimensional materials”. In: *Nano Today* 27 (Aug. 2019), pp. 99–119. DOI: [10.1016/j.nantod.2019.05.005](https://doi.org/10.1016/j.nantod.2019.05.005).
- [132] Byoung Hee Moon et al. “Quantum critical scaling for finite-temperature Mott-like metal-insulator crossover in few-layered MoS₂”. In: *Physical Review B* 102.24 (Dec. 2020), p. 245424. DOI: [10.1103/physrevb.102.245424](https://doi.org/10.1103/physrevb.102.245424).
- [133] Byoung Hee Moon. “Metal-insulator transition in two-dimensional transition metal dichalcogenides”. In: *Emergent Materials* 4.4 (Mar. 2021), pp. 989–998. DOI: [10.1007/s42247-021-00202-9](https://doi.org/10.1007/s42247-021-00202-9).
- [134] Huynh V. Phuc et al. “Tuning the Electronic Properties, Effective Mass and Carrier Mobility of MoS₂ Monolayer by Strain Engineering: First-Principle Calculations”. In: *Journal of Electronic Materials* 47.1 (Jan. 2018), pp. 730–736. ISSN: 1543-186X. DOI: [10.1007/s11664-017-5843-8](https://doi.org/10.1007/s11664-017-5843-8).
- [135] Hongliang Shi et al. “Quasiparticle band structures and optical properties of strained monolayer MoS₂ and WS₂”. In: *Physical Review B* 87 (15 Apr. 2013), p. 155304. DOI: [10.1103/PhysRevB.87.155304](https://doi.org/10.1103/PhysRevB.87.155304).
- [136] L. V. Keldysh. “Coulomb interaction in thin semiconductor and semimetal films”. In: *Soviet Journal of Experimental and Theoretical Physics Letters* 29 (June 1979), p. 658.
- [137] F. Giannazzo et al. “Impact of contact resistance on the electrical properties of MoS₂ transistors at practical operating temperatures”. In: *Beilstein journal of nanotechnology* 8.1 (2017), pp. 254–263. DOI: [10.3762/bjnano.8.28](https://doi.org/10.3762/bjnano.8.28).
- [138] Mehdi Salmani-Jelodar, Yaohua Tan, and Gerhard Klimeck. “Single layer MoS₂ band structure and transport”. In: *2011 International Semiconductor Device Research Symposium (ISDRS)*. IEEE, Dec. 2011. DOI: [10.1109/isdrs.2011.6135408](https://doi.org/10.1109/isdrs.2011.6135408).
- [139] Jianhong Xue et al. “Mott variable-range hopping transport in a MoS₂ nanoflake”. In: *RSC Adv.* 9 (31 2019), pp. 17885–17890. DOI: [10.1039/C9RA03150B](https://doi.org/10.1039/C9RA03150B).
- [140] Serge Luryi. “Quantum capacitance devices”. In: *Applied Physics Letters* 52.6 (1988), pp. 501–503. DOI: [10.1063/1.99649](https://doi.org/10.1063/1.99649).
- [141] K. Bennaceur et al. “Unveiling quantum Hall transport by Efros-Shklovskii to Mott variable-range hopping transition in graphene”. In: *Phys. Rev. B* 86 (8 Aug. 2012), p. 085433. DOI: [10.1103/PhysRevB.86.085433](https://doi.org/10.1103/PhysRevB.86.085433).

- [142] M. Furlan. “Electronic transport and the localization length in the quantum Hall effect”. In: *Physical Review B* 57.23 (June 1998), pp. 14818–14828. DOI: [10.1103/physrevb.57.14818](https://doi.org/10.1103/physrevb.57.14818).
- [143] F. W. Van Keuls et al. “Screening of the Coulomb interaction in two-dimensional variable-range hopping”. In: *Physical Review B* 56.3 (July 1997), pp. 1161–1169. DOI: [10.1103/physrevb.56.1161](https://doi.org/10.1103/physrevb.56.1161).
- [144] I Shlimak, K.-J Friedland, and S.D Baranovskii. “Hopping conductivity in gated δ -doped GaAs: universality of prefactor”. In: *Solid State Communications* 112.1 (Aug. 1999), pp. 21–24. DOI: [10.1016/s0038-1098\(99\)00286-0](https://doi.org/10.1016/s0038-1098(99)00286-0).
- [145] S. I. Khondaker et al. “Two-dimensional hopping conductivity in a δ -doped GaAs/Al_xGa_{1-x}As heterostructure”. In: *Physical Review B* 59.7 (Feb. 1999), pp. 4580–4583. DOI: [10.1103/physrevb.59.4580](https://doi.org/10.1103/physrevb.59.4580).
- [146] Whitney Mason et al. “Experimental evidence for a Coulomb gap in two dimensions”. In: *Physical Review B* 52.11 (Sept. 1995), pp. 7857–7859. DOI: [10.1103/physrevb.52.7857](https://doi.org/10.1103/physrevb.52.7857).
- [147] M. P Sarachik and P Dai. “Scaling of the conductivity of insulating Si:B: A temperature-independent hopping prefactor”. In: *Europhysics Letters (EPL)* 59.1 (July 2002), pp. 100–106. DOI: [10.1209/epl/i2002-00164-y](https://doi.org/10.1209/epl/i2002-00164-y).
- [148] A. L Efros and M. Pollak. “Electron-Electron Interactions in Disordered Systems”. In: *March 1*. De Gruyter, Dec. 1986, pp. 497–498. DOI: [10.1515/9783112494721-070](https://doi.org/10.1515/9783112494721-070).
- [149] Nevill Francis Mott. *Metal-Insulator Transitions*. CRC Press, 1990, p. 51. ISBN: 9781466576452.
- [150] L. Fleishman, D. C. Licciardello, and P. W. Anderson. “Elementary Excitations in the Fermi Glass”. In: *Physical Review Letters* 40.20 (May 1978), pp. 1340–1343. DOI: [10.1103/physrevlett.40.1340](https://doi.org/10.1103/physrevlett.40.1340).
- [151] I. L. Aleiner, D.G. Polyakov, and B.I. Shklovski. In: *22nd International Conference on the Physics of Semiconductors, Vancouver, 1994, edited by D.J. Lockwood World Scientific ... 1994*.
- [152] R Berkovits and B I Shklovskii. “Statistics of energy spectra of a strongly disordered system of interacting electrons”. In: *Journal of Physics: Condensed Matter* 11.3 (Jan. 1999), pp. 779–786. DOI: [10.1088/0953-8984/11/3/017](https://doi.org/10.1088/0953-8984/11/3/017).
- [153] V.I Kozub, S.D Baranovskii, and I Shlimak. “Fluctuation-stimulated variable-range hopping”. In: *Solid State Communications* 113.10 (Feb. 2000), pp. 587–591. DOI: [10.1016/s0038-1098\(99\)00537-2](https://doi.org/10.1016/s0038-1098(99)00537-2).
- [154] Songang Peng et al. “Metal-Contact-Induced Transition of Electrical Transport in Monolayer MoS₂: From Thermally Activated to Variable-Range Hopping”. In: *Advanced Electronic Materials* 5.7 (June 2019), p. 1900042. DOI: [10.1002/aelm.201900042](https://doi.org/10.1002/aelm.201900042).
- [155] A. Pérez-Garrido et al. “Conductivity of the two-dimensional Coulomb glass”. In: *Physical Review B* 55.14 (Apr. 1997), R8630–R8633. DOI: [10.1103/physrevb.55.r8630](https://doi.org/10.1103/physrevb.55.r8630).
- [156] Kristen Kaasbjerg, Kristian S. Thygesen, and Karsten W. Jacobsen. “Phonon-limited mobility in *n*-type single-layer MoS₂ from first principles”. In: *Phys. Rev. B* 85 (11 Mar. 2012), p. 115317. DOI: [10.1103/PhysRevB.85.115317](https://doi.org/10.1103/PhysRevB.85.115317).

- [157] S. Das Sarma and E. H. Hwang. “Screening and transport in 2D semiconductor systems at low temperatures”. In: *Scientific Reports* 5.1 (Nov. 2015), p. 16655. ISSN: 2045-2322. DOI: [10.1038/srep16655](https://doi.org/10.1038/srep16655).
- [158] Debdeep Jena and Aniruddha Konar. “Enhancement of Carrier Mobility in Semiconductor Nanostructures by Dielectric Engineering”. In: *Phys. Rev. Lett.* 98 (13 Mar. 2007), p. 136805. DOI: [10.1103/PhysRevLett.98.136805](https://doi.org/10.1103/PhysRevLett.98.136805).
- [159] Matthew P. A. Fisher. “Quantum phase transitions in disordered two-dimensional superconductors”. In: *Phys. Rev. Lett.* 65 (7 Aug. 1990), pp. 923–926. DOI: [10.1103/PhysRevLett.65.923](https://doi.org/10.1103/PhysRevLett.65.923).
- [160] Matthew P. A. Fisher, G. Grinstein, and S. M. Girvin. “Presence of quantum diffusion in two dimensions: Universal resistance at the superconductor-insulator transition”. In: *Phys. Rev. Lett.* 64 (5 Jan. 1990), pp. 587–590. DOI: [10.1103/PhysRevLett.64.587](https://doi.org/10.1103/PhysRevLett.64.587).
- [161] H. Aubin et al. “Magnetic-field-induced quantum superconductor-insulator transition in $\text{Nb}_{0.15}\text{Si}_{0.85}$ ”. In: *Phys. Rev. B* 73 (9 Mar. 2006), p. 094521. DOI: [10.1103/PhysRevB.73.094521](https://doi.org/10.1103/PhysRevB.73.094521).
- [162] Ping V. Lin. “Critical Behavior of a Strongly Disordered 2D Electron System: The Cases of Long-Range and Screened Coulomb Interactions”. In: *Phys. Rev. Lett.* 114 (16 Apr. 2015), p. 166401. DOI: [10.1103/PhysRevLett.114.166401](https://doi.org/10.1103/PhysRevLett.114.166401).
- [163] Nan Fang and Kosuke Nagashio. “Band tail interface states and quantum capacitance in a monolayer molybdenum disulfide field-effect-transistor”. In: *Journal of Physics D: Applied Physics* 51.6 (16 Jan. 2018), p. 065110. DOI: [10.1088/1361-6463/aaa58c](https://doi.org/10.1088/1361-6463/aaa58c).
- [164] Bum-Kyu Kim et al. “Origins of genuine Ohmic van der Waals contact between indium and MoS_2 ”. In: *npj 2D Materials and Applications* 5 (16 Dec. 2021), p. 9. DOI: [10.1038/s41699-020-00191-z](https://doi.org/10.1038/s41699-020-00191-z).
- [165] Jozef Osvald. “Back-to-back connected asymmetric Schottky diodes with series resistance as a single diode”. In: *physica status solidi (a)* 212.12 (16 Apr. 2015), pp. 2754–2758. DOI: [10.1002/pssa.201532374](https://doi.org/10.1002/pssa.201532374).
- [166] Yonatan Vaknin, Ronen Dagan, and Yossi Rosenwaks. “Schottky Barrier Height and Image Force Lowering in Monolayer MoS_2 Field Effect Transistors”. In: *Nanomaterials* 10.12 (16 Apr. 2020), p. 166401. ISSN: 2079-4991. DOI: [10.3390/nano10122346](https://doi.org/10.3390/nano10122346).
- [167] Jeremy M. Beebe et al. “Transition from Direct Tunneling to Field Emission in Metal-Molecule-Metal Junctions”. In: *Phys. Rev. Lett.* 97 (2 July 2006), p. 026801. DOI: [10.1103/PhysRevLett.97.026801](https://doi.org/10.1103/PhysRevLett.97.026801).
- [168] Ping V. Lin. *WolfrAlpha computational intelligence*. <https://www.wolframalpha.com/>. Accessed: 2022-06-22. Apr. 2015. DOI: [10.1103/PhysRevLett.114.166401](https://doi.org/10.1103/PhysRevLett.114.166401).